

# Enhancing the Features of Vertical Axis Wind Turbines with Active Flap Control and Airfoil Design

Sercan Ertem

21 August 2015

Image copyright: Technip / Nenuphar / EDF EN





# **Enhancing the Features of Vertical Axis Wind Turbines with Active Flap Control and Airfoil Design**

MASTER OF SCIENCE THESIS

For obtaining the degree of Master of Science in Engineering Wind  
Energy at Technical University of Denmark and in Aerospace  
Engineering at Delft University of Technology.

Sercan Ertem

21 August 2015

European Wind Energy Master - EWEM  
DUWIND - Delft University of Technology  
DTU Wind Energy - Denmark Technical University



DTU Wind Energy  
Department of Wind Energy



Copyright © Sercan Ertem  
All rights reserved.

EUROPEAN WIND ENERGY MASTER - EWEM  
OF  
ROTOR DESIGN TRACK

The undersigned hereby certify that they have read and recommend to the European Wind Energy Master - EWEM for acceptance a thesis entitled “**Enhancing the Features of Vertical Axis Wind Turbines with Active Flap Control and Airfoil Design**” by **Sercan Ertem** in partial fulfillment of the requirements for the degree of **Master of Science**.

Dated: 21 August 2015

Supervisor:

\_\_\_\_\_  
Dr.ir. Carlos J. Simão Ferreira of TU Delft

Supervisor:

\_\_\_\_\_  
Dr. Mac Gaunaa of DTU Wind Energy

Reader:

\_\_\_\_\_  
Ir. W.A. Timmer of TU Delft

Reader:

\_\_\_\_\_  
Prof. Dr. Gerard J.W. van Bussel of TU Delft



---

# Abstract

In recent years, the research on Vertical Axis Wind Turbines (VAWTs) have been paving the way for the very large-scale (10-20 MW) floating offshore applications. For a cost-effective utilization, VAWTs need to deliver superior aerodynamic and structural performance. Nowadays, the complex flow phenomenon of VAWTs have been better understood and the computational tools have reached to a mature level. It is time to explore the capabilities of this concept and improve its aerodynamic features by innovative design ideas.

The main goal of this thesis is to enhance the performance of the lift-driven VAWTs by customized airfoil design and the active flow control with trailing edge flaps. To achieve the research goals, four main lines of work are carried out: 1) performance exploration of an actuator cylinder, 2) design of the azimuthal flap control sequences, 3) comparison between the Actuator Cylinder Model and Panel Model in the presence of the active flap control and 4) airfoil design that is specified for effective flap operation on a VAWT blade.

The flap control sequences are optimized with the use of the Actuator Cylinder Model for three aerodynamic objectives. These objectives are aiming to improve the power efficiency by maximizing the  $C_P$ , provide a rated power control by minimizing the  $C_P$  and decrease the cyclic load ranges by minimizing the  $C_T$ . Whereas, RFOIL and NSGA-II genetic algorithm are coupled for the airfoil design, which aims for objectives such as superior single airfoil performance, extended flap sensitivity and high flap-wise bending stiffness.

For a rotor solidity of 0.1 operating at tip speed ratio of 4, a 10% active flap is able to increase the  $C_P$  by 7% , decrease the  $C_P$  by 10% and alleviate 12% of the  $C_T$  by sacrificing 3% of the  $C_P$ . It is shown that depending on the solidity, tip speed ratio and the flap authority these figures could be increased. It is possible to brake the rotor with a relatively larger flap authority. The airfoils designed in this work are slightly cambered and span from 27% to 35% thickness, deliver higher maximum  $C_P$  than a NACA 0018, show good performance in the dirty conditions and have high flap effectivity.

Overall, the performance gains acquired by the new airfoils and flap control promises extensive improvements in multiple features of VAWTs such as power efficiency, power control, load control that lead to reduced weight and decreased Cost of Energy.



---

# Acknowledgements

This document marks the end of an influential era in my life. I should first thank to the anonymous people who provided me a priceless opportunity with a full-scholarship for the European Wind Energy Master. Later, big thanks go to each person that gave us lectures in DTU and TU Delft. I am sure that the methodologies and ideas I have created during the thesis would not be realized without the knowledge and engineering jargon that they have given us.

For the thesis work, the biggest gratitude goes to Carlos Ferreira for offering me this fantastic subject and supervising me in a great extent despite his busy schedule. I would not grasp VAWTs without his critical perspectives on my results. Secondly, thanks to Mac Gaunaa for supervising me as much as possible from Denmark. His feedbacks during the DTU special course and thesis period have increased the quality of this thesis. Thanks to Helge Madsen for being my un-official supervisor. His helps on the Actuator Cylinder Model and HAWC2 gave me speed and self-confidence. I am grateful to Rody Kemp for providing me the tips and tricks for the panel code and the airfoil optimizer. I am also thankful to Gael de Oliveira for sharing the base code for the airfoil optimization.

The state-of-the-art education has only been the tip of the iceberg during past two years. The most valuable gain of mine was the group of great people with big warm hearts from the globe. We enjoyed the life, we shared journeys, we exchanged perspectives and we transformed ourselves. Finally, the biggest thanks goes to my mom and dad, Gulsen and Mahmut Ertem. While I was becoming the master of science, they were mastering how to support me from home as much as possible. If there was a school of life they would obtain a cum laude for the past efforts.

Again and again thanks for everybody who have contributed to the person and the engineer who I am today.

Delft, The Netherlands  
21 August 2015

Sercan Ertem



---

# Contents

<b>Abstract</b>	<b>v</b>
<b>Acknowledgements</b>	<b>vii</b>
<b>List of Figures</b>	<b>xi</b>
<b>List of Tables</b>	<b>xiii</b>
<b>1 Introduction</b>	<b>1</b>
1.1 Research aim and questions . . . . .	2
1.2 Methodology of the work . . . . .	3
<b>2 Literature Review</b>	<b>5</b>
2.1 VAWT aerodynamics . . . . .	5
2.2 Aerodynamic models . . . . .	8
2.3 Circulation control of a VAWT rotor . . . . .	13
2.4 Airfoil design . . . . .	18
<b>3 Exploring the <math>C_P - C_T</math> Relation of the Actuator Cylinder</b>	<b>27</b>
3.1 Implementation of the Actuator Cylinder Model (ACM) . . . . .	27
3.1.1 The validation of the code . . . . .	30
3.2 Exploring the design space of the actuator cylinder by analytic expressions of the loadforms . . . . .	32
3.2.1 A parametric study to explore the $C_P - C_T$ relations . . . . .	32
3.2.2 Optimization of the loadforms to obtain the $C_{P,max} - C_T$ curve . . . . .	35
3.3 Exploring the design space of the actuator cylinder by Bezier curves . . . . .	36
3.3.1 Unconstrained search . . . . .	37
3.3.2 Constrained search . . . . .	38
3.4 Conclusions of the chapter . . . . .	40

<b>4</b>	<b>Generation of the Active Flap Control Sequences</b>	<b>43</b>
4.1	Inverse method . . . . .	43
4.1.1	Unconstrained inverse method via optimized loadforms . . . . .	44
4.1.2	Constrained inverse method via hybrid loadforms . . . . .	46
4.2	Direct method . . . . .	48
4.2.1	Direct method with inviscid airfoil polars . . . . .	48
4.2.2	Direct method with a viscous NACA 0018 polar . . . . .	59
4.3	Conclusions of the chapter . . . . .	64
<b>5</b>	<b>Assessment of the Active Flap Control with the 2-D Panel Code</b>	<b>67</b>
5.1	Performance of the NACA 0018 airfoil (the reference case) . . . . .	68
5.2	$C_P$ maximization . . . . .	70
5.3	$C_P$ minimization . . . . .	76
5.4	$C_T$ minimization . . . . .	78
5.5	New wake paths . . . . .	81
5.6	Conclusions of the chapter . . . . .	83
<b>6</b>	<b>Airfoil Design for the VAWT Blades with Active Trailing Edge Flaps</b>	<b>85</b>
6.1	Airfoil Design: The requirements and the methodology . . . . .	85
6.1.1	Airfoil design requirements . . . . .	85
6.1.2	The airfoil design methodology . . . . .	87
6.2	Performance analysis of the new airfoils . . . . .	94
6.2.1	MGS-270 . . . . .	96
6.2.2	MGS-279 . . . . .	97
6.2.3	MGS-292 . . . . .	99
6.2.4	MGS-313 . . . . .	101
6.2.5	Performance and characteristic comparisons . . . . .	102
6.3	Conclusions of the chapter . . . . .	108
<b>7</b>	<b>Final Remarks</b>	<b>111</b>
7.1	Conclusion . . . . .	111
7.2	Future work . . . . .	112
	<b>References</b>	<b>115</b>
<b>A</b>	<b>MGS airfoils</b>	<b>121</b>

---

## List of Figures

2.1	$F_T$ and $F_N$ for different fixed pitch settings (PM:Panel Method, VTM: Vorticity-Transport Model) [20]. . . . .	6
2.2	Geometric angle of attack affected by an induction field [55]. . . . .	6
2.3	A demonstration of blade-wake interaction [55]. . . . .	8
2.4	Loading on the actuator cylinder [44]. . . . .	10
2.5	Horseshoe model formed by the vortex system [32]. . . . .	11
2.6	Representation of a wing by panels [32]. . . . .	12
2.7	The angle of attack and tangential force for moderately loaded case[19]. . . . .	13
2.8	Optimum pitch angle to maximize the torque coefficient area [43]. . . . .	15
2.9	Control authority of different flow control systems [2]. . . . .	17
2.10	Comparison of the SAND 0015/47 and NACA 0015 [37]. . . . .	18
2.11	Comparison of the GUYA10 and NACA 0018 [23]. . . . .	20
2.12	Comparison of the DU 06-W-200 with NACA 0018 [7]. . . . .	21
2.13	The Air001 airfoil and its performance in a VAWT rotor [17]. . . . .	22
2.14	A VAWT specific airfoil: DU12-W-262 [54]. . . . .	22
2.15	The optimized airfoils for different design strategies [33]. . . . .	23
2.16	Constraints on the $C_l$ curve for the stall region [8]. . . . .	24
3.1	The coordinate system used for the ACM implementation in Matlab. . . . .	28
3.2	Validation of the ACM in Matlab, the $C_P$ and $C_T$ . . . . .	31
3.3	Validation of the ACM in Matlab, the $Q_n$ and $Q_t$ . . . . .	31
3.4	Validation of the ACM in Matlab, the $w_x$ and $w_y$ . . . . .	31
3.5	The global view on the $C_P$ - $C_T$ relation of the VAWT. . . . .	33
3.6	A closer look to the high $C_P$ region. . . . .	33

3.7	Loadforms with the same $C_P$ but different $C_T$ . . . . .	34
3.8	Loadforms with same the $C_T$ but different $C_P$ . . . . .	35
3.9	Optimized analytic loadforms for maximizing and minimizing the $C_P$ . . .	36
3.10	Sensitivity analysis on the Bezier curve order (for the loadform analysis).	37
3.11	Optimized Beizer loadforms for maximizing and minimizing the $C_P$ . . . .	38
3.12	Reference loadforms used to set the bounds of the design space. . . . .	38
3.13	Optimized loadforms by the constrained Bezier curves to the 15% of the $Q_{n_{ref,max}}$ . . . . .	39
3.14	$C_P$ improvement on the reference loadforms with different values of constraints ( $f_{\Delta Q_n}$ ). . . . .	40
3.15	$C_P$ alleviation on the reference loadforms with different values of constraints ( $f_{\Delta Q_n}$ ). . . . .	40
4.1	Normal loading ( $Q_n$ ) of the reference and optimized loadforms. . . . .	44
4.2	Required flap sequences to obtain the optimized analytic loadform. . . . .	45
4.3	Required flap sequences to obtain the optimized loadform by a unconstrained Bezier curve. . . . .	46
4.4	Required flap sequences to obtain the optimized loadform by a constrained Bezier curve with $f_{\Delta Q_n}$ of 30%. . . . .	46
4.5	Normal loading ( $Q_n$ ), induction velocities ( $w_x$ , $w_y$ ) and flap angles ( $\beta$ ) obtained by limiting the flap deflection of a hybrid loadform. . . . .	47
4.6	Reference turbine performance ( $C_P$ and $C_T$ ). . . . .	49
4.7	Optimized $C_P$ and the improvement in $C_P$ when $\beta_{range}$ is $\pm 10$ degrees. .	50
4.8	Optimized $C_P$ and the improvement in $C_P$ when $\beta_{range}$ is $\pm 20$ degrees. .	50
4.9	Optimized $C_P$ and the improvement in $C_P$ when $\beta_{range}$ is $\pm 30$ degrees. .	50
4.10	Improvement in the $C_P$ for all cases and for all deflection constraints. . .	51
4.11	Optimized flap sequences for various $\sigma$ and $\lambda$ when $\beta_{range}$ is $\pm 20$ degrees ( $C_P$ maximization case) . . . . .	52
4.12	Comparison of the optimized loadforms and sequences ( $C_P$ maximization case). . . . .	52
4.13	Optimized $C_P$ and the alleviation in $C_P$ when $\beta_{range}$ is $\pm 10$ degrees. . .	53
4.14	Optimized $C_P$ and the alleviation in $C_P$ when $\beta_{range}$ is $\pm 20$ degrees. . .	53
4.15	Optimized $C_P$ and the alleviation in $C_P$ when $\beta_{range}$ is $\pm 30$ degrees. . .	54
4.16	Alleviation in the $C_P$ for all cases and for all deflection constraints. . . . .	54
4.17	Optimized flap sequences for various $\sigma$ and $\lambda$ when $\beta_{range}$ is $\pm 20$ degrees ( $C_P$ minimization case). . . . .	55
4.18	Comparison of the optimized loadforms and sequences ( $C_P$ minimization case). . . . .	56
4.19	Optimized $C_T$ and the alleviation in $C_T$ when $C_{P,gap}$ is $\pm 0.00$ . . . . .	56
4.20	Optimized $C_T$ and the alleviation in $C_T$ when $C_{P,gap}$ is $\pm 0.03$ . . . . .	57
4.21	Optimized $C_T$ and the alleviation in $C_T$ when $C_{P,gap}$ is $\pm 0.05$ . . . . .	57

4.22	Alleviation in the $C_T$ for all cases when the $\beta_{range}$ is $\pm 20$ degrees. . . . .	58
4.23	Optimized flap sequences for various $\sigma$ and $\lambda$ when $C_{P,gap}$ is $\pm 0.05$ ( $C_T$ minimization case). . . . .	58
4.24	Comparison of the optimized loadforms and sequences ( $C_T$ minimization case). . . . .	59
4.25	Flap sensitivity ( $C_{l\beta}$ ) of the viscous airfoil polars. . . . .	59
4.26	$C_P$ and $C_T$ comparisons for the viscous $C_P$ maximization case. . . . .	60
4.27	Optimized flap sequences for the $C_P$ maximization with different flap sizes. . . . .	61
4.28	$C_P$ and $C_T$ comparisons for the viscous $C_P$ minimization case. . . . .	61
4.29	Optimized flap sequences for the $C_P$ minimization with different flap sizes. . . . .	62
4.30	$C_P$ and $C_T$ comparisons for the viscous $C_T$ minimization case. . . . .	63
4.31	Optimized flap sequences for the $C_T$ minimization with different flap sizes. . . . .	63
5.1	The coordinate system and active flap configuration. . . . .	68
5.2	$Q_n$ and $Q_t$ calculated by the panel model and ACM at $\lambda = 4$ without the active flap. . . . .	69
5.3	$Q_n$ and $Q_t$ calculated by the panel model and ACM at $\lambda = 6$ without the active flap. . . . .	69
5.4	Angle of attack and axial induction calculated by the panel model and ACM at $\lambda = 4$ without the active flap. . . . .	69
5.5	Angle of attack and axial induction calculated by the panel model and ACM at $\lambda = 6$ without the active flap. . . . .	70
5.6	Flap sequences applied for the $C_P$ maximization with the 10% flap. . . . .	71
5.7	$Q_n$ and $Q_t$ calculated by the panel model and ACM at $\lambda = 4$ with the 10% flap for the $C_P$ maximization case. . . . .	71
5.8	$Q_n$ and $Q_t$ calculated by the panel model and ACM at $\lambda = 6$ with the 10% flap for the $C_P$ maximization case. . . . .	71
5.9	Angle of attack and axial induction calculated by the panel model and ACM at $\lambda = 4$ with the 10% flap for the $C_P$ maximization case. . . . .	72
5.10	Angle of attack and axial induction calculated by the panel model and ACM at $\lambda = 6$ with the 10% flap for the $C_P$ maximization case. . . . .	72
5.11	Flap sequences applied for the $C_P$ maximization with the 20% flap for the $C_P$ maximization case. . . . .	73
5.12	$Q_n$ and $Q_t$ calculated by the panel model and ACM at $\lambda = 4$ with the 20% flap for the $C_P$ maximization case. . . . .	74
5.13	$Q_n$ and $Q_t$ calculated by the panel model and ACM at $\lambda = 6$ with the 20% flap for the $C_P$ maximization case. . . . .	74
5.14	Angle of attack and axial induction calculated by the panel model and ACM at $\lambda = 4$ with the 20% flap for the $C_P$ maximization case. . . . .	74
5.15	Angle of attack and axial induction calculated by the panel model and ACM at $\lambda = 6$ with the 20% flap for the $C_P$ maximization case. . . . .	75
5.16	Flap sequences applied for the $C_P$ minimization with the 10% flap. . . . .	76
5.17	$Q_n$ and $Q_t$ calculated by the panel model and ACM at $\lambda = 4$ with the 10% flap for the $C_P$ minimization case. . . . .	76

5.18	$Q_n$ and $Q_t$ calculated by the panel model and ACM at $\lambda = 6$ with the 10% flap for the $C_P$ minimization case. . . . .	77
5.19	Angle of attack and axial induction calculated by the panel model and ACM at $\lambda = 4$ with the 10% flap for the $C_P$ minimization case. . . . .	77
5.20	Angle of attack and axial induction calculated by the panel model and ACM at $\lambda = 6$ with the 10% flap for the $C_P$ minimization case. . . . .	77
5.21	Flap sequences applied for the $C_T$ minimization with the 10% flap. . . . .	79
5.22	$Q_n$ and $Q_t$ calculated by the panel model and ACM at $\lambda = 4$ with the 10% flap for the $C_T$ minimization case. . . . .	79
5.23	$Q_n$ and $Q_t$ calculated by the panel model and ACM at $\lambda = 6$ with the 10% flap for the $C_T$ minimization case. . . . .	79
5.24	Angle of attack and axial induction calculated by the panel model and ACM at $\lambda = 4$ with the 10% flap for the $C_T$ minimization case. . . . .	80
5.25	Angle of attack and axial induction calculated by the panel model and ACM at $\lambda = 6$ with the 10% flap for the $C_T$ minimization case. . . . .	80
5.26	Wake path and the flap sequence for undeflected case at $\lambda = 3$ . . . . .	82
5.27	Wake path and the flap sequence for $C_P$ maximization case with 10% flap at $\lambda = 3$ . . . . .	82
5.28	Wake path and the flap sequence for $C_P$ minimization case with 10% flap at $\lambda = 3$ . . . . .	82
5.29	Wake path and the flap sequence for $C_T$ minimization case with 10% flap at $\lambda = 3$ . . . . .	83
6.1	Optimization structure. . . . .	88
6.2	Creation of the hybrid polars. . . . .	90
6.3	An example of the design space bounded by the upper and lower values for each surface. . . . .	92
6.4	An example of the pareto front. . . . .	95
6.5	Geometry of the MGS-270. . . . .	96
6.6	Aerodynamic polars of the MGS-270. . . . .	97
6.7	VAWT performance of the undeflected MGS-270 for the clean and dirty conditions. . . . .	97
6.8	Geometry of the MGS-279. . . . .	98
6.9	Aerodynamic polars of the MGS-279. . . . .	98
6.10	VAWT performance of the undeflected MGS-279 for the clean and dirty conditions. . . . .	99
6.11	Geometry of the MGS-292. . . . .	99
6.12	Aerodynamic polars of the MGS-292. . . . .	100
6.13	VAWT performance of the undeflected MGS-292 for the clean and dirty conditions. . . . .	100
6.14	Geometry of the MGS-313. . . . .	101
6.15	Aerodynamic polars of the MGS-313. . . . .	101
6.16	VAWT performance of the undeflected MGS-313 for the clean and dirty conditions. . . . .	102
6.17	Comparison of the MGS airfoil geometries. . . . .	103

---

6.18	Comparison of the flap sensitivities. . . . .	103
6.19	Boundary layer transition location of the airfoils in the clean conditions. . .	104
6.20	Comparison of the VAWT performances at clean and dirty conditions. . .	105
6.21	Performance of the undeflected airfoils in the ACM both for the clean and dirty airfoils - The reference case. . . . .	106
6.22	Performance of the clean and dirty airfoils in the presence of active flap control (10% flap with $\pm 20^\circ$ deflection). . . . .	106
6.23	Normalized optimization scores of all the airfoils. . . . .	108
A.1	Geometry of the MGS-269. . . . .	122
A.2	Aerodynamic polars of the MGS-269. . . . .	122
A.3	VAWT performance of the undeflected MGS-269 for the clean and dirty conditions. . . . .	122
A.4	Geometry of the MGS-283. . . . .	123
A.5	Aerodynamic polars of the MGS-283. . . . .	123
A.6	VAWT performance of the undeflected MGS-283 for the clean and dirty conditions. . . . .	123
A.7	Geometry of the MGS-286. . . . .	124
A.8	Aerodynamic polars of the MGS-286. . . . .	124
A.9	VAWT performance of the undeflected MGS-286 for the clean and dirty conditions. . . . .	124
A.10	Geometry of the MGS-309. . . . .	125
A.11	Aerodynamic polars of the MGS-309. . . . .	125
A.12	VAWT performance of the undeflected MGS-309 for the clean and dirty conditions. . . . .	125
A.13	Geometry of the MGS-322. . . . .	126
A.14	Aerodynamic polars of the MGS-322. . . . .	126
A.15	VAWT performance of the undeflected MGS-322 for the clean and dirty conditions. . . . .	126
A.16	Geometry of the MGS-331. . . . .	127
A.17	Aerodynamic polars of the MGS-331. . . . .	127
A.18	VAWT performance of the undeflected MGS-331 for the clean and dirty conditions. . . . .	127
A.19	Geometry of the MGS-343. . . . .	128
A.20	Aerodynamic polars of the MGS-343. . . . .	128
A.21	VAWT performance of the undeflected MGS-343 for the clean and dirty conditions. . . . .	128
A.22	Geometry of the MGS-349. . . . .	129
A.23	Aerodynamic polars of the MGS-349. . . . .	129
A.24	VAWT performance of the undeflected MGS-349 for the clean and dirty conditions. . . . .	129



---

# List of Tables

2.1	Classification of the active flow control systems [30]. . . . .	16
4.1	$C_P$ of the reference, the optimum and the hybrid loadform with the percent gains in the performance. . . . .	48
4.2	Percentage gains in the $C_P$ by the 10% and the 20% flaps. . . . .	60
4.3	Percentage alleviation in the $C_P$ for different flap sizes. . . . .	62
4.4	Percentage alleviation in the $C_T$ for different $C_{P,gap}$ . . . . .	63
5.1	Comparison of the reference $C_P$ and $C_T$ between the panel model and ACM for a single element airfoil. . . . .	70
5.2	Comparison of the $C_P$ and $C_T$ estimated by the panel model and ACM with the 10% active flap for the $C_P$ maximization case. . . . .	73
5.3	Comparison of the $C_P$ and $C_T$ estimated by the panel model and ACM with the 20% active flap for the $C_P$ maximization case. . . . .	75
5.4	Comparison of the $C_P$ and $C_T$ estimated by the panel model and ACM with the 10% active flap for the $C_P$ minimization case. . . . .	78
5.5	Comparison of the $C_P$ and $C_T$ estimated by the panel model and ACM with the 10% active flap for the $C_T$ minimization case. . . . .	81
6.1	Penalty functions used in the airfoil optimization. . . . .	93
6.2	Structural properties of the airfoils. . . . .	103
6.3	Aerodynamic properties of the airfoils. . . . .	104
6.4	Improvements in the $C_P$ in the clean and dirty conditions of airfoils with 10% flap. . . . .	107
6.5	CST variables for the MGS airfoils (270, 279, 292, 313). . . . .	108
A.1	CST variables for the MGS airfoils (269, 283, 286, 309). . . . .	121
A.2	CST variables for the MGS airfoils (322, 331, 343, 348). . . . .	121



---

# Nomenclature

## Latin Symbols

$B$	Number of blades
$C_d$	Drag coefficient [-]
$C_{d0}$	Drag coefficient at zero angle of attack [-]
$\frac{c_f}{c}$	Relative flap length [-]
$c$	Chord length [ $m$ ]
$C_l$	Lift coefficient [-]
$C_{l\alpha}$	Lift curve slope [ $1/\text{rad.}$ ]
$C_{l\beta}$	Flap sensitivity on the lift [ $\frac{1}{\text{deg.}}$ ]
$\frac{C_l}{C_d}$	Lift-to-drag ratio [-]
$C_{l,design}$	Lift coefficient at best glide ratio [-]
$C_{l0}$	Lift coefficient at zero angle of attack [-]
$C_P$	Power coefficient [-]
$C_{P,gap}$	Deviation ratio from the reference $C_P$ [-]
$C_{Pi}$	Ideal power coefficient [-]
$C_T$	Thrust coefficient [-]
$f_{\Delta Q_n}$	Deviation ratio from the reference load [-]
$f_{hybrid}$	Mixing ratio between two loadforms [-]
$F_t$	Tangential force on the blade [N]
$F_n$	Normal force on the blade [N]
$\Gamma_b$	Strength of the bound vortex [ $m^2/s$ ]
$(\frac{h}{c})_{max}$	Maximum relative camber of airfoil [-]

---

$I_{xx}$	Area moment of inertia in x-axis [ $m^4$ ]
$I_{yy}$	Area moment of inertia in y-axis [ $m^4$ ]
$m$	Exponential to create an analytic loadform [-]
$N_{crit}$	Amplification factor for boundary layer transition in X/RFOIL [-]
$Q_n$	Non-dimensional normal loading [-]
$Q_{n,max}$	Maximum magnitude in the normal loading [-]
$Q_t$	Non-dimensional tangential loading [ $m/s$ ]
$R$	Rotor radius [ $m$ ]
$Re$	Reynolds number [-]
$\frac{R_{LE}}{c}$	Normalized leading edge radius [-]
$X_{tr}$	Boundary layer transition location on chord [-]
$R_{wx}$	Influence coefficients for axial induction [-]
$R_{wy}$	Influence coefficients for lateral induction [-]
$(\frac{t}{c})_{max}$	Maximum relative thickness of airfoil [-]
$t_{TE}$	Trailing edge thickness [ $m$ ]
$V_\infty$	Free stream velocity [ $m/s$ ]
$V_n$	Normal velocity component [ $m/s$ ]
$V_{rel}$	Relative velocity [ $m/s$ ]
$w_x$	Axial induction velocity [-]
$w_y$	Lateral induction velocity [-]

## Greek Symbols

$\alpha$	Angle of attack [deg.]
$\alpha_{stall}$	Angle of attack at stall [deg.]
$\beta$	Flap deflection [deg.]
$\beta^-$	An arbitrary negative flap deflection [deg.]
$\beta^+$	An arbitrary positive flap deflection [deg.]
$\beta_{range}$	Maximum absolute flap deflection [deg.]
$\Delta\alpha$	An arbitrary angle of attack range [deg.]
$\Delta\theta$	Shift in the azimuth position [deg.]
$\lambda$	Tip speed ratio [-]
$\omega$	Rotational speed [rad./s]
$\rho$	Air density [ $kg/m^3$ ]
$\theta_{TE}$	Trailing edge angle [deg.]
$\sigma$	Rotor solidity [-]
$\theta$	Azimuth position [deg.]

$\theta_p$  Blade pitch angle [deg.]

## Abbreviations

*ACM* Actuator Cylinder Model

*BEM* Blade Element Momentum Model

BWI Blade-Wake Interaction

CoE Cost of Energy

*CST* Class-Shape Transformation

HAWT Horizontal Axis Wind Turbine

*J* Optimization objective

*J<sub>AERO</sub>* Aerodynamic objective for airfoil design

*J<sub>STRUCT</sub>* Structural objective for airfoil design

*Mod – Lin* Modified-Linear

*PM* Panel Model

VAWT Vertical Axis Wind Turbine



---

# Chapter 1

---

## Introduction

Cost of Energy (CoE) is the main driver in the wind energy research. Most of the studies are constructed around the aim of reducing the CoE so that the wind power could become a major energy source. European Wind Energy Technology Platform states that the need for an advanced and innovative rotor design for very large floating offshore applications are required to decrease the CoE [14]. Similarly, European Wind Energy Association (EWEA) prioritize the introduction of very large scale (10-20 MW) wind turbine design in their strategic technology areas list [13]. For this type of applications VAWTs comes into the focus due to its inherent features which might be advantageous over HAWTs. Unlike HAWTs, the center of gravity location of VAWTs is closer to the ground and there are easy manufacturing and maintenance possibilities which makes VAWTs competitive for future large offshore applications [69]. Moreover VAWT blades experience less gravitational fatigue due to the orientation of its blades. Although the modern VAWT has lower power conversion efficiency than a modern HAWT, it is believed that there is a large design space to enhance VAWTs' aerodynamic performance. Such improvements could be obtained by innovative airfoil design, blade design and the circulation control design. In this work, an attempt is taken to document the gains that could be obtained with the co-operation of the active trailing edge flaps and novel airfoils.

Until now, the vast majority of the circulation control research for VAWTs has been carried out by using the variable pitch control systems. On the other hand, the active flap control becomes a powerful candidate to enhance the capabilities of VAWTs when very-large scale (10-20 MW) applications are considered. The pitch control of a very large blade would demand large actuation power and spend relatively longer times to act due to the excessive blade inertia. Conceptually, the flap control would have faster response time, require less actuation power, smaller actuators and bearings. Therefore, the flapped blade could be more cost efficient than the pitch controlled blade. Furthermore, the application of the blade pitching is limited to the H-rotor concept where the discretized flaps could easily be applied to any rotor concept. On the other hand, the flap usage will neutralize one of the biggest features of VAWTs', the insensitivity to the wind direction. In the presence of a cyclic flap actuation the phase of the actuation signal should be shifted with

the wind direction. This is a case for any active control design on VAWTs and can be accepted if it leads to a cheaper energy conversion.

In past, symmetric airfoils were widely used in the manufactured VAWT blades. Moreover, most of the past airfoil designs were done by using NACA 4-series as a baseline. The symmetrical airfoils were believed to be the most appropriate choice for VAWTs since both of the airfoil surfaces act as the suction and the pressure side depending on the azimuth position. The modern research showed that the optimum performance lays in the slightly cambered airfoils. There are several noticeable works but this research field is far from being mature. Therefore, this work introduces a new airfoil design methodology that is specified for the VAWT blades with the active trailing edge flaps.

In this study, a wide range of topics are covered to establish a reference study for the flap control and the airfoil design of the lift-driven VAWT. The work can be classified in 4 main sections. First, the  $C_P - C_T$  relations of the VAWT with infinite number of blades are explored. This section tries to answer the potentials of VAWTs with the flow model named as the Actuator Cylinder Model. Secondly, the inverse and direct methods to attain the optimum flap sequences are introduced. Azimuthal sequences of the flap actuation are optimized to document the flap control authority on VAWTs for various aerodynamic objectives. These studies are done by using the modified-linear derivation of the Actuator Cylinder Model. Later, a 2D inviscid unsteady panel model (PM) is used to verify the gains obtained by the Actuator Cylinder Model (ACM). The differences between the ACM and PM are documented for various types of flap objectives. Finally, the airfoil design study is carried out. This is done by using a tool that couples multi-objective genetic algorithm with the RFOIL flow solver. A unique objective function is suggested to increase the performance of the airfoil with a trailing edge flap for the VAWT operation.

## 1.1 Research aim and questions

**Research aim:** The main goal of this thesis is to decrease the cost of energy of the Vertical-Axis Wind Turbine concept by applying innovative design approaches on the aerodynamic shape design and load control.

**Research question:** How much performance enhancement on the aerodynamic and operational features of VAWTs could be obtained by the active flap control and the tailored airfoils ?

The sub-questions to answer the research question are constructed as:

1. Which aerodynamic models/tools are appropriate for the use with the numerical optimizer to design the flap control and airfoils ?
  - (a) What is the classification of the existing models in the means of fidelity and computation time ?
  - (b) Which of the aerodynamic phenomena could be discarded for the sake of computational time ?

2. How could the flap control enhance the capabilities and the performance of the VAWT rotor ? Could the flap be used for multiple purposes ?
  - (a) What sort of tasks (e.g. load control) could be done with a trailing edge flap ?
  - (b) What should be the methodology to obtain optimum flap sequences ?
  - (c) What is the appropriate size and deflection limitations of the flap ?
3. What are the design requirements for a robust VAWT airfoil both from the aerodynamic and the structural point of view ?
  - (a) How could a new airfoil design methodology be defined so that the airfoil would be tailored for the active flap operation ?
  - (b) What are the target airfoil properties in order to have enhanced aerodynamics both in design point and the off-design conditions ?
  - (c) What are the structural objectives of the VAWT airfoil ? Which structural failure types are more critical for a VAWT blade ? How could the structural objectives be assessed ?
4. How should the numerical optimization techniques be used so that the optimum design could be obtained both for the airfoil design and the flap control sequences ?
  - (a) Which optimization algorithm(s) should be used for the definition of flap control sequence and the airfoil design ?
  - (b) How could the objective function, constraints and design bounds be defined according to the design requirements both for the airfoil and flap control sequence?

## 1.2 Methodology of the work

Each chapter of this work contains many methodologies to answer the research questions. Here, only the main components of the methodology will be introduced. One can find detailed explanations in the further chapters. Main components of the methodology along this study can be listed within their chapters as:

- CHAPTER 2: Review the existing relevant research for the topic and make deductions for the work to be carried out.
- CHAPTER 3: Explore the  $C_P - C_T$  relation of an actuator cylinder by the help of the non-dimensional normal loadings ( $Q_n$ )
  - Implement the modified-linear (Mod-Lin) derivation of the Actuator Cylinder Model (ACM) in Matlab. Validate with the HAWC2 [40].
  - Use the Mod-Lin ACM to simulate the performance of a VAWT with infinite number of blades, the actuator cylinder.
  - Use the normal loadforms ( $Q_n$ ) to assess the performance of the actuator cylinder. Create new loadforms by two methods: 1) Analytic loadform expressions, 2) Bezier curves.

- Couple a numerical optimizer to the loadform generation to explore new loadforms in a robust fashion.
- Study the gains in performance of an actuator cylinder both in unconstrained and constrained design space. Build the link between the circulation system for an actuator cylinder and the circulation control demands for a VAWT with finite number of blades.
- CHAPTER 4: Generate the optimized flap control sequences by establishing the inverse and the direct methods.
  - Use the Mod-Lin ACM to simulate the VAWT performance.
  - The inverse method: Derive the required flap angles analytically to obtain a target loadform that has a favorable performance. The target loadforms are the optimum loadforms found in the previous chapter.
  - The direct method: Create an arbitrary flap sequence curve and assess its performance. Couple a numerical optimizer to the ACM in order to find the favorable flap sequences out of a wide design space. Define the flap sequence signals by the Bezier curves.
  - Obtain the optimized flap sequences for different aerodynamic objectives. Those objectives are: 1) maximizing the  $C_P$ , 2) minimizing the  $C_P$  and 3) minimizing the  $C_T$  for a given tolerance on the initial  $C_P$ .
  - Do the analysis and the optimization with the inviscid airfoil polars. Study only one viscous case to observe the preliminary viscous effects.
- CHAPTER 5: Use the unsteady, inviscid 2-D panel code (U2DiVA) to verify the performance of the flap control sequences found in the previous section.
  - Compare the results obtained by the ACM with the panel model estimations.
- CHAPTER 6: Design an airfoil family for the VAWT blades with active trailing edge flaps.
  - Define the airfoil design requirements for the VAWT operation.
  - Define the airfoil design methodology, design objectives and design constraints.
  - Verify the performance of the new airfoils with the panel model.
  - Demonstrate an active flap control of the new airfoils.

---

## Chapter 2

---

# Literature Review

This chapter summarizes the past research on the fields that are critical to understand and answer the research question of the thesis. First of all, the fundamental aerodynamic phenomenons for the VAWT airfoil are summarized. Later, the aerodynamic models to estimate the VAWT performance are introduced in the order of computational fidelity. The second section presents the knowledge on the circulation control of a VAWT rotor. In that section, first, the research on the blade pitch control then the relevant research on the trailing edge flaps are documented. At last, the past airfoil design works on the VAWT research are given. Moreover, the studies on the HAWT airfoil design are shortly mentioned since that field is more mature and might give insight for the case in this thesis work.

### 2.1 VAWT aerodynamics

In this section the most important phenomenons over the VAWT blade are introduced. First of all, the explanation of the energy conversion process of VAWT is made. Later one can see the introduction to the dynamic stall, flow curvature, blade-wake interaction and viscosity effects on the rotor.

#### Energy conversion

The energy exchange for the VAWT is a 2D phenomenon which consists of the bound and shed vorticity [18]. This feature creates the biggest difference in energy conversion process between the HAWT and the VAWT. Ferreira mentioned that the rate of the shed vorticity, so the rate of azimuthal change in the bound circulation ( $\frac{\partial \Gamma_b}{\partial \theta}$ ) of an airfoil, is strongly related to the wake generation therefore the energy conversion. Moreover, this perspective showed that the bound circulation affects the temporal blade loads and the trailing vorticity is responsible for the additional aerodynamics losses [15].

VAWT has another fundamental difference over HAWT. It has been shown by Ferreira and Scheurich [20] that, in 2D, the instantaneous loads on blades are decoupled from the power generation. The change in the fixed pitch angle transfers the tangential loads between the downwind and upwind regions of rotor. But the integral value (Torque) remains constant. On the other hand, the integral value for the normal loads differ with the change in the fixed pitch angle. Figure 2.1 shows the comparison between normal and tangential loads for different pitch settings and flow models. This effect is also shown in the work of Madsen [44]. Note that these findings are valid for the inviscid case so in real case they can differ slightly due to the viscous contributions.

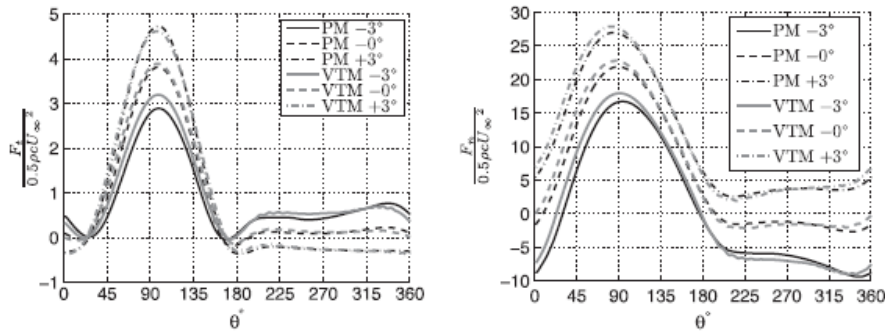


**Figure 2.1:**  $F_T$  and  $F_N$  for different fixed pitch settings (PM:Panel Method, VTM: Vorticity-Transport Model) [20].

### Angle of attack range

It is mentioned that the variation of the bound circulation creates the wake. This variation of the loads are due to the azimuthal changes in the angle of attack ( $\alpha$ ) and the perceived velocity,  $V_{rel}$ . One should consider the contributions due to the induction field as well. The effect of the axial induction over the geometric  $\alpha$  can be seen in Figure 2.2. Geometric angle of attack can be defined as in Equation 2.1. As seen, the VAWT airfoil operates in a wide  $\alpha$  range. For an efficient power production the VAWT airfoil needs to operate quite robustly for a very large  $\alpha$  range.

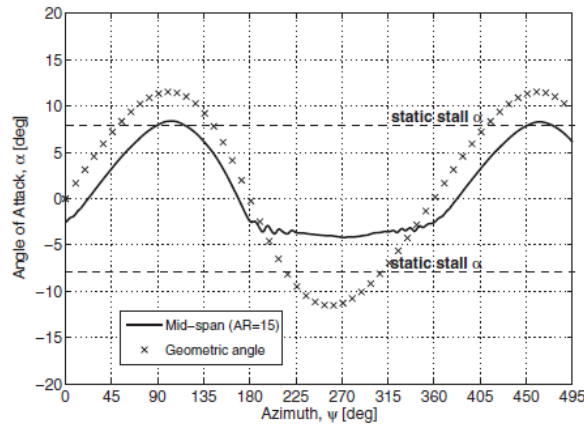


**Figure 2.2:** Geometric angle of attack affected by an induction field [55].

$$\alpha_{geo} = \text{atan} \left( \frac{\sin\theta}{\lambda + \cos\theta} \right) \quad (2.1)$$

## Dynamic stall

Circumferential motion introduces unsteady aerodynamic forces in the 2-D VAWT plane. The rate of angle of attack ( $\frac{d\alpha}{dt}$ ) causes delays both in the stall and the recovery from a post-stall state [36]. Those delays are based on the delays in the boundary layer formation due to the viscous effects. Unsteady operation creates a hysteresis curve so the static polar is not representative. A typical behavior during dynamic stall is that the airfoil shed vortices from the leading edge as well. It has been stated by Fujisawa and Shibuya [22] that the leading edge vortex and the trailing edge vortex acts as two counter rotating vortices where a doublet is formed which moves downstream and thus affects the downwind performance of a VAWT rotor. Troldborg [66] explained the dynamic stall as a combination of the delayed motion of the separation point and the additional suction caused by the leading edge vortex. For the VAWT, Ferreira [15] mentioned that the dynamic stall becomes sensible when high blade solidities operates at low tip-speed ratios.

## Flow curvature

An extra circulatory effect has been seen over VAWT airfoils due to the virtual pitching which arises by the airfoil motion through a radial path. This effect was called in many names as flow curvature, virtual camber or virtual incidence. As the perceived angle of attack changes at each azimuth position, so called, the virtual camber changes azimuthally as well. The flow curvature effects on a Darrieus turbine has been studied by Migliore [49] elaborately. Migliore found that the flow curvature effects are strongly dependent on the blade chord-to-radius,  $\frac{c}{R}$ . It has been reported that the perceived angle of attack along the chord have a  $12^\circ$  difference between the leading edge and the trailing edge for  $\frac{c}{R} = 0.260$  and  $5^\circ$  for  $\frac{c}{R} = 0.114$  [49].

## Blade-wake interaction - BWI

The BWI is another inherent phenomenon that is experienced by the VAWT blades [36]. This effect increases the unsteady features of the downwind passage. Scheurich [55] mentioned that the characteristic of the upwind and the downwind part of the rotor differs significantly from an aerodynamic point of view. Aerodynamic loads are smoothly changing in the upstream while in downstream part the blade experiences series of impulsive and sudden local changes on the loads. BWI creates an impulsive force on the blade therefore decreasing the aerodynamic performance locally and the fatigue life. In general, the aerodynamic loading due to the BWI increases if  $\lambda$  is increased. BWI is increased when the convection velocities are low. In such cases the blade encounters tightly packed wake groups in a rotation. It has also been shown by that the BWI causes transient increase on the angle of attack which could trigger local dynamic stall events [55]. In Figure 2.3 one can see the VTM simulation of a two bladed turbine and the complex downwind flow that the blade passes thorough.

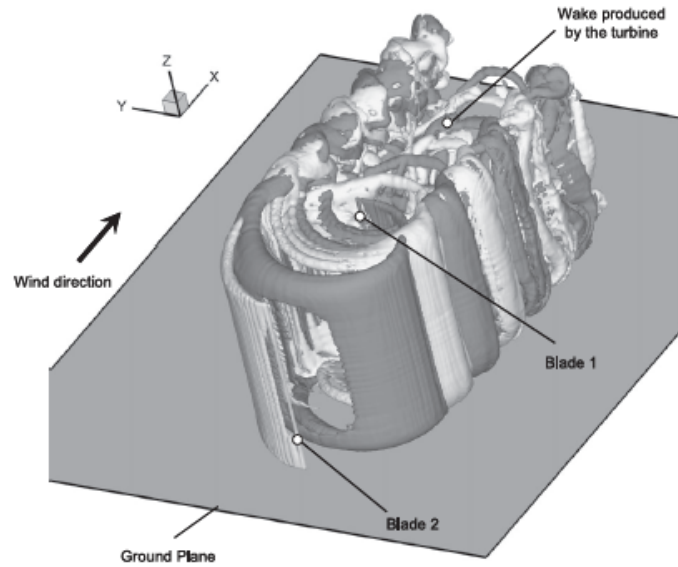


*Figure 2.3: A demonstration of blade-wake interaction [55].*

## Viscosity

The viscosity changes the rate of dissipation of a vortical structure. Moreover, the viscous effects dominate at high angle of attacks and airfoil experiences non-linear aerodynamic effects as de-cambering and stall. In a viscous environment radial pressure gradients arise on the airfoil which changes the state of the boundary layer [49]. During the upwind passage, the airfoil surface facing the rotor center experiences additional favorable pressure gradients while the other side becomes prone to boundary layer separation due to the radial effects. Radial effects are flipped for the airfoil surface at the downwind passage. It has mentioned that the constant bound circulation does not have significant effect on the energy conversion. But in reality this suggestion is not true since the bound circulation changes the flow field via affecting the viscous forces.

## 2.2 Aerodynamic models

### Blade element momentum models (BEM)

BEM models are the most basic and fastest tools to estimate the aerodynamic performance of the VAWT. BEM is based on the conservation of momentum across the actuator disc with a body force. The induction is solved iteratively by balancing the thrust force obtained from the momentum conservation law and the thrust from the blade element forces. Airfoil polars has to be predefined for a BEM model to work.

Single streamtube model (SST) is the earliest model to calculate the VAWT performance which has been derived by Templin [62] in 1974. This simple model assumes a constant induction value for the whole rotor. A single actuator disc lays inside a single stream

tube. To improve the modeling, Strickland [58] derived a model with a single actuator disc with multiple streamtubes (MST). By this way, multiple axial induction values could be assigned to each streamtube that is parallel to the free-stream. MST is known of its good performance for low  $\lambda$  and low  $\sigma$  cases. In 1981, a new model has been derived by Paraschivoiu [51], the double-multiple stream tube (DMST). The DMST is the most complex BEM model for VAWTs that has been derived so far. It places two tandem actuator discs in a flow-field with multiple streamtubes. The upstream rotor affects the downstream rotor by influencing its induction field. Dynamic stall and tip corrections have been implemented to the DMST by many authors. The DMST is appropriate for the light loaded cases in a wide  $\lambda$  range. However, this model can not capture high induction cases as in all of the BEM models. Another inherent characteristic of all BEM models is that they over-predict the efficiency of the rotor.

A misconception in the BEM methods is the treatment to induction as it is a local property of the streamtube [15]. BEM models does not take the distance between the upwind part and the downwind part into account while calculating the inductions, but they accept that the upwind wake is expanded fully inside the rotor [19]. It has been mentioned by Ferreira [15] that the expansion of a streamtube in the free-stream direction is neglected in the BEM models which causes a false estimation of the tangential forces. Madsen [44] mentioned that in BEM models only the axial force component is calculated. Therefore, any BEM model fails down for VAWT by its definition. A Sandia study showed the low accuracy of BEM models when compared with the Sandia 5m and 17m VAWT blade experiments [38].

### Actuator cylinder model (ACM)

The Actuator Cylinder Model has been derived by Madsen [44] in 1982 . Physical representation of the flow is in such detail that this model stands between a BEM model and a vortex/panel model. Unlike the BEM models in the ACM VAWTs has been described as 2D cylinder surface instead of 1D actuator disc. Moreover, the calculation of the induction relies on the Euler equations, a solid physical basis when compared with the BEM models.

The aerodynamic relations in the ACM have directly been derived from the Euler and the continuity equations. As shown in Figure 2.4 the radial and the tangential forces have been applied on the cylinder surface. The existence of the radial forces generates a pressure jump across the cylinder surface. The pressure jump ( $\Delta p$ ) and the perceived velocity ( $V_{rel}$ ) on the cylinder boundary have been used to calculate the power conversion across the surface. Note that the ACM has been derived for a VAWT with infinite number of blades. The finite blade implementation can done by satisfying the total pressure jump on the actuator surface by the blades.

The relation between the blade forces and pressure jump has been solved by introducing the perturbation velocity ( $w_x, w_y$ ) concept. The pressure derivatives in the Euler equation has been balanced by the body forces and the convective forces. Solution of this Poisson type equation reveals that perturbation velocities are the functions of the prescribed body forces (linear part) and the second order induced forces (nonlinear part). Nonlinear solution of the velocities require a mesh in the flow field and increases the computational

cost. The linear solution could be obtained by replacing the body forces with doublets on the cylinder surface so that linear Laplace equation can be solved analytically [44].

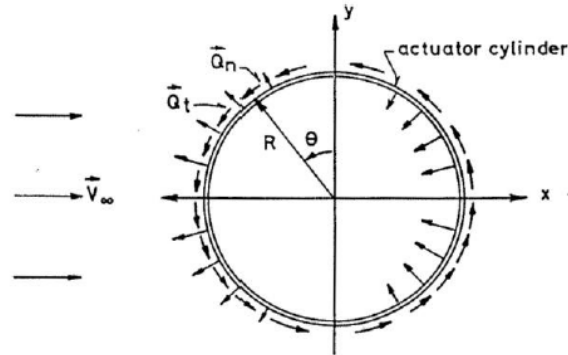


*Figure 2.4: Loading on the actuator cylinder [44].*

Recently there are three different fidelity levels for the ACM, the nonlinear, the linear and the modified-linear (Mod-Lin) solutions. The nonlinear model requires several minutes to solve a case while other two solutions need few seconds only. The linear solution is not accurate for the downwind region therefore the a correction on the induction velocities have been introduced by the modified-linear version. Mod-Lin solution is in a good agreement with the non-linear model [45].

ACM has not been widely used as a VAWT aerodynamics model whereas it has been implemented in aero-elastic solver HAWC2 to carry out time domain simulation of a VAWT and used widely by Vita [69]. Moreover, HAWC2 implementation was made viable for a floating wind turbine [45]. ACM is a powerful tool but in [19] it has been shown that the modified linear solution starts to give inaccurate results at very high loaded cases ( $C_T \sim 1$ ).

## Vortex and panel models

The vortex and panel methods have been widely used in the aerospace and wind industry. They serve a fidelity between the BEM and Navier-Stokes (N-S) solvers. Flow problem is solved by equations which are simplified forms of the N-S equations. So these models are constructed on a stronger physical basis than the BEM models. Such methods can also give detailed information about the flow field around the main body.

### Vortex models

Vortex models are based on the vorticity equation which could be derived from the Navier-Stokes (N-S) equations. In vortex model solutions, airfoils are modeled as 2D lifting lines. Each lifting line has a bound vortex at quarter chord point and zero-normal velocity boundary condition on the three quarter chord. According to the Helmholtz theorem, a vortex filament can not end in space, therefore a closed environment that includes the complete vortex system has to be created. The vortex system consists of the bound, the

shed and the trailing vortices. This closed vorticity system is called horseshoe vortex which is shown in Figure 2.5.

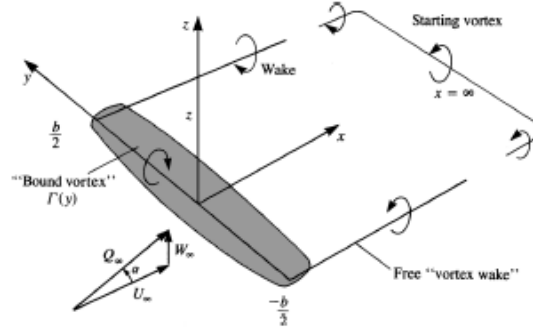


*Figure 2.5: Horseshoe model formed by the vortex system [32].*

As dictated by the Kelvin's theorem, in a barotropic ideal fluid, the circulation around a closed curve, which encloses the same fluid elements, will stay the same in time. This principle is used to shed new vortices if there is a temporal change in the bound circulation. To find the induced velocities in any point in the environment the Biot-Savarts law is used. To obtain the circulation values on each panel the Kutta-Joukowski theorem is used for the closure. This theorem explains the relation between the airfoil lift force and bound circulation. The vortex models have been applied to VAWT rotors by various authors. Work of Strickland [59] is known as the first 3D model with simulating the stall behavior. In time, that model has been incorporated with dynamic stall, flow curvature and apparent mass effects as well. It has been shown that his model has a good agreement with Sandia 17-m VAWT rotor measurements. The main disadvantages of the vortex models can be listed as moderate computational cost and decreased fidelity due to inviscid assumptions.

### Panel models

The lifting line approach of modeling the vortex system was extended by the panel models. Now the aerodynamic surface is modeled with panels along its dimensions. Every panel satisfies the zero-normal velocity condition within their circulation values. A representation of the lifting surface by panels is shown in Figure 2.6.

The potential flow assumption is made to simplify the numerical solution. In potential flow, the velocity field is represented as the gradient of a velocity potential ( $\Phi$ ). With further derivations found in [32], the velocity potential in 2-D can be represented as in Equation 2.2. In the equation the term  $S$  houses the body, wake and the boundary at infinity. This equation is a powerful statement since it only demands the velocity potential and the normal vector ( $\vec{n}$ ) on the surface to compute the velocity and pressure domain. This information can be determined anywhere in the flow field. Here  $r$  is the distance from point of interest.

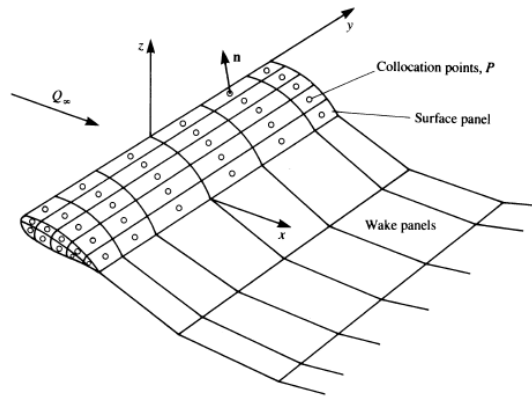


Figure 2.6: Representation of a wing by panels [32].

$$\Phi(x) = \int_S \left( \frac{1}{r} \nabla \Phi - \Phi \nabla \frac{1}{r} \right) \cdot \vec{n} dS \quad (2.2)$$

The assumption of potential flow allows the superposition of the elementary solutions which speeds up the computation. Usually the panels on the airfoil surface are modeled as doublet-source couples. Unique solution for the velocity potentials are made viable by the Kutta condition which imposes that streamlines has to leave the trailing edge in a smooth fashion.

One can couple the semi-empirical boundary layer equations with the inviscid solution. One representation of this type of solvers can be shown as XFOIL [9]. More advanced type can be shown as the double-wake model. In the double-wake panel methods a new trailing vorticity sheet is created at the point of boundary layer separation. This sheet creates a closed surface by meeting the trailing edge vorticity sheet. A VAWT application of the double-wake panel method with viscous coupling can be found in [73]. A similar study with the double-wake method can be seen for a general wind turbine use in Garcia's work [24].

BEM, ACM, vortex and panel models have been tested for VAWT with three different cases in [19]. One can see a comparison plot of the several methods in Figure 2.7. It has been shown that the DMST is invalid after directional induction factor goes above 0.5. Inability to operate at high loading and error cancellation behavior of the BEM models are verified. Although the  $C_P$  and  $C_T$  values were good for light loading, the MST failed to estimate the azimuthal induction distribution. Moreover, it was confirmed that the DMST could not estimate the effect of different fixed pitch correctly since it isolates the upwind and downwind parts of the actuator. The Mod-Lin Actuator Cylinder Model performed better than the BEM models and estimations matched with the vortex/panel code estimations. On the other hand, the ACM had high uncertainty at very high loading ( $C_T \sim 1$ ). The estimations of the vortex and panel methods were quite similar to each other.

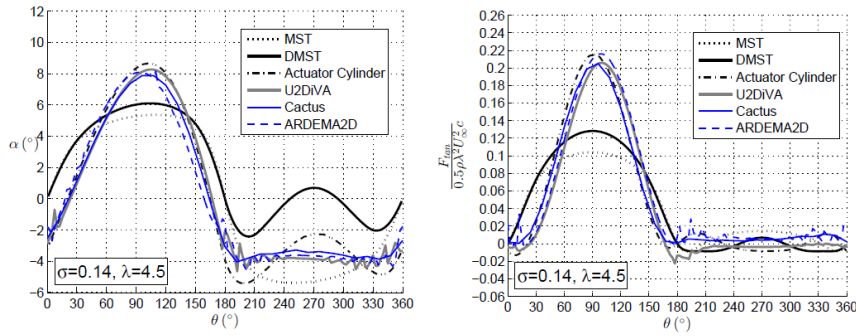


Figure 2.7: The angle of attack and tangential force for moderately loaded case[19].

### Computational Fluid Dynamic models (CFD)

The most complex forms of flow solvers can be shown as the high-fidelity CFD methods. For VAWT, the CFD methods have been used to increase the insight in the VAWT aerodynamics. Effects of the viscosity can be solved with a high-fidelity CFD methods. Body and far-field has to be meshed in order to resolve the physics but the computational cost of the CFD models are increases significantly with the mesh count. In each mesh cell, the conservation laws are satisfied and representation of the velocity and pressure fields are obtained. The CFD methods can be classified by how they solve the viscous part of the flow. Direct Numerical Simulation (DNS) solves full N-S equation with a mesh size in Kolmogorov scale. The Large Eddy Simulation (LES) is a space-filtered method where it only solves large scales of turbulence. One can apply sub-grid scale models to LES in order to capture the airfoil boundary layer. Unsteady Reynolds-Averaged Navier-Stokes (URANS) model solves the time-averaged N-S equations therefore it provides less details of the flow field than the DNS and LES do. The closure problem caused by the Reynolds decomposition is solved by the turbulence models as  $k - \epsilon$  and  $k - \omega$ . These turbulence models consists of two transport equations for the average turbulence kinetic energy and turbulent dissipation. The RANS or URANS models are often chosen by researchers to simulate airfoil aerodynamics. Although the solution is with a lower detail due to time-averaging, they solve turbulent boundary layers in relatively reasonable time. If one aims for a more detailed flow field representation with a faster turbulent boundary layer estimation, the Detached-Eddy Simulation (DES) can be a viable option. The DES is a hybrid method created by combining the URANS for wall region and the LES for outer flow solution. Alternatively, a method that lays between the N-S solvers and vortex models is introduced to VAWT research by Scheurich, the vorticity-transport model (VTM) [55]. In contrast to N-S equations (pressure-velocity), the vorticity-velocity formulation is used in this model.

### 2.3 Circulation control of a VAWT rotor

The active flow control have been used for the lift adjustment, drag reduction, boundary layer separation avoidance and noise suppression. In rotor aerodynamics, these main adjustments could help to decrease the excessive loading, vibration loading and increase

the aerodynamic efficiency. Therefore control systems offer a great potential to reduce the CoE of wind turbine systems by various ways.

### The blade pitch control

Active circulation control of the VAWT could be done with various objectives in mind. The dynamic stall alleviation, the power efficiency enhancement and the improvement of the self-starting capabilities can be counted as the the hot topics on the field. Until now, most of the research on the VAWT circulation control has been carried out on the variable blade pitching. A wide research field on this subject was the mechanism design for the pitch control. Pitch control can be done actively by the actuators (servo, hydraulic, etc.) or passively by the mass-spring-damper systems. Researchers concentrated their work on the passive control systems due to lower complexity, lower capital cost and lower maintenance costs of those systems. Walter and Migliore mentioned about the advantages of the pitch control and required aerodynamic tools to assess the performance [70]. The DMST has been widely used due to its ease of modeling and low computational cost. The vortex models were used when one sought for the unsteady performance. Zervos et.al. [75] computed the blade pitch variations with respect to the rotor specifications, airfoil characteristics and operating conditions. Moreover, they have compared the performance of different pitch variations. Vandenberghe and Dick have worked on the theoretical and experimental quantification of various harmonic pitch control methodologies [67]. Moreover, they have obtained optimum pitch control by using a numerical optimizer [68]. They have found that the second order harmonic pitch variation increases the efficiency more than a first order harmonic pitch control does. The reason was shown as the difference of the perceived angles attacks in the upstream and downstream. The second order harmonic pitch control is applied by a gear mechanism. They have shown that peak  $C_P$  could be increased 19% with this concept.

Kirke [34] has presented an extensive work on the passive control mechanism in order to solve the self-start problem of the VAWT. It has been shown by the wind tunnel and field tests that a lift-driven VAWT could reliably self-start. He has assessed the variable pitch concept, flexible blades/sails and cambered fixed-pitch blades. The flexible blade was found very complex and expensive. The use of the cambered fixed-pitched airfoils was the cheapest and the most simple solution above all. Lazauskas and Kirke have created a model to explore the optimized pitch control for various aerodynamic objectives as maximum starting torque and maximum power coefficient [43]. The model showed that the peak power coefficient can be increased by 25% when compared with the fixed-pitch configuration. They have reported that the optimized pitch variations have better performance than a sinusoidal actuation. Examples of such optimized variations in order to increase the starting torque can be seen in Figure 2.8. Lazauskas compared the performances of three different pitch actuation system as Pinson, mass-stabilized and aerodynamic-pitching in [42]. He emphasized the complexity of finding optimum pitch angles since they are functions of many variables affecting the mechanism and the load characteristics of the blades.

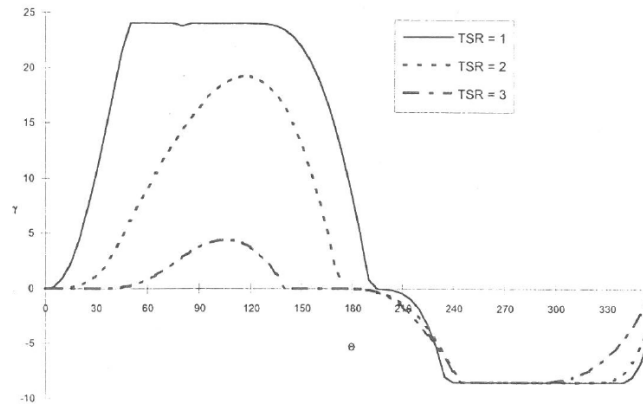


**Figure 2.8:** Optimum pitch angle to maximize the torque coefficient area [43].

In his PhD thesis, Pawsey has evaluated various concepts of pitch control and introduced two new concepts for the passive variable pitching, the elastic and inertial means of counter momenting [53]. The main purpose was to improve the self-start capabilities. He mentioned that the active control with hydraulic or electric actuators needs controller design and might be more expensive and complex than a passively controlled pitch angle. Passive systems balance the aerodynamic and inertial forces to create a favorable pitch variation. On the other hand, the passive systems could suffer from the increased turbine drag due to new mechanisms, long-term changes in material properties, fatigue, moisture absorption and temperature effects. A pitch mechanism might not operate as intended due to these effects. Moreover, Pawsey has drawn attention to the actuation frequency and the blade natural frequency; the pitch control might suffer when the flap operation is in those critical regions.

A numerical optimization to obtain polynomial optimal pitch control was used by Paraschivoiu [52]. A genetic algorithm was coupled to the DMST model to find the optimum actuation sequence. The optimizer have sought for the appropriate variables of the base equation:  $\theta_p = x_1 \cos\theta + x_2 \sin^3\theta$ . In this work, the AEP was increased around 30% with the polynomial pitch. Erickson et. al. [12] have studied the effects of the cyclic pitch control on the turbine efficiency both numerically and experimentally. It was shown by the experiments that a tuned first order sinusoidal pitch actuation could improve the peak power coefficient to 0.436. This was a 35% increase with respect to the fixed-pitch blade performance. Chougule and Nielsen has over-viewed various pitch control mechanisms and designed a new pitch-control linkage mechanism [6]. They have reported that with a  $5^\circ$  change in the blade pitch amplitude the  $C_P$  could be increased by 12%.

The variable pitch control systems have been studied by many researchers but this never led to a commercialized turbine. Lazauskas and Kirke have stated that it is very likely due to the mechanical complexity of the active control systems and suspicious effectiveness of the passive control systems since they are driven by the complex relation between aerodynamic, inertial and other forces [35].

## Trailing edge flaps

The active control can be designed in two main forms, the predetermined and interactive control [30]. The predetermined control does not need any sensors where the interactive control is carried out by the co-operation of sensors, controllers and actuators. As a type of interactive control, the closed-loop control is more applicable to the wind turbines since they consume less energy and their operation is safer than the other systems [30]. Table 2.1 shows the classification of the active flow control devices where the technique of control, location of the control device, aerodynamic effect on the airfoil polar and actuator actuation concept are shown.

Devices		Geometric (G)	Fluidic (F)	Plasma (P)	Leading Edge (LE)	Trailing Edge (TE)	Mid-Chord (MC)	Inc. Lift (I)	Dec. Lift (D)	Delay Stall (DS)	Steady (S)	Unsteady (U)
1	Traditional Trailing-Edge Flaps	G			TE			I / D		S / U		
2	Nontraditional Trailing-Edge Flaps	G			TE			I / D		S / U		
3	Microtabs	G			TE			I / D		S / U		
4	Miniature Trailing-Edge Effectors	G			TE			I / D		S / U		
5	Microflaps	G			TE			I / D		S / U		
6	Active Stall Strips	G			LE				D		S	
7	Vortex Generators	G			LE				DS		S	
8	Blowing and Suction	F			LE / TE				DS		S / U	
9	Circulation Control	F			TE			I / D			S	
10	Plasma Actuators	P			LE				DS		S	
11	Vortex Generator Jets	F			LE				DS		S / U	
12	High-Frequency Micro Vortex Generators	G			LE				DS		U	
13	Synthetic Jets	G / F			LE				DS		U	
14	Active Flexible Wall	G			LE				DS		U	
15	Shape Change Airfoil	G			MC			I			S / U	

**Table 2.1:** Classification of the active flow control systems [30].

The choice of the flow control system would depend on its size, actuation speed, power requirements, reliability, durability, robustness and manufacturing and the maintenance costs [30]. Overall, the cost of energy should be decreased by adopting the additional control system. Barlas mentioned that the flaps are strong candidates for the flow control in wind turbine rotors due to their proven performance, reliability gained in the aerospace industry and very high control authority [2]. A comparison of different control systems by their control authority is presented in Figure 2.9. As seen, the control authority of the trailing edge flaps are the most favorable among all the systems.

One can count two main flap deflection types as the smooth deflections and the fixed deflections. When compared with the smooth deflections, the traditional fixed deflection scheme would trigger early trailing edge separation and create a larger drag. Furthermore, less energy is required in the case of smooth flaps for the same  $C_l$  difference. As an additional disadvantage, traditional flaps lead to complex internal structure which requires more maintenance [66]. The design of the flap surfaces requires many considerations to accomplish their task robustly. Shen and Chopra [56] have done a parametric study to find the best flap sizing for the vibration control on the helicopter rotor. To find the optimal sizing, the required flap angle, hinge moment, actuation power were calculated for each flap to span ratio ( $r_{flap}/R$ ), flap spanwise location and flap to chord ratio ( $c_{flap}/c$ ). Then, deductions were made to chose the final flap size. Troldborg used measures as flap hinge

moment, flap effectiveness and maximum achievable  $C_l$  to choose a proper flap length [66]. These parameters could also be used for the flap design of a VAWT blade.

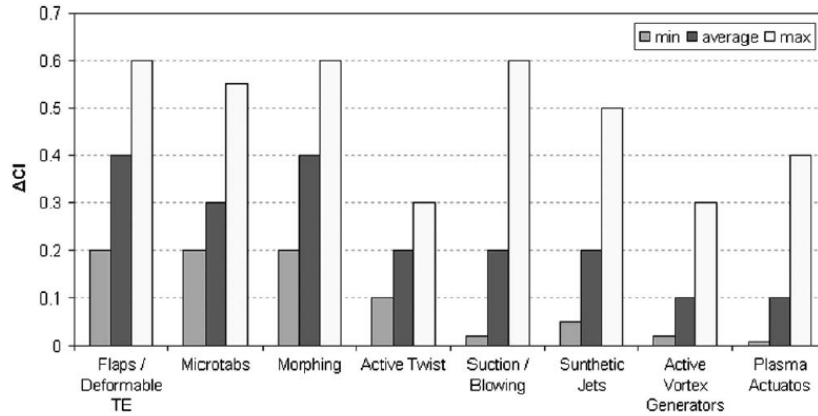


Figure 2.9: Control authority of different flow control systems [2].

Unsteady aerodynamics is another topic that is related with the operation of the flap in a VAWT rotor. Since the angle of attack is always changing along the azimuth, the unsteady vortex shedding of the airfoil affects its performance. Furthermore, reduced frequency is an important measure for this analysis. It is defined as  $k = \frac{\omega c}{2U}$ . It gives insight on how often the pitching motion is experienced in a unit forward translation of an airfoil. As the reduced frequency ( $k$ ) increases the hysteresis loops of airfoil polars get wider, the  $C_l$  curve slopes ( $C_{l\alpha}$ ,  $C_{l\beta}$ ) decreases [3] and  $C_d$  slopes increases. Furthermore,  $\frac{L}{D}$  and  $\alpha_{design}$  were found highly sensitive to flap to chord ratio. This is mainly due to the increased drag by longer flaps. An unsteady flap affect the airfoil lift-curve slope more than an unsteady airfoil pitching motion. Moreover the flap authority decreases with increased  $k$ . As an advantage in small  $\alpha$  operation, drag increase by the flap deflection is very low. Wolff also mentioned that the flow separation is stronger in the presence of flap movement since the flap is loading the aft portion of the airfoil heavily [71]. Aerodynamic effect of the trailing edge flap was decreased in the stall region and could be neglected in the deep stall conditions. Dynamic oscillations at highly stalled operation introduces another challenge for the flap deflections due to the unsteady vortex street shed in the wake [3]. These issues might be experienced by the VAWT blade depending on the solidity and tip speed ratio.

The research on the flap-controlled VAWT rotor has not been done widely in the past. In fact, it is hard to find noticeable works on this subject. Several studies have been done by gurney flaps but there are not any evident work for the active flaps on a VAWT blade. The most relevant study on this issue was carried out in Xiao's work [72]. He showed that the power efficiency of the vertical axis tidal turbines could be improved around 28% when controlled by the trailing edge flaps. In 1990, an idea on the flow control of the VAWT blades with trailing edge surface has been patented [10]. It was a system that measures the perceived angle of attack for each blade and control them accordingly. The patent proposed the usage of blade pitching and flap control at the same time. The azimuthal flap sequence would be a function of the instantaneous blade pitch angle and the power output demand. Note that the blade should be pitched to have the zero angle of attack

since it was thought that the best  $\frac{L}{D}$  of a blade with a flap could be obtained at that conditions. Unfortunately, any application for this idea was not found in the literature.

## 2.4 Airfoil design

### Research on VAWT airfoils

There are only few works for the airfoil design specified for VAWT operation. Many studies on airfoils have only documented the application of the existing aviation airfoils to the VAWT rotors. In this section, the reader can find most of the recognizable design works and few of the important airfoil analysis works.

Sandia National Laboratories (SNL) became the top player in the VAWT research for the period before 80's. The research was funded by the US Department of Energy. Early SNL research extended the understanding of VAWT rotors, their manufacturing and design. Many experiences were obtained on the computer models, wind tunnel models, full-site experiments and commercial applications; those information were summarized in [60]. SNL designed several symmetrical airfoils based on the symmetrical NACA 4-series. Klimas has mentioned that the early VAWT rotors used NACA 00xx airfoils since their characteristics were well known and they provide reliability and confidence to the designer. On the other hand, those airfoils suffered in VAWT rotor by having low power efficiency, showed cyclic stress characteristics which caused shorter fatigue lifetime [37]. SNL has listed the critical airfoil requirements as: 1) modest  $C_{l,max}$ , 2) sharp stall behavior, 3) low zero-lift drag ( $C_{d0}$ ) and 4) wide drag buckets. First two demands were set to satisfy the higher fatigue life aim and the last two demands were introduced to decrease the overall energy loss due to drag. A wide drag bucket was critical since the VAWT airfoil experiences a wide range of angle of attack along the azimuth. During the work of Klimas, the Eppler code [11] was used for the airfoil assessment and the MST was used for the VAWT aerodynamic performance estimation. Three new airfoils were designed, namely SAND 0015/47, 0018/50 and 0021/50. A comparison between SAND 0015/47 and NACA 0015 geometries can be seen in Figure 2.10. The main difference was that the SNL airfoil had a smaller nose radius and a surface contour that allowed laminar flow until 47% of the chord. The experiments showed that the  $C_{P,max}$  was lower for the SAND 0015/47 airfoil. On the other hand, SNL airfoils had lower average and RMS values for the vibratory forces. By the new design it has been shown that the CoE could be decreased 10%-20% and fatigue lifetime was improved.

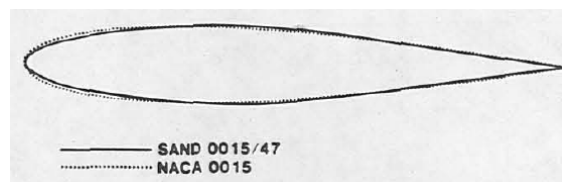


*Figure 2.10: Comparison of the SAND 0015/47 and NACA 0015 [37].*

FloWind, a commercial project, observed many characteristics of the VAWT blades. It has been seen that the dirt and bug accumulation on the blades affects the performance

significantly at high wind speeds. SNL reported that the accumulation of the dirt on the blades caused a delayed stall, a higher maximum peak power but lower power efficiency [60]. During the development in FloWind, the chosen operating speed required a new adapted airfoil. This airfoil was designed by Dan Somers and named as S824. This was a symmetrical airfoil with a moderate  $C_{l,max}$  and it was less insensitive to the roughness than a NACA 0024.

Wichita State University found that a larger blade thickness improves the power efficiency of VAWTs. This deduction was made by using the DMST code of SNL. Then, experiments showed that the increasing  $C_{l,max}$  improves the maximum  $C_P$ . This was seen by comparing two different rotors constructed from the NACA 0012 airfoil and WSU 0021 airfoil. During the tests it has also been shown that the rotor performance improves at high Reynolds numbers. It was concluded that a high  $C_{l,max}$  and high stall angle are more critical for the power performance than the decreased drag that comes with a thin airfoil. Furthermore, the experiments with passive turbulator devices on the blade did not improve the  $C_P$ , in fact decreased it [57].

In 1978, Healy has worked on the VAWT airfoils and compared their performances. A new airfoil was not designed but several favorable airfoil characteristics are reported. In his first work he compared the symmetrical airfoils such as NACA 0009, 0012, 0015 and 0018 for various Reynolds numbers and various tip speed ratios. The MST was used as the VAWT aerodynamic model. It was concluded that the thick airfoils operate more efficient at low Reynolds numbers. The thin airfoils tend to stall earlier and decrease the  $C_P$  by increasing the loss due to drag [28]. In a later study, Healy looked at the performance of the Göttingen type cambered airfoils. It was concluded that very high lift airfoils are undesirable because of the operating characteristics. The slightly cambered airfoils had higher power output and smoother power trends [27].

Tokai University has conducted a research on VAWTs after the energy crisis. Kato et.al. [31] designed a cambered airfoil, T.W.T. 11215-1. The design objectives for the airfoil were derived by using the SST aerodynamic model. Authors found that for a high power efficiency the airfoil needs to have a large lift-curve slope ( $C_{l\alpha}$ ), low  $C_d$ , low  $C_{d0}$  and a large pitching moment ( $C_{m0}$ ) [31]. The T.W.T. 11215-1 airfoil has increased the power efficiency when compared with NACA 0012.

Migliore and Fritschen worked on the airfoil performance on VAWTs by testing 10 different NACA airfoils for various rotor solidity. It was found that the NACA 6-series could obtain similar  $C_P$  as the widely used NACA 4-series. Moreover a NACA 6-series airfoil could provide a broader and flatter power curve over a tip speed ratio range. Depending on the rotor solidity, the NACA 63<sub>2</sub>-015 airfoil could have 17% to 27% more improvement in AEP than the NACA 0015 [48]. The MST was used as the aerodynamic model throughout this work. The NACA 63<sub>2</sub>-015 was modified so that the flow curvature effects could be taken into account in the airfoil shape. This modification was done by fixing a target solidity and the strut mounting point of the blade. Unfortunately, they did not report the performance comparison between the original and modified airfoil. Migliore emphasized that the existence of the flow curvature effects destroy the idea of using symmetrical airfoils for VAWT. It was estimated that the optimal airfoil would be an asymmetrical shape [49].

An airfoil design study by regarding the rotational effects (flow curvature, radial bound-

ary layer gradients, etc.) and the instantaneous aerodynamic loading has been carried out in the work of Zervos [74]. An inviscid panel model was used to assess the VAWT aerodynamic performance. It was reported that the cambered airfoils are very advantageous when the rotational and instantaneous effects are considered. Due to the virtual camber, a symmetrical airfoil produces more lift upstream than the downstream. Therefore the loading gets asymmetric and also provokes stall. On the other hand, a cambered airfoil could be independent of such phenomenon. Zervos has compensated this effects of symmetrical airfoil by applying its thickness distribution to a mean line defined by the arc of the circle of rotation; this new airfoil was named as ARC 0015. This new airfoil obtained the smallest peak pressure gradient near leading edge therefore the separation could be delayed [74].

The airfoil design research in Glasgow University was concentrated on designing airfoils for longer fatigue life and passive stall regulation [23]. An airfoil design tool has been generated in this research which coupled a geometry creator and a performance assessment module. The geometry could be defined by direct modification of an existing airfoil or by inverse airfoil design techniques. The aerodynamic solver was an unsteady prescribed wake model coupled with Beddoes-Leishman dynamic stall model. The new airfoils were named as GUYA. The GUYA 4 and GUYA 9 had the most desirable static characteristics and it was shown that those airfoils were experiencing dynamic stall earlier than the NACA 0018. To obtain an improved airfoil the GUYA 9 and NACA 0018 geometries were mixed and the new geometry was called as the GUYA 10. The GUYA 10 was shown in Figure 2.11, its nose part was inherited from the GUYA 9 and downstream section was a NACA 0018 geometry. In order to have lower bending stress on the blades, thicker airfoils were required. Therefore thick NACA sections were taken into account. But it was reported that the static and dynamic stalling performances of the thick sections were unfavorable when compared with the moderately-thick airfoils.

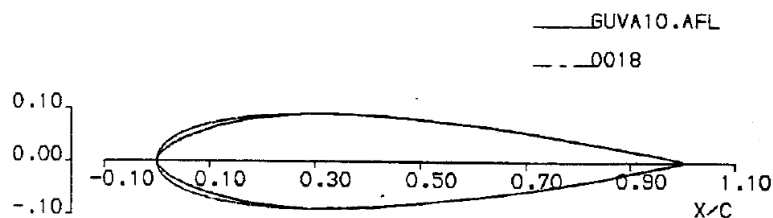


**Figure 2.11:** Comparison of the GUYA10 and NACA 0018 [23].

Kirke [34] has made an extensive work on active pitch-controlled VAWTs but in a short section he also mentioned about the favorable airfoil characteristics. It was reported that the laminar flow, thick and slightly cambered airfoils with a proper pitch preset would be suitable for VAWTs. He mentioned that if the stall angle and  $C_{l,max}$  are large then the starting capabilities of VAWTs could be enhanced. As they affect to the torque,  $C_l$  should be maximized for a wide range of  $\alpha$  while keeping  $C_d$  relatively low. The cambered airfoil will capture more energy upwind but will decrease the power conversion downwind. It was believed that a cambered airfoil will still produce more power than a symmetrical since most of the power is extracted in the upwind passage.

The desirable airfoil characteristics for a small scale VAWT were documented by Islam [29]. He obtained those characteristics by comparing the existing airfoils and assessing the past literature. Nine airfoil requirements were listed as: 1) high stall angle, 2) wide drag bucket, 3) low  $C_{d0}$ , 4) high  $\frac{C_l}{C_d}$ , 5) high  $C_{l,max}$ , 6) delayed dynamic stall characteristic, 7) low roughness sensitivity, 8) low trailing edge noise and 9) large negative  $C_m$ . Those requirements would increase the self-start capabilities and power yield. It was concluded that, geometrically, the airfoil needs to have large thickness, camber, large nose radius and sharp trailing edge [29].

Claessens [7] designed an airfoil based on the NACA 0018 for small scale VAWT applications. The new airfoil was named as DU 06-W-200 with a camber of 0.8 % and thickness of 20% of the chord. DU 06-W-200 can be seen in Figure 2.12. Moreover, the roughness sensitivity was increased with respect to NACA 0018. During the design work, a wide drag bucket, larger airfoil thickness, less laminar bubbles and a smooth stall were sought. Contrary to the early work, a smooth stall was demanded to decrease the aerodynamic noise. The design work was done with RFOIL flow solver and the DMST model was used to assess the aerodynamic performance. Claessens mentioned that the Natural Laminar Flow (NLF) airfoils have favorable characteristics for VAWT applications therefore they should be the baseline airfoils for a new design.

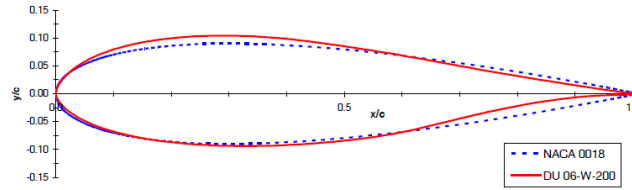


**Figure 2.12:** Comparison of the DU 06-W-200 with NACA 0018 [7].

A relatively different approach to VAWT airfoil design has been presented by Ferreira et.al. [16, 17, 54]. The focus was taken as the vorticity created in the vicinity of the VAWT rotor. The energy exchange is increased if the azimuthal variation of the bound circulation ( $\frac{\partial \Gamma_b}{\partial \theta}$ ) is increased. To find a critical relationship for the airfoil design, the definition of the aerodynamic lift force by circulation was included,  $L = \rho V_\infty \Gamma$ . From here, if one assumes a constant perceived velocity and constant chord, the derivation of the  $\frac{\partial \Gamma_b}{\partial \theta}$  would be equivalent to the azimuthal rate of change in the lift coefficient ( $\frac{\partial C_l}{\partial \theta}$ ) which could easily be related to the lift-curve slope ( $\frac{\partial C_l}{\partial \alpha}$ ). This relation was first shown by Ferreira and Scheurich [20]. Another contribution to the aerodynamic objective was obtained by simplifying the torque loss due to the drag term. By combining those two aerodynamic objectives Ferreira and Geurts obtained Equation 2.3. Here  $X$  was between -20 and 5 degrees and  $\Delta \alpha_r$  was taken as 15 degrees.  $b(\alpha)$  was the weighting function that is similar to the definition of the probability distribution function. It represented the probability of each angle of attack that is perceived during VAWTs' operation.

$$F_{aero} = -max \left( \frac{\int_X^{X+\Delta \alpha_r} C_{l\alpha} d\alpha}{\int_X^{X+\Delta \alpha_r} C_{db}(\alpha) d\alpha} \right) \quad (2.3)$$

In order to take the roughness effects into account, Ferreira et.al. [17] applied forced transition at 10% chord both for the upper and lower surface. The NSGA-II genetic algorithm was coupled with RFOIL airfoil analysis tool for the airfoil design. Later, the panel code solutions were used to assess the performance of the new airfoils. The optimized airfoils have high thickness, a broad drag bucket, high  $C_{l\alpha}$  and smooth stall characteristics. It was numerically shown that the optimized airfoils could reach  $C_P$  values around 0.5. Figure 2.13 shows an optimized airfoil and its performance for a  $\sigma$ - $\lambda$  range.

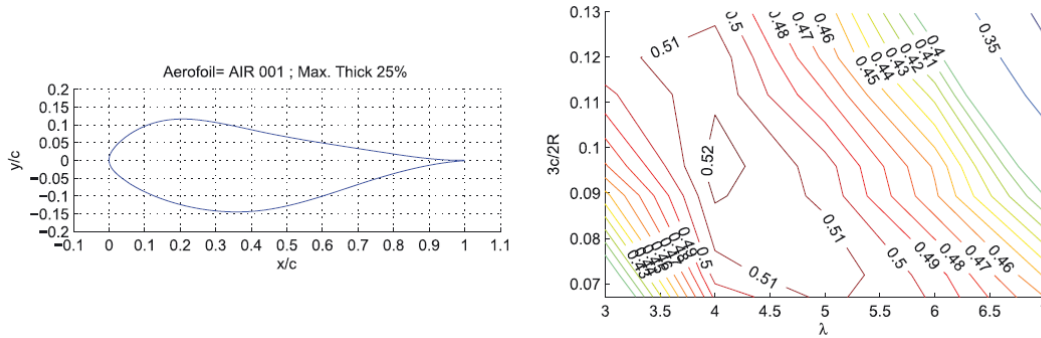


**Figure 2.13:** The Air001 airfoil and its performance in a VAWT rotor [17].

In an experimental work by Ragni [54], the wind tunnel verification of the VAWT-specific airfoil DU12-W-262 has been carried out. This airfoil was designed by Ferreira with the same approach in [17] and shown in Figure 2.15. The airfoil polar obtained from wind tunnel was implemented into the panel code. As a conclusion high  $C_P$  values around 0.4 were reported from  $\lambda$  of 4 to 6. For a rotor solidity of 0.1 at  $\lambda = 4$  a  $C_{P,max}$  of 0.48 was obtained.

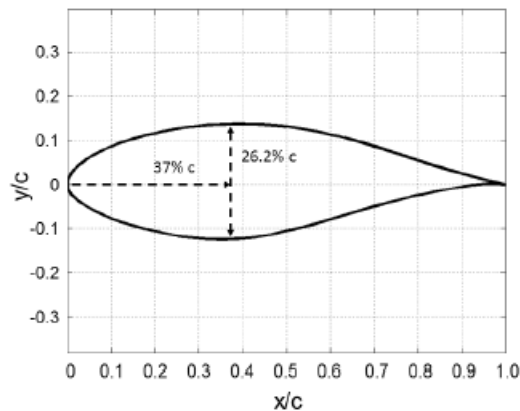


**Figure 2.14:** A VAWT specific airfoil: DU12-W-262 [54].

Recently, Kemp showed a new airfoil design work in his master thesis [33]. This study was partly presented in [16] and in line with the previous work of Ferreira. In this study, an airfoil family was designed for a large scale VAWT ( $\sim 5$  MW). A multi-objective optimization approach was used to find the balance between the structural and aerodynamic

objectives. Moreover, the roughness insensitivity was aimed. For the structural fineness, the flap-wise bending moment of the airfoil was taken as the key measure. For the aerodynamic objective five different strategies were put in trial. Those strategies were the combinations of different aerodynamic objectives ( $\frac{C_{l\alpha}}{C_d}$ ,  $C_{l\alpha}$ ) and weighting ratios (0, 0.5, 1) between the clean and soiled cases. The aerodynamic performance of the new airfoils were assessed by three different models: inviscid panel model, double-wake panel model and detached-eddy simulation. The optimized airfoils span from 27% to 32%. Thick airfoils with favorable VAWT performance are created.

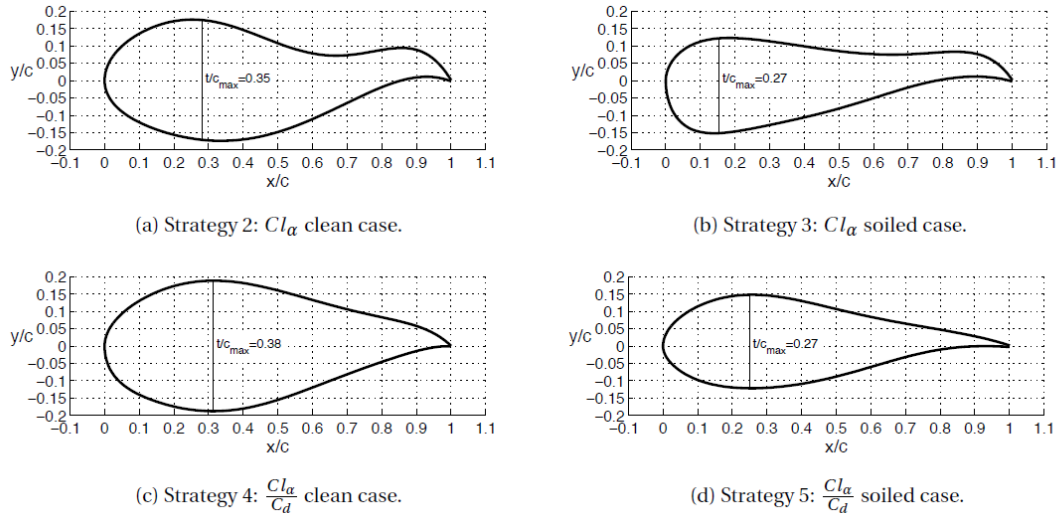


**Figure 2.15:** The optimized airfoils for different design strategies [33].

It has been highlighted by several researchers that the complex flow phenomenon in a VAWT rotor and wake would lead the designer to use the moderate/high fidelity tools. Klimas [36] has indicated that rotor aerodynamics of a VAWT are highly complex where surface pressure distributions are driven by curvilinear motion. Phenomenons like dynamic stall and blade-wake interaction make the design problem even more complex. Hence a good airfoil design methodology for VAWTs should have an aerodynamic model that could take these various effects into account. Similarly, it has been noticed by Scheurich [55] that designing airfoils and blades without neglecting the blade-wake interactions and dynamic airfoil effects would lead to incorrect works. The complexity of the model for VAWTs has to be in such fidelity that major aerodynamic phenomenons should be solved in an acceptable time so that the model could be used in optimization structures. Therefore the validity and reliability of the past design work with low-fidelity aerodynamic models are subjects of concern.

### Research on HAWT airfoils

Although the research field is similar with VAWTs, the airfoil design for HAWTs differs significantly. It is due to the different conditions and phenomenons that airfoils operate in. Therefore, in this section the motivation is to acknowledge the differences between the maturity levels of HAWT and VAWT airfoil design methodologies. One can mention

about four main parameters for the airfoil design for HAWT blades. They are the  $C_l - C_d$  considerations, stall behavior, roughness sensitivity and structural strength.

A desired  $C_{l,max}$  and  $C_{l\alpha}$  were obtained in Risø-A family airfoils by applying upper and lower limits to the lift curve. This was done for an angle of attack range that contains the  $\alpha_{stall}$ .  $C_{l,design}$  kept closer to  $C_{l,max}$ . For Risø-B1 airfoils  $C_{l,design}$  and  $C_{l,max}$  targets were defined as constraints in order to get the desired airfoil polar [21]. Björck's aim was to design an airfoil family along the blade so that the  $c \cdot Cl$  would be constant along the blade. This was done to obtain an aerodynamically optimum loading on the blade [5]. Bak [1] chose the  $Cl_{max}$  as large as possible which would also increase the  $Cl_{design}$ . By this way smaller chords, so cheaper blades could be produced. Furthermore, the aft camber concept has been heavily used in order to reduce the adverse pressure gradients on the suction side by reducing the aerodynamic loading. For most of the cases, the  $\frac{C_l}{C_d}$  was chosen as the aerodynamic design objective since it is a primary measure for the airfoils' efficiency. Therefore many constraints have been applied to this property. The Risø-A family was designed with an aerodynamic objective which is the sum of  $L/D$  values for  $\alpha = 2, 4, 6, 8$  and  $10$  degrees. A similar design methodology was seen in the work of Grasso [26] where  $L/D$  was kept relatively higher for a broader  $\alpha$  range than aviation airfoils operate in. Most of the designers have used a very wide range of angle of attack. This was due to the need for optimizing the airfoil for the off-design conditions. This issue is also valid for the airfoil performance of the VAWT rotor.

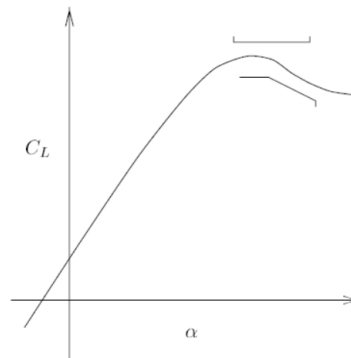


**Figure 2.16:** Constraints on the  $C_l$  curve for the stall region [8].

A smooth stall is a favorable characteristic for the HAWT blades since this will induce less vibration loads in the case of operating near stall angle. Moreover, the experienced load range during the gust events will be smaller. The stall character for the Risø-A family was dictated by applying an upper and lower limits to a target  $Cl - \alpha$  curve (see Figure 2.16). Björck checked the boundary layer shape parameter ( $H$ ) and designed airfoils with gradually increasing  $H$ . Furthermore, to avoid the adverse pressure gradients on the airfoil suction side, the thickness of the upper surface was kept relatively small than the lower surface thicknesses. Moreover, the thickness on the lower surface was moved towards leading edge to reduce the adverse pressure gradients locally [64]. Different thickness distributions of the upper and lower surfaces might not be a case for VAWT but the position of thickness could be an interesting parameter. Timmer also mentioned that the airfoils thicker than 25% or more have a high chance to suffer from a performance

degrading due to roughness effects [63]. To have a smooth stall, Grasso [4] applied a constraint on the post-stall part of the lift curve slope.

The surface roughness insensitivity could be dictated by limiting the  $C_l$  difference between the rough and clean cases to a very small value [76]. It is shown by Tangler [61] and Timmer [65] that sensitivity to roughness is likely to increase with increasing  $C_{l,design}$ . The Risø B1-family has relatively larger difference between  $C_{l,max}$  and  $C_{l,design}$  which leads to an airfoil that is less prone to the roughness effects. Another important variable for the stall characteristic was the nose radius. It was shown by the combination of several experimental data that there is a quasi-linear relation between  $\alpha_{deep\ stall}$  and the thickness at 1.25% chord (see Equation 2.4 [65]). This information could be very useful for a designer when assessing the deep stall angle.

$$\alpha_{deepstall} = 1114(y/c)_{x/c=0.0125} \quad (2.4)$$

The maximum relative thickness of an airfoil is the main property to determine its structural strength. Besides this primary effect of  $(t/c)_{max}$ ; its location has a significant impact on the structural properties as well. If one keeps that point close to airfoil upstream, the shear and gravity centers will be close to the aerodynamic center which would solve some of the aero-elastic instability problems. On the other hand, keeping the location in airfoil downstream would allow larger maximum strain values. For Risø airfoil families the maximum thickness location was fixed between 27% and 33% of the chord. Timmer and van Rooij fixed the location of  $(t/c)_{max}$  at 27% of the chord. This was done to prevent the early transition and separation.

Another structural constraint for the airfoil was the geometric compatibility. This constraint could be applied to ensure a smooth surface when the airfoil family was used along a blade. To ensure the geometric compatibility one can limit the curvature of the leading edge and aft camber on the pressure side [21]. This constraint was very important for the manufacturing ease and quality. It could become an important parameter for VAWT if one aims to design an airfoil family for all spanwise locations.

Trailing edge thickness can also be constrained by the optimizer. This would guarantee a high edgewise bending stiffness and ease in manufacturing. Bak and Grasso limited it to 2.5% of the relative thickness where Timmer fixed the trailing edge thickness between 0.5% - 1.0% of the chord [1, 4, 65]. The thick airfoils of Risø-A1, P and B1 families have trailing edge thicknesses around 1% chord as well.

The roughness on leading edge will cause an early transition to turbulence as well as it will thicken the boundary layer which pronounces the de-cambering effects as well. The thick boundary layer will separate earlier due to the pronounced adverse pressure gradients. In the case of the roughness sensitive airfoils the properties like  $C_{l,max}$ ,  $C_{l\alpha}$  would decrease and  $C_d$  would increase due to increased pressure drag [61, 64].

Roughness sensitivity for the Risø-A1 and B1 families were kept low by controlling the transition point on the suction side. The transition point was kept far downstream at  $\alpha_{design}$  to maximize the  $L/D$ . Roughness insensitivity was depicted by forcing the transition point to be on the leading edge just before the  $C_{l,max}$  was reached. Therefore, the peak pressure location would have a turbulent boundary layer even if the flow is disturbed by the leading edge roughness. This condition is an important sign for the

roughness insensitivity. For the Risø-B1 airfoils the difference between the  $C_{l,max,lean}$  and  $C_{l,max,rough}$  were limited to a value during optimization. To make  $C_{l,max}$  relatively insensitive to roughness, Tangler and Somers have used the same methodology as Risø. In a clean operation, the transition point was kept close to 50% of chord which created a higher  $L/D$ . Furthermore, Zhu optimized the  $C_P$  by creating an aerodynamic objective as the sum of 75% of  $C_P$  in the rough case and 25% of the  $C_P$  in the clean airfoil case for various angle of attacks. Airfoils which are very insensitive to surface roughness were obtained by that study. The comparison of the FFA-W3 and Risø-A1 airfoils in the wind tunnel showed once again that a thicker nose would lead a smoother stall due to decreased pressure peaks [64]. For most of the works the roughness effects were simulated by setting the forced transition at 1% of chord on the suction side and 10% on the pressure side. Forced transition location on the pressure side was taken slightly downstream in order to numerically guarantee that the transition point will be downstream of stagnation point for high  $\alpha$  values.

Another airfoil design methodology could be counted as the integrated design process. By saying integrated design, the coupled design of the spanwise airfoils and the rotor is meant. In such case, an airfoil flow solver and a turbine aerodynamic model (e.g. BEM) would be coupled with a numerical optimizer [76]. The integrated airfoil design process is inherently more sophisticated for the wind turbine use but it increases the computational cost.

The modern airfoil design has been carried out by coupling a numerical optimizer to an airfoil analysis tool (XFOIL, RFOIL, etc.). In the modern literature, the airfoil surface was defined either by the Bezier splines or Class-Shape Transformation (CST) methods. Selig used 7<sup>th</sup> order Bezier curves for front portion and 6<sup>th</sup> order curves for the aft part of the airfoil [25]. Risø used 5<sup>th</sup> order Bezier curves for each side. Grasso divided the airfoil into four sections and applied 3<sup>rd</sup> order Bezier curves to each section [4]. Furthermore, Selig mentioned that using B-splines could produce wavy airfoil surfaces which could cause the pressure distribution to be wavy as well. This problem could lead the optimizer to discard such geometries that could have been efficient geometries without the waviness. On the other hand, the CST method was found capable of creating wide range of airfoil geometries with less number of variables among others. The CST method was mathematically efficient, produced smooth shapes, allowed specifying the nose radius and trailing edge angle explicitly [39].

# Exploring the $C_P - C_T$ Relation of the Actuator Cylinder

This chapter focuses on the performance limits of the VAWT estimated by the Mod-Lin ACM for an infinite number of blades. Here, this type of turbine is called as the actuator cylinder. The term is introduced by Madsen [44] and it represents a 2D cylinder with a normal/radial ( $Q_n$ ) and tangential body forces ( $Q_t$ ). Throughout the the thesis,  $Q_n$  and  $Q_t$  are referred as the blade forces non-dimesionalized by the rotor size and free-stream conditions.  $Q_n$  is a key measure in the performance of the VAWT since, by definition, it is related to the pressure jump across the turbine periphery. Along the chapter, first, the implementation and the validation of the Mod-Lin ACM code is documented. Later, the exploration of the performance of an actuator cylinder is carried out by designing new loadforms ( $Q_n$ ). One can also find preliminary deductions for the flap actuation design from the loadform perspective.

### 3.1 Implementation of the Actuator Cylinder Model (ACM)

The Mod-Lin ACM is chosen as the main aerodynamic model for the work conducted in this thesis. It is more precise than a BEM model and its computational cost is very low compared to panel methods. These features of ACM allow it to be used in an optimization structure. The Matlab implementation is done based on the information given in [41, 44, 45].

The coordinate system that is used to formulate the equations is shown in Figure 3.3. Here,  $+x$  is the free-stream direction from west to east and  $+y$  is towards north so that  $+z$  is out of the 2-D rotor plane. Initial azimuth position ( $\theta = 0^\circ$ ) is on the north pole of a unit circle centered at (0,0) in 2-D plane. So the  $90^\circ$  azimuth is at (-1,0),  $180^\circ$  azimuth is at (0,-1) and  $270^\circ$  azimuth is at (1,0). The rotor rotates towards counter clock-wise. Normal vector is out of the rotor plane and tangential vector is on the same direction with the rotational speed. The rotor can be divided into four characteristic regions which are 1)

upwind ( $45^\circ < \theta < 135^\circ$ ), 2) leeward ( $135^\circ < \theta < 225^\circ$ ), 3) downwind ( $225^\circ < \theta < 315^\circ$ ) and 4) windward ( $315^\circ < \theta < 45^\circ$ ).

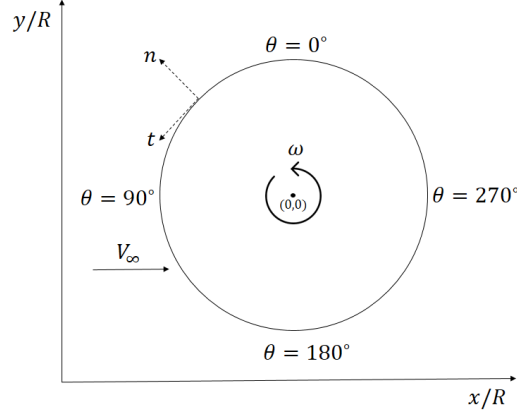


**Figure 3.1:** The coordinate system used for the ACM implementation in Matlab.

The recipe for the implementation can be listed as:

1. Discretize the rotor periphery to ' $N$ ' equal pieces along the azimuth and take the mid point of those pieces as the control points,  $(x, y)$  positions. Madsen recommends that 36 control points are enough to obtain a precise solution. Those positions are linearly spaced between in the azimuth ( $\theta \in [\frac{\pi}{N}, 2\pi - \frac{\pi}{N}]$ ). Then, create a slightly scaled rotor where new azimuth locations will be used as control points. This scaling is done since the solution on the rotor periphery is singular. A typical scaling factor is  $\pm 5\%$ .
2. Calculate the influence coefficients ( $R_{wx}, R_{wy}$ ) for each control point on the rotor. Note that the influence coefficient definition is similar to the one in vortex methods. In vortex methods it is based on Biot-Savarts law where in AC model it is derived from the Laplace solution of the doublet distributions.

$$R_{wx,j,i} = - \int_{\theta_i - 0.5\Delta\theta}^{\theta_i + 0.5\Delta\theta} \frac{-(x + \sin\theta) \sin\theta + (y - \cos\theta) \cos\theta}{(x + \sin\theta)^2 + (y - \cos\theta)^2} d\theta \quad (3.1)$$

$$R_{wy,j,i} = - \int_{\theta_i - 0.5\Delta\theta}^{\theta_i + 0.5\Delta\theta} \frac{-(x + \sin\theta) \cos\theta - (y - \cos\theta) \sin\theta}{(x + \sin\theta)^2 + (y - \cos\theta)^2} d\theta \quad (3.2)$$

3. Use iteration procedure to find induction velocities ( $w_x, w_y$ ) for each control point. This iteration procedure is inherited from BEM models where the only difference is the estimation of induced velocities. Firstly, the normal ( $V_n$ ), tangential ( $V_t$ ) and perceived velocities ( $V_{rel}$ ) at each control point are obtained by taking free-stream velocity ( $V_\infty$ ), rotational velocity ( $\omega$ ) and induced velocities into account. After obtaining the perceived angle of attack, with the airfoil polar data, one can

calculate the dimensional and non-dimensional normal and tangential forces ( $F_n$ ,  $F_t$ ,  $Q_n$ ,  $Q_t$ ) on the blades. Later, the calculation for the new induction velocities can be done by using Equation 3.11 and Equation 3.12. The formulation of aforementioned properties can be written as:

$$V_n = V_\infty \sin\theta + V_\infty (w_x \sin\theta - w_y \cos\theta) \quad (3.3)$$

$$V_t = -V_\infty \cos\theta - V_\infty (w_x \cos\theta + w_y \sin\theta) - V_\infty \lambda \quad (3.4)$$

$$V_{rel} = \sqrt{V_n^2 + V_t^2} \quad (3.5)$$

$$\alpha = \frac{V_n}{-V_t} - \theta_p \quad (3.6)$$

$$F_n = 0.5 \rho V_{rel}^2 c (C_l \cos \alpha + C_d \sin \alpha) \quad (3.7)$$

$$F_t = 0.5 \rho V_{rel}^2 c (C_l \sin \alpha - C_d \cos \alpha) \quad (3.8)$$

$$Q_n = B \cdot \frac{F_n \cos \theta_p - F_t \sin \theta_p}{2 \pi R \rho V_\infty^2} \quad (3.9)$$

$$Q_t = B \cdot \frac{F_n \sin \theta_p - F_t \cos \theta_p}{2 \pi R \rho V_\infty^2} \quad (3.10)$$

$$w_x(j) = \sum_{i=1}^{i=N} Q_{n,i} R_{wx}(i,j) - Q_{n,j}^* + Q_{n,N-j}^{**} \quad (3.11)$$

Here the single star term (\*) is added to the calculation if the control point is inside the actuator cylinder; the double star (\*\*) term is added if the control point lies in the wake of the actuator cylinder. These different equations are incorporated to take the pressure jumps across the upwind and downwind regions of the rotor into account.

$$w_y(j) = \sum_{i=1}^{i=N} Q_{n,i} R_{wy}(i,j) \quad (3.12)$$

4. Calculate the thrust coefficient of the rotor so that the linear solution could be modified. So the 'LIN' solution could become a 'MOD-LIN' solution.

$$C_T = \int_0^{2\pi} (Q_n \sin\theta - Q_t \cos\theta) d\theta \quad (3.13)$$

5. Estimate the correction factor  $k_a$  (Equation 3.14) with the help of thrust coefficient found from linear solution. The axial induction ( $a$ ) estimation for this calculation can be seen in Equation 3.15. Foundation of this modification could be found in [45].

$$k_a = \frac{1}{1 - a} \quad (3.14)$$

$$a = 0.0892 C_T^3 + 0.0544 C_T^2 + 0.2511 C_T - 0.0017 \quad (3.15)$$

6. Multiply the correction factor with the induced velocities ( $w_x, w_y$ ) and check for the convergence of these quantities. Note that at high loadings a relaxation factor is recommended on the induction velocities in order to avoid divergence in the solution. From this point, iterate until the induction velocities converge.
7. After obtaining convergence, calculate the  $C_P$  and  $C_T$ . Madsen introduces two ways of obtaining  $C_P$ . The first one is for the actuator cylinder (infinite blades) and the second one is for the finite bladed VAWT analysis. Here,  $B$  is the blade number,  $\theta_P$  is the fixed pitch angle of the blade and  $\omega$  is the rotational speed of the rotor.

$$C_{Pi} = \int_0^{2\pi} Q_n \frac{V_n}{V_\infty} d\theta \quad (3.16)$$

$$C_P = \frac{1}{2\pi} \frac{\int_0^{2\pi} B (F_t \cos \theta_p + F_n \sin \theta_p) \omega d\theta}{\rho V_\infty^3} \quad (3.17)$$

### 3.1.1 The validation of the code

The code is validated against the HAWC2 simulations. HAWC2 is a powerful tool for simulation of the wind turbine performance in the time domain. The reader can find the information regarding the implementation of the Mod-Lin ACM in HAWC2 in [45]. In order to compare the HAWC2 simulation with the Matlab, the forces in a single revolution are post-processed only. The turbine in HAWC2 is a rigid structure and have the same free-stream conditions with the Matlab code. For the validation case a rotor with  $\sigma = 0.1$  is simulated for a  $\lambda$  range from 2 to 5. A simplified airfoil polar is used in which the  $C_l = 2\pi \sin \alpha$  and  $C_d = 0.023$ .

The comparisons in terms of  $C_P$  and  $C_T$  are given in Figure 3.2. A close match is obtained between the simulations of the HAWC2 and Matlab implementation. The difference in the estimations are more pronounced at high  $\lambda$  where the rotor is highly loaded. The cause of the error could be the difference of the implementation in HAWC2 environment and the extra filters in HAWC2 or simply the uncertainty of the Mod-Lin ACM at highly loaded cases.

The  $Q_n$  and  $Q_t$  estimations for  $\lambda$  of 2 and 4 are presented in Figure 3.3. The loadings match closely for the most of the regions. The biggest differences exist in the estimations of the downwind part and this difference increases with the higher  $\lambda$ . Similarly, the

comparison of the axial and lateral induction velocities are shown in Figure 3.4. These plots are more helpful to see the cause of the error. The biggest mismatch occurs in the axial induction estimation when  $\lambda$  is higher. At  $\lambda = 5$  the  $C_P$  difference between the codes is 4.5% and the  $C_T$  difference is 0.5%. But for the other simulation points the errors are much smaller, therefore this fidelity is found acceptable and the Matlab implementation is used throughout the thesis. It should be noted that, the Matlab code is proof-checked many times and the model is correctly constructed. Therefore, the difference in the results are most likely due the extra treatments in the HAWC2.

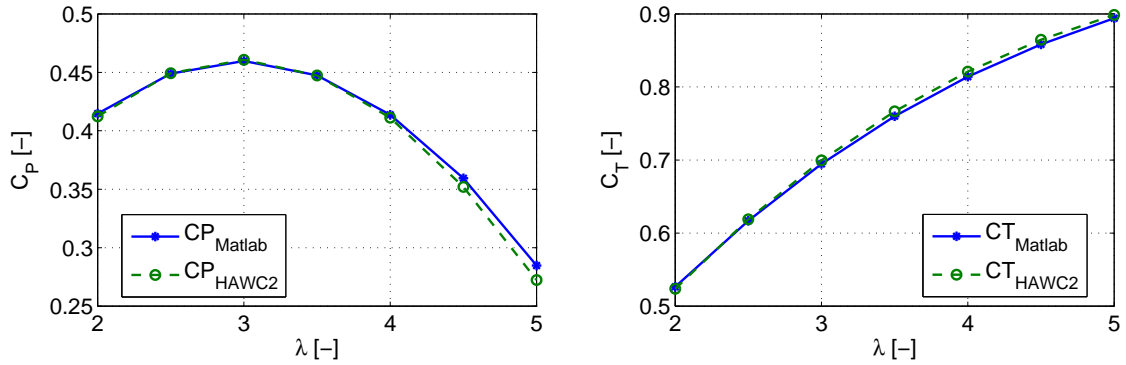


Figure 3.2: Validation of the ACM in Matlab, the  $C_P$  and  $C_T$ .

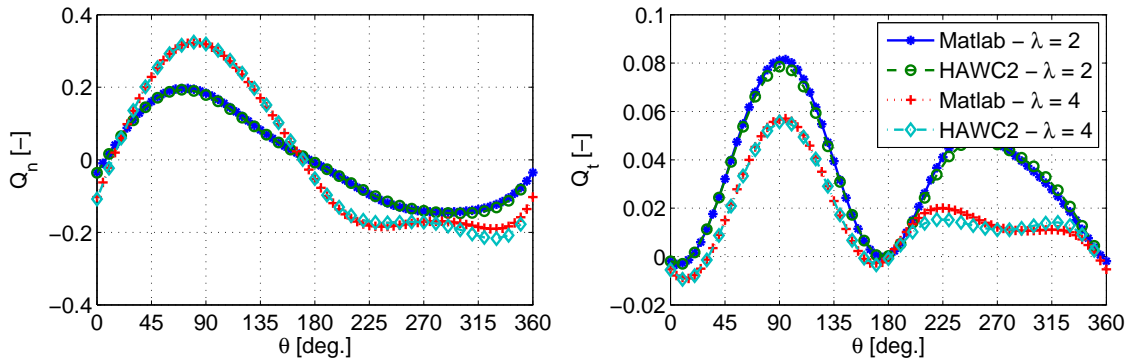


Figure 3.3: Validation of the ACM in Matlab, the  $Q_n$  and  $Q_t$ .

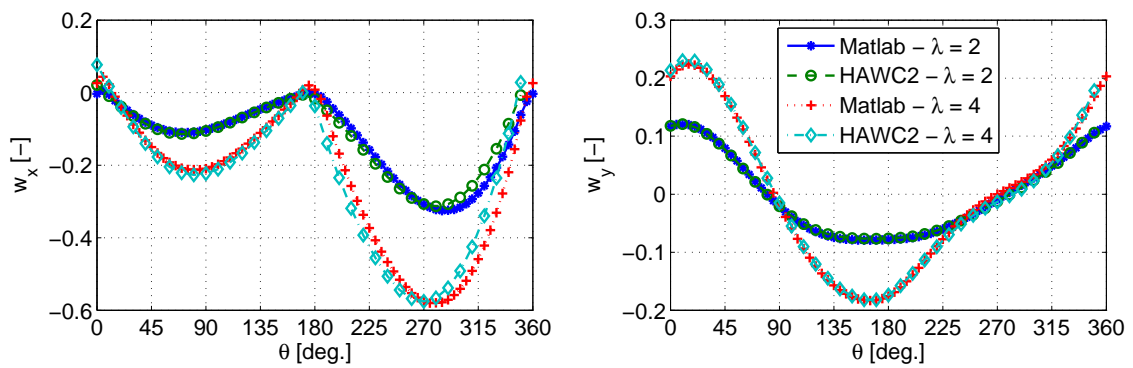


Figure 3.4: Validation of the ACM in Matlab, the  $w_x$  and  $w_y$ .

## 3.2 Exploring the design space of the actuator cylinder by analytic expressions of the loadforms

Performance estimations for this chapter are based on the ideal energy conversion study of Madsen et al. [46]. According to that study the assessment of the  $C_P$  and  $C_T$  could be carried out with the ACM by only knowing the normal loading,  $Q_n$ . Along the text this loading type is called as the *loadform*. Once the  $Q_n$  is known then the induction velocities, normal and tangential velocities for the actuator surface are calculated without any iteration. Finally, the  $C_P$  and the  $C_T$  are assessed.

Two different analytic loadform equations are used along this work. Both are the modified versions of the loadform expression defined by Madsen [46]. The first expression (Equation 3.18) adds one new variable ( $\Delta\theta$ ) which allows stretching/compressing the loading between the upwind and the downwind regions. This modification is introduced to account for the flow expansion around the windward and the leeward regions of the rotor. The second expression (Equation 3.19) includes two more variables which enables setting different curve types for the upwind and the downwind part. This expression increases the variety in the loadform types which would lead to a refined exploration on the loadforms.

$$Q_n(\theta) = Q_{n,max} \cdot \frac{\sin(\tilde{\theta})}{|\sin(\tilde{\theta})|} \cdot \left( 1 - |\cos(\tilde{\theta})|^m + \frac{1}{2\pi} \sin\left(2\pi|\cos(\tilde{\theta})|^m\right) \right) \quad (3.18)$$

Here  $\tilde{\theta} = \theta - \Delta\theta \cos(\theta) \frac{\pi}{180}$ .  $\Delta\theta$  is a real number defined in degrees and controls the level of stretching on the loadform.  $Q_{n,max}$  sets the peak value of the loadform and  $m$  is an exponential factor responsible of the curve shape. A small  $m$  leads to a peaky loadforms while a large  $m$  creates uniform loadforms.

$$Q_n(\theta) = Q_{n,max1} \cdot \frac{\left(\frac{\sin(\tilde{\theta})}{|\sin(\tilde{\theta})|} + 1\right)}{2} \cdot \left( 1 - |\cos(\tilde{\theta})|^{m_1} + \frac{1}{2\pi} \sin\left(2\pi|\cos(\tilde{\theta})|^{m_1}\right) \right) + \quad (3.19)$$

$$Q_{n,max2} \cdot \frac{\left(\frac{\sin(\tilde{\theta})}{|\sin(\tilde{\theta})|} - 1\right)}{2} \cdot \left( 1 - |\cos(\tilde{\theta})|^{m_2} + \frac{1}{2\pi} \sin\left(2\pi|\cos(\tilde{\theta})|^{m_2}\right) \right)$$

### 3.2.1 A parametric study to explore the $C_P-C_T$ relations

The parametric study is based on evaluating the Equation 3.18. A wide range of inputs are evaluated for each variables in the equation:  $Q_{n,max} \in [-0.6, 0.6]$ ,  $m \in [1, 300]$  and  $\Delta\theta \in [-10^\circ, 80^\circ]$ . As a result, a global view on the actuator cylinder performance is obtained and shown in Figure 3.5. This is a scatter plot where each point corresponds to a combination of the inputs mentioned above. One can also see the propeller state ( $C_T < 0$ ) of the actuator cylinder. The estimations with  $C_T$  larger than 1 is not shown since the uncertainty of the Mod-Lin model increases significantly. Maximum  $C_P$  is obtained as 0.5958. Note that the maximum value obtained by the non-linear ACM was reported as 0.633 with similar loadforms by Madsen [46]. In that sense, a significant

difference between the Mod-Lin and the nonlinear ACM is observed for the highly loaded region cases.

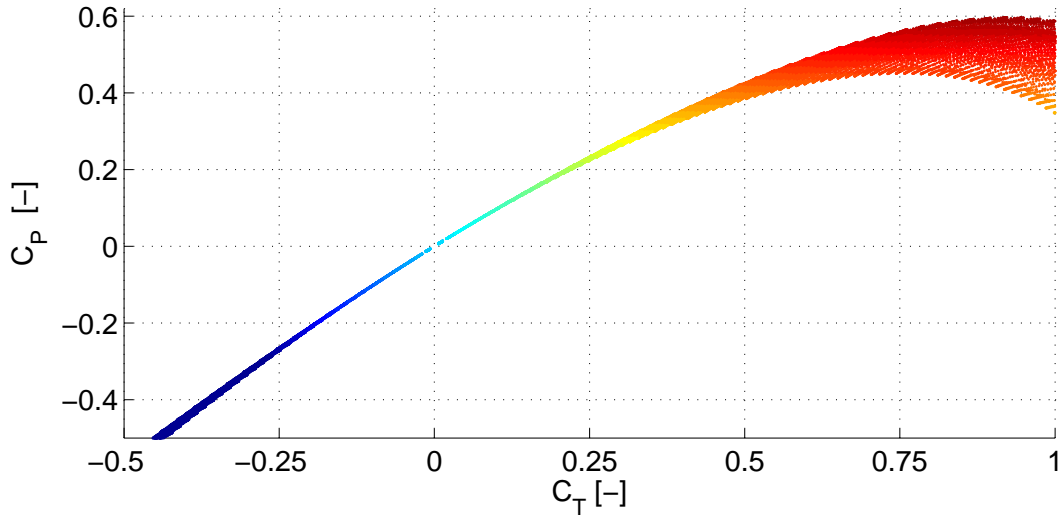


Figure 3.5: The global view on the  $C_P$ - $C_T$  relation of the VAWT.

Figure 3.6 shows a closer look to the high  $C_P$  region. It is deduced that the VAWT design space enlarges as the  $C_T$  increases. This result shows one of the key feature of the VAWT which is the capability to decrease the  $C_T$  while keeping the  $C_P$  same or vice versa. This sort of modification on the performance could be governed by changing the distribution of the loading in the upwind and the downwind region accordingly. This phenomenon has been shown by many authors such as Madsen [46] and Ferreira et.al. [20].

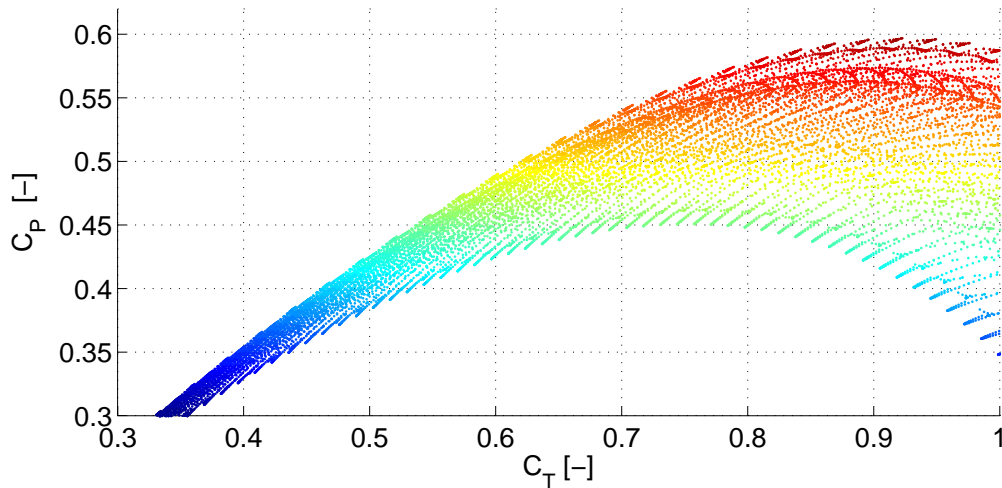
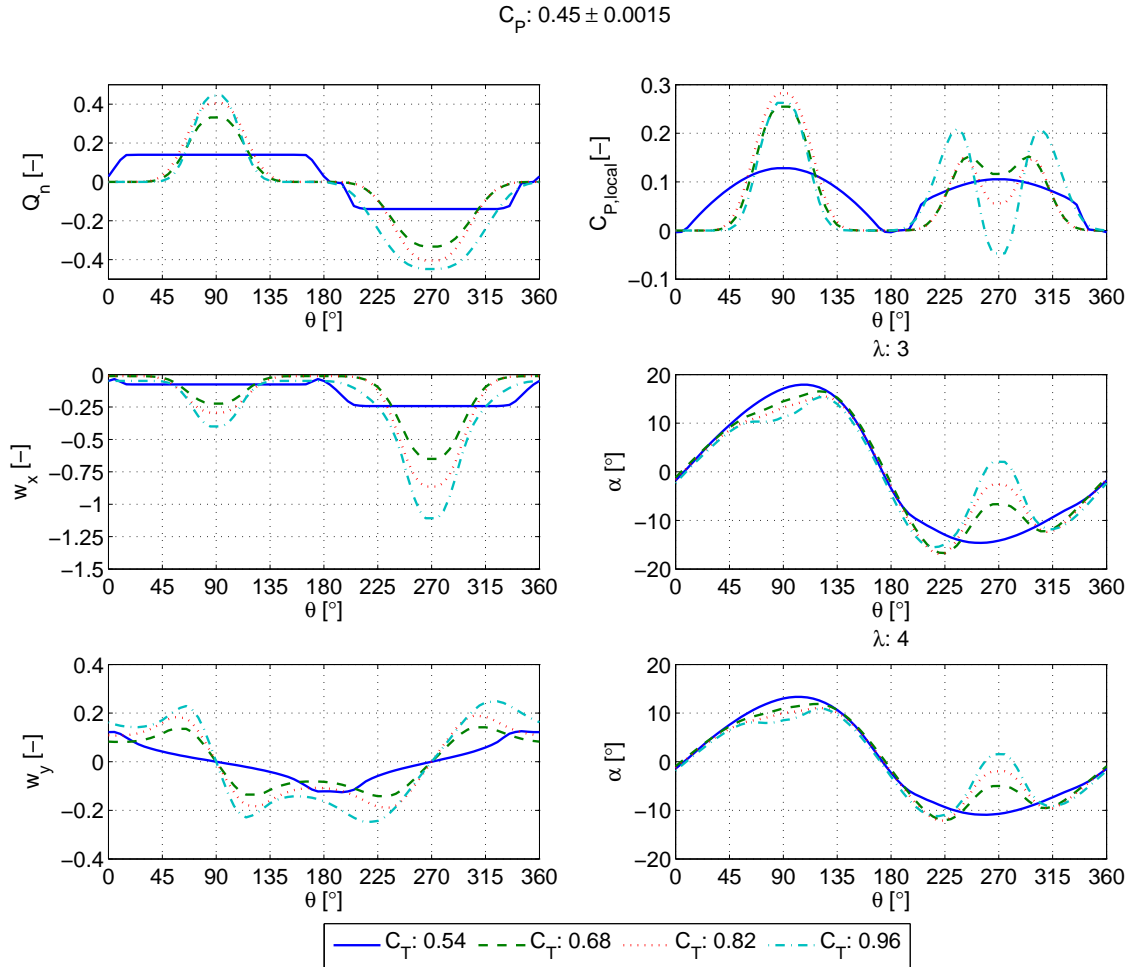


Figure 3.6: A closer look to the high  $C_P$  region.

The performance of four different loadforms with the same  $C_P$  but a different  $C_T$  are shown in Figure 3.7. Subplots are showing the loadform, local power coefficient, axial and lateral induction velocities and the perceived angle of attack for tip speed ratio of 3

and 4. The main outcome is the increment of the  $C_T$  with the larger peaks ( $Q_{n,max}$ ) in the loading. A uniform loading with smaller magnitudes leads to an operation point with a low  $C_T$  and a high  $C_P$ . Among different loadforms, the angle of attack does not change significantly for the upwind part; the difference in the downwind part is more pronounced. This is due to larger difference in the axial induction in downwind.



**Figure 3.7:** Loadforms with the same  $C_P$  but different  $C_T$ .

Similarly, Figure 3.8 shows four different loadforms with the same  $C_T$  but different  $C_P$ . An analogous result is observed: the  $C_P$  could be increased while keeping the  $C_T$  constant if the maximum loading is alleviated and the load distribution is made more uniform. As the axial induction level increases the  $C_P$  decreases, therefore for an optimum loading the inductions should not be very large. It is interesting that the loadforms that corresponds to  $C_P$  equal to 0.43, 0.49 and 0.54 look very similar. According to this similarity, it can be concluded that the  $C_P$  could be changed significantly only with a small deviation from the loadform. This deduction supports the idea of using small trailing edge flaps on the VAWT blades for the performance enhancement.

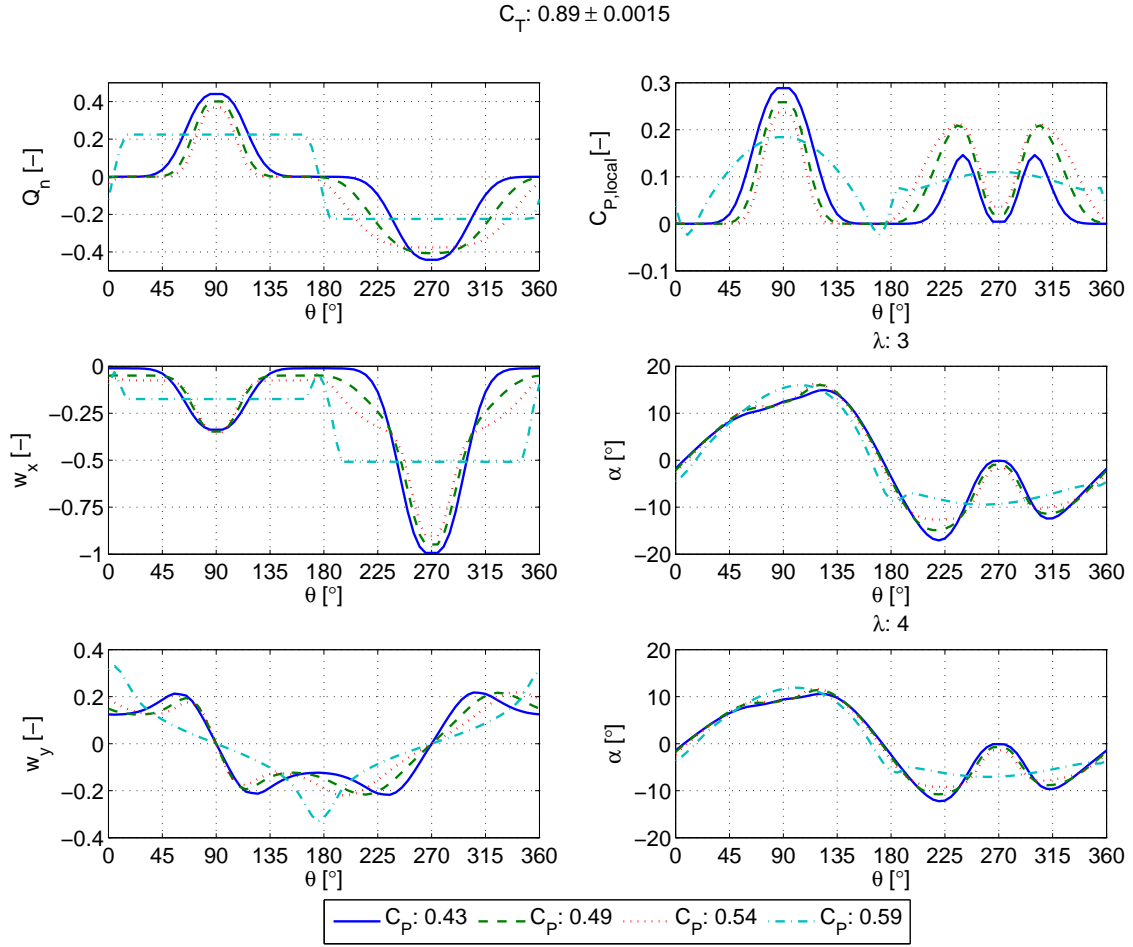


Figure 3.8: Loadforms with same the  $C_T$  but different  $C_P$ .

### 3.2.2 Optimization of the loadforms to obtain the $C_{P,max} - C_T$ curve

The parametric study in the previous section showed the result of a manual loadform search. Now, a simple numerical optimizer is set to have a more robust search. The optimizer algorithm is used as the gradient-based *SQP* algorithm in the Matlab Optimization Toolbox [47].

The aim is to see the maximum achievable power coefficient ( $C_{P,max}$ ) with the analytic loadforms. Equation 3.19 is used to allow a wide range of loadforms. Note that the  $Q_{n,max2}$  is set to the same value of  $Q_{n,max1}$  along the optimization. This assumption is based on the fact that the transfer of loads between the upwind and downwind region does not change the energy conversion process [20, 46]. The computational cost of this case could be decreased by 20% if the peak loadings are assumed equivalent. So the optimizer searches for the best combinations of the  $Q_{n,max1}$ ,  $m_1$ ,  $m_2$  and  $\Delta\theta$  to obtain the highest possible  $C_P$  for a target  $C_T$ . For the  $C_{P,max}$  case the objective is set as  $J = -C_P$ .

Figure 3.9 shows the optimized  $C_P - C_T$  curve and the optimized loadforms for various  $C_T$  values. The  $C_P - C_T$  curve from the optimization is compared with the actuator disc

theory modified with the Glauert correction. The optimization shows a close match with the estimations of the parametric study. The estimation of the maximum  $C_P$  is the same as well, 0.5985. There are not any significant differences between the maximized actuator cylinder performance and the actuator disc performance. Only significant difference is that it is possible to keep the  $C_P$  higher than the actuator disc for the  $C_T$  values larger than 0.89. As observed in the parametric study, the optimum loadforms are uniformly loaded and require low magnitudes of load. A slight stretching of the loadform in upwind is apparent for the loadform with  $C_T = 1$ .

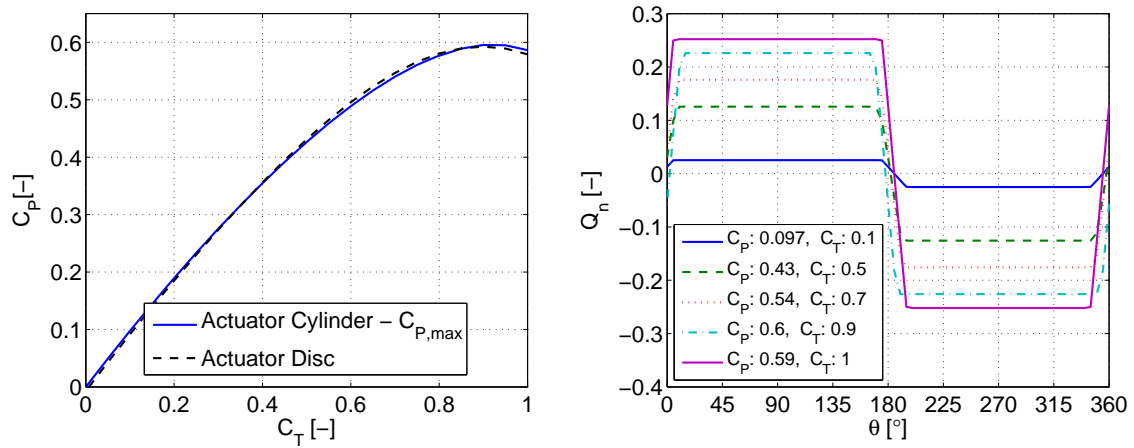


*Figure 3.9: Optimized analytic loadforms for maximizing and minimizing the  $C_P$ .*

### 3.3 Exploring the design space of the actuator cylinder by Bezier curves

A new approach to the loadform creation is introduced in this section, the Bezier curves. Bezier curves are chosen to increase the variety and types of the loadforms that the analytic loadforms can not provide. A sensitivity analysis for the Bezier curve order is done by checking the deviation in the optimized  $C_P$  and the computation time with different number of bezier points ( $N_{Bezier}$ ). Sensitivity analysis is carried out for various tip speed ratios to obtain a global deduction for the Bezier curve order. The result of this study can be seen in Figure 3.10.

As a conclusion it is decided to use 15 Bezier points along the azimuth. Azimuth position of the Bezier points are fixed and linearly spaced. To create periodic curves, the coefficients for  $\theta$  of 0 and 360 degrees are taken the same. This section presents both an unconstrained and a constrained optimization of the loadforms with Bezier curves. Since the relation between 15 Bezier points and the performance of the actuator cylinder is highly nonlinear, a genetic algorithm is used for the corresponding study.

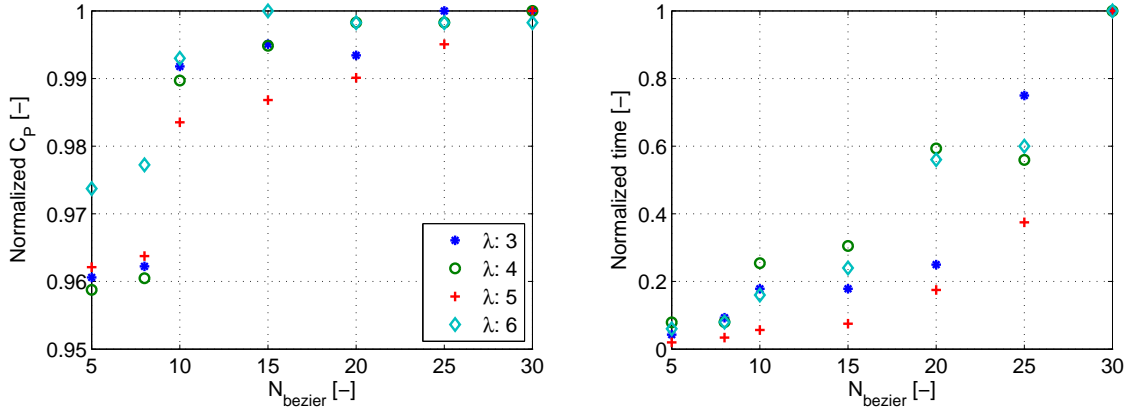


Figure 3.10: Sensitivity analysis on the Bezier curve order (for the loadform analysis).

### 3.3.1 Unconstrained search

The unconstrained optimization is performed in order to find the loadforms with the maximum achievable  $C_P$  for a given  $C_T$ . In fact, a single constraint is applied in order to sustain the numerical stability of the ACM. Therefore by *unconstrained search* we mean that there are not limitations on the shape of the loadform. The corresponding numerical constraint limits the maximum absolute  $Q_n$  to 0.35. It is observed that above this value the optimizer tend to produce very optimistic but false results. The Mod-Lin ACM has its validity limits and the user should be aware of it. Rest of the optimization set-up is very similar to the methodology in the previous section; the  $Q_n$  is designed then its performance is estimated for an infinite number of blades with Equation 3.16. Now, the design vector is the y-axis coefficients of the Bezier points.

Figure 3.11 shows the optimum  $C_P - C_T$  curve and the corresponding loadforms to obtain such performance. The  $C_{P,max} - C_T$  curve and the actuator disc theory are again compared. The result is similar to the one from analytic loadform optimization but with slightly higher  $C_P$  values. The maximum  $C_P$  is obtained as 0.6011. Although the optimum loadings have similar ranges of magnitudes in upwind and downwind region; the loading is not uniform. As the  $C_P$  increases the loading becomes more uniform in the upwind but in the downwind region most of the loadings have an apparent bump near 270 degree of azimuth.

The bump in the downwind region of an optimized loadform could be a favorable feature in the real application. Because, in a real VAWT rotor that region will be affected by the tower wake so that the  $Q_n$  will be low at that region inherently. Hence dedicated design improvements would not be necessary for the regarding region. But the bumpy loadforms should be assessed with higher order models before making solid deductions.

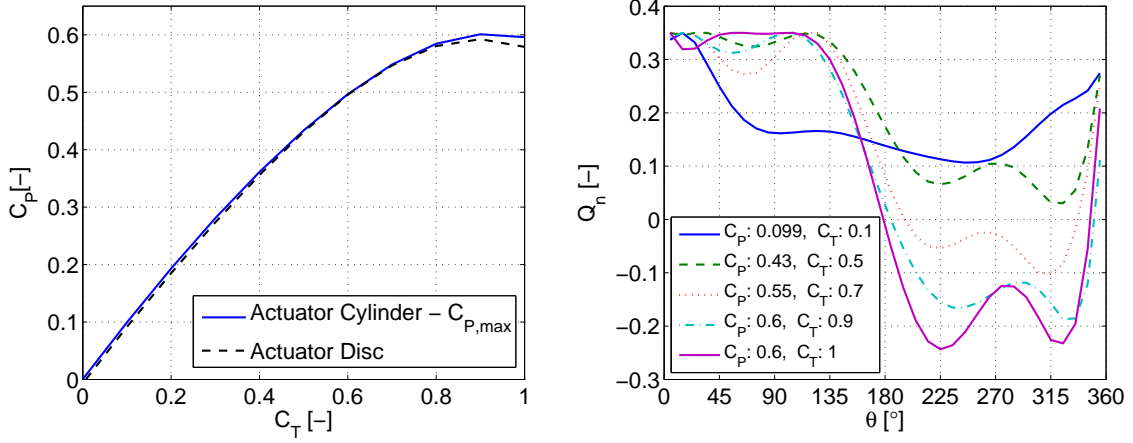


Figure 3.11: Optimized Bezier loadforms for maximizing and minimizing the  $C_P$ .

### 3.3.2 Constrained search

In this section the design space of the loadform is constrained by a range which is defined through a reference loadform ( $Q_{n,ref}$ ) and a percentage of the deviation ( $f_{\Delta Q_n}$ ) from the reference loadform. The mathematical representation of the feasible design space is given in Equation 3.20. Except the new constraints, the optimization methodology is the same with the unconstrained Bezier loadform optimization.

$$Q_n(\theta) \in (Q_{n,ref} \pm f_{\Delta Q_n} \cdot \max(Q_{n,ref})) \quad (3.20)$$

Four different reference loadforms are taken into account for this work. Figure 3.12 shows the reference loadforms and their  $C_P$ . The  $C_P$  and  $C_T$  values of these loadforms differ from each other. These loadforms are chosen carefully so that they would represent different tip speed ratios. Hence, an idea of the flow control authority for different  $\lambda$  could be obtained at this stage. Four different  $f_{\Delta Q_n}$  are used for this study as 5%, 15%, 30% and 50%. It is important to mention that the change in  $Q_n$  for a fixed  $\sigma$  and  $\lambda$  will be linearly proportional to the change in  $C_l$  of the blade section. Therefore this section answers the preliminary question of how much improvement on  $C_P$  could be made with various levels of control authority on the aerodynamic forces.

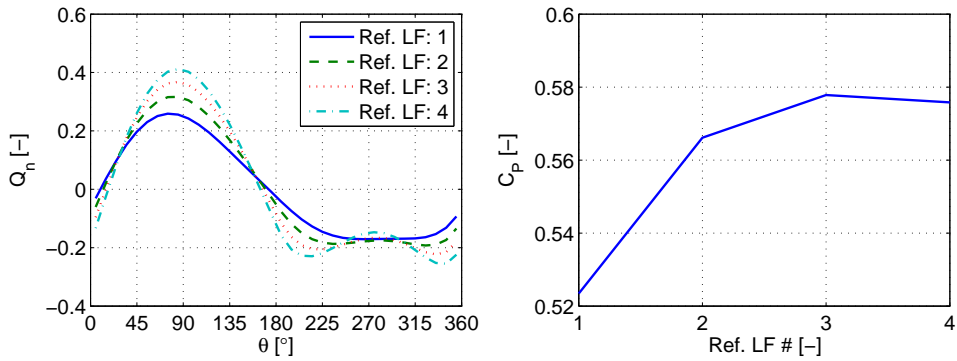
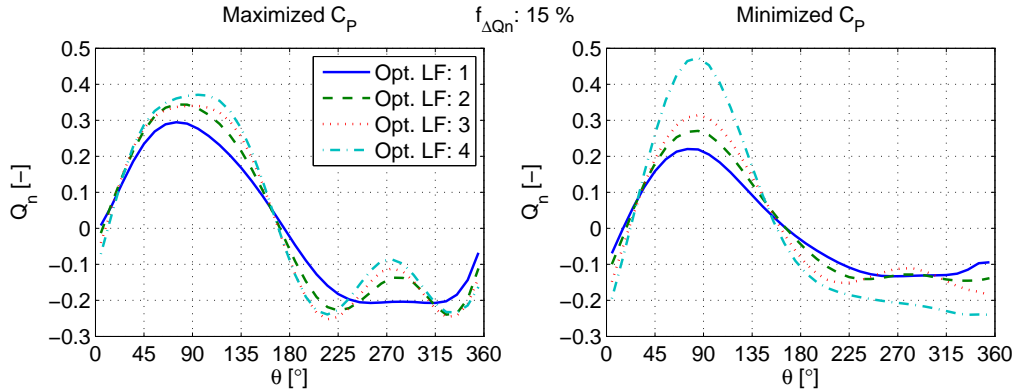


Figure 3.12: Reference loadforms used to set the bounds of the design space.

The loadforms are optimized for two different objectives: 1) maximizing the  $C_P$  and 2) minimizing the  $C_P$ . In Figure 3.13 the optimized loadforms for these tasks are shown for the case that  $f_{\Delta Q_n}$  is set as 15%. The line types and colors are inherited from the Figure 3.12 so that the reference and optimized loadforms can be compared easily with the naked eye. To maximize the  $C_P$ , a more uniform loading is created in the upwind region and the loading near 270 degrees is decreased by creating a bump in the loading. This outcome matches with the findings of the unconstrained optimization. To minimize the  $C_P$  of the reference loadforms, the upwind loading is constructed with higher peaks and the loading on the downwind is increased with respect to the reference loadform. Optimizer chose to decrease the  $C_P$  by increasing the  $C_T$  and inductions. This modification could also be done by decreasing the  $C_T$  but the corresponding loadforms were not feasible in the constrained design space.



**Figure 3.13:** Optimized loadforms by the constrained Bezier curves to the 15% of the  $Q_{n_{ref,max}}$ .

In Figure 3.14 the improvements on the  $C_P$  (y-axis) of each reference loadform (x-axis) are given for four different deviations ( $f_{\Delta Q_n}$ ). In a general view, the  $C_P$  has increased more with larger  $f_{\Delta Q_n}$  but this increment does not increase linearly. This leads to a conclusion on the flap authority: the increase in the flap authority might not improve the  $C_P$  in a proportional fashion due to the efficiency limits of the VAWT. Therefore, large flap size might not be required. This issue will be investigated in the next chapter. Figure 3.15 shows the results for the  $C_P$  alleviation. Here, it is seen that the  $C_P$  of the reference loadforms decrease in a linear fashion with the  $f_{\Delta Q_n}$ . This result shows that there is a high control potential to decrease the  $C_P$ . The same flap authority is more effective in decreasing the  $C_P$  than its increment. The alleviation in the  $C_P$  goes up to 74% when a 50% deviation from the reference load is allowed. This alleviation rate is roughly enough for a rated power control. Therefore, as a preliminary conclusion we can say that if a flap could change the lift by at least 50% than a rated power control of the VAWT could be done by the flap.

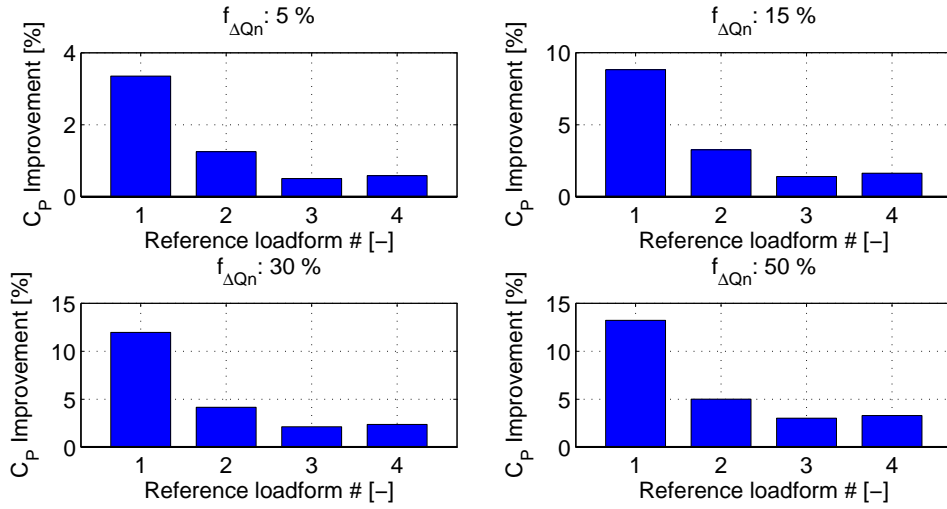


Figure 3.14:  $C_P$  improvement on the reference loadforms with different values of constraints ( $f_{\Delta Q_n}$ ).

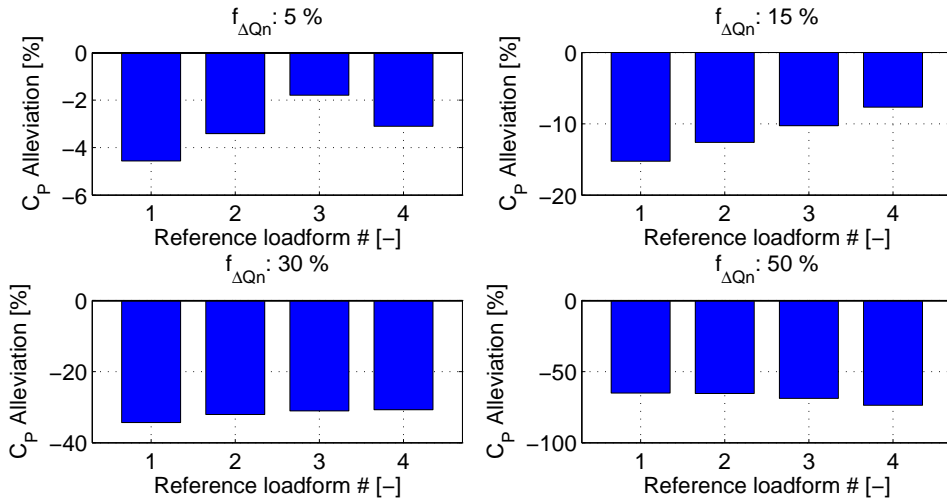


Figure 3.15:  $C_P$  alleviation on the reference loadforms with different values of constraints ( $f_{\Delta Q_n}$ ).

### 3.4 Conclusions of the chapter

Various methods are used in this chapter to explore the potentials of the VAWT with the help of the Actuator Cylinder Model. The effect of different types of loadforms are documented and preliminary deductions on the flow control authority are drawn. The main conclusions of this chapter can be shown as:

- A uniform loading with relatively smaller aerodynamic loading would have a higher  $C_P$  and a lower  $C_T$  than a peaky loadform with a higher maximum loading.

- The  $C_P$  regarding to a specific loadform could be changed significantly by small deviations from the loading. The idea of using flaps effectively for the VAWT rotor has a support from the loadform perspective.
- The loadforms created with the Bezier curves showed that the non-uniform loadings could have high power efficiencies as well. Moreover, the optimized Bezier loadforms have a bump in the downwind region which might be a favorable feature when the existence of the tower wake is considered.
- With the same control authority more gains are achieved for the minimization of  $C_P$  than the maximization task. The  $C_P$  maximization case is more challenging since the aerodynamic loads can not be increased arbitrarily due to the borders set by high axial inductions. On the other hand, this relation might change if the baseline efficiency of the considered turbine is low. In this chapter, we optimized loadforms that already have high efficiency.
- As a first impression from the constrained analysis, it is seen that the improvement on the  $C_P$  would not increase proportional to the increase in the flap control authority. Besides, the alleviation percentages of the  $C_P$  is strongly correlated with the flow control authority.
- The uncertainty of the Mod-Lin ACM increases at high  $C_T$ . Also the maximum achievable  $C_P$  is estimated lower than the non-linear ACM result in the literature. The user of this model should be aware of those features.



# Generation of the Active Flap Control Sequences

In this chapter, several methods are created and studied in order to design azimuthal flap sequences for a finite bladed VAWT. Later, examples with different flap authorities are presented both with inviscid and viscous airfoil polars. Two main paths are taken: 1) the inverse method and 2) the direct method. The *inverse method* makes a the direct analytic derivation of the flap sequences that leads to an already known target loading. Besides, the *direct method* is based on the creation of the target loadform by designing a flap sequence in a specified design space. Unlike the inverse method which is not an iterative process, the direct method requires a search algorithm in order to figure out the flap sequence that performs the best for given objectives and constraints. Throughout the section, the reader will encounter 3 main objectives that is used to find optimum flap sequences. These objective are: 1) Maximizing the power efficiency ( $C_P$ ), 2) Minimizing the power efficiency and 3) Minimizing the mean thrust coefficient ( $C_T$ ) while sustaining a high power efficiency value. The first objective is set to decrease the CoE of the VAWT. The second objective is formulated to explore the power control capabilities of the flap so that a rated power control could be established. Finally, the third objective is adopted because a low  $C_T$  is favorable for lower cyclic load-ranges and dynamic stability considerations of the floating wind turbine concepts.

### 4.1 Inverse method

There are two main parts in this section: the unconstrained inverse method and the constrained inverse method. The first part does not have any restrictions on the maximum flap angle deflection, but the latter is constrained with such rule. In the previous chapter, the optimum loadforms are obtained from the analysis of the VAWT with an infinite number of blades. Here, several of those optimized loadforms are used as an input to the inverse method.

#### 4.1.1 Unconstrained inverse method via optimized loadforms

The unconstrained inverse method is the most simple version of the inverse derivation. To obtain the required flap sequence, a reference loadform, a target loadform, a flapped-airfoil polar, rotor solidity ( $\sigma$ ) and tip speed ratio ( $\lambda$ ) has to be defined. The method finds a flap sequence that would be applied on a reference loadform to reach a target loadform. A potential flow approach is chosen to generate the airfoil polar. The lift coefficient is calculated by  $C_l = C_{l\alpha}\alpha + C_{l\beta}\beta$ , the airfoil does not experience a stall and the drag coefficient ( $C_d$ ) is 0. The lift curve slope ( $C_{l\alpha}$ ) is chosen as  $2\pi$  and the flap sensitivity ( $C_{l\beta}$ ) is taken as  $0.035 [\frac{1}{deg}]$ . This value is representative for maximum the flap authority that a 10%-15% flap could obtain in a viscous flow.

To derive the flap sequences, first, the induction velocities ( $w_x, w_y$ ) for the target loadform are found with a Mod-Lin ACM. The formulation of that process can be found in Madsen's works [44, 46]. Later, the axial velocities, the relative velocity and the angle of attack are computed. Finally the target  $C_l$  is calculated with Equation 4.1 and the required flap sequence is then found with Equation 4.2. The formulation is clear and easy due to the simplified form of the airfoil data. In case of real polars one needs to use look-up tables.

$$C_{l,target} = \frac{2\pi \cdot V_\infty^2 \cdot Q_{n,target}}{V_{rel}^2 \cdot \cos(\alpha) \cdot \sigma} \quad (4.1)$$

$$\beta_{required} = \frac{C_{l,target} - C_{l,\alpha} \cdot \sin(\alpha)}{C_{l\beta}} \quad (4.2)$$

To demonstrate the inverse method, two different reference loadforms and three different target loadforms are taken into account. These loadforms are shown in Figure 4.1. Reference loadforms represent the VAWT with a  $\sigma$  of 0.1 which operates at  $\lambda = 4$  and 5 where the  $C_P$  is 0.566 and 0.578 respectively. The target loadforms are inherited from the studies in the previous chapter. These are from the analytic loadform, unconstrained Bezier loadform and constrained Bezier loadform optimization studies, which have  $C_P$  of 0.596, 0.601 and 0.590 respectively.

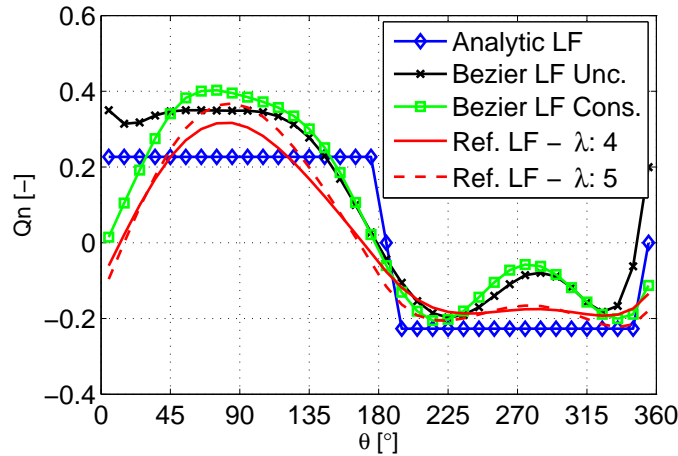


Figure 4.1: Normal loading ( $Q_n$ ) of the reference and optimized loadforms.

Figure 4.2 shows the flap sequences to reach the analytic loadform, sub-figures show the results for different  $\lambda$ . It is seen that the required flap angles, for some azimuth positions, are excessive and beyond the practical limits of a flap deflection. The regions with very large flap demand exist due to two main reasons. First, the difference between the reference loadform and the analytic loadform is the highest in those regions (see Figure 4.1). Secondly the perceived angle of attack and the relative velocity decreases dramatically in those regions which decreases the loads. Once the relative velocity is decreased, more flap deflection is demanded to compensate the gap. Moreover, the analytic loadform has very high gradients near 180 and 360 degrees which becomes a critical issue in practical flap design. Because none of the modern flap actuators can guarantee such high actuation gradients. This study also shows that the maximum value of the flap angle demand decreases with the  $\lambda$  since the relative velocities are increasing. From a similar perspective, a higher solidity rotor requires less flap deflection since its chord is larger. Here, it is assumed that the solidity is changed by the chord size.

The required flap sequences to mimic the optimized unconstrained Bezier loadform are presented in Figure 4.3. When compared with the flap demands for the analytic loadform, smoother curve shapes are obtained. On the other hand, there are still excessive flap deflection demands. In fact, for properly chosen rotor solidity, the flap deflection demands become acceptable.

The required flap angles to reach the optimum constrained Bezier loadform are shown in Figure 4.4. The results are very similar to what is obtained from the unconstrained Bezier curve. Again, the flap demands for the higher solidity rotor ( $\sigma=0.1$ ) are smooth, has smaller gradients and in acceptable limits of the flap actuation. By saying *acceptable limits*, a deflection range roughly between -30 and +30 degrees is meant. This range of deflection can be accomplished easily by the traditional actuators and by few of the smart actuators [2]. Note that, here we used the constrained Bezier loadform in the case of  $f_{\Delta Q_n} = 30\%$ . A more strict constraint would give smaller flap demands but the target  $C_P$  would be decreased in that case.

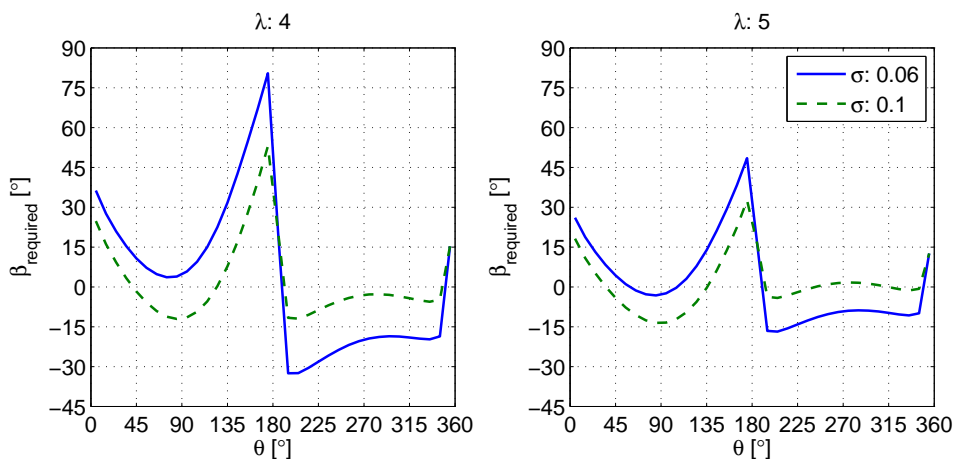
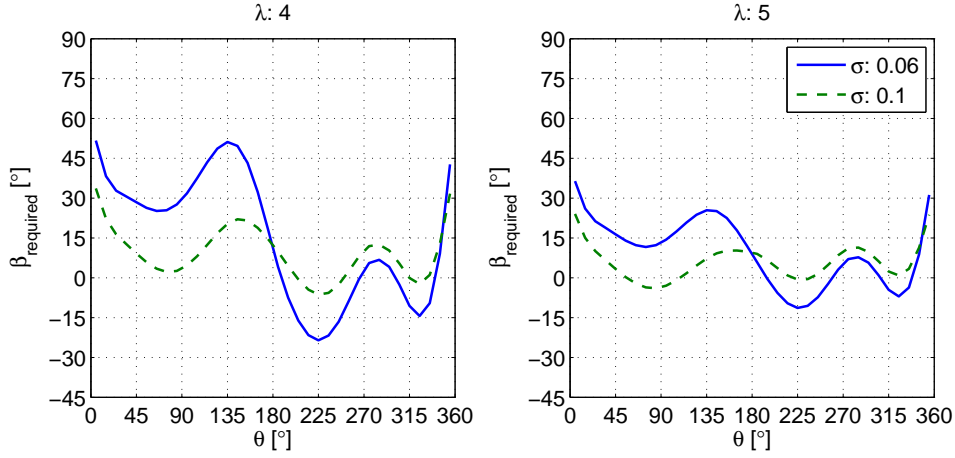
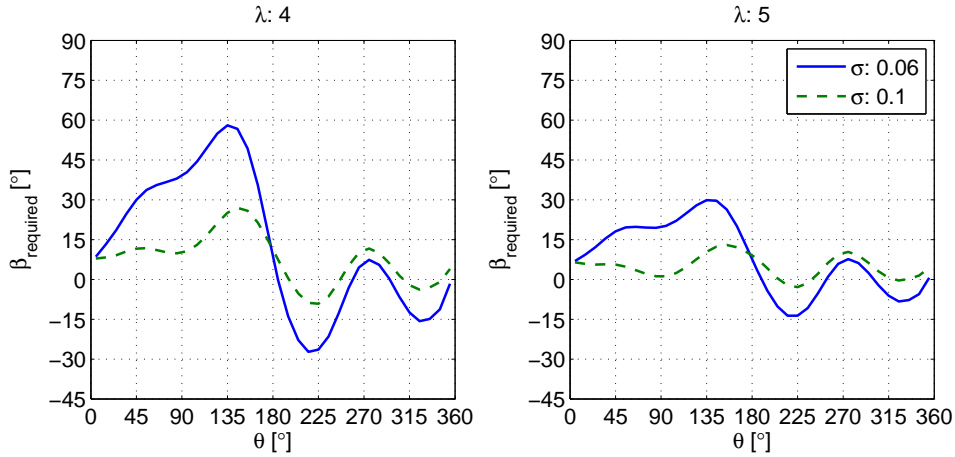


Figure 4.2: Required flap sequences to obtain the optimized analytic loadform.



**Figure 4.3:** Required flap sequences to obtain the optimized loadform by a unconstrained Bezier curve.



**Figure 4.4:** Required flap sequences to obtain the optimized loadform by a constrained Bezier curve with  $f_{\Delta Q_n}$  of 30%.

#### 4.1.2 Constrained inverse method via hybrid loadforms

In the previous section, it is shown that the plain inverse method is a very fast tool but it could lead to flap demands which are excessive. Now, the aim is to see how much the  $C_P$  decreases when the maximum flap deflection is limited. A simple iterative method is used to find the limited case with the least loss from the target  $C_P$ . This method starts with the choice of an optimum loadform with a very high  $C_P$ . Then the mean line of the optimum loadform is normalized with respect to the mean line of the reference loadform. This step helps to normalize the flap sequence around 0 degree. Later, a group of hybrid loadforms are created by using different mixing coefficients ( $f_{\text{hybrid}}$ ) span from 0 to 1. The linear relation that is used to create hybrid loadforms can be seen in Equation 4.3. Then, the flap sequences required to obtain the hybrid loadforms are computed and further limited by the flap deflection constraint. Finally, the new  $C_P$ 's that correspond to the constrained

flap sequences are computed. The mixing coefficient which gives the constrained hybrid loadform with the highest  $C_P$  is chosen as the final design point.

$$Q_{n,hybrid} = f_{hybrid} \cdot Q_{n,reference} + (1 - f_{hybrid}) \cdot Q_{n,optimum} \quad (4.3)$$

The reference loadforms are obtained by analyzing the VAWT performance for  $\sigma$  of 0.06 and 0.1 at  $\lambda$  of 3, 4 and 5.  $C_l$  is taken as  $2\pi\sin(\alpha)$ ,  $C_d$  is 0 and  $C_{l\beta}$  is taken as  $0.035 \left[\frac{1}{deg.}\right]$ . The optimum loadform is chosen as the unconstrained Bezier loadform with the highest  $C_P$  and the flap deflection limit is chosen as  $\pm 20$  degrees. Figure 4.5 shows the final hybrid loadforms and the induction velocities on the left column of plots where the right column shows the flap deflection demands for different  $\lambda$  and  $\sigma$ . The result revealed that the trimming on the original flap demands are more severe if the  $\sigma$  and/or  $\lambda$  is low.

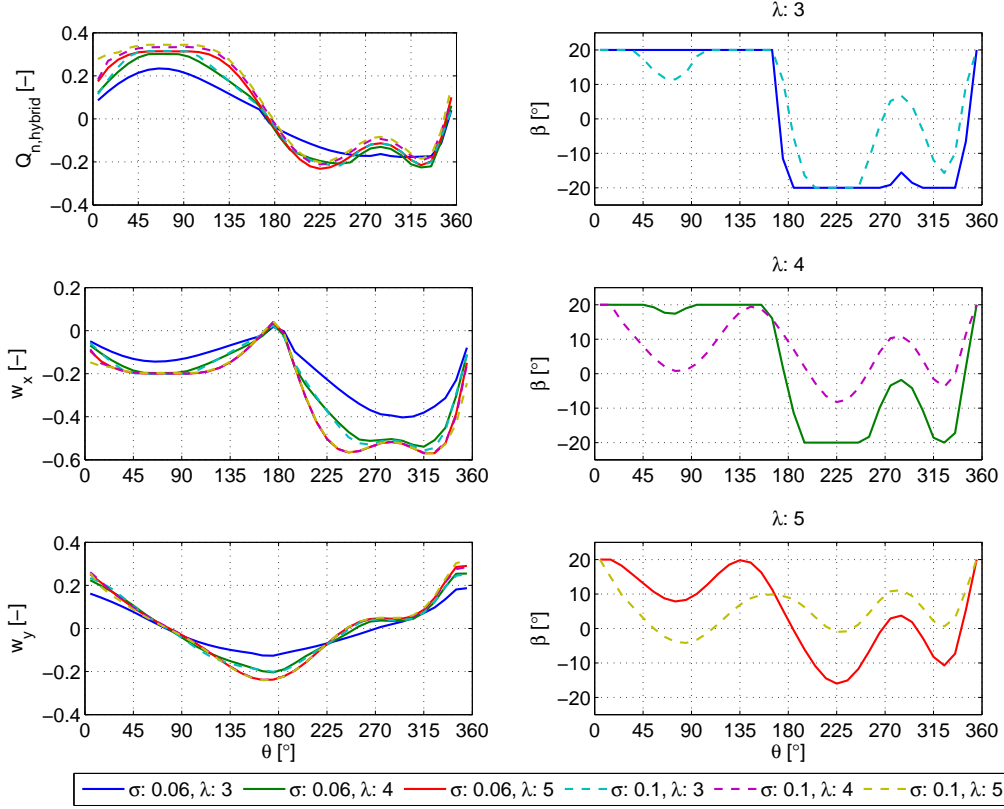


**Figure 4.5:** Normal loading ( $Q_n$ ), induction velocities ( $w_x$ ,  $w_y$ ) and flap angles ( $\beta$ ) obtained by limiting the flap deflection of a hybrid loadform.

Table 4.1 presents the  $C_P$  of the reference, optimum and hybrid loadforms. Furthermore the gains in the  $C_P$  with respect to the reference loadforms are shown. It is documented that the constrained loadforms could also improve the  $C_P$  significantly. In the case of  $\sigma = 0.06$  at  $\lambda = 3$  the optimum loadform leads to 50.06%  $C_P$  increase while the hybrid loadform obtains 28.53% improvement, the gains for the  $\sigma = 0.1$  at  $\lambda = 3$  are 15.66% and 11.77% respectively. Naturally, the difference between the gains by the optimum and hybrid loadforms decreases for the cases with less trimming. Higher solidity rotors lose

less efficiency since the optimum flap sequences have relatively lower deflection demands thus they are less trimmed. Note that the gradients of the flap actuation is not considered as a design driver for the trimmed deflections since this study is done to show a first image on the performance of the small flap deflections.

**Table 4.1:**  $C_P$  of the reference, the optimum and the hybrid loadform with the percent gains in the performance.

$(\sigma, \lambda)$	(0.06, 3)	(0.06, 4)	(0.06, 5)	(0.1, 3)	(0.1, 4)	(0.1, 5)
$C_{P,reference}$ [-]	0.4027	0.4762	0.5252	0.5225	0.5648	0.5764
$C_{P,optimum}$ [-]	0.6043	0.6043	0.6043	0.6043	0.6043	0.6043
$C_{P,hybrid}$ [-]	0.5176	0.5831	0.5953	0.584	0.5959	0.6007
Gain by $C_{P,optimum}$ [%]	50.06	26.90	15.06	15.66	6.99	4.84
Gain by $C_{P,hybrid}$ [%]	28.53	22.45	13.35	11.77	5.51	4.22

## 4.2 Direct method

In this section, two different types of airfoil polars are used to explore the effect of the flap on the VAWT performance. Most of the work is carried out by a simple inviscid airfoil polar to show the maximum capabilities of the flap actuation. Later, a viscous polar of NACA 0018 is used to show the preliminary viscous effects on the flap performance. It is preliminary because the viscosity is only valid for the airfoil polar but not for the free-stream conditions. The flap authority for three aerodynamic objectives are documented. Throughout the work, either the flap sensitivity ( $C_{l\beta}$ ) or the flap deflection limits ( $\beta_{range}$ ) are set as variables to observe the performance gains by different control authorities. These objectives have been mentioned in the beginning of the chapter. For the inviscid study a single flap sensitivity is used in corporation with different deflection limits. On the other hand, the viscous study analyses two different flap lengths and a single deflection limit.

### 4.2.1 Direct method with inviscid airfoil polars

In the direct method, numerous flap sequences are assessed with a numerical optimizer in order to find the best scoring sequence within the given constraints. The flap curves are defined with a 10<sup>th</sup> order Bezier curve. Bezier curve is chosen as the design medium because of its robustness to create a broad range of curves. Moreover the smoothness of the curves are always assured in the Bezier curve definition. The azimuth positions of the Bezier points are fixed and linearly spaced. Periodic curves are obtained by taking the same Bezier coefficients for  $\theta$  of 0 and 360 degrees. In the ACM code, the effect of each flap deflections is added to the circulation system by modifying the  $C_l(\theta)$ . The rest of the ACM solution remained unchanged. The simple relation that is used for the  $C_l(\theta)$  is given in Equation 4.4. This relation is used for all the inviscid cases. The numerical optimizer is chosen as the hybrid optimization algorithm in the Matlab Optimization Toolbox [47]. The hybrid algorithm is a coupled version of a genetic algorithm and a gradient-based algorithm. In this algorithm, first, the genetic algorithm searches for the

region which, very likely, contains the global optimum. Then, the gradient algorithm searches an optimum in that high scoring region. The gradient method is used at the end since it performs better for the local optimization cases. During the optimization three main constraints are used. A constraint for numerical stability ( $\max(C_T) \leq 1$ ) and two constraints for the upper and the lower limits of the flap deflection. The deflection limits are defined by a single variable,  $\beta_{range}$ .

$$C_l(\theta) = C_{l\alpha} \cdot \sin(\alpha) + C_{l\beta} \cdot \beta(\theta) \quad (4.4)$$

As mentioned earlier, within the optimization cases of this section, three different aerodynamic objectives are set to observe the potentials of the flap authority for each case. These objectives are: 1) improving the  $C_P$ , 2) alleviating the  $C_P$  and 3) alleviating the  $C_T$  while keeping the  $C_P$  close to the reference values. A single  $C_{l\beta}$  is used as  $0.035 \left[\frac{1}{deg.}\right]$  and three different flap deflection limits ( $\beta_{range}$ ) are used as  $\pm 10$ ,  $\pm 20$  and  $\pm 30$  degrees. Different actuation limits are included in analysis to observe the effect of flap control authority on the rotor performance. This perspective is equivalent to consider a single flap deflection limit but three different  $C_{l\beta}$ . In the airfoil polar, stall is disregarded and the  $C_d$  is taken as 0. Flap sequences are optimized for the range of  $\sigma$  from 0.06 to 0.12 and the range of  $\lambda$  from 3 to 6. Important to mention that for this section the  $C_P$  is not calculated with the Equation 3.16 but by integrating the blade forces as formulated in Equation 3.17. It is reported by Madsen [44] that Equation 3.17 could estimate slightly higher values of  $C_P$  than the values obtained by Equation 3.16. Because, the contribution due to the non-dimensional tangential force ( $Q_t$ ) is disregarded in Equation 3.16. So, the main focus for the flap performance assessment should not be the absolute values of  $C_P$  and  $C_T$  but the relative changes with respect to the reference values. The reference turbine performance is presented in Figure 4.6. All the relative changes in the further plots of this section will be given with respect to the values in Figure 4.6.

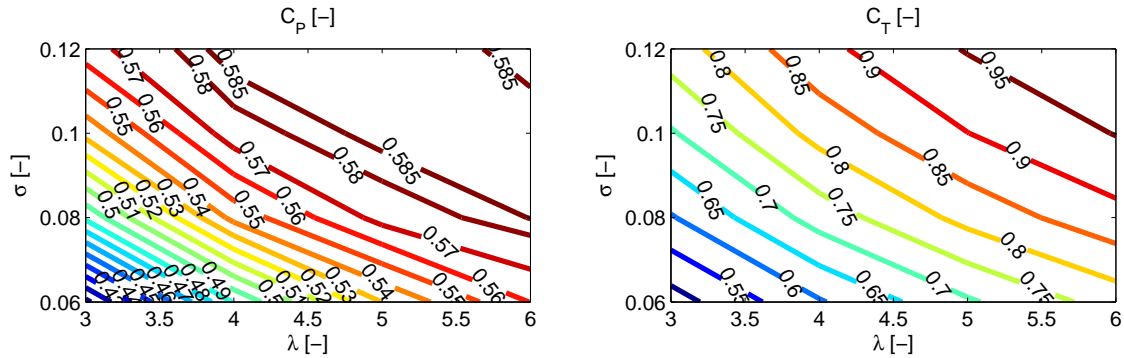


Figure 4.6: Reference turbine performance ( $C_P$  and  $C_T$ ).

### Maximizing the $C_P$

To maximize the  $C_P$  the objective function is set as  $J = -C_P$ . Figure 4.7, Figure 4.8 and Figure 4.9 show the contour of the optimized  $C_P$  and the contour of the relative improvements with respect to the reference performance. These figures represent different flap deflection constraints as  $\pm 10$ ,  $\pm 20$  and  $\pm 30$  degrees respectively. Similar to the

inverse method, the performance at low  $\sigma$  and/or low  $\lambda$  cases improved the most since the reference  $C_P$  values are relatively lower. In all the figures the absolute  $C_P$  goes beyond the maximum values found by the loadform optimization in section 3.3. This mismatch has two preliminary causes: 1) the usage of different formulas to estimate the  $C_P$ , 2) increased uncertainty of the Mod-Lin ACM at highly loaded cases [19]. Therefore, those cases require validation with the higher order models. Nevertheless, significant improvements on the performance is documented. Depending on the flap authority,  $\lambda$  and  $\sigma$  the improvement in  $C_P$  could vary between 4% to 24%.

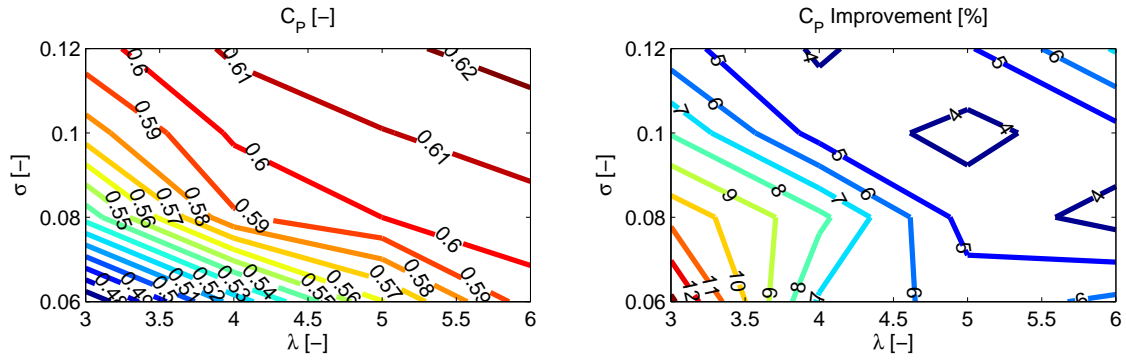


Figure 4.7: Optimized  $C_P$  and the improvement in  $C_P$  when  $\beta_{range}$  is  $\pm 10$  degrees.

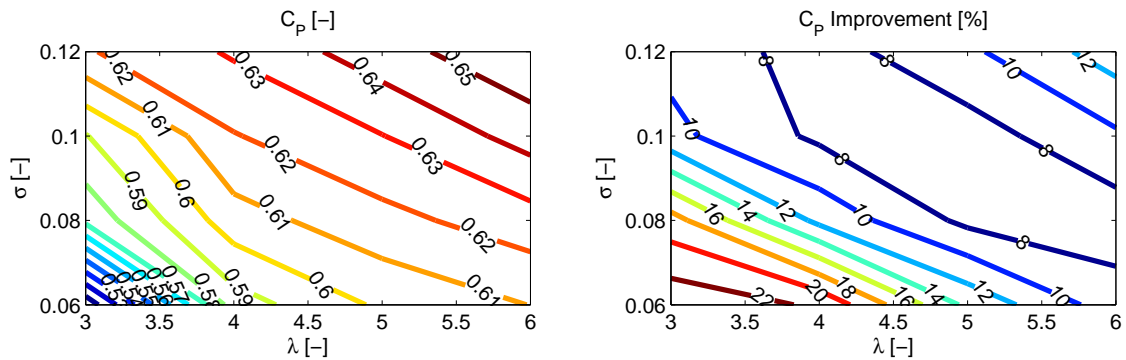


Figure 4.8: Optimized  $C_P$  and the improvement in  $C_P$  when  $\beta_{range}$  is  $\pm 20$  degrees.

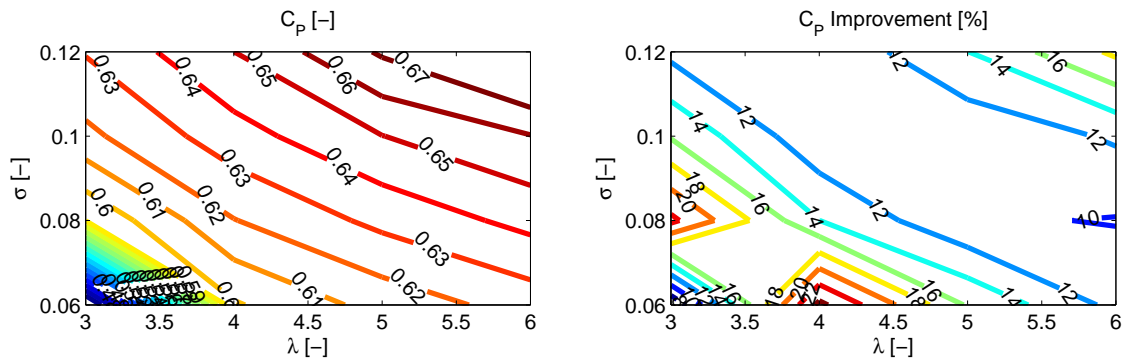
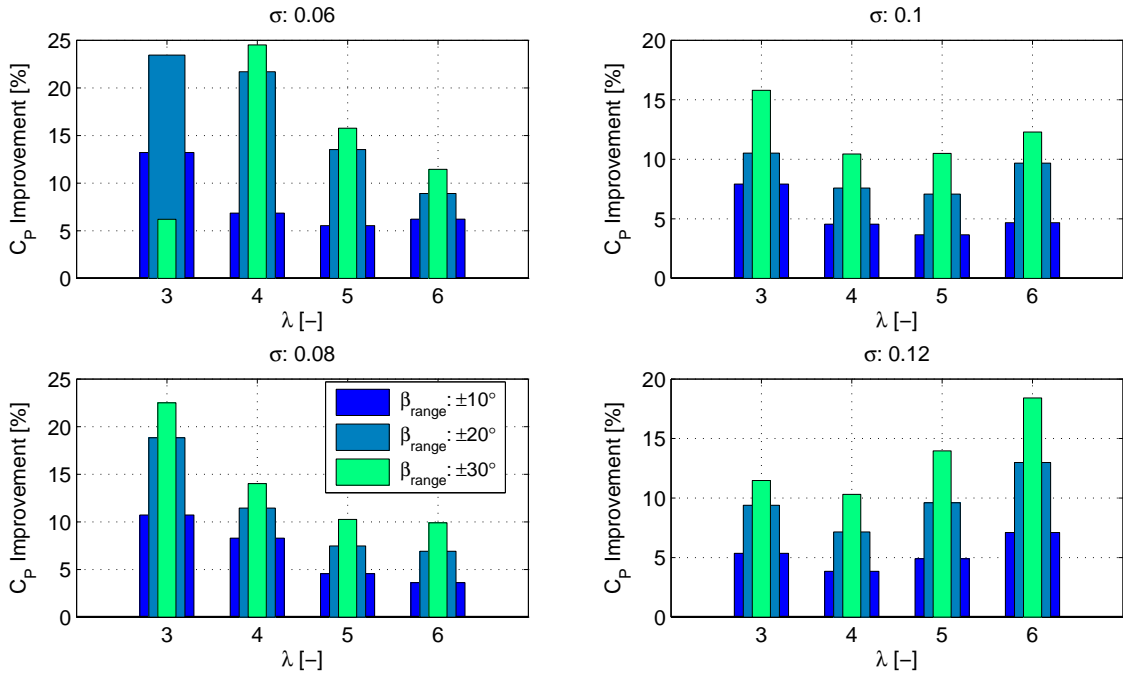


Figure 4.9: Optimized  $C_P$  and the improvement in  $C_P$  when  $\beta_{range}$  is  $\pm 30$  degrees.

The performance gains by different flap deflection constraints for the same  $\sigma - \lambda$  couples are compared on top of each other in Figure 4.10. This figure helps to show a more clear image of the relation between aerodynamic gains and flap authority. As expected, the gains are higher with larger flap deflection limits. For most of the cases, the aerodynamic gain does not increase linearly with the given flap authority,  $\beta_{range}$ . At this point, a direct comparison between the gains by the hybrid inverse method and direct method could be made. Because the case with  $\beta_{range} = \pm 20^\circ$  for  $\sigma = 0.1$  has been considered for both methods (see Table 4.1 for the inverse method result). For the  $\lambda = 3, 4$  and  $5$  the inverse hybrid method obtained 11.7%, 5.5% and 4.2% improvement where the direct method created 10.5%, 7.6% and 7.1% of improvement. So we see that both of the methods are able to cause significant changes. The direct method tries to increase the performance evenly with respect to  $\lambda$ . On the other hand, with the inverse method the decrease in the gains with  $\lambda$  is inevitable.



**Figure 4.10:** Improvement in the  $C_P$  for all cases and for all deflection constraints.

The optimized flap sequences for  $\pm 20$  degrees of maximum flap deflection are given in Figure 4.11; the subplots show different tip speed ratios. For  $\lambda$  of 3, all of the optimum flap sequences are in sinusoidal shape regardless of solidity. At higher  $\lambda$ , the curve shapes transform from sine-wave to cosine-wave type of curves. This is done to decrease the loading at high  $\lambda$ . One can see that at high  $\lambda$  as 5 and 6, negative flap deflections are applied in the upwind to decrease the induction loading. In all of the cases, positive flap angles are applied in downwind to decrease the local loading. In other words, the optimizer sacrifices the downwind performance over upwind. This effect can be seen in Figure 4.12 where the optimized loadforms for the  $\sigma$  of 0.1 at  $\lambda = 4$  are compared for three different flap sequences. As the flap magnitudes increase, the loading in the upwind region is enhanced while the loading in the downwind is slightly alleviated. The load alleviation

in downwind takes place between 270 and 360 degrees of azimuth. Such methodology is chosen by the optimizer since the energy exchange is more efficient in the upwind region. Moreover, the highest loaded region in upwind is the 0-90 degree range. It is believed that this choice is due to the higher relative velocities in windward than any region along the azimuth. By this way, more torque could be generated. From the flap sequences in Figure 4.12 one can see that regions of the positive flap deflections in the downwind enlarge, causing less energy exchange, since the induction is already increased by the flap actuation in upwind.

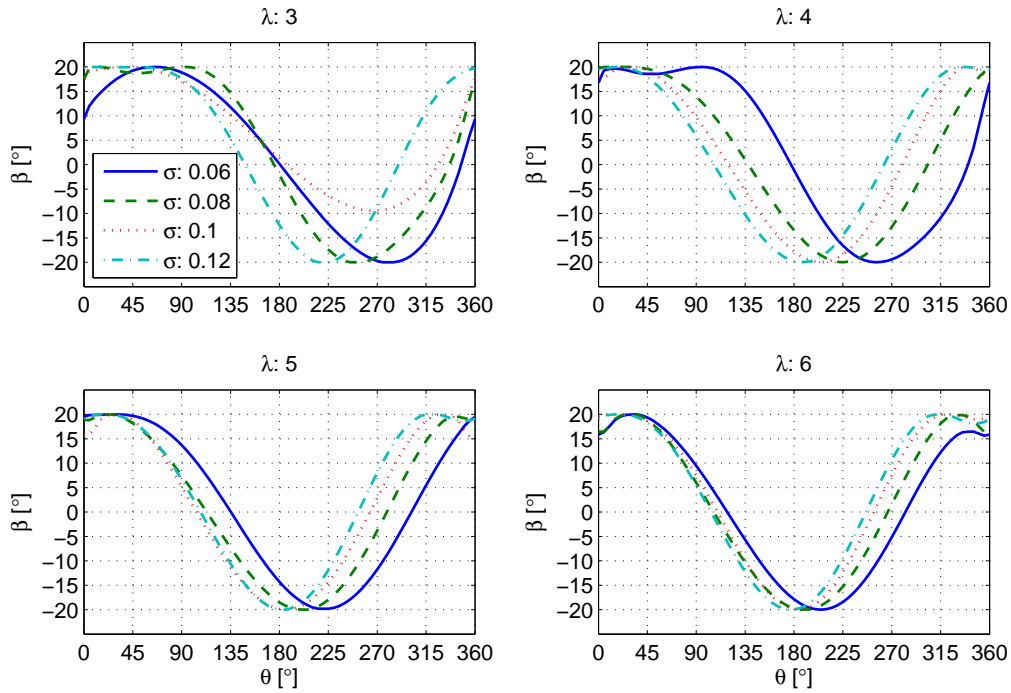


**Figure 4.11:** Optimized flap sequences for various  $\sigma$  and  $\lambda$  when  $\beta_{range}$  is  $\pm 20$  degrees ( $C_P$  maximization case)

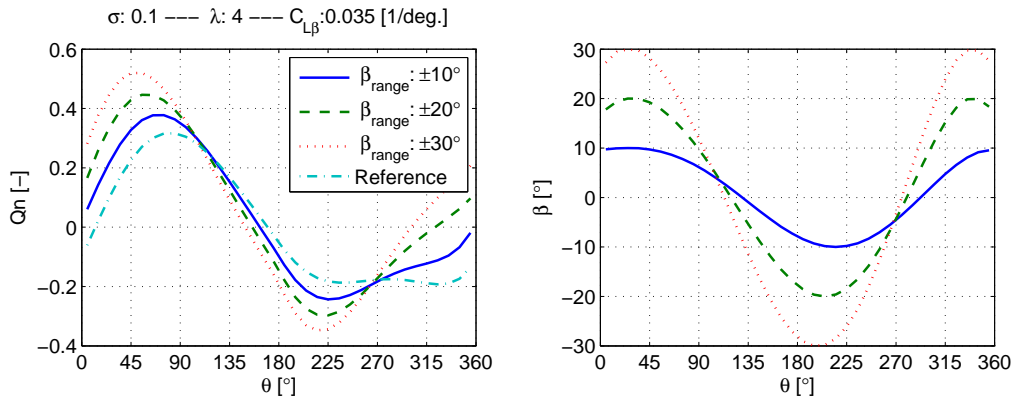


**Figure 4.12:** Comparison of the optimized loadforms and sequences ( $C_P$  maximization case).

### Minimizing the $C_P$

The design methodology of this section is same as the previous section; only the objective is changed to  $J = C_P$ . The constraints are kept the same. Similar to the result obtained in the Bezier loadform analysis in chapter 3, we see that the  $C_P$  has alleviated in a great extent by the flap actuation. The optimized  $C_P$  contour and the contour of the relative changes in the  $C_P$  are presented. Figure 4.13, Figure 4.14 and Figure 4.15 show these contours for different limits of maximum the flap deflection. Even for  $\pm 10$  degree range of flap actuation, the  $C_P$  is decreased up to 24%. Lower solidity rotors are more sensitive to the flap actuation so that power could be alleviated more than larger solidities. Similar conclusion can be drawn for the  $C_P$  maximization case as well.

As the maximum flap deflections are increased, it is possible to see alleviations in 100% range. Therefore, it has been partly shown that if the flap authority is high enough, then the flap could also be used as an effective air brake in the VAWT rotor. It is very likely that the percentage alleviations are larger in the case of a viscous flow. In such case, the airfoil drag will be increased significantly with the large flap deflections which would lead to increased power loss due to drag.

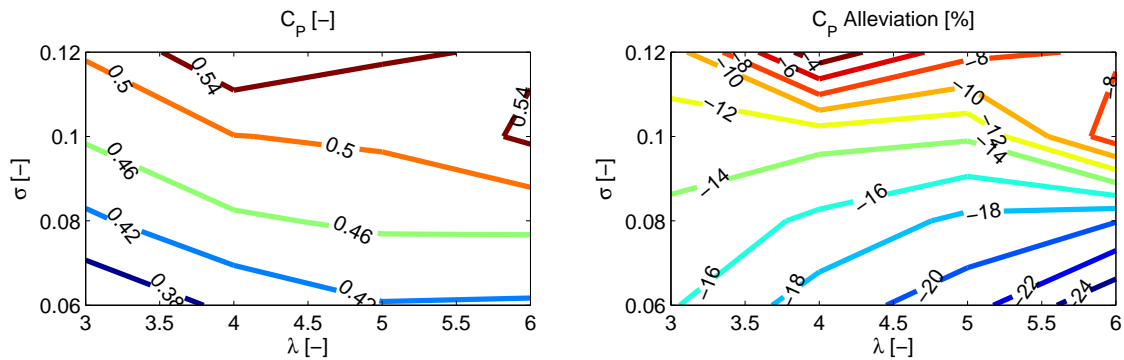


Figure 4.13: Optimized  $C_P$  and the alleviation in  $C_P$  when  $\beta_{range}$  is  $\pm 10$  degrees.

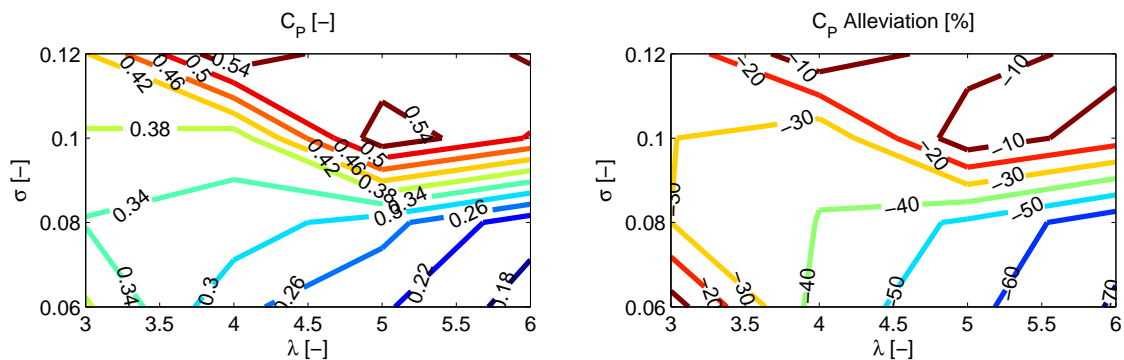


Figure 4.14: Optimized  $C_P$  and the alleviation in  $C_P$  when  $\beta_{range}$  is  $\pm 20$  degrees.

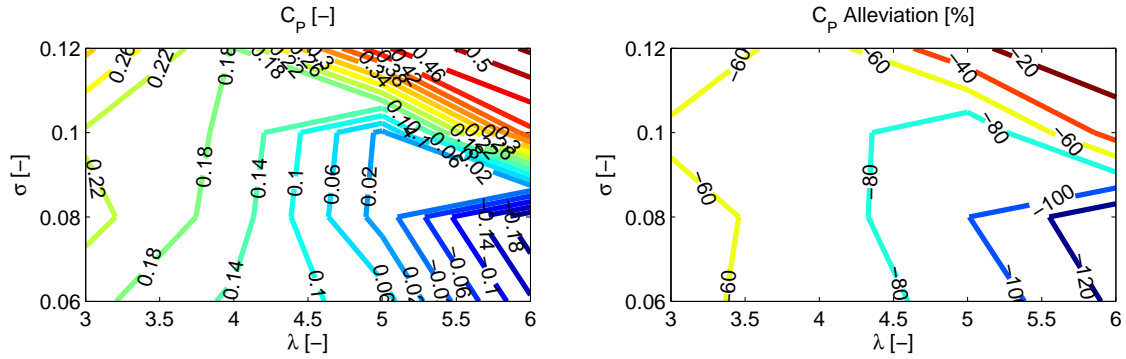


Figure 4.15: Optimized  $C_p$  and the alleviation in  $C_p$  when  $\beta_{range}$  is  $\pm 30$  degrees.

In Figure 4.16 the relative decrements on the  $C_p$  are given for three different flap deflection constraint. The effectivity of the flap is much more when compared with the  $C_p$  maximization case (see Figure 4.10). For the  $\sigma = 0.08$  case, with  $\pm 30$  degree deflection range the  $C_p$  could be decreased between 51.3% and 137% where the  $C_p$  could only be maximized between 9.89% to 22.5%. The performance of the reference loadforms are downgraded by creating adverse loads along the azimuth. For most of the cases, the alleviation is linearly proportional to the flap authority. There are several cases that obtained more alleviation than expected. For instance, the alleviation for the 30 degree of  $\beta_{range}$  for  $\sigma = 0.1$  at  $\lambda = 5$  is around 100%. These unexpected results are very likely due to the divergences in the optimization. In these cases, the optimizer finds soft spots of the Mod-Lin ACM and leads to very optimistic results.

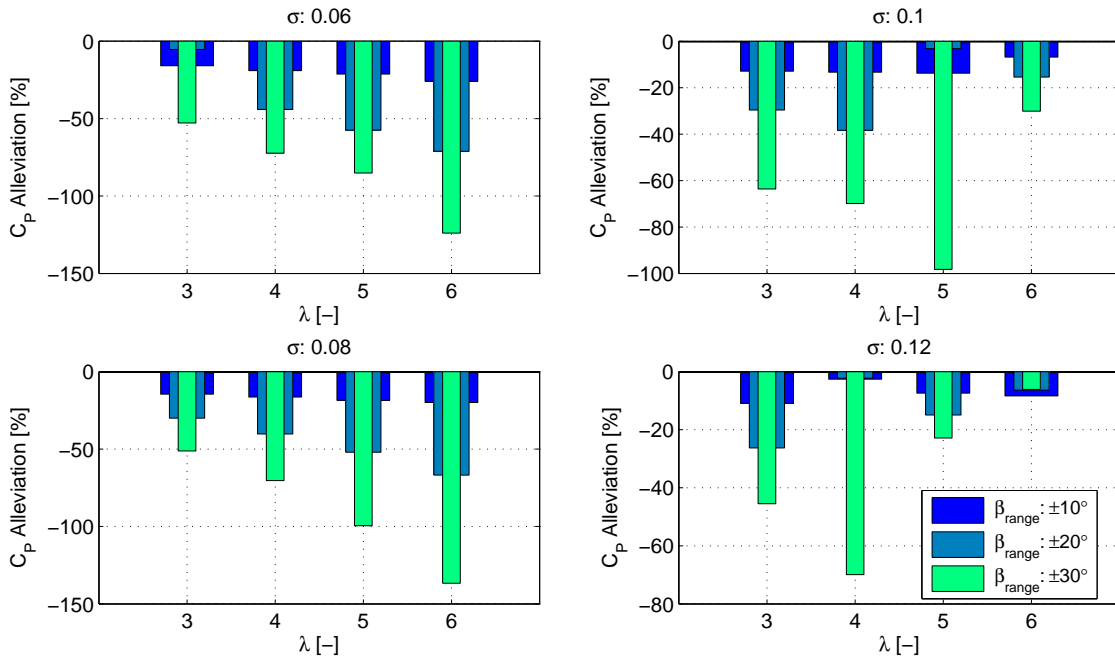
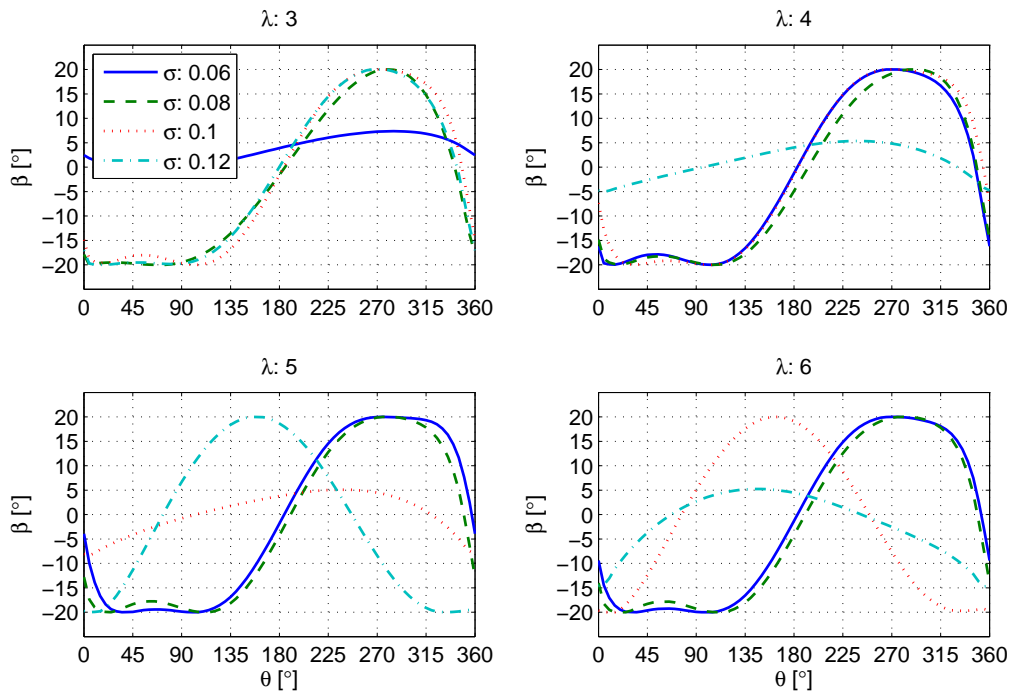


Figure 4.16: Alleviation in the  $C_p$  for all cases and for all deflection constraints.

The optimized flap sequences to minimize the  $C_p$  with 20 degrees of maximum flap

deflection are shown in Figure 4.17. Although the flap demands are with different sign, the curve shapes are very similar to the ones obtained for the  $C_P$  maximization. The loads are decreased both in upwind and downwind. Some of the flap cases are very different from the main actuation trend. Those differences are due to the optimizations converging to a local minimum instead of a global minimum. These cases should not be taken as reference for the flap effectivity on VAWT rotor. For example, the flap actuation at  $\lambda = 4$  for  $\sigma = 0.12$  is done very small deflections and almost has no effect on the performance; only a 2%  $C_P$  alleviation. For the  $\sigma$  of 0.08 the optimized flap sequences change only slightly with the  $\lambda$ . This feature might become handy for the variable speed VAWTs since it will decrease the complexity of the control. In this case there will be less transient losses in the turbulent flow since the optimum flap actuation is constant for all the wind speeds.

Figure 4.18 shows the optimized loadforms and the corresponding flap sequences for minimizing the  $C_P$  at  $\sigma$  of 0.1 and  $\lambda$  of 4. The major part of the  $C_P$  alleviation is based on the load decrements in the upwind region. Loads are also decreased in the downwind region but relatively smaller than the upwind region. Unlike the  $C_P$  maximization results, the flap sequences for the downwind region is not limited by the downwind induction therefore large flap deflections could be applied in downwind. This is one of the reasons of why the relative changes in  $C_P$  is larger in the alleviation case than the maximization case.



**Figure 4.17:** Optimized flap sequences for various  $\sigma$  and  $\lambda$  when  $\beta_{range}$  is  $\pm 20$  degrees ( $C_P$  minimization case).

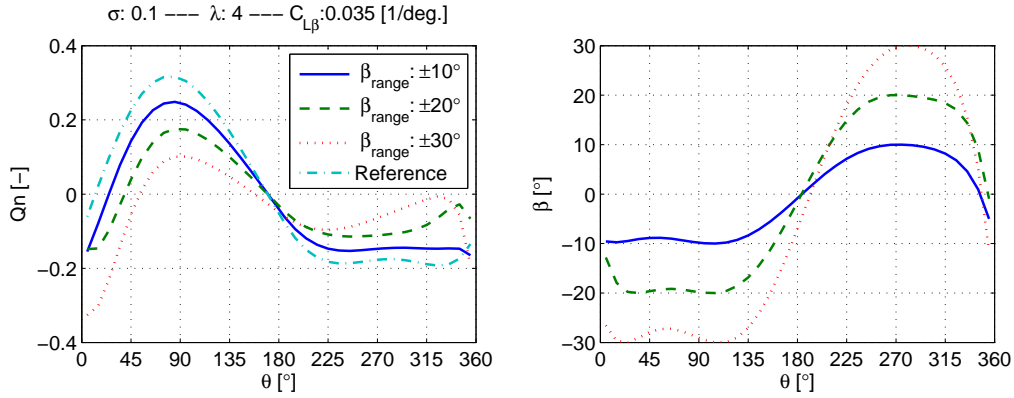


Figure 4.18: Comparison of the optimized loadforms and sequences ( $C_P$  minimization case).

### Minimizing the $C_T$ for a range of reference $C_P$

The aim in this section is to see how much the  $C_T$  could be decreased by keeping the  $C_P$  in a range close to the reference rotor performance. The minimization of the  $C_T$  requires a constraint on the  $C_P$  otherwise the optimizer would easily decrease the  $C_T$  by decreasing the  $C_P$  of the rotor. Here, an extra equality constraint is added in the optimizer to keep the  $C_P$  high. The new constraint is formulated in Equation 4.5. The  $C_{P,gap}$  is a ratio of the allowed  $C_P$  deviation from the reference value. Three different  $C_{P,gap}$  are set as 0.00, 0.03 and 0.05 to see the relation between the sacrifice on  $C_P$  and the authority on the minimization of  $C_T$ . A single maximum flap deflection limit is considered and it is chosen as  $\pm 20$  degrees. The plots of the minimized  $C_T$  and the relative alleviation on  $C_T$  are given for three of the  $C_{P,gap}$  inputs in Figure 4.19, Figure 4.20 and Figure 4.21. If no tolerance is given on the reference  $C_P$  then it is hard to obtain decrements on the  $C_T$  for all of the flow conditions. Low solidity and low  $\lambda$  regions only have few percents of  $C_T$  decrement in that case. For highly loaded cases, the  $C_T$  could be alleviated up to 22% while keeping the  $C_P$  same.

$$C_{P,new} - \frac{C_{P,ref}}{1 + C_{P,gap}} \geq 0 \quad (4.5)$$

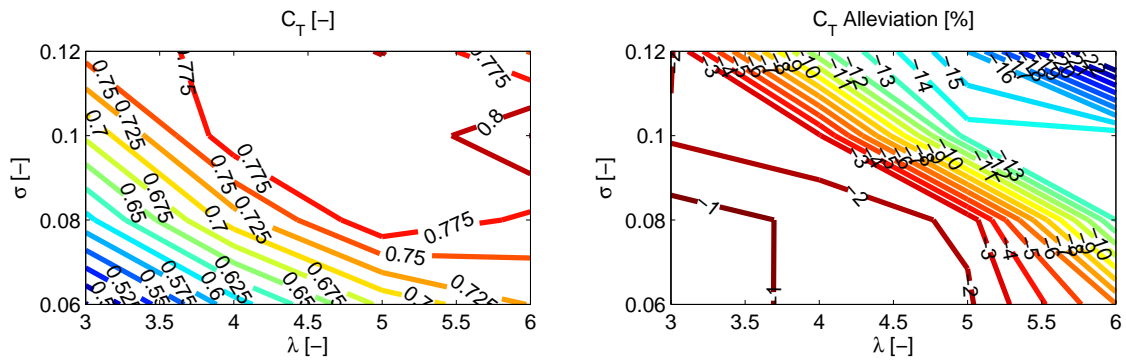


Figure 4.19: Optimized  $C_T$  and the alleviation in  $C_T$  when  $C_{P,gap}$  is  $\pm 0.00$ .

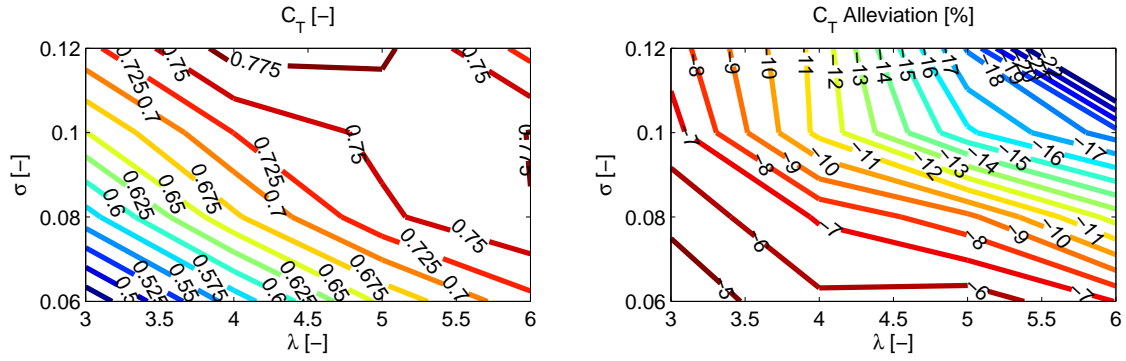


Figure 4.20: Optimized  $C_T$  and the alleviation in  $C_T$  when  $C_{P,gap}$  is  $\pm 0.03$ .

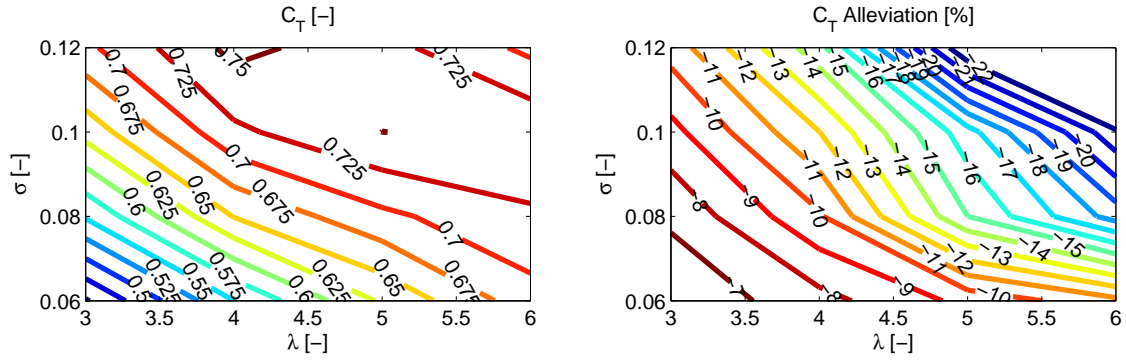


Figure 4.21: Optimized  $C_T$  and the alleviation in  $C_T$  when  $C_{P,gap}$  is  $\pm 0.05$ .

The contours clearly show the importance of the rotor solidity for applicability and effectiveness of the aerodynamic objective. These issues should be taken into account during the preliminary design of a VAWT rotor. Figure 4.22 shows the relative changes in the  $C_T$  for all of the cases. At high  $\lambda$  the alleviation in the  $C_T$  is more effective since the reference  $C_T$  values are larger so there is more room for new loadform designs. As expected, the alleviations for the most strict case (no deviation from  $C_{P,ref}$ ) are smaller than the other cases. The difference in minimized  $C_T$  for the 3% and 5%  $C_P$  tolerances are very small for most of the cases. So, the  $C_P$  tolerance can be kept small but not zero if an effective  $C_T$  minimization is demanded. From the rotor design perspective, it is promising that the  $C_T$  could be decreased more at the high  $\lambda$  region. Because, during operation the highest values of  $C_T$  are experienced in that conditions, therefore it is the region that would exploit the ability to control on  $C_T$ .

The optimized flap sequences with the  $C_{P,gap}$  of 0.05 are given in Figure 4.23. It is harder to motivate on the choice of flap demands since this is a multi-objective case. Except few of the results, the optimizer converged to sequences with positive flap angles both for the upwind and the downwind. These sequences are chosen to establish a balance between the low  $C_T$  and the bounded  $C_P$ . In most of the cases, the upwind loadings are slightly increased while the downwind loadings are decreased with a higher rate. Figure 4.24 shows the optimized loadforms and the flap angles at  $\sigma = 0.1$  and  $\lambda = 4$  for three different constraints. Here the  $C_T$  is alleviated 2.88%, 11.3% and 12.0% for the

$C_{P,gap}$  of 0, 0.03 and 0.05 respectively. The loadforms of 0% and 5%  $C_P$  tolerances are similar. They show that the loading is increased in upwind and decreased in downwind. The 3% tolerance case is much more complex result where the loading is increased in 0-75 degree and 180-300 degree regions and decreased in the rest of the azimuth positions.

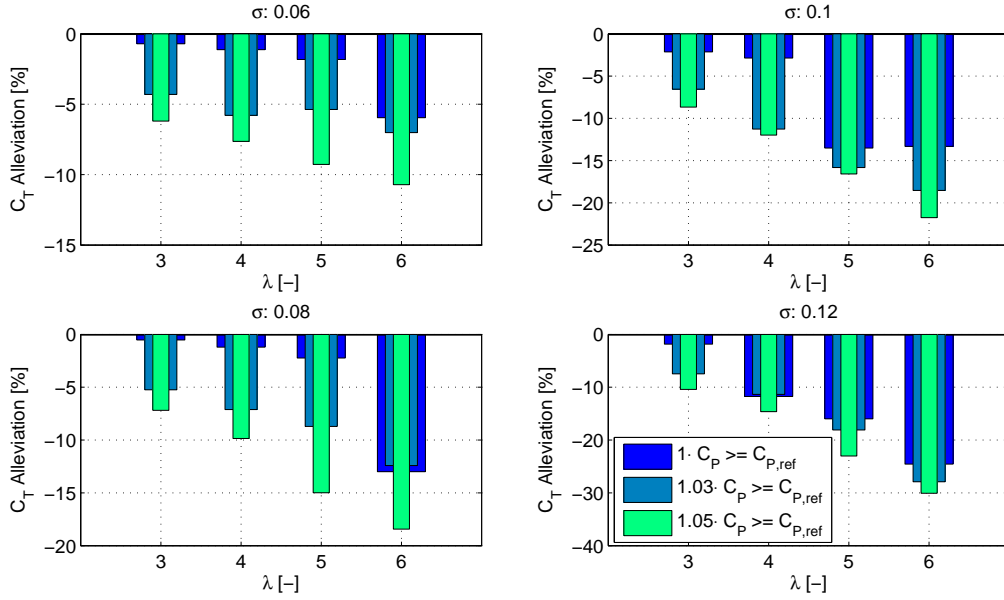


Figure 4.22: Alleviation in the  $C_T$  for all cases when the  $\beta_{range}$  is  $\pm 20$  degrees.

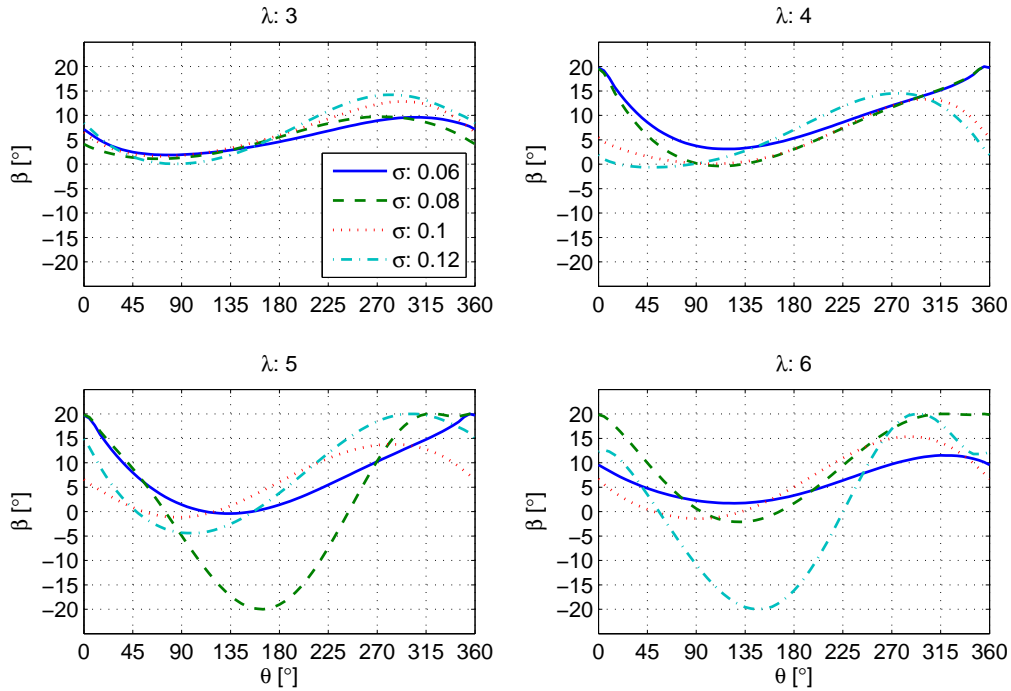


Figure 4.23: Optimized flap sequences for various  $\sigma$  and  $\lambda$  when  $C_{P,gap}$  is  $\pm 0.05$  ( $C_T$  minimization case).

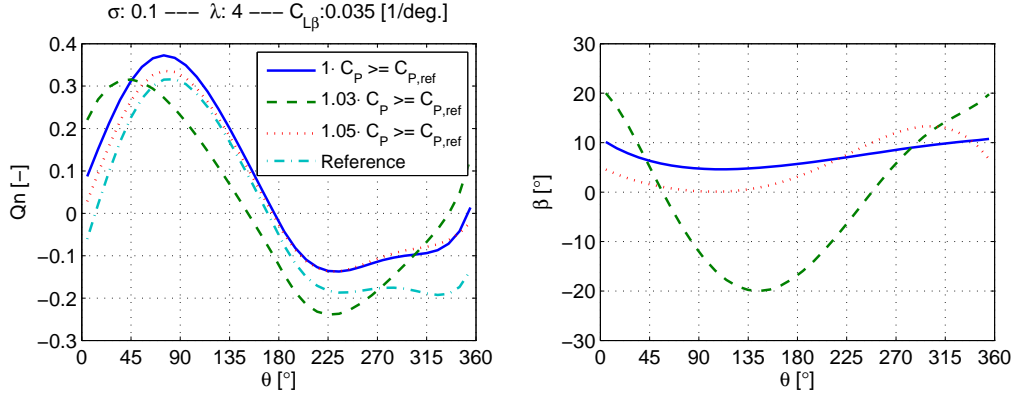


Figure 4.24: Comparison of the optimized loadforms and sequences ( $C_T$  minimization case).

#### 4.2.2 Direct method with a viscous NACA 0018 polar

It has been shown that significant changes on the VAWT performance could be made with the flap in the absence of airfoil viscous effects. Now, viscous airfoil polars are used to observe the influences due to airfoil drag, stall and the non-linearities in the lift polar due to the de-cambering effect. A NACA 0018 airfoil is used throughout the simulations and XFOIL is used to create the airfoil polar data [9]. The airfoil polars are created by assuming a Reynolds number of 5,000,000, free transition conditions and  $N_{crit}$  of 9. Two different flap sizes ( $\frac{c_f}{c}$ ) are used which are equal to the 10% and 20% of the airfoil chord. Airfoil polars are created in a flap deflection range of  $[-20, 20]$  degrees and angle of attack range of  $[-24, 24]$  degrees. Later, the angle of attack information is extrapolated by the Viterna correction to a range of  $[-180, 180]$  degrees. The optimization methodology is exactly same as the one used for the inviscid part. The viscous optimizations are carried out only for  $\sigma$  of 0.1 and  $\lambda$  of 3, 4, 5 and 6. The flap sensitivities ( $C_{l\beta}$ ) for 10% and 20% flap with respect to angle of attack are plotted in Figure 4.25. These values are obtained by taking the mean flap sensitivity of the deflection range specified as  $\beta \in [-8^\circ, +8^\circ]$ . During the inviscid optimizations the  $C_{l\beta}$  was assumed constant as 0.035, where in the viscous flow it decreases significantly outside an angle of attack range of 8 to 10 degrees. This will be one of the key issues of the flap actuation performance during the optimization cases in this section.

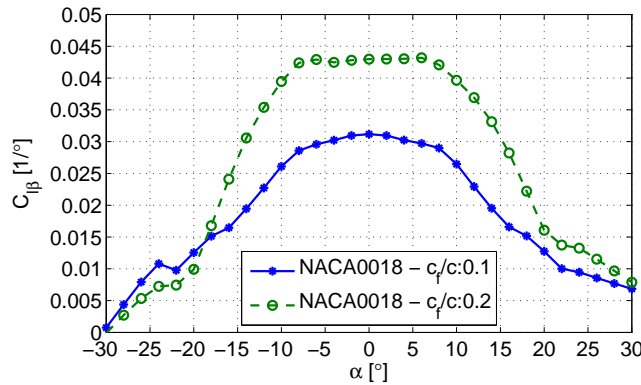


Figure 4.25: Flap sensitivity ( $C_{l\beta}$ ) of the viscous airfoil polars.

### Maximizing the $C_P$

The  $C_P$  and  $C_T$  for the reference (non-flapped) rotor and the flap-controlled rotors are compared in Figure 4.26. Noticeable  $C_P$  improvements are obtained for both of the flaps. Since there are not any constraints on the  $C_T$ , the flapped rotors have relatively higher axial loading than the reference turbine. The percentage improvements on the  $C_P$  by the 10% and the 20% flaps are given in Table 4.2. Small flap has slightly higher gain for the  $\lambda = 3$  case but the 20% flap has better performance for the rest of the cases. In  $\lambda = 3$  high angle of attack values are experienced and in such conditions the  $C_d$  of the 20% flap increases with a very high rate thus causes significant power loss. The 10% flap does not experience pronounced drag values for the  $\pm 20$  degree flap range. For the  $C_P$  maximization case, the inviscid optimization has led to 10.5%, 7.6%, 7.1% and 9.68% improvements (in Figure 4.10). A precise comparison with the inviscid optimization is hard to make, but one can make rough deductions. The flap sensitivity of the inviscid case was 0.035, for the 10% flap  $C_{l\beta}$  is around 0.03 and for the 20% flap it is around 0.045 at  $\alpha = 0$ . So, if the viscous effects were negligible on the rotor performance, the  $C_P$  improvements of the inviscid airfoil would lay between two of the viscous flaps'. But we see that the improvements of the inviscid is higher than the viscous case. The difference between those results goes up to 2.5%.

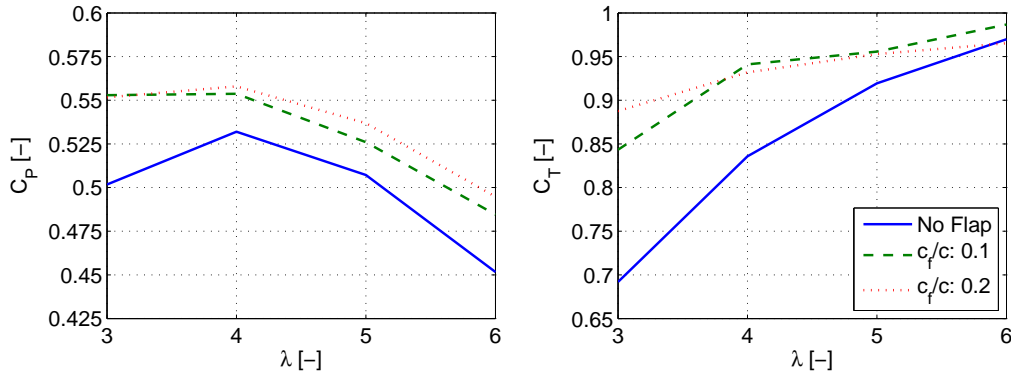


Figure 4.26:  $C_P$  and  $C_T$  comparisons for the viscous  $C_P$  maximization case.

Table 4.2: Percentage gains in the  $C_P$  by the 10% and the 20% flaps.

Flap size	$\lambda=3$	$\lambda=4$	$\lambda=5$	$\lambda=6$
$\frac{c_f}{c} = 0.1$	10.163 %	4.135 %	3.864 %	5.957 %
$\frac{c_f}{c} = 0.2$	9.904 %	5.188 %	5.698 %	9.588 %

The optimized flap sequences are presented in Figure 4.27 for two of the flaps. The difference in flap size affected the optimized curve types notably. So, even if the airfoil is same, there are different optimum actuation laws for different flap lengths which are mainly due to different drag polars. In the inviscid case, the only limitation for the large flap deflections was the high axial inductions, now a second variable is added, drag. The existence of drag led to flap sequences that have smaller ranges of actuation. Note that, in

the inviscid optimizations flaps were deflected up to the maximum deflection constraints (see Figure 4.11). Besides, in the viscous case, the entire potential on the lift authority is not used to avoid high penalties due to drag.

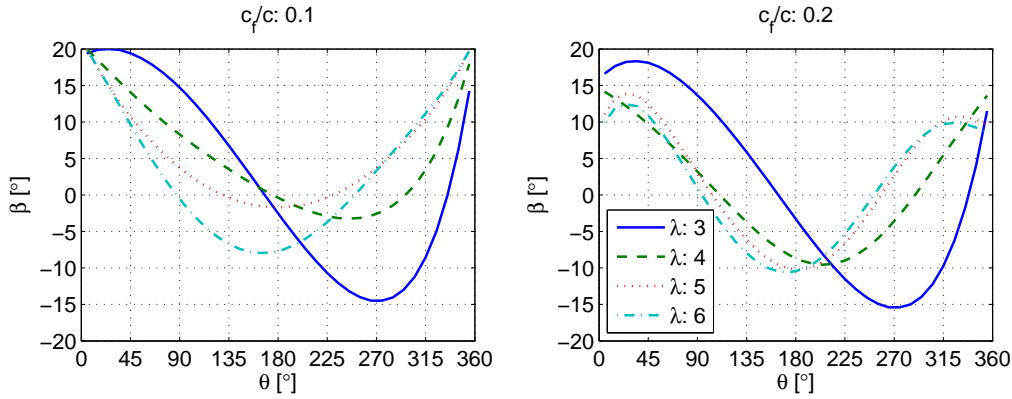


Figure 4.27: Optimized flap sequences for the  $C_P$  maximization with different flap sizes.

### Minimizing the $C_P$

The  $C_P$  and  $C_T$  comparisons of the reference and flap controlled rotors are given in Figure 4.28. Both of the flap lengths are able to lead to considerable amounts of  $C_P$  alleviation. The percentage decrements of the  $C_P$  for different flap sizes are presented in Table 4.3. The alleviation quantity increases significantly with a larger flap size. The difference in the effectivity of the 10% and 20% flap for this case is much more than the  $C_P$  maximization case. During the inviscid optimization for the  $\sigma = 0.1$  at  $\lambda = 3, 4, 5, 6$  and the same actuation limits, the percentage alleviations were reported as 29.7%, 38.4%, 3.1% 15.5% (see Figure 4.16). As seen, these values are much more smaller than the alleviation percentages obtained here. This is a very clear image for the effect of viscous drag on the VAWT performance. In Figure 4.28 the resulting  $C_P - C_T$  curves are not smooth. It is believed that the uncertainty in the result for the  $\lambda = 5$  and 6 cases are high. This is caused both by the ACM uncertainties at high  $\lambda$  and the irregularities in the viscous airfoil polar. Unfortunately, the XFOIL simulations for the flapped airfoils does not create smooth polars for each flap deflection.

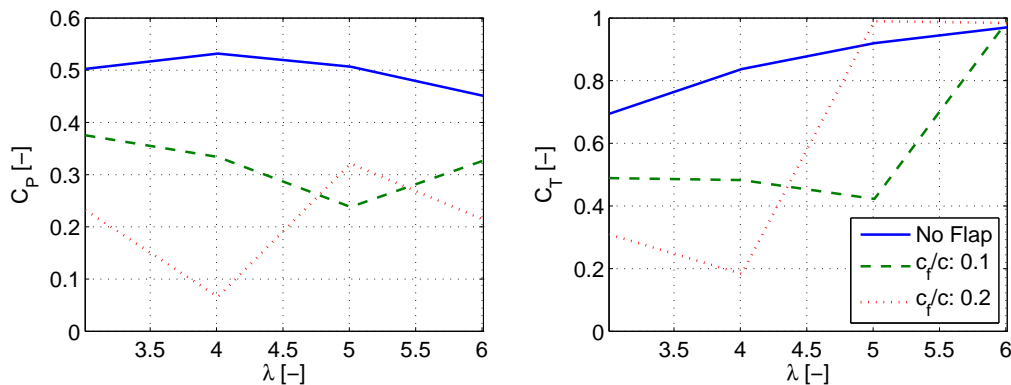
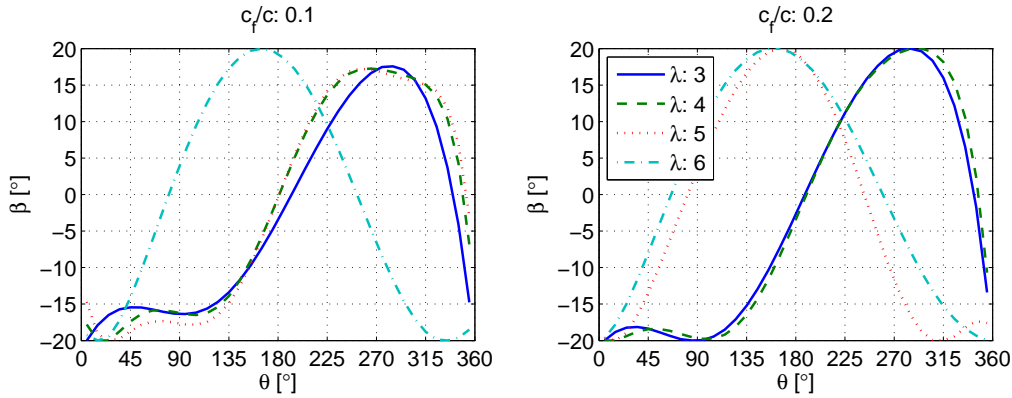


Figure 4.28:  $C_P$  and  $C_T$  comparisons for the viscous  $C_P$  minimization case.

**Table 4.3:** Percentage alleviation in the  $C_P$  for different flap sizes.

Flap size	$\lambda=3$	$\lambda=4$	$\lambda=5$	$\lambda=6$
$\frac{c_f}{c} = 0.1$	-25.301 %	-37.263 %	-53.035 %	-27.541 %
$\frac{c_f}{c} = 0.2$	-53.815 %	-87.589 %	-36.613 %	-52.610 %

Figure 4.29 shows the optimized flap sequences in order to minimize the  $C_P$ . The results are similar to the ones obtained from the optimization with the inviscid airfoils. In a general view, the loads are decreased both in upwind and downwind. The optimum flap sequences for the  $C_P$  maximization were different for each flap length, here we see that the sequences for  $C_P$  minimization is nearly independent of the flap size. Moreover, the difference between the curve shapes of flap sequences explains non-smooth  $C_P$  and  $C_T$  curves in Figure 4.28. Apparently the optimizer converged to a non-optimal conditions. The reader should be aware that the optimization case have been run with very refined search conditions but the result remained unchanged.

**Figure 4.29:** Optimized flap sequences for the  $C_P$  minimization with different flap sizes.

### Minimizing the $C_T$ for a range of reference $C_P$

Figure 4.30 shows the optimized  $C_P$  and  $C_T$  results for the objective of  $C_T$  minimization. For this part only one flap length is used which is the 20% flap. Similar to the concept in the inviscid optimization the  $C_{P,gap}$  definition is used. Two different  $C_P$  deviation limits are set: 0 and 0.05. The  $C_T$  decrement for the zero tolerance case is found very effective. The effect on  $C_T$  in the viscous case is larger than than the effect in the inviscid case. As the  $C_{P,gap}$  is increased from 0 to 0.05 the alleviation percentage on the  $C_T$  shows an increment around 7% for all the  $\lambda$ . Table 4.4 shows the percentage alleviations at various  $\lambda$  with different tolerances on the  $C_{P,ref}$  values. Similar to the results found in the inviscid optimization, the decrement gets larger if the reference value of the  $C_T$  is larger.

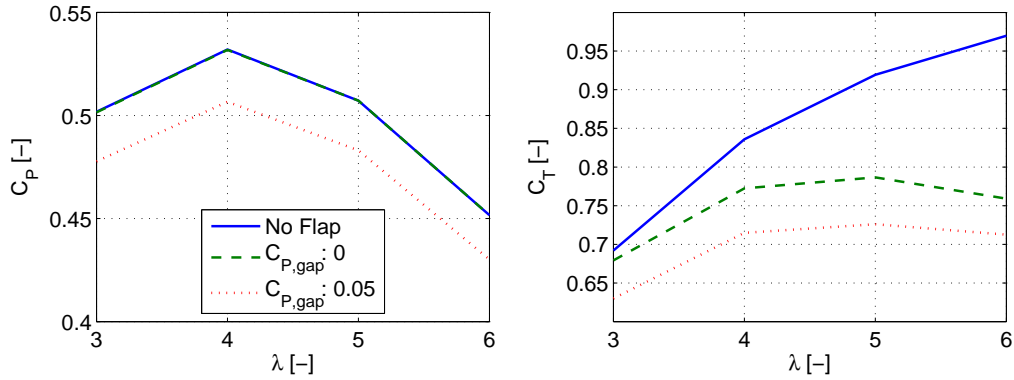


Figure 4.30:  $C_P$  and  $C_T$  comparisons for the viscous  $C_T$  minimization case.

Table 4.4: Percentage alleviation in the  $C_T$  for different  $C_{P,gap}$ .

$C_{P,gap}$	$\lambda=3$	$\lambda=4$	$\lambda=5$	$\lambda=6$
0.00	-1.834 %	-7.588 %	-14.429 %	-21.735 %
0.05	-8.974 %	-14.475 %	-21.022 %	-26.540 %

The optimized flap sequences for the  $C_T$  minimization objective are shown in Figure 4.31. The optimized actuation leads to increased loading in the majority of the upwind region and decreased loading in downwind. It is hard to see the difference in the optimum actuation laws for different  $C_{P,gap}$  values. On the other hand one can mention that the curves are slightly skewed towards the upwind region for the  $C_{P,gap}$  of 0.05. The  $C_T$  is changed mainly by decreasing the peak loading along the azimuth.

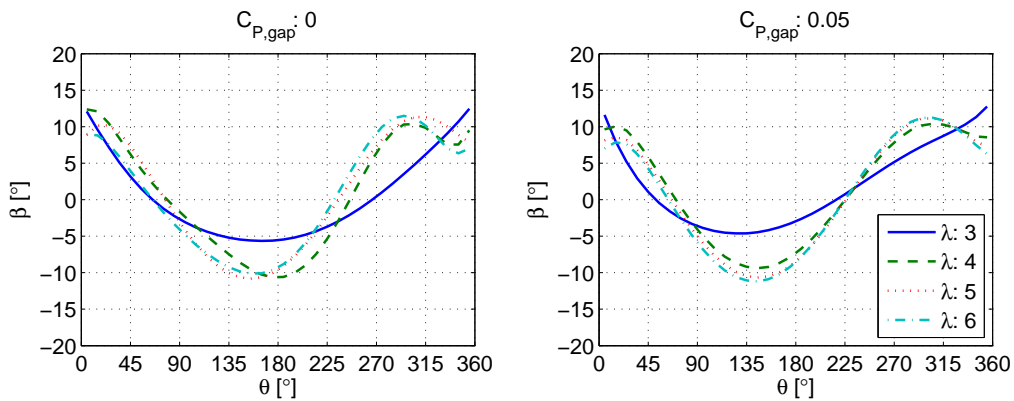


Figure 4.31: Optimized flap sequences for the  $C_T$  minimization with different flap sizes.

### 4.3 Conclusions of the chapter

In this chapter, two main methods of finding effective flap sequences are introduced, the inverse and direct method. A simple demonstration of the inverse method is shown while the direct method is used extensively for many cases. Various flap control authorities, aerodynamic objectives are assessed with a wide range of rotor solidity and tip speed ratio. Important deductions have been made through this chapter on the corresponding issues. The main conclusions of this chapter can be shown as:

- The inverse method is a very fast way to find the flap sequences to achieve a known/target loading. Inverse method showed that very high  $C_P$  values could be obtained if the rotor size and flap size are chosen accordingly. For most of the low  $\sigma$  and low  $\lambda$  cases the flap demands are excessive and unacceptable. The flap actuation gradients could be very high depending on the target loading. Therefore the target loading should be chosen wisely. The inverse method could be more effective if the Bezier loadform optimization is equipped with more design considerations. The trimmed flap sequences by maximum deflection bounds still lead to noticeable improvements in the  $C_P$ . Unfortunately it is hard to generalize the inverse method for an arbitrary  $\sigma$ - $\lambda$  couple.
- The direct method requires more time since each case with different  $\sigma$ ,  $\lambda$ , airfoil and flap size has to be optimized individually. But, it is a very powerful method to find smooth, realizable flap sequences with significant aerodynamic gains. It is easier to control the shape of the flap sequence curves. Another drawback of the optimizer is that it could lead to non-optimal results in some cases. On the other hand, for the inverse method the optimum performance is assured.
- For maximizing the  $C_P$ , the improvements does not increase linearly with the given flap authority. The efficiency of the flow control decreases due to increased inductions. For the cases with relatively lower induction field, the optimized flap sequences resemble to sinusoidal signals. As the induction increases with larger  $\sigma$  or  $\lambda$  the sequences get more unique shapes. With the flap authority used in this chapter it is shown that the  $C_P$  could be increased between 3% to 25% depending on the solidity and tip speed ratio. These values are only representative and more gains could easily be obtained by bigger authorities. Note that the  $C_{l\beta}$  used in this chapter was representative for 10% flap of a general purpose aviation airfoil.
- The optimum flap sequences did not lead to the optimum loading types that have been reported in the previous chapter of the thesis. Instead of uniform loading, we see peaky optimum loadings in this chapter. The optimum loadings in this chapter are influenced by two main variables: The perceived velocity field and the higher importance of the upwind loading to the performance than the downwind loading. Therefore one of the reasons of the mismatch could be the different ways of  $C_P$  calculation in the corresponding works.
- For the  $C_P$  alleviation case, the effect on the performance is somewhat linear to the actuation authority. If the flap authority is large enough, the flap could be used for braking the VAWT rotor.

- Both for the  $C_P$  maximization and the minimization, the major part of the change in the  $C_P$  is provided by the loadform changes of the upwind region.
- For the case of  $C_T$  minimization, it is seen that by scarifying few percents of  $C_P$  the  $C_T$  could be decreased significantly.
- To give values for the comparison of the flap effectivity in different objectives the  $\sigma = 1$  case at  $\lambda = 4$  can be shown. For the  $C_{l\beta} = 0.035 \frac{1}{deg}$  and  $\pm 30$  degrees of flap actuation limit, the  $C_P$  is increased with 10.5%, decreased with 69.9% and the  $C_T$  is decreased 12%.
- For the viscous case, smaller flap size obtains more improvement when the perceived  $\alpha$  is high ( $\lambda = 3$ ). Because, the viscous losses for a larger flap size are excessive for low  $\lambda$  cases. As the  $\lambda$  increases, the aerodynamic gains obtained by a larger flap increases with respect to a smaller flap. In the viscous case the percentage improvement in the  $C_P$  is smaller than the improvements in the inviscid case. On the other hand, the  $C_P$  and  $C_T$  alleviation could be done with a greater percentage in the viscous flow.
- In the viscous case, the optimum flap sequences for different flap lengths of the same airfoil are not identical. The reason is based on the difference in the drag polars.



# Assessment of the Active Flap Control with the 2-D Panel Code

This chapter documents the comparison of the performance estimations by two different aerodynamic models, the Actuator Cylinder Model (ACM) and the 2-D inviscid, unsteady panel model (PM). NACA 0018 airfoil is used for all of the simulations and XFOIL is used to generate the inviscid polar for the use in the ACM. The panel model validation is not presented since its capabilities are shown by many publications and a thesis work before [15, 16, 17, 20, 33]. On the other hand, this is the first work that the corresponding panel code is used for the active flap control. Therefore, for the majority of the simulations, the flap size is taken small (10%) in order to avoid the numerical issues that could be triggered by large pressure gradients based on the dynamic flap actuation in the complex VAWT environment. In fact, several previous runs with the 20% flap showed unexpected results at high  $\lambda$ . During the simulations, the rotor solidity is fixed to 0.1 and  $\lambda$  from 3 to 6 are simulated. The active flap sequences applied in the PM are inherited from the inviscid direct method results obtained by using the inviscid NACA 0018 polars.

The chapter consists of four main sections: 1) Single element airfoil simulation: A case without any flap actuation is introduced to have a reference case for the performance assessment of the flapped cases, 2)  $C_P$  maximization both with the 10% flap and 20% flap, 3)  $C_P$  minimization with the 10% flap and 4)  $C_T$  minimization with the 10% flap.

Several flow and force coefficients/variables are compared between ACM and PM for the tip speed ratios of 4 and 6.  $\lambda$  of 4 is used since it is generally chosen as the optimal operation point for a VAWT;  $\lambda$  of 6 is chosen since the axial loading is the highest among the considered  $\lambda$  range. By this choice the models are compared for the high loading performance which usually lead to increased uncertainties. The non-dimensional axial and tangential loadings ( $Q_n$ ,  $Q_t$ ), perceived angle of attack ( $\alpha$ ) and the non-dimensional axial induction velocities ( $w_x$ ) are presented throughout the chapter. The  $C_P$  and  $C_T$  estimations for both of the models at  $\lambda = 3, 4, 5$  and 6 are tabulated. The differences in the performance estimations are presented. Also the performance gains/alleviations estimated by the ACM and PM with respect to their own reference cases are reported.

The coordinate system is inherited from what is used in the previous chapters in the ACM code. Figure 5.1 shows the fundamentals of this coordinate system. One can also see an example of the cyclic flap sequence on the airfoils. Note that the rotation is towards counter-clockwise.

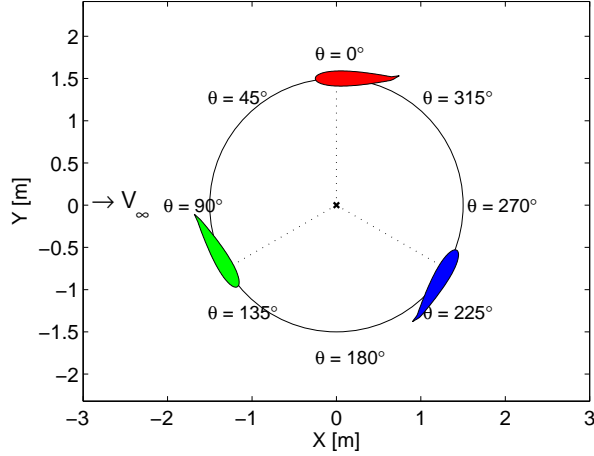


*Figure 5.1: The coordinate system and active flap configuration.*

## 5.1 Performance of the NACA 0018 airfoil (the reference case)

The non-dimensional loadings  $Q_n$  and  $Q_t$  are shown for  $\lambda = 4$  case in Figure 5.2. Similarly, Figure 5.3 shows the loadings at  $\lambda = 6$  case. One of the biggest difference between the PM and ACM estimations is that the mean values of  $Q_n$  are different. This difference resembles the loading of the same rotor with two different fixed-pitch settings. This analogy can be verified if one looks at the  $Q_t$ ; for the PM the loads are transferred from downwind to upwind with respect to the loading estimated by the ACM. Note that during the simulations the fixed-pitch angle was set to 0 degree, therefore this effect is very likely due to the unsteady aerodynamics and flow-curvature that are implicitly accounted in the PM. The difference in the loading estimations of the ACM and PM increase with the increasing  $\lambda$ . One can also mention that the bump in the downwind loadings by the ACM are not apparent in the PM results. The difference is due to the different ways of calculating the induction velocities. The ACM has a discrete way of wake calculation where the PM accounts for all of the vortices apparent on the airfoils and the wake.

The perceived angle of attack and the axial induction velocity for the  $\lambda$  of 4 are shown in Figure 5.4 and the results corresponding to  $\lambda = 6$  are given in Figure 5.5. For both of the  $\lambda$ , the angle of attack for the upwind region is estimated quite similarly by the ACM and PM. On the other hand, the differences in the downwind region are noticeable and increases at high  $\lambda$ . Similarly, the axial induction calculations for the upwind regions have a good match, but the windward, leeward and downwind regions have significant differences. Those results agree with the comparisons in the literature [19]. The wiggles experienced in the downwind region by the PM are due to the blade-wake interaction

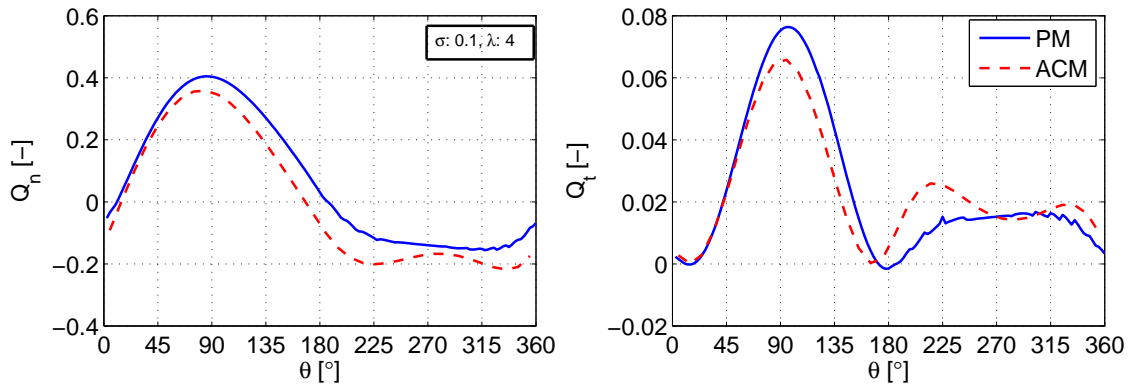


Figure 5.2:  $Q_n$  and  $Q_t$  calculated by the panel model and ACM at  $\lambda = 4$  without the active flap.

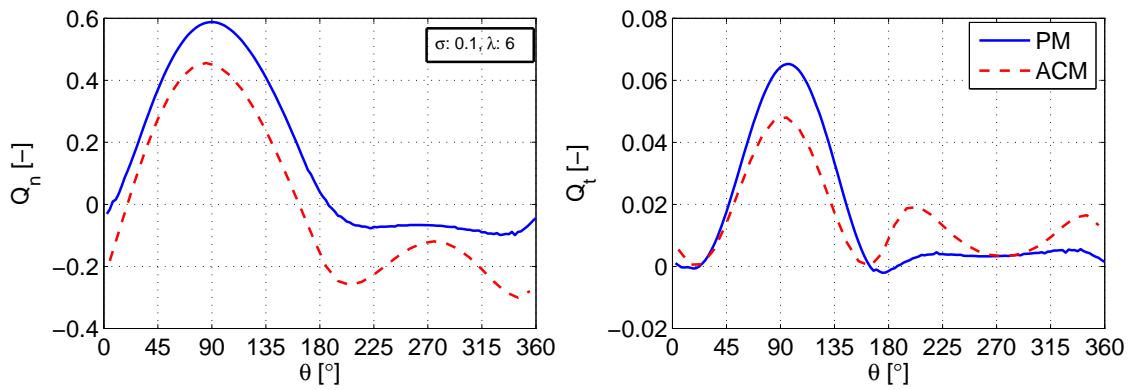


Figure 5.3:  $Q_n$  and  $Q_t$  calculated by the panel model and ACM at  $\lambda = 6$  without the active flap.

(BWI) phenomenon which causes instantaneous perturbations in the angle of attack. As mentioned previously, this effect is not modeled in the ACM.

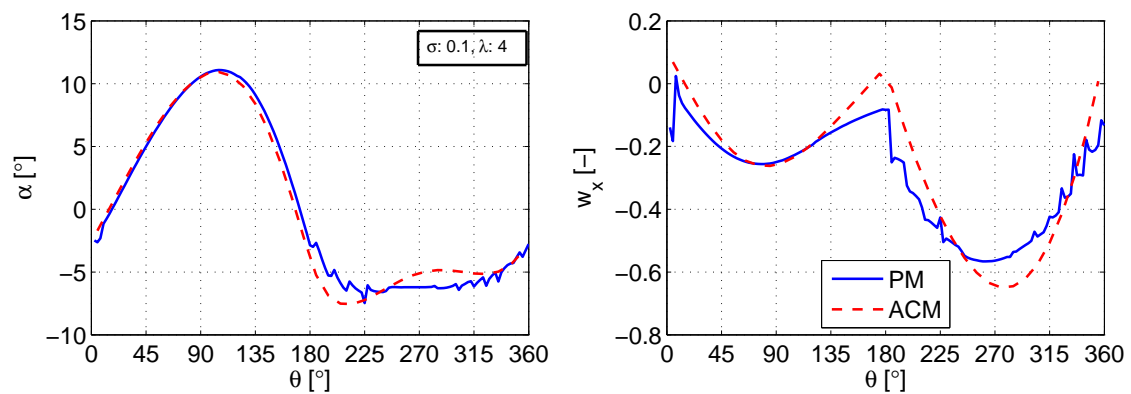
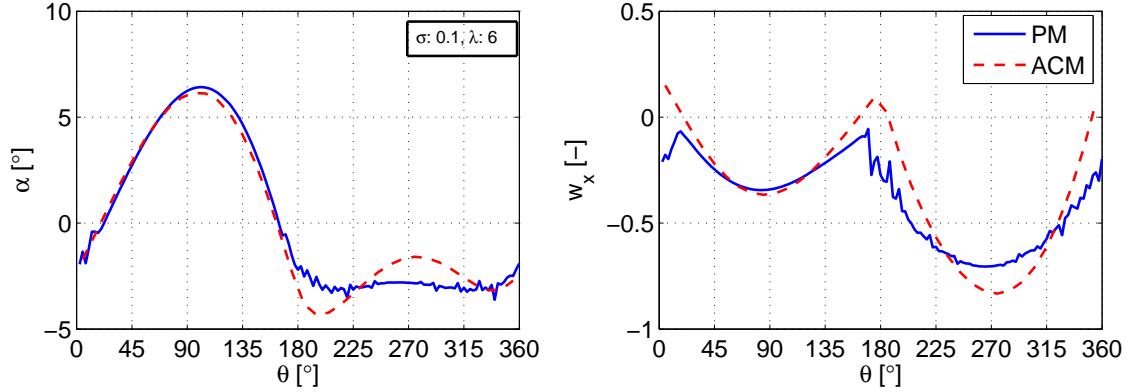


Figure 5.4: Angle of attack and axial induction calculated by the panel model and ACM at  $\lambda = 4$  without the active flap.



**Figure 5.5:** Angle of attack and axial induction calculated by the panel model and ACM at  $\lambda = 6$  without the active flap.

The results consisting of the  $C_P$  and  $C_T$  estimations by the ACM and PM at  $\lambda = 3, 4, 5$  and 6 are given in Table 5.1. Moreover, one can find the percentage differences between the corresponding calculations by the ACM and PM simulations. In a general view, a close match in the estimations are observed. The difference in the  $C_P$  estimations is in 0% to 2% range and for the  $C_T$  the difference is between 0% to 6.3%. The difference in the  $C_T$  increases at highly loaded cases. Note that the  $C_T$  estimated by the ACM does not go above 1 since it has been constrained due to the numerical stability during the optimizations. On the other hand, PM does not have this limitation therefore capable of having more reliable solutions at high loadings. In further sections the values in Table 5.1 are used as the reference values to report the gains obtained by each model.

**Table 5.1:** Comparison of the reference  $C_P$  and  $C_T$  between the panel model and ACM for a single element airfoil.

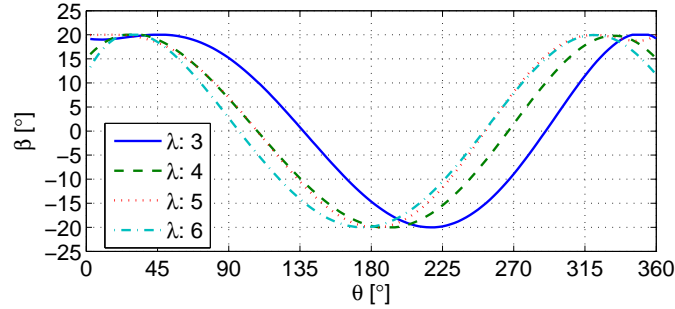
Parameter	$C_{P,ref}$				$C_{T,ref}$			
	3	4	5	6	3	4	5	6
$\lambda$ [-]	3	4	5	6	3	4	5	6
PM	0.55	0.59	0.60	0.60	0.76	0.89	0.98	1.05
ACM	0.56	0.59	0.59	0.58	0.77	0.88	0.95	0.99
Difference between models [%]	2.14	0.72	2.13	2.57	2.12	0.76	3.47	6.28

## 5.2 $C_P$ maximization

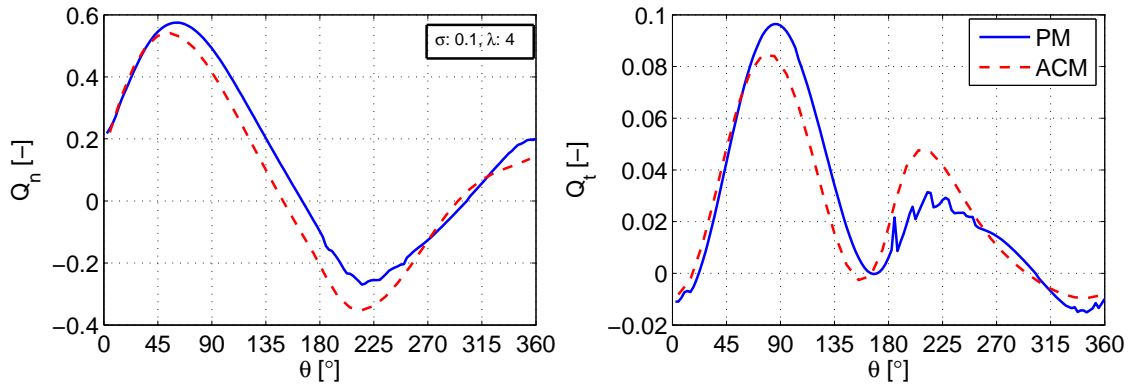
### 10% flap case

The flap sequences used during the 10% flap case are given in Figure 5.6 for the whole  $\lambda$  range. The corresponding  $Q_n$  and  $Q_t$  are given in Figure 5.7 and Figure 5.8 for the  $\lambda$  of 4 and 6 respectively. In general, similar loading trends are estimated by the ACM and PM. The aforementioned shift in the  $Q_n$  still visible, so that the distribution of the tangential loading is different depending on the model. The effect of the BWI in the downwind loadings are apparent in PM calculations. It is interesting to see that the

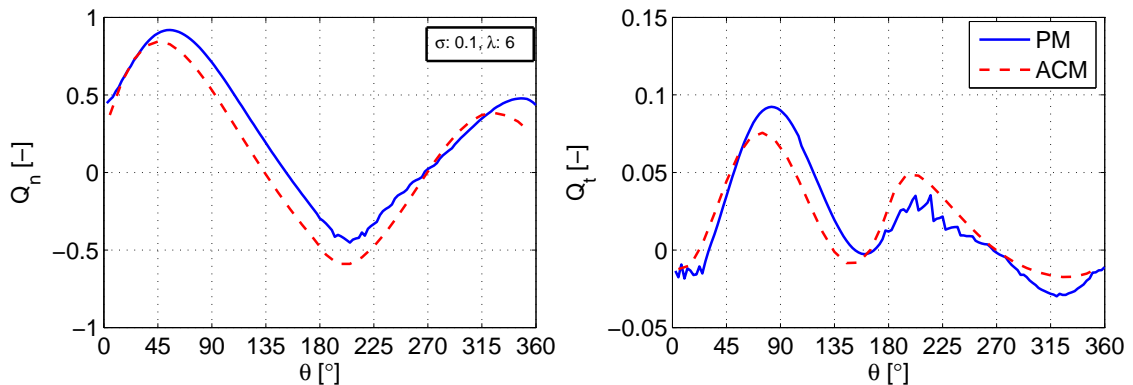
optimum flap sequences dictate a negative tangential loading between 315 and 360 degree azimuth positions. This is very likely chosen to compensate the increased induction due to high loading in upwind. For the  $\lambda = 6$  case almost no power is extracted in downwind; the positive and negative loadings of  $Q_t$  occupy similar areas.



*Figure 5.6: Flap sequences applied for the  $C_P$  maximization with the 10% flap.*



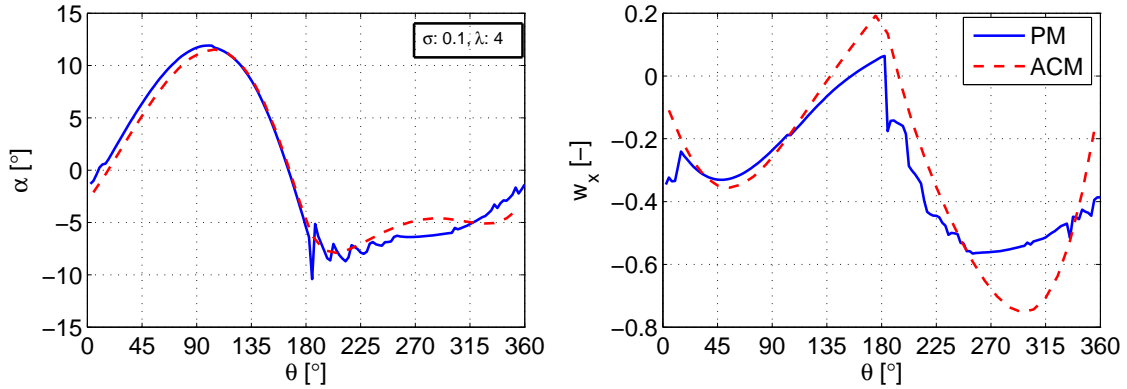
*Figure 5.7:  $Q_n$  and  $Q_t$  calculated by the panel model and ACM at  $\lambda = 4$  with the 10% flap for the  $C_P$  maximization case.*



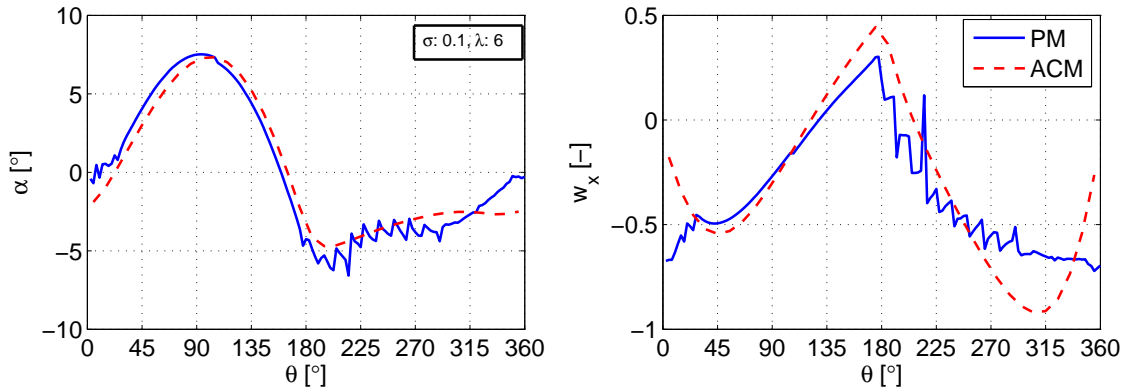
*Figure 5.8:  $Q_n$  and  $Q_t$  calculated by the panel model and ACM at  $\lambda = 6$  with the 10% flap for the  $C_P$  maximization case.*

Figure 5.9 shows the angle of attack and axial induction at  $\lambda=4$ . Similarly, Figure 5.10 presents the same plots for the  $\lambda=6$  case. Except for a phase shift, the angle of attack

estimations of PM and ACM matches quite close for the upwind. This shift is very likely due to the dynamic effects in the PM. For both of the  $\lambda$  points, the axial induction estimations between the two models show similarities in the upwind but there are significant differences in the downwind part. The ACM estimates larger induction values for the downwind part. It is also important to mention that the BWI effect increases with the increased  $\lambda$  since the upwind wake is tightly packed in such conditions. Therefore instantaneous perturbations on the angle of attack are larger in the flapped case than the cases without the active flap. The flap actuation increases the BWI effects.



**Figure 5.9:** Angle of attack and axial induction calculated by the panel model and ACM at  $\lambda = 4$  with the 10% flap for the  $C_P$  maximization case.



**Figure 5.10:** Angle of attack and axial induction calculated by the panel model and ACM at  $\lambda = 6$  with the 10% flap for the  $C_P$  maximization case.

The estimations of the  $C_P$  and  $C_T$  are given in Table 5.2 for both of the models. It is promising to see that the PM also estimates significant improvements on the VAWT performance. Furthermore, both of the methods estimates larger  $C_P$  than the Betz limit. Although the PM and ACM estimations are in line at  $\lambda$  of 3 and 4; the difference between the models increases at high loadings. Nevertheless the performance gains with respect to the reference values are in the same range for both of the models. On the other hand, when  $\lambda$  is increased to 5 or 6 this relation breaks. At  $\lambda$  of 6, for the same active flap sequence, the ACM reports 12.85% gain in the  $C_P$  where PM only estimates 1.71% improvement. It is apparent that the ACM have led to wrong optimal flap sequences at

the high loadings. The flap sequence optimization scheme should include a higher order model for the heavily loaded rotors. Moreover, it can be deduced that, for the high rotor loading cases the maximum flap angle deflections should be kept lower to avoid high inductions in downwind. So that the energy can be harvested in a more efficient state.

**Table 5.2:** Comparison of the  $C_P$  and  $C_T$  estimated by the panel model and ACM with the 10% active flap for the  $C_P$  maximization case.

Parameter	$C_P$				$C_T$			
	3	4	5	6	3	4	5	6
$\lambda$ [-]	3	4	5	6	3	4	5	6
PM	0.60	0.63	0.61	0.61	0.94	1.01	1.06	1.10
ACM	0.62	0.63	0.65	0.66	0.94	0.96	0.98	0.98
Difference between models [%]	2.04	0.30	5.69	7.55	0.66	4.93	8.49	12.85
Change on PM reference [%]	9.49	6.37	1.81	1.71	24.18	13.49	8.22	5.08
Change on ACM reference [%]	9.37	7.45	10.24	12.85	20.76	8.99	3.21	-1.04

### 20% flap case

The applied flap sequences with the 20% flap are given in Figure 5.11. It is quite similar to the sequences for the 10% flap. Therefore the loadforms in this section are in a similar trend with the previous section, but with a larger magnitude since the flap authority is larger now. Since the rotor loadings are even higher, the uncertainty of the ACM results increase dramatically.  $Q_n$  and  $Q_t$  results corresponding to each  $\lambda$  are given in consecutive order in Figure 5.12 and Figure 5.13. Although the final loads have differences in phase angle and magnitude, the loading trends are similar between the estimations of the ACM and PM.

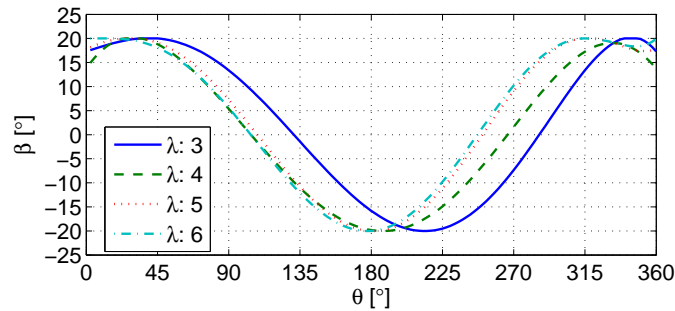


**Figure 5.11:** Flap sequences applied for the  $C_P$  maximization with the 20% flap for the  $C_P$  maximization case.

The angle of attack and axial induction at  $\lambda=4$  are given in Figure 5.14 and the estimations for the  $\lambda=6$  case are presented in Figure 5.15. The induction values in the upwind passage have a good agreement between PM and ACM results, but the downwind estimations differ significantly. The BWI effects are larger with a larger flap. Although the angle of attack curves are in a similar trend, the curves estimated by the ACM and PM have a phase shift in the upwind region. This phase shift was also apparent in the 10% flap case and more pronounced in the 20% flap case. This effect is probably due to difference between static

XFOIL polars used in ACM and the dynamic airfoil polars used in the PM. The angle of attack estimations for the downwind are completely different due to the big mismatch in the downwind induction estimation of the PM and ACM.

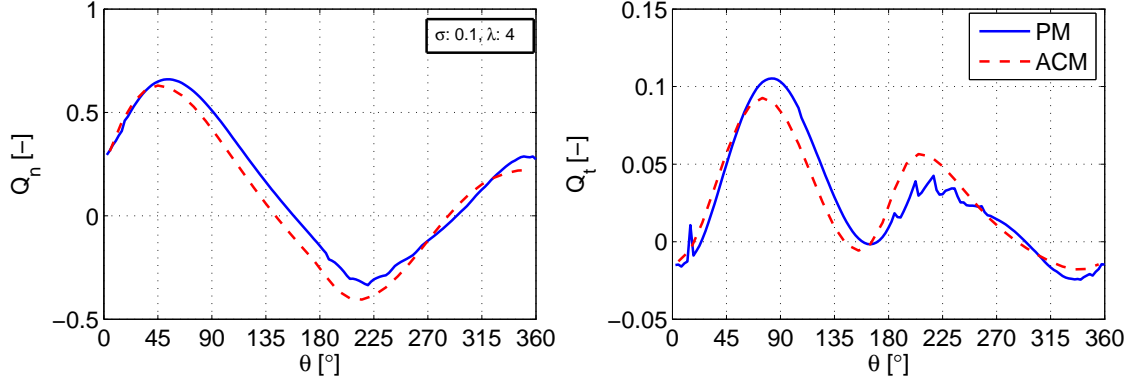


**Figure 5.12:**  $Q_n$  and  $Q_t$  calculated by the panel model and ACM at  $\lambda = 4$  with the 20% flap for the  $C_P$  maximization case.

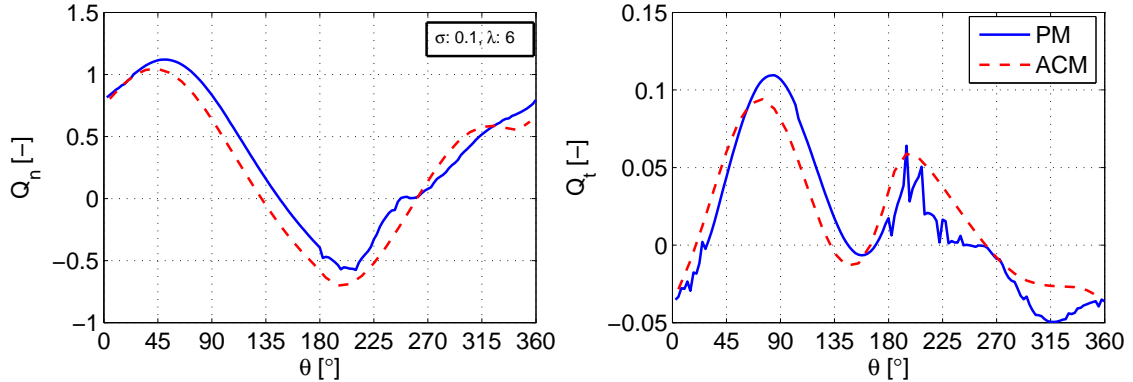


**Figure 5.13:**  $Q_n$  and  $Q_t$  calculated by the panel model and ACM at  $\lambda = 6$  with the 20% flap for the  $C_P$  maximization case.

The effect of the 20% flap on  $C_P$  and  $C_T$  at various  $\lambda$  is presented in Table 5.3. One can also see the relative errors between models and the relative improvement with respect to the references. The larger flap caused larger rotor loadings so the PM estimated  $C_T$  values above 1 for  $\lambda$  of 4,5 and 6. Therefore, the uncertainty in the ACM is high. The percentage  $C_P$  improvements at  $\lambda = 3$  and 4 are in similar order for each model. PM reports 11.22%  $C_P$  increment at  $\lambda=3$  and 8.25% at  $\lambda=4$ , while for ACM those values are 11.51% and 10.06%. On the other hand, the increased loading for the  $\lambda$  above 4 caused a dramatic decrease in the performance that is calculated by the PM. The reference  $C_P$  estimated by the PM is decreased by 17.11% with the active flap control which was applied to increase the power efficiency. For the same case the ACM estimates 28.04%  $C_P$  improvement. The ACM is highly uncertain when the  $C_T$  is close to 1 or above 1. For the future work, the ACM needs a new modification/correction for highly loaded cases. Alternatively, one can limit the maximum allowed  $C_T$  during the flap sequence optimization to a lower the uncertainties, so that the results will be reliable in the expense of a lower gain in the

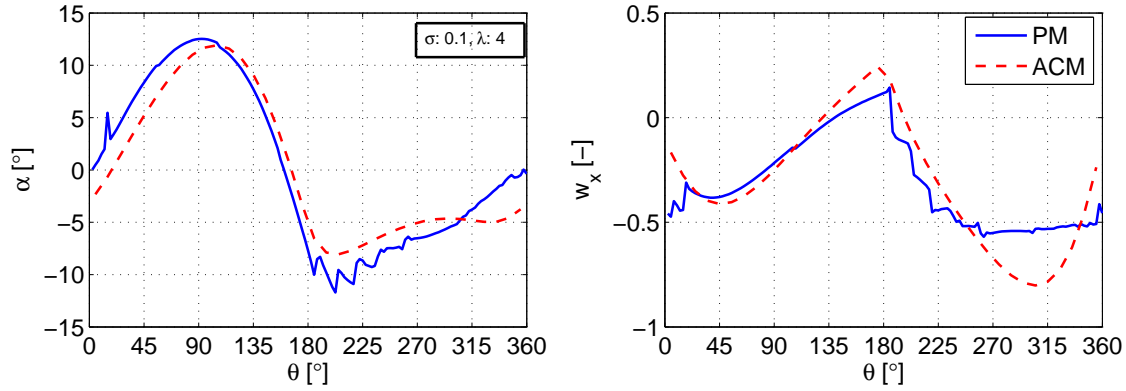


**Figure 5.14:** Angle of attack and axial induction calculated by the panel model and ACM at  $\lambda = 4$  with the 20% flap for the  $C_P$  maximization case.

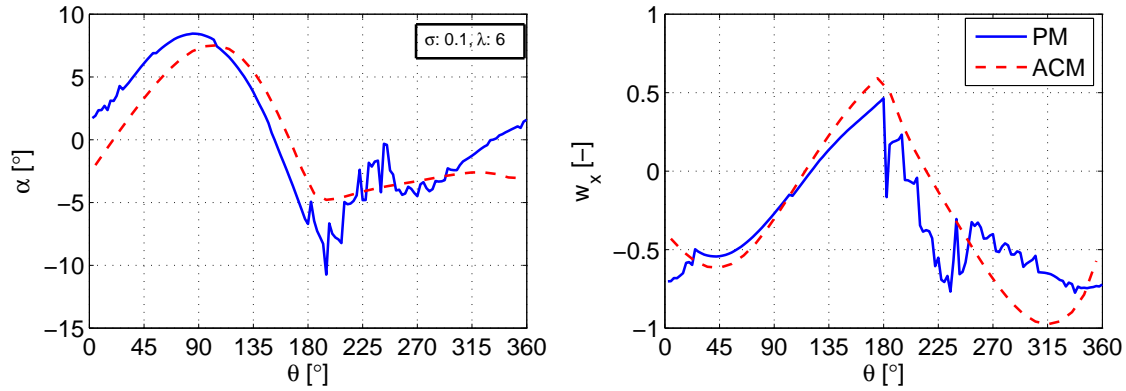


**Figure 5.15:** Angle of attack and axial induction calculated by the panel model and ACM at  $\lambda = 6$  with the 20% flap for the  $C_P$  maximization case.

$C_P$ . Nevertheless it is seen that the power efficiency of the VAWT could significantly be improved in the presence of the flap actuation.

**Table 5.3:** Comparison of the  $C_P$  and  $C_T$  estimated by the panel model and ACM with the 20% active flap for the  $C_P$  maximization case.

Parameter	$C_P$				$C_T$			
	3	4	5	6	3	4	5	6
$\lambda$ [-]	3	4	5	6	3	4	5	6
PM	0.61	0.64	0.56	0.49	0.99	1.04	1.08	1.14
ACM	0.63	0.65	0.67	0.69	0.97	0.98	0.98	0.98
Difference between models [%]	2.40	0.93	16.15	28.04	1.93	6.57	10.25	17.18
Change on PM reference [%]	11.22	8.25	-6.29	-17.11	30.36	17.36	9.74	8.89
Change on ACM reference [%]	11.51	10.06	14.14	18.15	25.17	10.96	3.00	-1.24

### 5.3 $C_P$ minimization

The active flap sequences to minimize the  $C_P$  with the 10% flap are shown in Figure 5.16. Except the  $\lambda=5$  case the flap sequences looks similar, clearly the optimization did not converge to the global minimum for the  $\lambda=5$  case. Figure 5.17 presents the  $Q_n$  and  $Q_t$  at  $\lambda$  of 4 while Figure 5.18 shows the same plots when the  $\lambda$  is 6. Similar to the load comparison in the single airfoil analysis, the normal loadings of PM and ACM have similar trends but with a magnitude shift in between. For the  $Q_t$  one can see that the loads of PM are transferred to the upwind from the downwind where the ACM shows relatively even distribution of  $Q_t$ . These differences does not affect the mean  $C_P$  and  $C_T$  excessively, therefore the performance estimations of models are pretty close to each other.

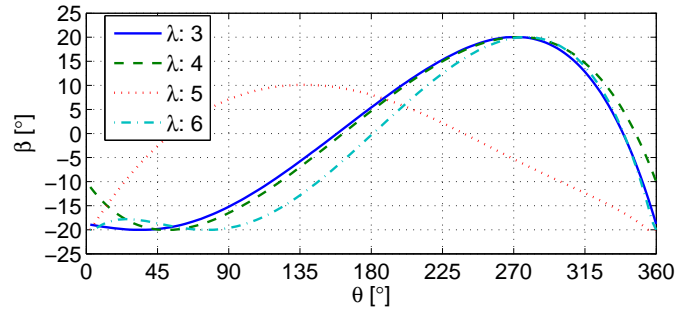


**Figure 5.16:** Flap sequences applied for the  $C_P$  minimization with the 10% flap.

Figure 5.19 and Figure 5.20 shows the angle of attack and the axial induction velocities for the  $\lambda = 4$  and 6. It is seen that the angle of attack trends are very similar but the peak values of PM are slightly lower. Moreover, the effect of the BWI is not pronounced at high  $\lambda$  as in the  $C_P$  maximization case. Also, the induction estimations of models match each other for both of the  $\lambda$ . It is believed that the estimation of induction velocity are similar due to the decreased rotor loading so that the ACM estimations are reliable, so the performance of the optimized flap sequences.

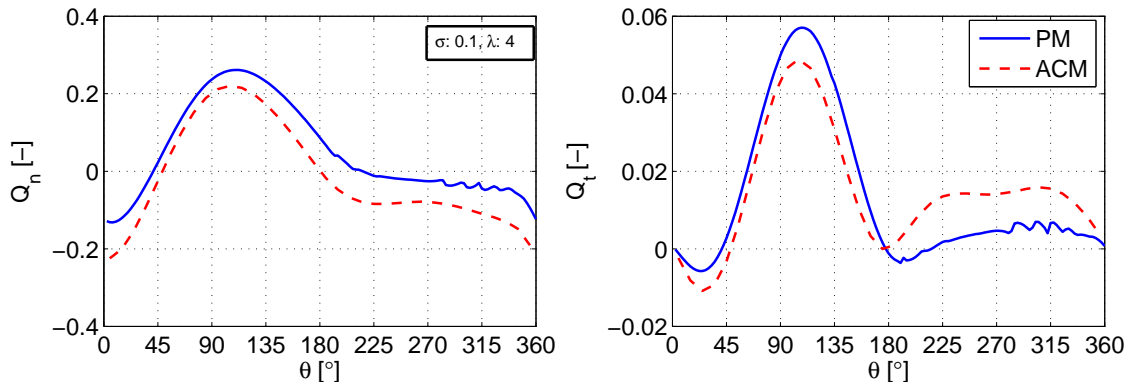


**Figure 5.17:**  $Q_n$  and  $Q_t$  calculated by the panel model and ACM at  $\lambda = 4$  with the 10% flap for the  $C_P$  minimization case.

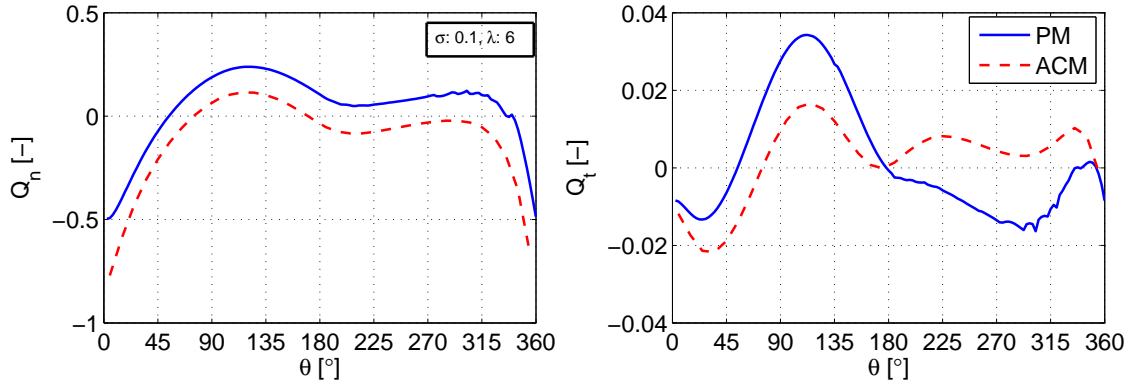


Figure 5.18:  $Q_n$  and  $Q_t$  calculated by the panel model and ACM at  $\lambda = 6$  with the 10% flap for the  $C_P$  minimization case.

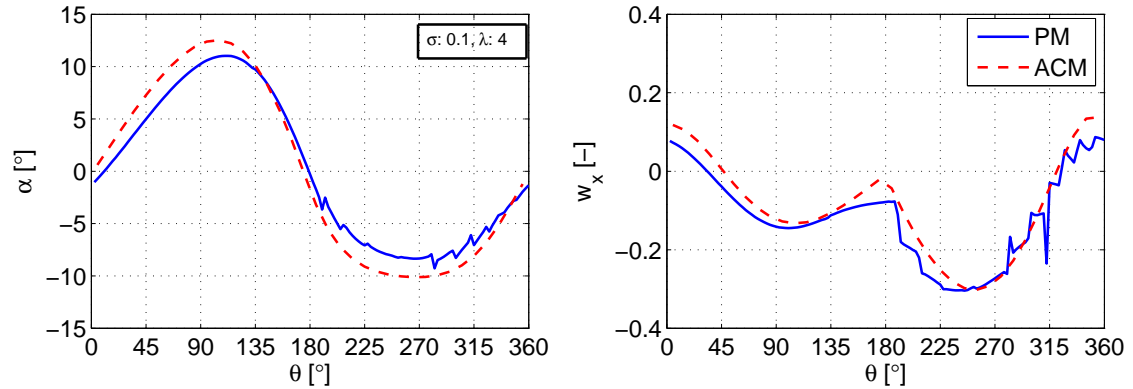


Figure 5.19: Angle of attack and axial induction calculated by the panel model and ACM at  $\lambda = 4$  with the 10% flap for the  $C_P$  minimization case.

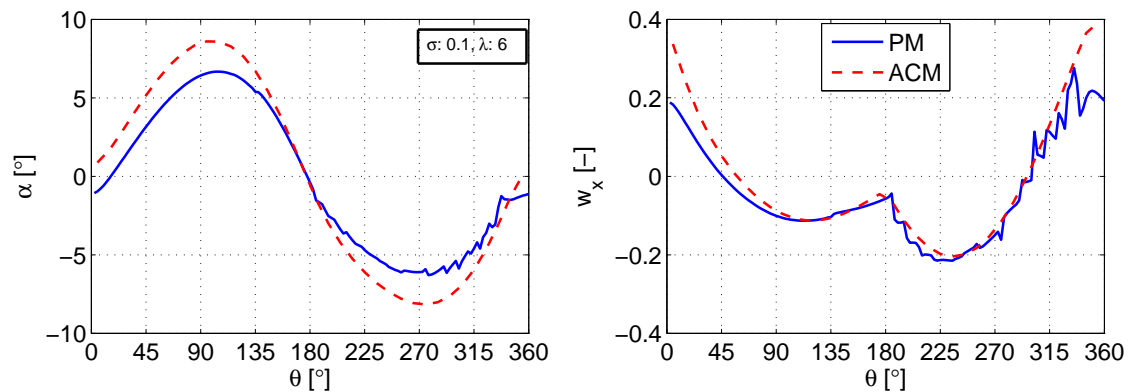


Figure 5.20: Angle of attack and axial induction calculated by the panel model and ACM at  $\lambda = 6$  with the 10% flap for the  $C_P$  minimization case.

The  $C_P$  and  $C_T$  estimations of the PM and ACM for the specified  $\lambda$  range are given in Table 5.4. Although the absolute values of  $C_P$  and  $C_T$  have a clear difference between the models, the percentage  $C_P$  alleviation with respect to the references are quite similar.

PM agrees with the estimations of the ACM for all the cases. By the help of a 10% flap that operates in  $\pm 20$  degree range, the  $C_P$  can be dropped between 15.61% to 88.85% depending on the operating conditions. The alleviation percentage for the  $\lambda = 5$  is very small compared to other flow states which is due to the non-optimal flap setting. This was mentioned during the introduction of Figure 5.16. Furthermore, the  $C_T$  estimations are also in line between the PM and ACM. As mentioned before, the  $C_P$  minimization is carried out to explore if the flap could be used for the rated power control. Although the exact values are depending on the rotor design, the rated power control will be a case for low tip speed ratios. Throughout the thesis tip speed ratios smaller than are not simulated since the models used here (ACM, PM) do not take the viscosity and dynamic stall effects into account. But as far as it is seen by the recent analysis the flap is a very effective tool to decrease the  $C_P$ . It is believed that with the presence of the viscous drag, the flap will help to decrease the  $C_P$  even further since the flap deflection will increase the profile drag significantly. On the other hand, for very low  $\lambda$  the flap might not be effective if the airfoil is in stall operation. Further studies in this field are required but they are out of the scope of this work.

**Table 5.4:** Comparison of the  $C_P$  and  $C_T$  estimated by the panel model and ACM with the 10% active flap for the  $C_P$  minimization case.

$C_P$				
$\lambda$ [-]	3	4	5	6
PM	0.37	0.33	0.51	0.07
ACM	0.40	0.36	0.52	0.08
Difference between models [%]	7.30	7.41	3.39	17.86
Change on PM reference [%]	-33.24	-43.41	-15.61	-88.85
Change on ACM reference [%]	-29.53	-38.44	-10.79	-86.07
$C_T$				
$\lambda$ [-]	3	4	5	6
PM	0.45	0.41	1.04	0.11
ACM	0.47	0.42	0.99	0.10
Difference between models [%]	5.16	4.26	4.89	3.66
Change on PM reference [%]	-41.15	-54.37	6.08	-90.00
Change on ACM reference [%]	-39.26	-51.97	4.64	-89.75

## 5.4 $C_T$ minimization

The flap sequences in order to alleviate the  $C_T$  values are given in Figure 5.21. These sequences are optimized by allowing maximum 3% deviation ( $C_{P,gap}$ ) from the reference  $C_P$ . As seen from the flap angles, the loading is slightly increased in the upwind by positive flap angles and heavily decreased in the downwind with positive flap deflections. The  $Q_n$  and  $Q_t$  for the  $\lambda = 4$  are given in Figure 5.22. The loadings for the  $\lambda = 6$  case can be seen in Figure 5.23. The loading trends are quite close between the two models but the aforementioned fixed-pitch effect is again apparent. The normal loading magnitudes for the PM is slightly shifted to the positive values, therefore the tangential loads are

transferred from downwind to upwind region. It is seen that both ACM and PM report negative torque for the downwind region at  $\lambda$  of 6. In order to decrease the  $C_T$  the loads in downwind are suppressed dramatically.

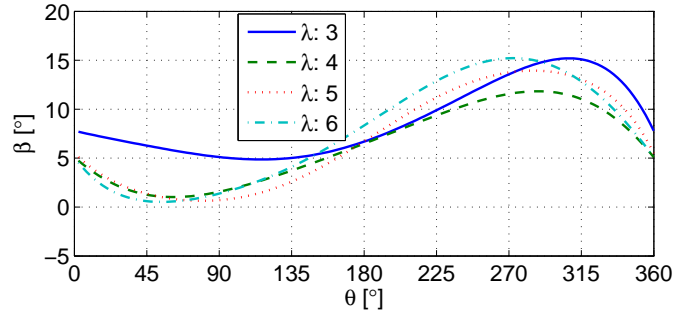


Figure 5.21: Flap sequences applied for the  $C_T$  minimization with the 10% flap.

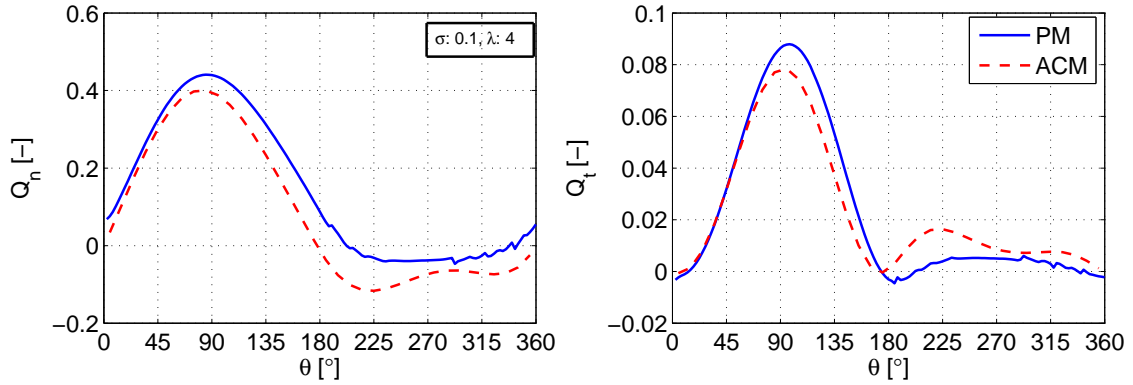


Figure 5.22:  $Q_n$  and  $Q_t$  calculated by the panel model and ACM at  $\lambda = 4$  with the 10% flap for the  $C_T$  minimization case.

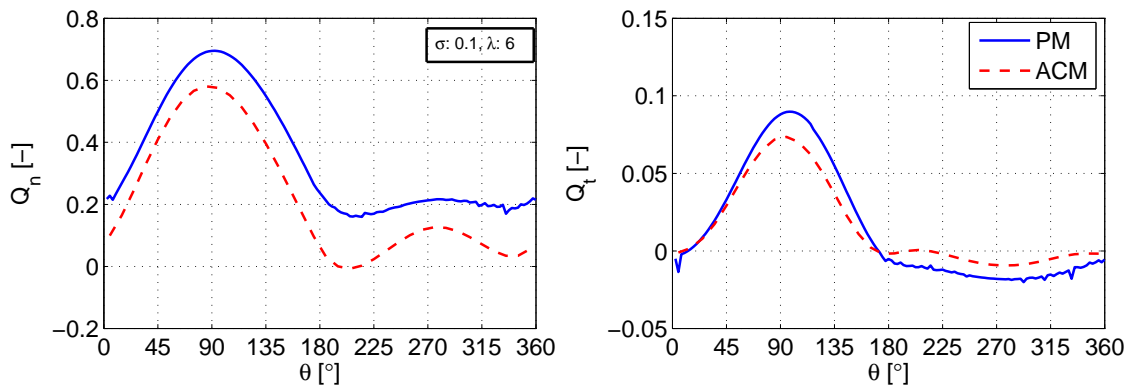
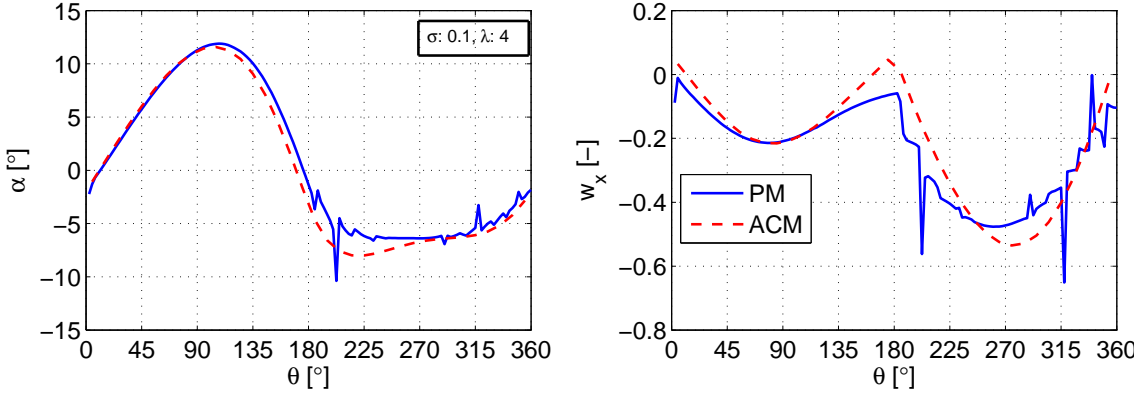


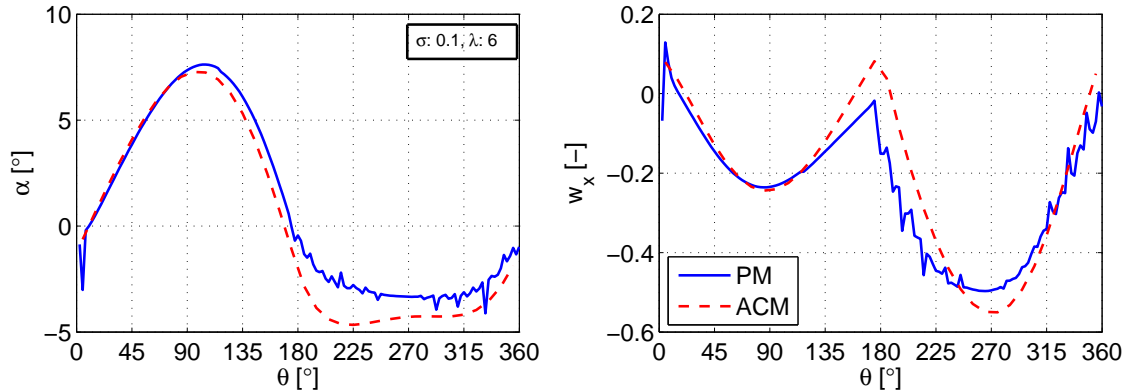
Figure 5.23:  $Q_n$  and  $Q_t$  calculated by the panel model and ACM at  $\lambda = 6$  with the 10% flap for the  $C_T$  minimization case.

Figure 5.24 and Figure 5.25 show the angle of attack and the axial induction comparisons at the  $\lambda$  of 4 and 6. The PM and ACM has predicted a very similar angle of attack

distribution along the azimuth. There are slight differences in the downwind as expected but those differences are in acceptable ranges. Similar to the estimations in the  $C_P$  minimization case, the induction estimations between the ACM and PM are quite close. The main differences between the induction estimations are in the windward and leeward sides. This was a valid case for all of the induction comparisons shown in this chapter. Clearly, the ACM has trouble in obtaining the inductions near those regions.



**Figure 5.24:** Angle of attack and axial induction calculated by the panel model and ACM at  $\lambda = 4$  with the 10% flap for the  $C_T$  minimization case.



**Figure 5.25:** Angle of attack and axial induction calculated by the panel model and ACM at  $\lambda = 6$  with the 10% flap for the  $C_T$  minimization case.

Table 5.5 shows the results related to the  $C_P$  and  $C_T$  estimations of the PM and ACM. Both the  $C_P$  and  $C_T$  estimations of the models are very close for the whole  $\lambda$  range. The differences between the estimations are between 0 - 2.5%. Therefore the  $C_T$  alleviations are in the similar orders for both of the models. It is verified by the PM that  $C_T$  can be decreased 7.13% at  $\lambda=3$ . The alleviation rates increase with the  $\lambda$  since the reference  $C_T$  is relatively high, so at  $\lambda = 6$  the  $C_T$  is decreased 26.13%. Although the  $C_P$  deviation from the reference is below 3% for the ACM, the PM simulations disobey this constraint. The largest  $C_P$  decrement in the PM estimations is experienced at  $\lambda = 6$  as 6.81% with respect to the PM reference. It is shown by this analysis that the  $C_T$  of the turbine can be decreased significantly if one is willing to sacrifice few percents of the power efficiency.

To determine the optimum tolerance for the  $C_P$  one should conduct a comparative study between the fatigue life analysis and life-time cost analysis of the blades. Because a lower  $C_T$  operation would require less material on the blade so the production costs could be decreased, but these savings should be higher than the lost amount of electricity due to less efficient operation.

**Table 5.5:** Comparison of the  $C_P$  and  $C_T$  estimated by the panel model and ACM with the 10% active flap for the  $C_T$  minimization case.

$C_P$				
$\lambda$ [-]	3	4	5	6
PM	0.53	0.56	0.57	0.56
ACM	0.55	0.57	0.57	0.56
Difference between models [%]	2.52	1.07	0.23	1.48
Change on the PM reference [%]	-3.32	-4.63	-5.12	-6.81
Change on the ACM reference [%]	-2.95	-2.91	-2.88	-2.98
$C_T$				
$\lambda$ [-]	3	4	5	6
PM	0.70	0.78	0.79	0.78
ACM	0.71	0.78	0.78	0.76
Difference between models [%]	1.08	0.37	1.59	1.90
Change on the PM reference [%]	-7.13	-12.04	-19.48	-26.13
Change on the ACM reference [%]	-8.10	-11.70	-17.98	-22.95

## 5.5 New wake paths

Along this chapter the effect of flap actuation on the VAWT performance are presented. The power efficiency or thrust coefficients are modified which means that the azimuthal vortex shedding is changed. Therefore, each case with a flap actuation acquires a new wake shape. In Figure 5.26, Figure 5.27, Figure 5.28 and Figure 5.29 series of wake paths and the corresponding flap sequences are given. These are the wake paths of the non-flapped reference case,  $C_P$  maximization case,  $C_P$  minimization case and  $C_T$  minimization case respectively. Only the 10% flap cases are presented. Wake paths are representative for the  $\lambda = 3$  condition since wake is less packed and easier to interpret. The characteristic cycloidal wake shape of a 2D VAWT is a common feature in all of the wake paths. One can also mention that wake is never symmetric in Y-axis even with the non-flapped case. This is due to different convection speeds in the leeward and windward regions. The wake expansion for the  $C_P$  maximization case (Figure 5.27) is the largest of all cases, as a sign of a larger power exchange. The wake is the most asymmetrical in the  $C_P$  maximization case since different signs of flap actuation are applied in downwind. We can also say that, for the similar reasons, the far wake of the  $C_P$  maximization case lose its entity faster which could be a favorable feature in a tandem operation. For the  $C_P$  minimization case in Figure 5.28, the wake expansion is the lowest. In this case the  $C_P$  is 0.37. Wake preserves its entity for longer distances. In the  $C_T$  minimization case in Figure 5.29, the wake resembles very much to the wake of the non-flapped case. Such result is expected

since the difference in the  $C_P$  between those cases are the smallest. Note that for the  $C_P$  maximization case this difference is 9.49%, for  $C_P$  minimization 33.24% and for  $C_T$  minimization 3.32%.

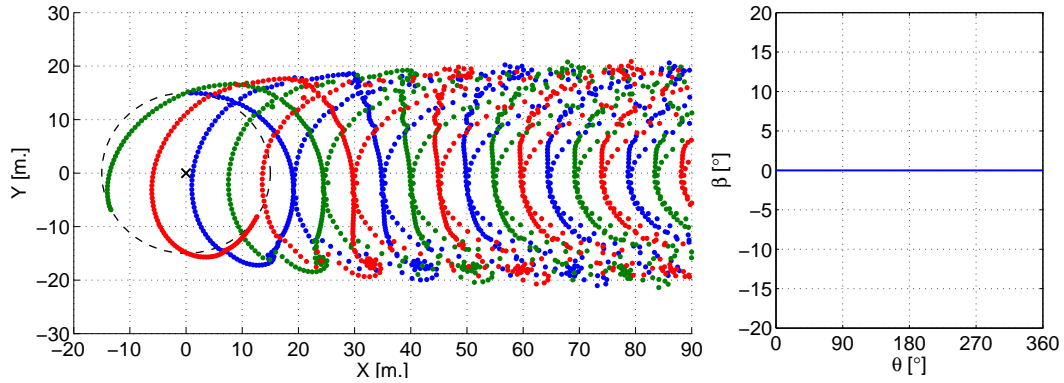


**Figure 5.26:** Wake path and the flap sequence for undeflected case at  $\lambda = 3$ .

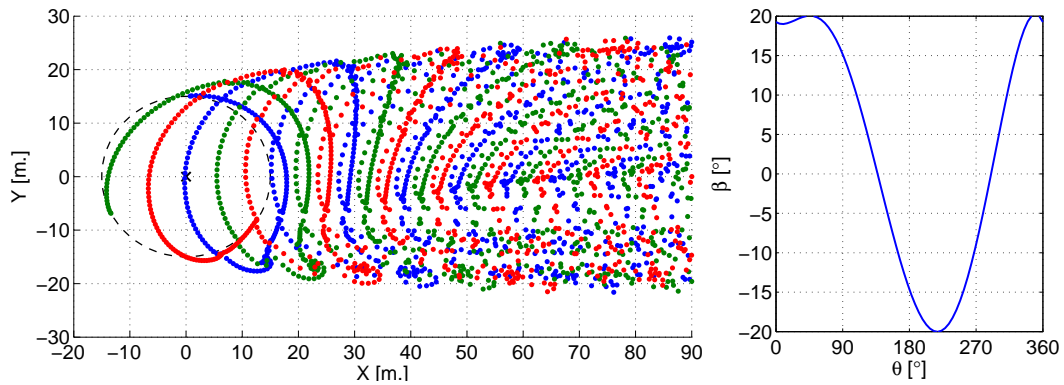


**Figure 5.27:** Wake path and the flap sequence for  $C_P$  maximization case with 10% flap at  $\lambda = 3$ .

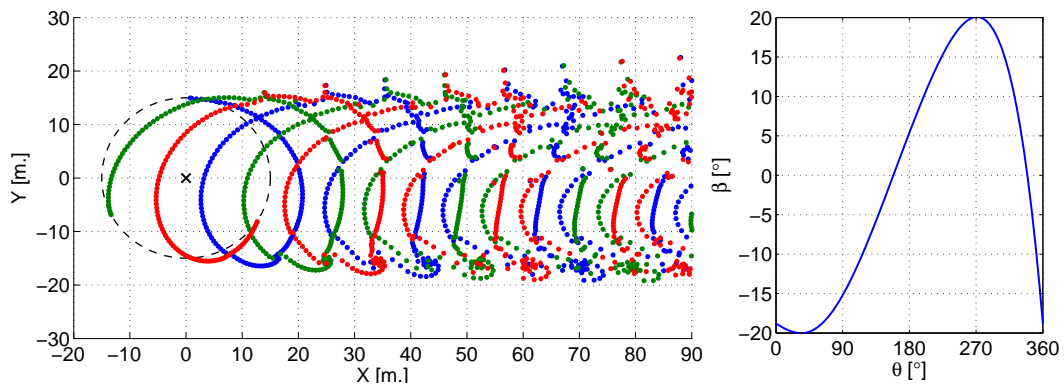


**Figure 5.28:** Wake path and the flap sequence for  $C_P$  minimization case with 10% flap at  $\lambda = 3$ .

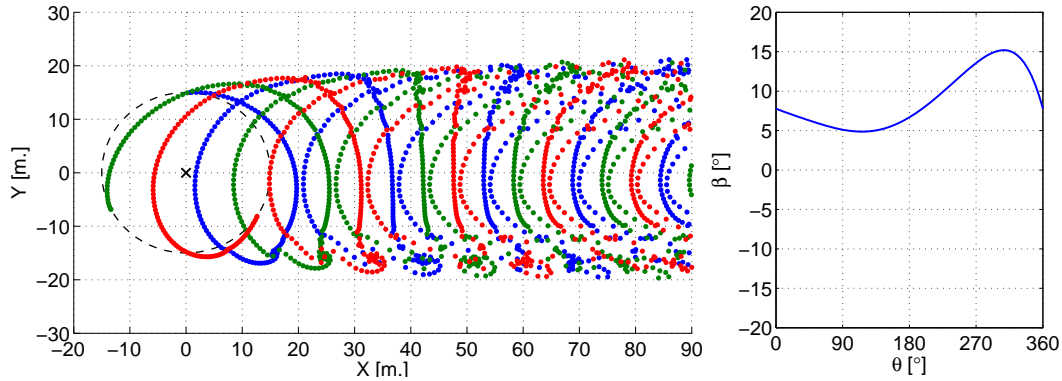


*Figure 5.29: Wake path and the flap sequence for  $C_T$  minimization case with 10% flap at  $\lambda = 3$ .*

## 5.6 Conclusions of the chapter

This chapter showed an extensive comparison study between the Panel Model (PM) and the Actuator Cylinder Model (ACM). The difference between the ACM and PM estimations differ from case to case. In the final section, the examples of the wake paths in the presence of different flap actuation are presented. The main conclusions of the chapter can be listed as:

- The PM showed that the major part of the ACM estimations are reliable therefore it can be used thoroughly within its certainty limits. The ACM estimations are very uncertain if the  $C_T \geq 1$ . This is a general case for the  $C_P$  maximization therefore the largest levels of mismatch between the ACM and PM are observed in those cases. Nevertheless, for the  $\lambda$  of 3 and 4, the PM showed that the  $C_P$  can be improved 9.5% and 6.4% with a 10% flap. These improvements goes up to 11.22% and 8.25% if 20% flap is used.
- The ACM and PM estimations for the  $C_P$  minimization and  $C_T$  minimization cases are in good agreement. Although the absolute  $C_P$  and  $C_T$  values are different, the percentage changes on the reference values are very close. The optimizations with the ACM are found reliable for these objectives.
- Differences in the aerodynamic loading estimations between the PM and ACM have two main characteristics. 1) Constant shift in the  $Q_n$  values, 2) Slight phase shift along the azimuth. It is believed that these differences are due to the dynamic effects in the PM calculations. The angle of attack estimations match quite good for the upwind region while the differences are bigger in downwind. This is due to the different wake calculation methodologies of the PM and ACM.
- The blade-wake interactions (BWI) in downwind rotor are well captured by the PM. These interactions are increasing at high  $\lambda$  values since the wake is tightly packed in the free-stream.

- In order to have reliable results from the ACM optimization for  $C_P$  maximization, two new ways are recommended: 1) to include a new correction in Mod-Lin ACM for highly loaded cases, 2) to limit the maximum  $C_T$  value to a lower value than 1, preferably some value around 0.89. This choice will decrease the maximum  $C_P$  but will make it more reliable.

# Airfoil Design for the VAWT Blades with Active Trailing Edge Flaps

This chapter presents a multi-objective design work that is specified to create airfoils that offer superior performance for the active flap controlled VAWT blades. The aerodynamic design objectives are the improvement of single-element airfoil performance in VAWT rotor and its flap performance at the same time. The second design objective is set to consider airfoils with favorable structural properties. A cost model is not used during the optimization but it is assured that the optimization objectives lead to a turbine with lower CoE implicitly. Along the chapter, firstly, the airfoil design requirements for the VAWT are listed and motivated. Later, the airfoil design methodology is introduced and the sub-modules of the optimization are explained briefly. The optimization results are presented in the final section of this chapter. The performances of the several good scoring airfoils in the pareto front are shown and compared with each other. Only four new airfoils are introduced in the text but the reader can find information for eight more airfoils in the Appendix A. Throughout the thesis, the airfoil surfaces are classified with the top-bottom or suction-pressure names. For the VAWT, these definitions are not valid since each surface serves both as a suction and pressure surface. The reader should note that, the airfoil surface facing the rotor center is referred as the suction/top side and the surface that is outside of the rotor periphery is referred as the pressure/bottom side.

## 6.1 Airfoil Design: The requirements and the methodology

### 6.1.1 Airfoil design requirements

In the literature study, the past work for the VAWT and HAWT airfoil design is summarized. It is seen that the design process for the HAWT airfoils is much more mature. For the VAWT, only several recent works have used modern design methodologies. In this section, the airfoil design requirements are listed for the VAWT blade with a trailing edge flap while having the past design works in mind.

CoE is the main design driver for the wind turbine industry. Therefore the most effective design optimization should be carried out with a turbine cost model. A cost model would consider the annual energy production (AEP), turbine manufacturing and installation costs, operation and maintenance (O&M) costs. Unfortunately, sophisticated cost models for the VAWT does not exist; therefore the design requirements should implicitly dictate a lower CoE than a baseline/reference design. Hence, the optimization objectives are chosen to obtain airfoils with high aerodynamic and structural fineness. Main motivation is that the aerodynamic fineness will increase the power efficiency so the AEP of the turbine while the structural fineness will decrease the manufacturing and O&M costs of the blades.

The first priority in the aerodynamic design is to increase the power efficiency of the rotor. For the recent case, we have the airfoil and flap performance as subjects for the design. The  $\frac{C_l}{C_d}$  is the measure that comes to mind when an aerodynamic objective is sought for. It dictates an airfoil with very high lift potential and low drag behavior. In the recent works by Ferreira et.al.[16, 17] it has been shown that a better aerodynamic objective for the VAWT could be  $\frac{C_{l\alpha}}{C_d}$  instead of  $\frac{C_l}{C_d}$ . The slope of a lift curve is critical since it is an important measure of the shed vorticity creation which is correlated with the power exchange rates of VAWTs. In the work of Ferreira et. al. [17] a relation to increase the power efficiency is derived as  $\frac{d(V_{rel} C_l c)}{d\theta}$ . This relation is obtained from the potential flow assumptions. Furthermore, for the same solidity and tip-speed ratio  $\frac{d(V_{rel} C_l c)}{d\theta}$  can be reduced to  $\frac{dC_l}{d\theta}$ , then to  $\frac{dC_l}{d\alpha}$ . The lift curve slope ( $\frac{dC_l}{d\alpha}$ ) is preferred over  $\frac{dC_l}{d\theta}$  since the performance assessment of an airfoil can be done by knowing its polars only. For the drag polar, the main intention should be to obtain a wide drag bucket so that the airfoil lose less power due to drag. The VAWT airfoils operate in a wide range of angle of attacks. Therefore an optimum design should be valid for a target range of perceived angle of attack. This range might be enlarged slightly to improve the off-design conditions such as gust events.

The effectivity of the flap should also be very high. This could be obtained by having a high flap sensitivity ( $C_{l\beta}$ ) for a wide range of angle of attack. This property shows how much lift could be increased with a unit deflection of a flap. A higher  $C_{l\beta}$  would allow a larger space for  $C_l$  authority so the versatility of the flap can be improved. The airfoil trailing edge shape should also be designed in a fashion that flap deflection does not worsen the overall performance. For instance, an airfoil with a high aft camber already has a large adverse pressure gradients near the trailing edge. A slight increase in camber due to flap would lead to early separation in such case. Moreover, the drag introduced by the flap actuation should be kept as low as possible. These relations are important to keep in mind for the airfoils with flaps.

Another critical issue for the aerodynamic fineness is the sensitivity of an airfoil to the surface roughness. The wind turbine blades operate very long hours without maintenance and care. During the operation dust, bug, ice, corrosion could accumulate on the blade's leading edge which would trigger a turbulent boundary layer. A roughness insensitive airfoil would almost have the same  $C_l$  polar of the clean case but the drag polar will not be the same since the turbulent boundary layer increases the profile drag dramatically. For the VAWT blade, during the downwind passage the airfoil operates in the upwind wake therefore the ambient turbulence intensity is high at that location. This phenomenon

would also turn the laminar boundary layer to the turbulent. Therefore for the VAWT, even if the blade is clean, the airfoil could experience perturbations on its boundary layer due to its wake.

The behavior of the stall is an important characteristic for the wind turbine airfoils. According to the needs, a designer would require a sharp or a soft stall. The intention in this work is to obtain airfoils with a soft stall. The soft stall is needed to decrease the fatigue loading in the case if a blade operates around stall angle. Moreover, gusty conditions could also lead to airfoil stall. The soft stall will decrease the life-time fatigue loads therefore less material could be used in the presence of the soft stalling airfoils. One can also mention about the deep stall angle as an important parameter for the VAWT airfoil. An airfoil with a larger deep stall angle could help the start-up capabilities of the VAWT. The deep stall angle is very much related to the leading edge radius and the maximum thickness of the airfoil.

The structural requirements of an airfoil differs greatly with its application environment. This work concentrates on creating airfoils that can be used along the major part of the blade span, so they should serve as general purpose airfoils. The blade should be durable for extreme loads and the fatigue loads during the life-time operation which makes the flapwise and edgewise stiffness of the blade critical measures. The edgewise stiffness is much less critical in VAWT since the cyclic gravity loads are not heavily experienced; fatigue is not a vital issue for the edgewise stiffness. If one aims for a large stiffness then the area moment of inertia of the structure should be kept high. The airfoil maximum relative thickness can be shown as the dominant variable of the flapwise bending stiffness of the blade. Hence, the maximum relative thickness of the airfoil must be as high as possible while assuring a high aerodynamic objective. Moreover the trailing edge thickness must be large enough to enable a manufacturable geometry. Furthermore, to avoid having very early and sharp stalls the leading edge radius should be limited by a lower bound.

### 6.1.2 The airfoil design methodology

The main components of the airfoil design methodology are introduced in this section. The block diagram of the optimization is shown and the working principles of each module are briefly explained. The motivations on the selection of the optimization algorithm, airfoil shape representation and the flow solver are given. The choice of objective functions and constraints are introduced. Note that the base code of the optimizer was developed by Gael de Oliveira during his master thesis work [50]. A detailed information on the implementation and validation can be found in the corresponding thesis. The main script is changed in this thesis in order to implement the new objectives, constraint, simulations and additional calculations. This base script has been used in the Wind Energy Department of TU Delft by various authors [16, 17, 33]. This tool acquires an object-oriented data structure and based on the symbolic computation and global optimization toolboxes of Matlab.

#### Main structure of the optimization

Figure 6.1 shows the main blocks of the optimization tool. The names of the object structures in the optimization tool are written in parenthesis under corresponding blocks. The

optimization is carried out by a complex communication between the blocks with different roles. This communication is provided by the *interface* block which is also responsible of evaluating the overall cost function. Note that several blocks are only providing information to the interface while other blocks are constantly exchanging information with the interface during an optimization. These relations can be observed with the arrow types in between the blocks. The definitions of multiple objectives are done in the *objectives* block. Discrete cost functions of different disciplines as well as the penalty functions are replaced in this block. Constraints and bounds for the design variables are defined in the *constraint manager* block. The definition of the feasible search area for the CST variables, trailing edge and leading edge shape coefficients are modeled in this block. Here, one can define both inequality and equality constraints. The required X/RFOIL simulations to assess the aerodynamic objectives are defined in the *simulations* block. The new airfoil geometries are created in the *airfoil* block which obtains the new CST variables from the *interface* block. Furthermore, the geometrical properties of the airfoils are evaluated and stored in the *airfoil* block. The aerodynamic and structural performance of the new airfoils are analyzed in the *flow and structural calculations* block. This block is responsible of creating the input files and post-processing the output files of the simulation codes, X/RFOIL. The numerical optimization algorithm is placed in the *optimizer* block. This block controls the evaluation of the multi-objective problem and plans the next iteration of the optimization. Finally, the critical outputs of the optimization are saved in a data structure in order to post-process the optimized airfoils.

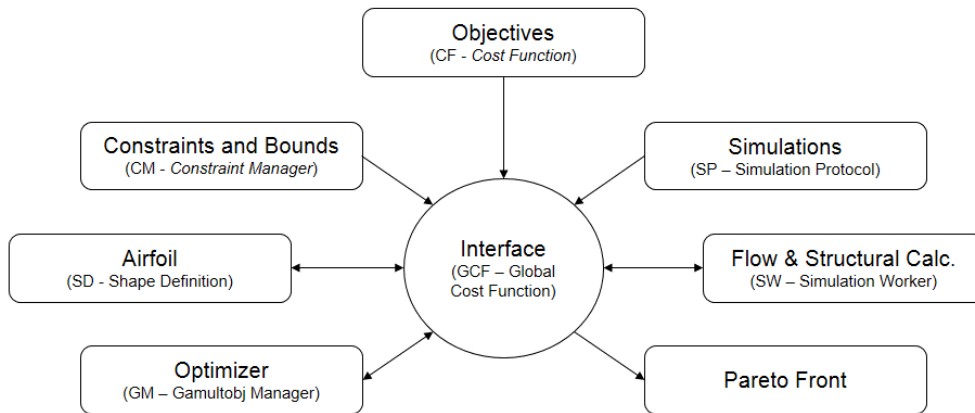


Figure 6.1: Optimization structure.

## Objectives

For the aerodynamic objective the perspective of Ferreira et.al. [17] is chosen since promising results have obtained earlier. In the corresponding works, the  $\frac{dC_l}{d\alpha}$  was used instead of  $\frac{dC_l}{d\theta}$  for the simplicity of the implementation. Such simplification can not be made if one takes the circulation control into account. Since the  $C_l$  is also a function of the flap deflection now, a new expression that represents the vortex shedding capability of an airfoil should be derived.

The new objective function is sought with the potential flow assumptions. In potential flow one can assume the  $C_l$  of a flapped airfoil with the simple relation in Equation 6.1. If the  $\frac{dC_l}{d\theta}$  is worked out by using the Equation 6.1 then a general statement for the vortex shedding rate could be found as in Equation 6.2. Here the second and the fourth expressions on the right hand side can be assumed as zero. Because in potential flow the  $C_{l\alpha}$  and  $C_{l\beta}$  are independent from the angle of attack, thus independent from the azimuth position. Therefore the final expression can be written as Equation 6.3.

$$C_l = C_{l\alpha}\alpha + C_{l\beta}\beta \quad (6.1)$$

$$\frac{dC_l}{d\theta} = \frac{\partial C_l}{\partial \alpha} \frac{d\alpha}{d\theta} + \alpha(\theta) \frac{dC_{l\alpha}}{d\theta} + \frac{\partial C_l}{\partial \beta} \frac{d\beta}{d\theta} + \beta(\theta) \frac{dC_{l\beta}}{d\theta} \quad (6.2)$$

$$\frac{dC_l}{d\theta} = C_{l\alpha} \frac{d\alpha}{d\theta} + C_{l\beta} \frac{d\beta}{d\theta} \quad (6.3)$$

The final expression requires the information of the  $\alpha(\theta)$  and  $\beta(\theta)$  along the azimuth. For a general purpose airfoil design these distributions can not be known. They are very much dependent on the objective of the flap, size of the flap and the operating conditions of the rotor. Therefore a need for a representative expression for the rate of vortex shedding (Equation 6.3) arises. This new expression should take the importance of the lift-curve slope ( $C_{l\alpha}$ ) and flap sensitivity ( $C_{l\beta}$ ) into account. The design of new airfoils should have a favorable  $C_{l\alpha}$  and  $C_{l\beta}$  with a good balance between each other. Besides the considerations on the  $C_l$  polar, the drag coefficient is also a crucial term in the objective. The minimization of the drag term would lead to less power loss due to viscous effects. One should keep in mind that the percentage increase in drag of a flapped case is closely related to the airfoil shape, especially the tail region. Therefore, the flapped polars should be taken into account in the drag term of the objective.

The analysis up to here showed a need to obtain compact expressions for the  $C_l(\alpha, \beta)$  and  $C_d(\alpha, \beta)$ . These expressions should contain the information of the undeflected and deflected flap performance of an airfoil. According to this intention, it is proposed to create hybrid airfoil polars. To create these hybrid polars at least two different flap settings has to be simulated, preferably a positive and a negative value ( $\beta^+$ ,  $\beta^-$ ). To create the hybrid polars, variable weighting between two of the flapped polars should be applied. In this work, a linear weighting is chosen for this task. In fact, the weighting between the flapped polars is equivalent to the  $\beta(\theta)$  term in Equation 6.3. The equations to calculate the hybrid polars are given in Equation 6.4 and Equation 6.5. Here,  $\Delta_\alpha$  is a fixed range of angle of attack and it is determined by choosing a design  $\lambda$  for a VAWT. It is chosen as 15 degrees to represent the state of  $\lambda \sim 4$ . The starting point of this angle of attack range is not fixed and can be changed by the  $\alpha_s$ . This variable is introduced to allow flexibility in the airfoil design space. The creation of the hybrid  $C_l$  and  $C_d$  polars for various  $\alpha_s$  are shown with an example in Figure 6.2. One can see that depending on the  $\alpha_s$  the lift curve slopes and  $C_d$  values of the hybrid polars differ significantly.

$$C_{l,hybrid}(\alpha) = \frac{\alpha - \alpha_s}{\Delta_\alpha} C_l(\alpha, \beta^+) + \frac{\Delta_\alpha + \alpha_s - \alpha}{\Delta_\alpha} C_l(\alpha, \beta^-) \quad (6.4)$$

$$C_{d,hybrid}(\alpha) = \frac{\alpha - \alpha_s}{\Delta\alpha} C_d(\alpha, \beta^+) + \frac{\Delta\alpha + \alpha_s - \alpha}{\Delta\alpha} C_d(\alpha, \beta^-) \quad (6.5)$$

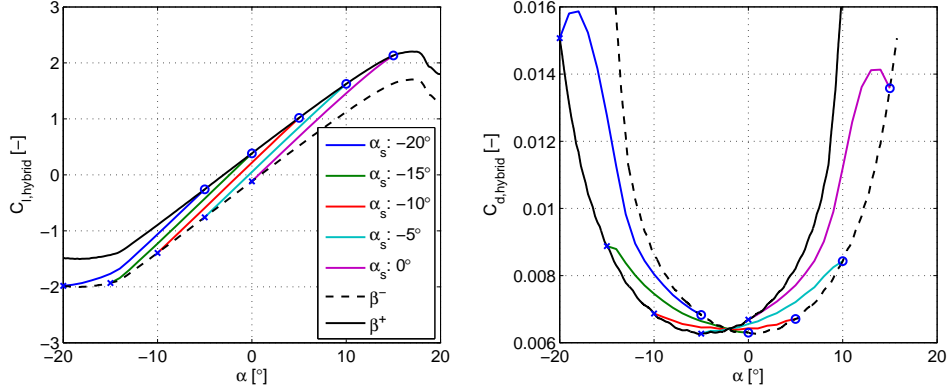


Figure 6.2: Creation of the hybrid polars.

Since multiple polars are transformed into a single hybrid polar, the approach of Ferreira for the aerodynamic objective could be used. The aerodynamic objective is given in Equation 6.6. The lift curve slope of the hybrid polar is integrated in the numerator while the denominator is the integral of the weighted  $C_{d,hybrid}$ . The weighting ( $p(\alpha)$ ) applied on the drag coefficient is a probability distribution function of the perceived angle of attack during VAWT operation. The aerodynamic objective function is responsible for choosing the best  $\alpha_s$  for each airfoil in the design process. At the end, the objective is multiplied by a minus sign in order to make the equation ready for a minimization problem.

$$J_{AERO} = -max \left( \left( \frac{\int_{\alpha_s}^{\alpha_s + \Delta\alpha} C_{l\alpha,hybrid} d\alpha}{\int_{\alpha_s}^{\alpha_s + \Delta\alpha} C_{d,hybrid} p(\alpha) d\alpha} \right), \forall \alpha_s \in [-20, 5] \right) \quad (6.6)$$

The choice of the structural objective could be as critical as the aerodynamic objective since it has a power to change the airfoil shape significantly. In this work the focus is to obtain high flapwise bending stiffness. Secondary consideration for the structural design is the area enclosed by the airfoil for housing the sub-structures and instrumentation. The structural objective function is chosen as the flapwise bending stiffness of a solid box that lies inside the area enclosed by the airfoil. The chordwise range for the box placement is chosen as a design constant that could be set by the designer. After obtaining user experience with the code, it is determined to define the box between the 0.2% and 0.55% of the chord. To formulate the objective function one needs to calculate the enclosed area and the neutral axis of the airfoil. These definitions are shown in Equation 6.7 and Equation 6.8. In the equations,  $Y_u$  and  $Y_l$  are the upper and lower surface coordinates on

the y-axis,  $\bar{Y}$  is the neutral axis,  $box_{begin}$  and  $box_{end}$  are the chordwise locations of the box structure. Finally, the structural objective can be written as Equation 6.9.

$$A = \int_{box_{begin}}^{box_{end}} (Y_u - Y_l) dx \quad (6.7)$$

$$\bar{Y} = \frac{1}{A} \int_{box_{begin}}^{box_{end}} \frac{Y_u^2 - Y_l^2}{2} dx \quad (6.8)$$

$$J_{STRUCT} = -max \left( \int_{box_{begin}}^{box_{end}} \frac{(Y_u - \bar{Y})^3 - (Y_l - \bar{Y})^3}{3} dx \right) \quad (6.9)$$

### Airfoil shape parameterization

A very common way to optimize an airfoil is to represent the airfoil shape with curves. By this way the number of variables to optimize could be decreased so that the optimization would take less time. Several methods exist for the airfoil geometry representation such as polynomial definitions, smooth perturbations, Nurbs, Parsec and CST methods. The best method would be the one that needs the least amount of variables to cover the widest range of airfoil shapes. In this work, the CST (Class-Shape-Transformation) method is chosen due to its powerful formulation specified for the airfoil design and its proven performance in the previous airfoil design works. Constraints and bounds could easily be applied to the CST variables during optimization. One can create refined regions on the airfoil surface thanks to the flexibility of the CST definition. Moreover, the CST method offers explicit parameters for the leading edge curvature and the trailing edge thickness, so that direct constraints can be applied for these properties.

A detailed explanation of the CST method could be found in [39]. Here, it will be introduced briefly. The airfoil shape ( $\psi$ ) is defined by the product of class ( $C$ ) and shape ( $S$ ) functions and combined with the trailing edge thickness function ( $\zeta_{TE}$ ). The definition of the airfoil shape can be found in Equation 6.10. The class function defines a main legend for the airfoil geometry while the shape function creates perturbations on the class definition and increases the diversity in the design space.

$$\psi \left( \frac{x}{c} \right) = C \left( \frac{x}{c} \right) S \left( \frac{x}{c} \right) + \zeta_{TE} \frac{x}{c} \quad (6.10)$$

The class function is defined in Equation 6.11 where  $N_1$  and  $N_2$  are the exponents that determines the characteristics of the class function. Usually,  $N_1$  is taken as 0.5 and the  $N_2$  is taken as 1 in the airfoil optimization problems. During optimization these variables are taken as fixed values to decrease the computational cost. The variables of the shape function is powerful enough to create a wide design space.

$$C \left( \frac{x}{c}, N_1, N_2 \right) = \left( \frac{x}{c} \right)^{N_1} \left( 1 - \frac{x}{c} \right)^{N_2} \quad (6.11)$$

The shape function is given in Equation 6.12 where  $K_i$  are the function coefficients to be chosen and  $n$  is the order of the Bezier curve. In the previous design works, the order for each sides are chosen between 6 to 8. It can be said that the 6<sup>th</sup> order curves could show the specific airfoil shape for the optimization case but larger orders are needed to refine the optimum geometry.

$$S\left(\frac{x}{c}\right) = \sum_{i=0}^{i=n} K_i \binom{n}{i} \left(1 - \frac{x}{c}\right)^{n-i} \left(\frac{x}{c}\right)^i \quad (6.12)$$

Finally, trailing edge thickness function is defined as Equation 6.13 where  $\Delta_{TE}$  is the absolute trailing edge thickness.

$$\zeta_{TE} = \frac{\Delta_{TE}}{c} \quad (6.13)$$

### Bounds, constraints and penalty functions

The bounds and constraints are applied on the design vector which is a set of CST variables that define the airfoil surface. These are included for two main reasons: 1) to create a design space that is big enough to allow wide range of different airfoils and small enough to provide faster convergence, 2) to prevent the creation of geometries that would cause convergence problems in the flow solver. Bounds are responsible of directly limiting the CST variables while constraints could be applied on a combination of CST variables (e.g. trailing edge angle). An example of the design space is shown in Figure 6.3. To create this space, first, the initial airfoil library is used to create a lower and upper bounds. Then the extension factors are applied on these bounds to enlarge the design space. As seen, the aft part of the bottom surface is bounded in a way that aft cambered airfoils could be designed. Two constraints are crucial to the problem. The first one restricts the lower surface CST variables to be smaller than upper surface variables. The second constraint ensures a continuous leading edge by controlling the surface gradients. Both of them are applied to avoid convergence problems in the flow solver. One can also apply constraints as maximum thickness, trailing edge angle, trailing edge thickness and leading edge radius. In this work, those types of geometrical constraints are either not applied or modeled as penalty functions.

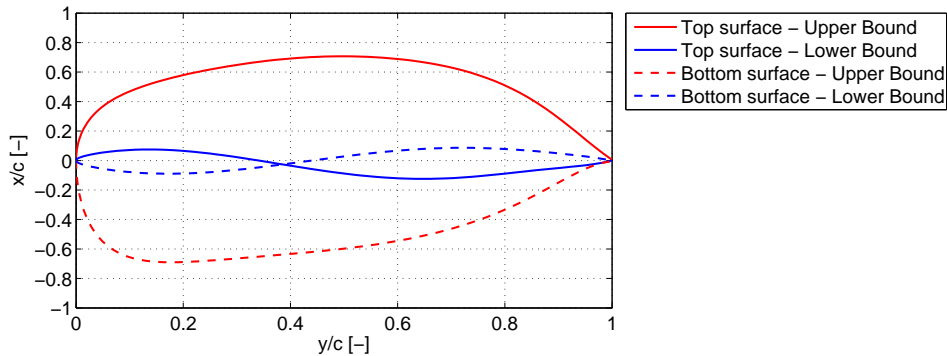


**Figure 6.3:** An example of the design space bounded by the upper and lower values for each surface.

The penalty functions can be seen as the constraints that are not directly applied on the design matrix but on the objective functions. The penalty criteria can be constructed with the geometrical and aerodynamic properties of an airfoil. If the target criteria is not met then the objective function is alleviated up to a degree defined by the user. In this work, six penalty functions are defined. These are applied to limit the maximum thickness of the airfoil ( $(\frac{t}{c})_{max}$ ), minimum relative leading edge radius ( $\frac{R_{LE}}{c}$ ), minimum trailing edge thickness ( $t_{TE}$ ), minimum trailing edge angle ( $\theta_{TE}$ ) and the boundary layer transition positions ( $X_{tr}$ ) at stall angle in clean conditions. All of the penalty criteria, threshold values and the penalty factors are given in Table 6.1. The maximum thickness has to be large in order to have high structural stiffness but the thickness must be limited so that the airfoil still ensures favorable aerodynamic properties. The leading edge penalty is the most strict penalty of all which makes the objective function equals to zero. A rigid criteria is applied to avoid sharp leading edge profiles. Because sharp leading edges would lead to sharp stall behavior. Moreover, this penalty helps to avoid very sharp noses that would cause numerical problems in the flow solver. The minimum trailing edge thickness and trailing edge angle penalties ensure a manufacturable trailing edge region. The last two penalties are applied in order to decrease the scoring of the airfoils with unfavorable roughness sensitivities. As seen, more strict conditions are set for the suction side of the airfoil since it experiences a relatively larger angle of attack range than the pressure side.

**Table 6.1:** Penalty functions used in the airfoil optimization.

Property ( $x$ )	Threshold ( $x_{crit}$ )	Penalty criteria	Penalty	Applies to
$(\frac{t}{c})_{max}$ [-]	0.36	$x > x_{crit}$	$ \frac{x_{crit}}{x} ^6$	$J_{struct}$
$\frac{R_{LE}}{c}$ [-]	0.015	$x < x_{crit}$	0	$J_{struct}$
$t_{TE}$ [-]	0.005	$x < x_{crit}$	$ \frac{x}{x_{crit}} ^2$	$J_{struct}$
$\theta_{TE}$ [°]	8	$x < x_{crit}$	$ \frac{x}{x_{crit}} ^2$	$J_{struct}$
$X_{tr,suc}$ @ stall [-]	0.08	$x > x_{crit}$	$ \frac{x_{crit}}{x} ^3$	$J_{aero}$
$X_{tr,pres}$ @ stall [-]	0.09	$x > x_{crit}$	$ \frac{x_{crit}}{x} ^3$	$J_{aero}$

## Optimization algorithm

Genetic algorithms can be treated as smart search machines. They are based on evolution theory of Charles Darwin where the next generation of a population is created with matching of successive individuals. To give chance to each individual, several complex relations are implemented as crossover ratio, mutation, elitism and migration. These algorithms are most likely to find the global optimum in the design space but require more time than gradient-based algorithms. For the discontinuous and nonlinear design spaces, genetic algorithms are recommended over gradient-based algorithms. Moreover, the direct airfoil designs are treated as highly nonlinear problems since the relation between airfoil surface and airfoil polar does not follow a simple characteristic. In this work a genetic algorithm is used for the airfoil optimization for its aforementioned advantages. The multi-objective optimization problem is solved by the NSGA-II algorithm in Matlab Optimization Toolbox. Moreover, the NSGA-II provides very diverse range of individuals

to the population and keep few of the non-optimal individuals in the next generation for gene diversity. For the airfoil design of a VAWT blade with a trailing edge a wide diversity search is required since there is no concrete ideas on how the optimized airfoils would look like.

### **Flow solver**

XFOIL is the mostly used code for the subsonic airfoil analysis and design in the aviation and wind turbine research. XFOIL has been validated by many experiments and it has been proved that XFOIL is a powerful tool when estimating the attached flow region. RFOIL is an improved version of XFOIL. In theory, the most significant modifications are to include the closure relation for the shear-lag coefficient and the Green's lag entrainment equation. These models lead to a better prediction of the shape factors so to more precise location for the separation. Modifications for the rotational flows are carried out by extending the Prandtl's integral boundary layer with Snel-Houwink model. Besides its good stall estimation, the comparisons with the experiments also showed that the performance prediction of thick airfoils could be more accurate with RFOIL [63]. Moreover, it is reported by several authors that RFOIL is more robust than the XFOIL. This feature would decrease the computational cost of the optimization process. For the application in this work, RFOIL is chosen as the airfoil analysis tool due to aforementioned advantages over XFOIL.

### **Simulations**

It is mentioned that the recent aerodynamic objective requires at least two polars for the different flap settings of the same airfoil. For the airfoil optimization, it is decided to simulate only two flap settings for each airfoil case due to time considerations. A 10% flap is defined and the flap deflections for the simulations are chosen as +10 and -10 degrees. A short flap and a relatively small deflection is chosen to ensure numerical stability in RFOIL simulations. The Reynolds number is chosen as 10 million. This is representative to the Reynolds number on the VAWT blade with a rated power between 10-20 MW. Each flap setting is analyzed between -20 and +20 degrees of angle of attack. Clean conditions are assumed so that the  $N_{crit}$  in RFOIL is set to 9 and a free transition is chosen. Important to note that the assessment for the roughness sensitivity is done by using the simulation with the positive flap configuration. The CST order of the suction and pressure side is chosen as 7, so 8 free variables should be designed for each side. For the optimizer, the maximum number of generations are taken as 45 and the population size of each generation is set to 200.

## **6.2 Performance analysis of the new airfoils**

This section presents 4 different airfoils that are chosen from the pareto front. For each airfoil three main figures are given: the geometry, airfoil polars and the  $C_P$  contours for the clean and dirty airfoil cases. The airfoil polars are obtained at  $Re = 10,000,000$  for 4 different case: 1) the clean undeflected airfoil, 2) dirty undeflected airfoil, 3) clean

10% flap with  $+10^\circ$  deflection and 4) clean 10% flap with  $-10^\circ$  deflection. The section finalizes with the performance comparison of the airfoils. The airfoil geometries, VAWT performances for a solidity of 0.1, flap sensitivities ( $C_{l\beta}$ ), transition locations ( $X_{tr}$ ) and normalized optimization scores are given. Moreover, one can find the tables for the aerodynamic and structural properties as well as the CST variables for the new airfoils. At last, the flap sequence optimization is carried out for two of the new airfoils and two NACA airfoils. In that study, the  $C_P$  is maximized for for the clean and dirty cases by using a 10% flap and  $\pm 20$  degree range of flap deflection.

The presented  $C_P$  contours document the performance of the airfoil with zero flap deflection. Each result is presented with the optimum fixed-pitch setting of the regarding airfoil. The VAWT performance is assessed with the PM simulations. Instead of simulating the performance directly, a solution library is used to approximate the performance of individual airfoils. This method has been used by Ferreira et.al [16, 17] and shown to be a reliable method. Briefly, it is based on the similarity of the induction field (so the perceived velocities) of the rotors with the same  $\frac{C_{l\alpha c}}{R}$ . This similarity is used to interpolate an induction field for the given viscous polar. After obtaining the velocity field, the viscous airfoil polar is used calculate the forces so that the  $C_P$  and  $C_T$  can be estimated. The clean airfoil conditions are simulated with  $N_{crit} = 9$  and free transition where the dirty conditions are simulated with  $N_{crit} = 1$  and forced transition at 10% of the chord for both of the surfaces. Figure 6.4 shows an example of the pareto front, here the  $x$  and  $y$  axes show the scores for the aerodynamic and structural objectives.

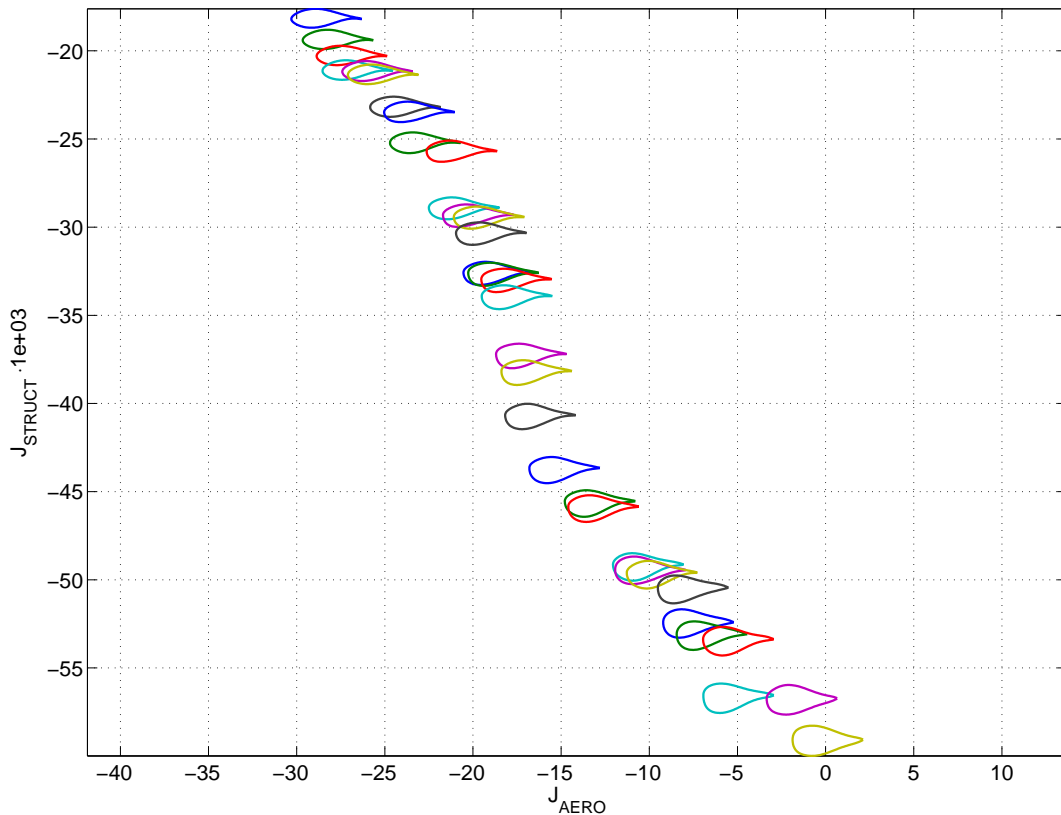
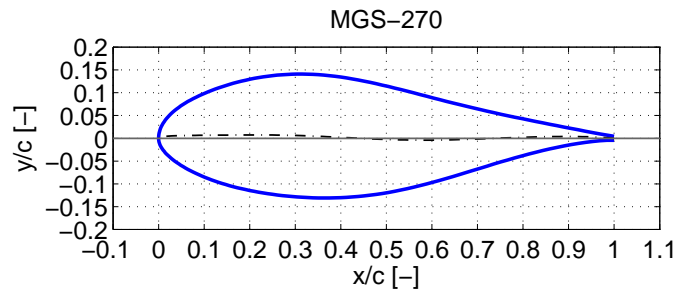


Figure 6.4: An example of the pareto front.

From top to the bottom the thickness and camber distributions change significantly. The airfoil on the top of pareto front represents the aerodynamically most efficient airfoil and the bottom airfoil is the best in structural means. The pareto front shows airfoils span from 27% to 35% maximum thickness. The airfoils that is to be analyzed in detail are chosen by the help of this imaging. The new airfoils are named as *MGS-XXX*. *MGS* is an acronym of personal names and the *XXX* stands for the first three digits of the maximum relative thickness of the airfoil. So an airfoil with a 32.56% thickness would be named as MGS-325.

### 6.2.1 MGS-270

The MGS-270 is a 27.09% thick airfoil with a 0.76% maximum camber. Figure 6.5 shows the airfoil geometry. Its maximum thickness is at 33% of the chord and the maximum camber is located at 21%. The suction side has slightly higher thickness than the pressure side, moreover the airfoil has a mild positive aft camber. Note that the camber-line is shown in Figure 6.5 as the dashed black line.



**Figure 6.5:** Geometry of the MGS-270.

The airfoil polar is shown in Figure 6.6. The lift polar of the dirty airfoil is very close to the  $C_l$  trend in the clean polar. The low drag bucket can still be maintained when the airfoil is dirty. The stall is experienced at 14.5 degrees and  $C_l$  is kept very close to the  $C_{l,stall}$  in the post-stall region. This might be a handy feature for the self-starting capability of the VAWT. It is observed that, in the whole simulation range the flap can be used to effectively. Moreover for the small ranges of angle of attack the  $C_d$  values of the deflected and undeflected polars are very similar. For such regions the flap deflection comes with no aerodynamic losses. Here, we see the importance of the wide-drag bucket from the flap's point of view. The VAWT performance is given in Figure 6.7. The maximum  $C_P$  is 0.519 in the clean case and 0.482 in the dirty case. There is a 7.13% decrease in the maximum performance due to the surface roughness. The difference between the dirty and clean performances increases if the  $\sigma$  or  $\lambda$  are increased. Because the increased inductions and velocities cause more loss due to the drag. The figures regarding the flap sensitivity and the overall optimization score will be presented in the performance comparison section.

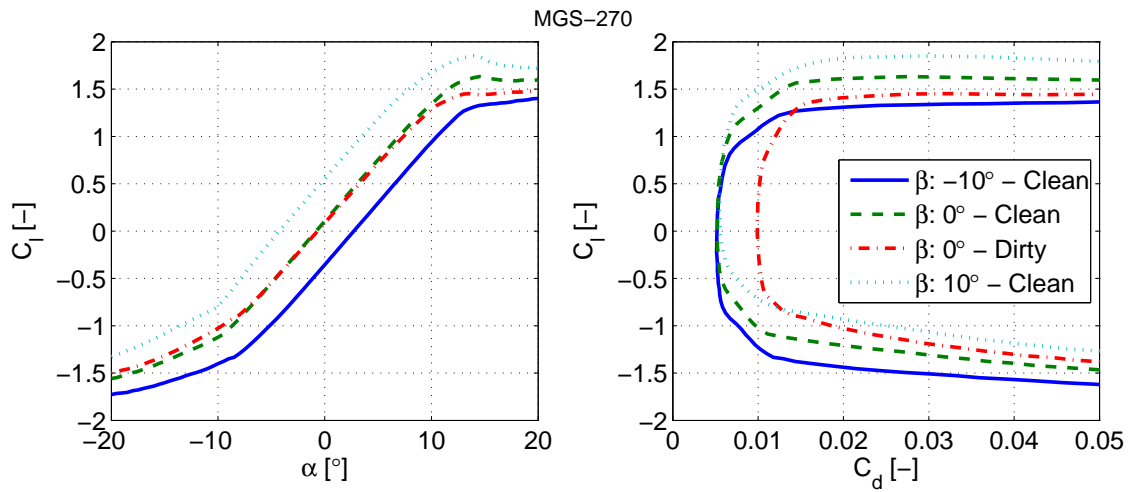


Figure 6.6: Aerodynamic polars of the MGS-270.

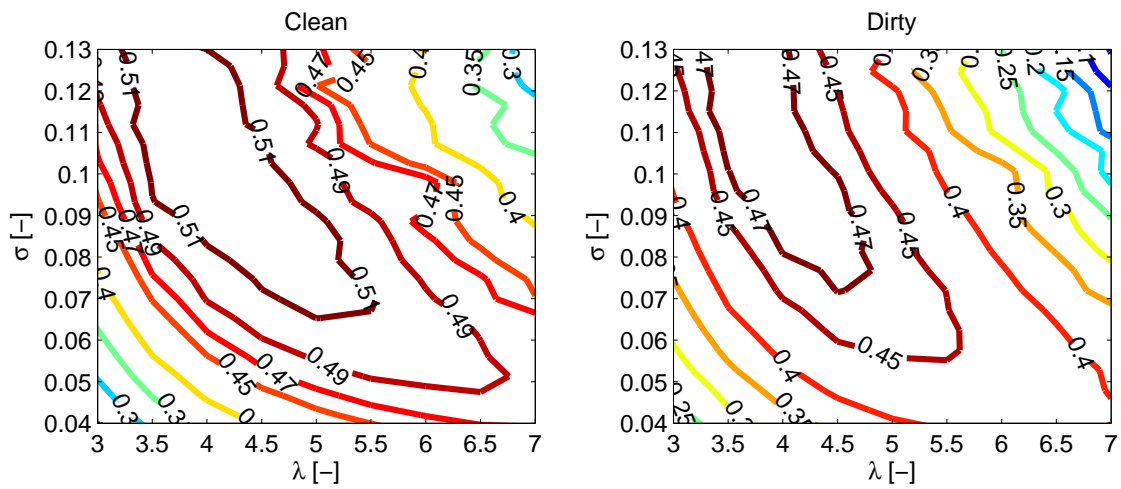


Figure 6.7: VAWT performance of the undeflected MGS-270 for the clean and dirty conditions.

### 6.2.2 MGS-279

The MGS-279 is a 27.99% thick airfoil with a 0.90% maximum camber. The airfoil geometry is shown in Figure 6.8. Its maximum thickness is at 31% and the maximum camber is located at 30% of the chord. Although the front part has a slight positive camber, after 50% of the chord the geometry is quite symmetric. This type of camber line create an equal flap sensitivity for the positive and negative deflections.

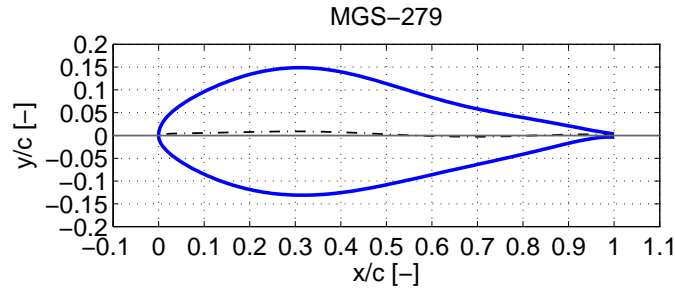


Figure 6.8: Geometry of the MGS-279.

The airfoil polar is shown in Figure 6.9. It can be said that MGS-279 has a favorable dirty performance. MGS-279 has a wide drag bucket, especially at the clean conditions. The  $C_d$  is very low in an angle of attack range around 18 degrees. The stall angle is 12 degrees. Although a sharp decrease in the  $C_l$  is experienced at the stall angle, this trend does not continue in the post stall region. It is believed that this sharp and temporary drop in the  $C_l$  is occurred because the transition location moves very fast after passing 0.35% of the chord around  $\alpha = 10$  degrees. This is a consequence of the thickness distribution which is affected by the structural design objective. Note that according to the structural objective the flap-wise bending stiffness should increased between the 20% and 55% of the chord.

Figure 6.10 documents the VAWT performance in the clean and dirty conditions. The maximum  $C_P$  is 0.528 in the clean case where the dirty case has a 7.77% lower value for the  $C_{P,max}$  as 0.487. The  $C_P$  contours near solidity of 0.11 disobeys the continuity in the whole image. This is physically not possible therefore it is referred as a numerical error. In fact, this behavior is also apparent in the same  $\sigma$  range of the further airfoils in this section.

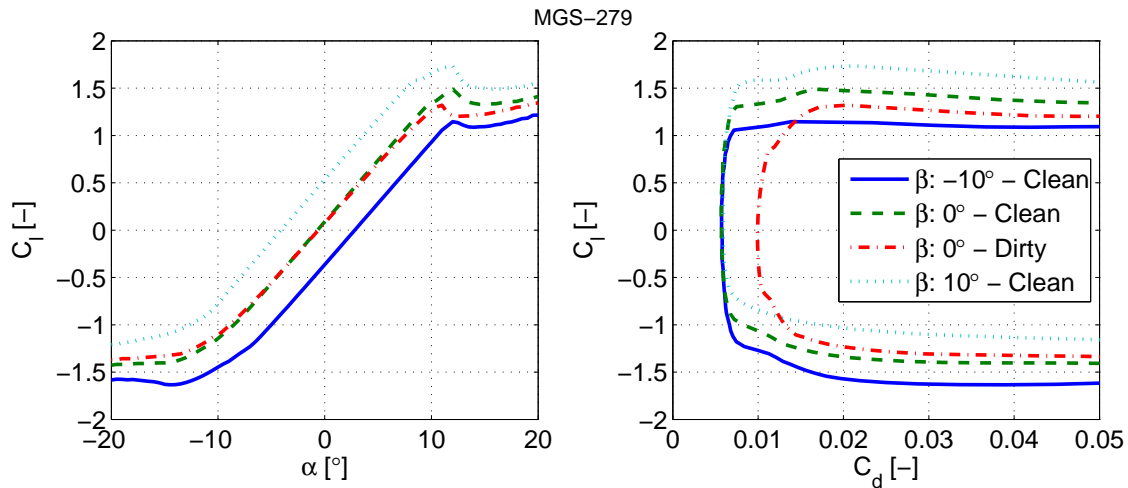
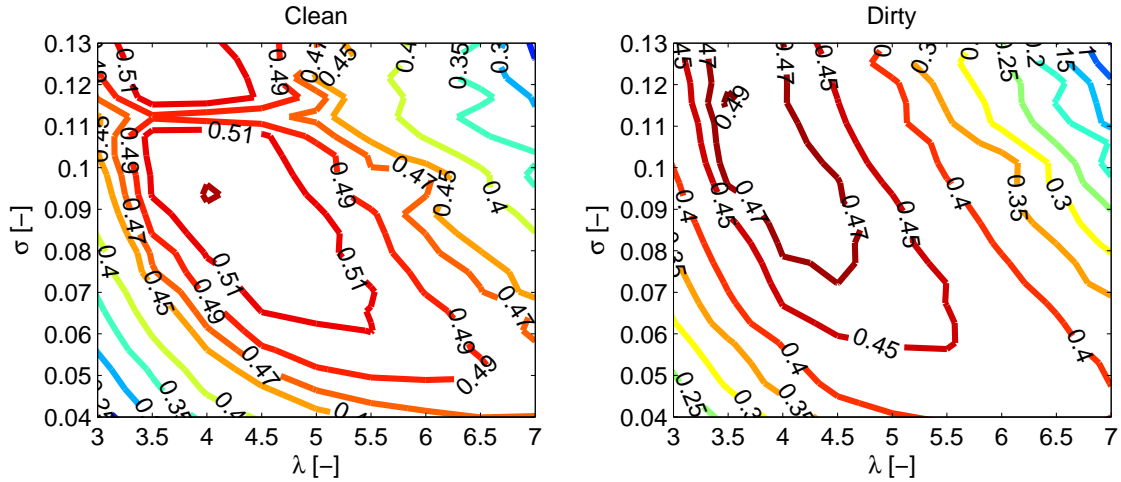


Figure 6.9: Aerodynamic polars of the MGS-279.



*Figure 6.10: VAWT performance of the undeflected MGS-279 for the clean and dirty conditions.*

### 6.2.3 MGS-292

The MGS-292 is a 29.28% thick airfoil with a -0.65% maximum camber. It belongs to the same airfoil family with the MGS-270 and MGS-279. This airfoil family has a slight positive camber in the front part ( $\frac{x}{c} \sim 0 - 0.5$ ), a negative camber in the mid-aft region ( $\frac{x}{c} \sim 0.5 - 0.8$ ) and ends with a small positive camber in the aft region ( $\frac{x}{c} \sim 0.8 - 1$ ). The geometry of MGS-292 can be seen in Figure 6.11. Its maximum thickness is at 33% of the chord and the maximum camber is located at 62%.

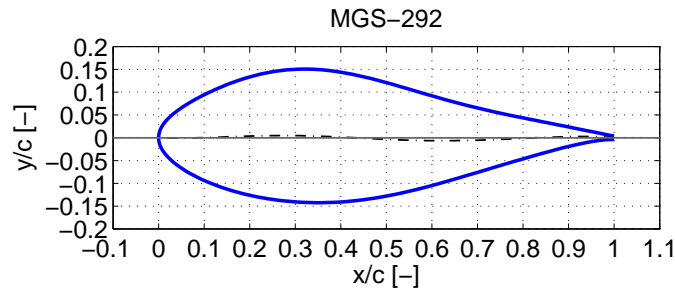


*Figure 6.11: Geometry of the MGS-292.*

Figure 6.12 shows the airfoil polars. MGS-292 is more sensitive to the roughness than the MGS-270 and MGS-279. The lift-curve slope of the rough polar is lower than the clean polar, also stall in the dirty conditions happens earlier. One can also see that the drag bucket loses its entity in the dirty conditions. Although the MGS-270, MGS-279 and MGS-292 are similar in the means of thickness distribution, the higher maximum thickness of MGS-292 creates larger peaks in the pressure distribution which pronounces the roughness effects. In fact the thickness distribution of the suction side has a more even distribution than MGS-279, but the roughness effects are inevitable for this much of thickness. It should be kept in mind that, the roughness performance is still favorable

which is very much related with the high Reynolds number operation. On the other hand, a slight increase in the thickness helps to cancel out the sharp lift drop of the MGS-279. The MGS-292 stall very softly at 12 degrees.

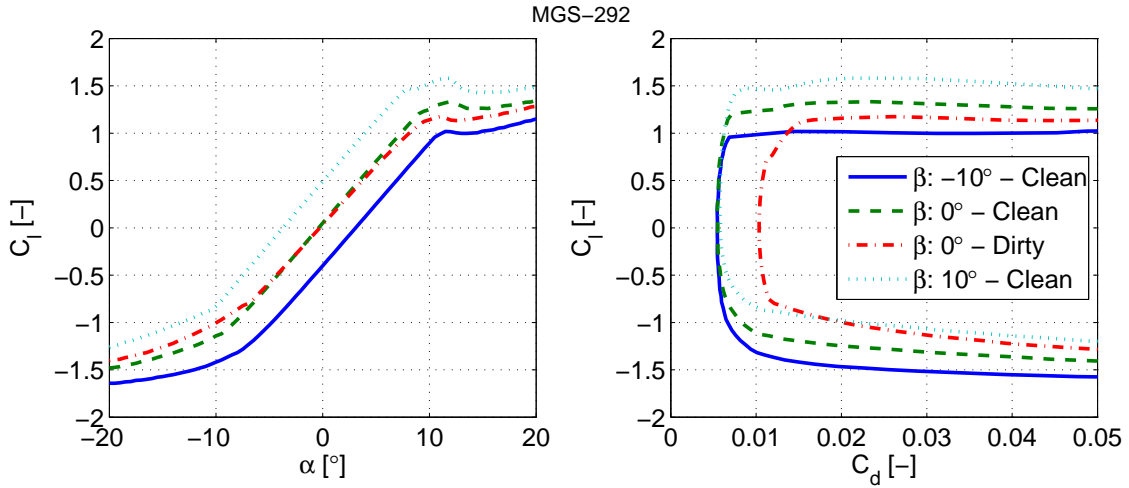


Figure 6.12: Aerodynamic polars of the MGS-292.

In Figure 6.13 one can see the VAWT performance of the undeflected MGS-292. It offer a maximum  $C_P$  of 0.520 in the clean condition and 0.468 in the rough condition. The maximum  $C_P$  decrease due to roughness is 10% which is a larger drop than MGS-270 and MGS-279 have. The main reason behind the larger drop is simply the worsened dirty performance of the airfoil.

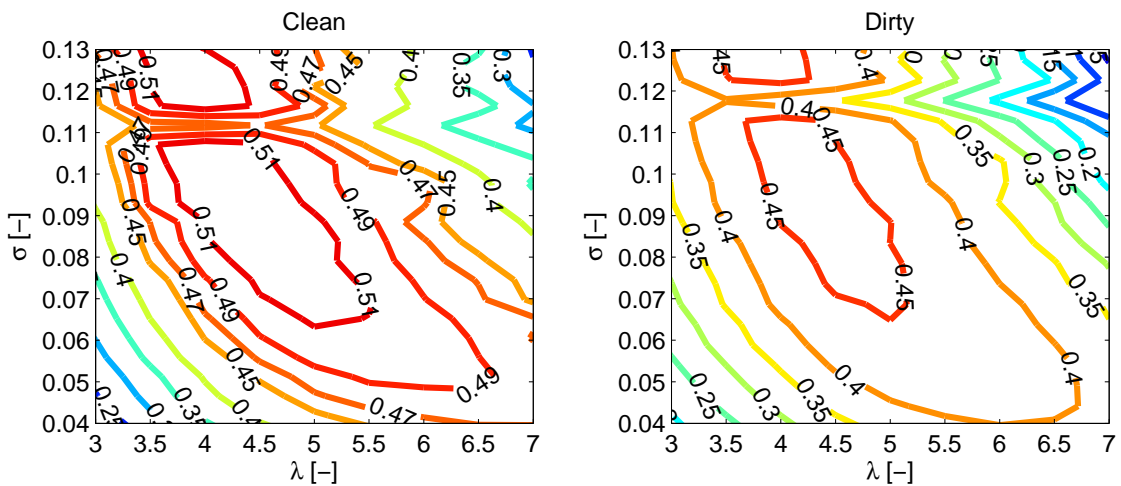


Figure 6.13: VAWT performance of the undeflected MGS-292 for the clean and dirty conditions.

## 6.2.4 MGS-313

The MGS-313 is a 31.31% thick airfoil with a -1.48% maximum camber. It is the thickest airfoil introduced in this chapter and its geometry is given in Figure 6.14. Its maximum thickness is at 32% of the chord and the maximum camber is located at 57% of the chord. MGS-313 has the largest negative camber among the given MGS airfoils. The airfoil polar is given in Figure 6.15. As a consequence of negative camber the  $C_{l0}$  has a negative sign. Nevertheless this airfoil does not show the lowest  $C_{l,max}$  because it has the highest lift-curve slope among the previously introduced airfoils. As expected, MGS-313 is the airfoil with the highest sensitivity to the surface roughness. Although the lift-curve slope in the linear region is not affected significantly we see a very early stall in both of the sides, especially in the pressure side. The clean airfoil is able to sustain a low drag range for 16 degree range of angle of attack. On the other hand, in the dirty conditions the  $C_{d0}$  of the clean condition increases around 47% and the low drag region decreases to an angle of attack range around 12.5 degrees.

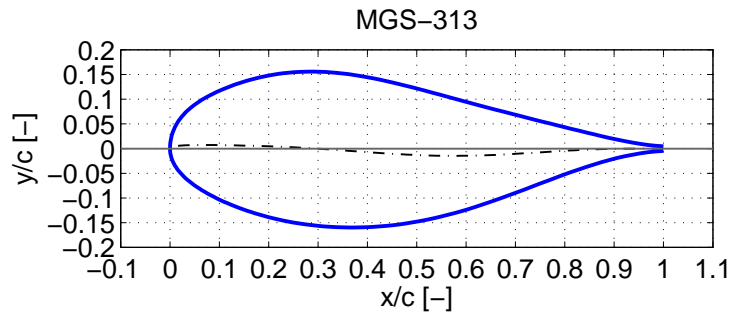


Figure 6.14: Geometry of the MGS-313.

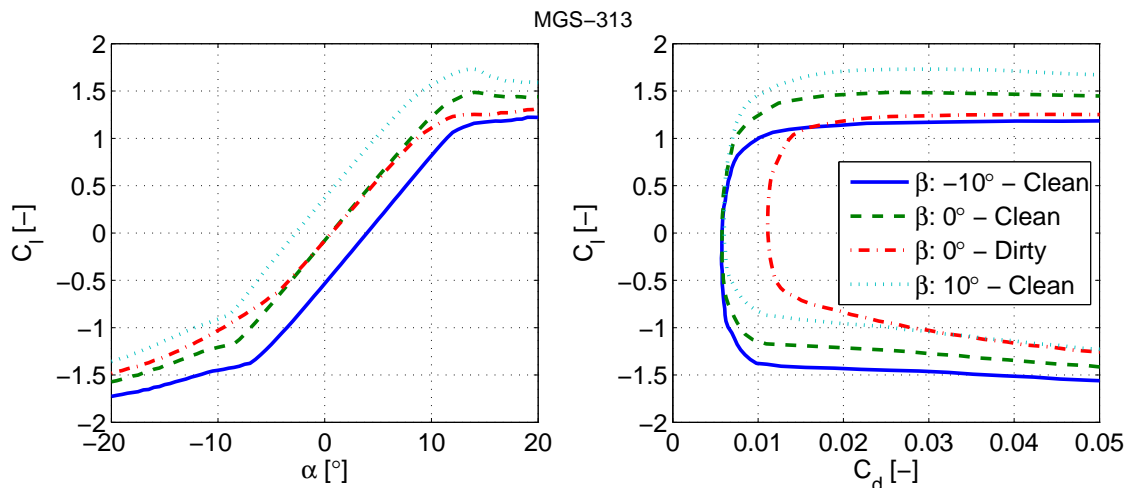


Figure 6.15: Aerodynamic polars of the MGS-313.

The VAWT performance of MGS-313 in the clean and dirty conditions are given in Figure 6.16. In the clean conditions the maximum  $C_P$  is 0.522 and it drops to 0.448 at the

dirty conditions, a 14.18% decrease. As seen from the contours, the  $C_P - \lambda$  curve is more peaky in the clean case. The contour is more even in the dirty conditions because the power loss at the small  $\lambda$  is now increased since the airfoil operates outside of the low-drag region. In other words, the lack of a wide drag bucket in the rough conditions is causing flatter  $C_P - \lambda$  curves.

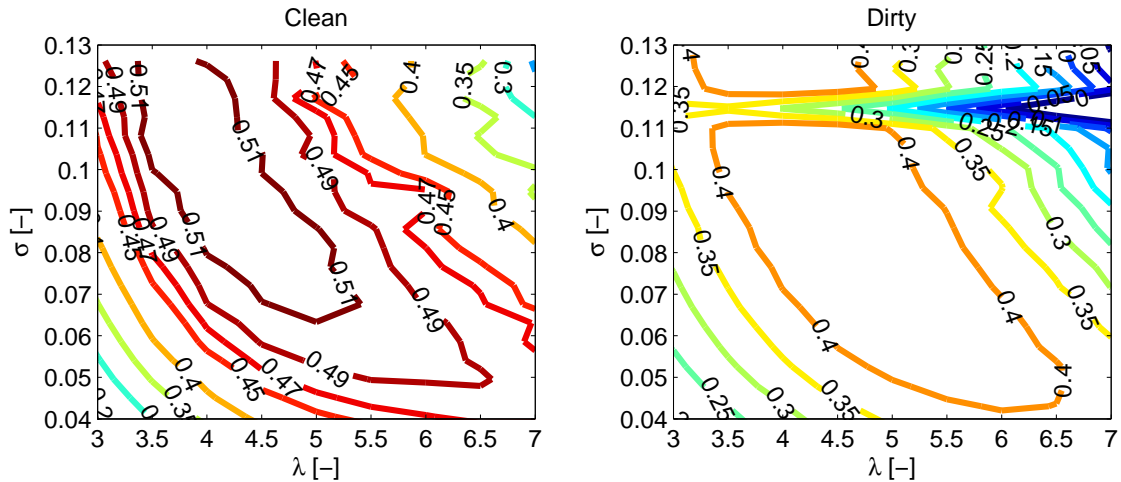


Figure 6.16: VAWT performance of the undeflected MGS-313 for the clean and dirty conditions.

### 6.2.5 Performance and characteristic comparisons

Performance comparison of the MGS airfoils are given in this section. NACA 0018 and NACA 0030 are also used to increase the insight in the properties of the MGS airfoils. NACA 0018 results are included since it has been widely used in the VAWT research and also in the previous chapters of this thesis, so it is a perfect reference. NACA 0030 is introduced to show an airfoil in the same thickness range as the MGS airfoils but not designed specifically for the flap controlled VAWT blade.

The new airfoil geometries are given on the same plot in Figure 6.17. The table regarding to airfoils' structural properties are documented in Table 6.2. In fact, the airfoils does not differ from each other in an overall look. All of the airfoils have maximum thickness position around 31% to 33% of the chord. None of the airfoils have a maximum camber bigger than 1%. In fact, the airfoils thicker than 29% has a negative camber. As the airfoil gets thicker, the thickness of the pressure surface enlarges with a higher rate than the suction surface does. An apparent aft camber is not preferred by the optimizer. It is believed that this choice is made to have an effective flap both for the negative and positive angle of attacks. Deflections towards both directions will create more or less the same pressure effects on the aft region. Thus the  $C_l$  and  $C_d$  difference created by the flap will be independent of direction, but magnitude. This property can be observed in the airfoil polars given earlier.

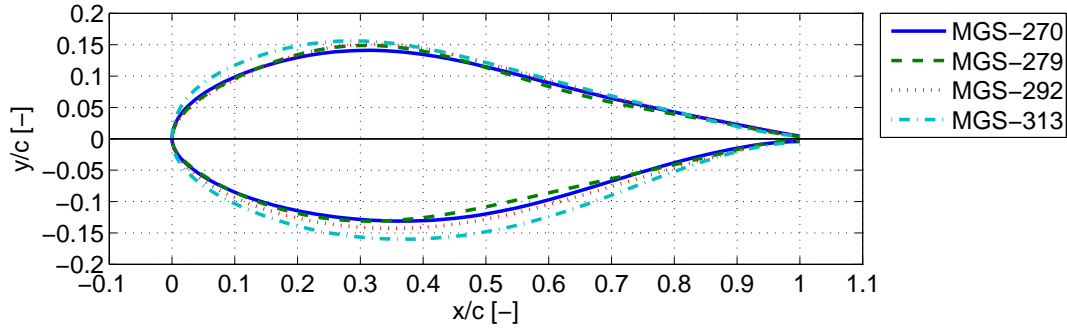


Figure 6.17: Comparison of the MGS airfoil geometries.

For the structural properties, we see that all the airfoils are obeying the trailing edge thickness constraint. There are several outliers for the trailing edge angle constraint but they are not penalized heavily. The flapwise stiffness is in correlation with the thickness distributions between 20% and 55% of the chord. On the other hand, the edgewise stiffness values are in the similar range for all of the airfoils.

Table 6.2: Structural properties of the airfoils.

Airfoil	$(\frac{t}{c})_{max}$ [%]	$(\frac{h}{c})_{max}$ [%]	$t_{TE}$ [-]	$\theta_{TE}$ [°]	$\frac{R_{LE}}{c}$ [%]	$\frac{I_{xx} \cdot 1e2}{t \cdot c^3}$ [-]	$\frac{I_{yy} \cdot 1e2}{t \cdot c^3}$ [-]
MGS-270	27.09	0.76	0.86	10.47	4.29	1.82	20.09
MGS-279	27.99	0.90	0.69	7.44	3.66	1.80	20.21
MGS-292	29.28	-0.65	0.72	13.13	4.25	2.08	20.10
MGS-313	31.31	-1.48	0.94	7.37	7.65	2.51	20.75

Figure 6.18 gives the flap sensitivity of the airfoils in an angle of attack range from -15 to 15 degrees. The  $C_{l\beta}$  is computed by taking the average lift jump between the -10 and +10 degrees of flap deflection polars.

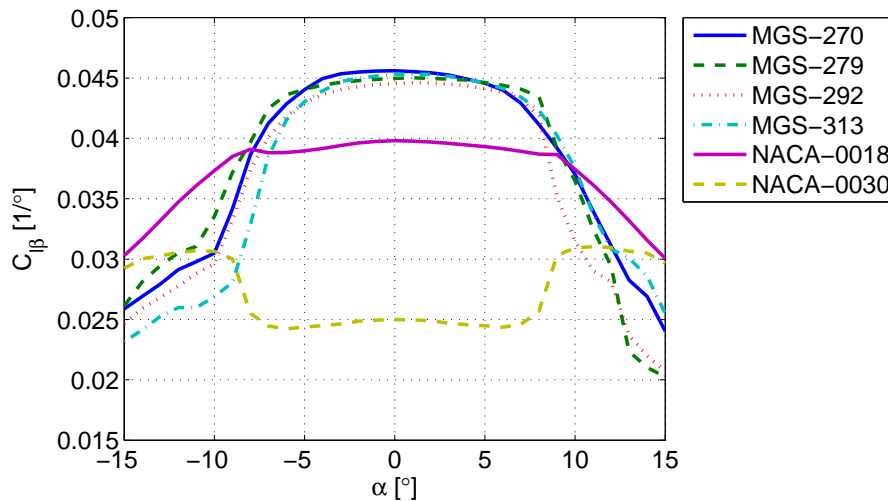


Figure 6.18: Comparison of the flap sensitivities.

The regarding performance of the NACA 0018 and NACA 0030 are also given for the ease of comparison. We see that the new airfoils are in a very similar range of flap sensitivity. As demanded by the objective functions the flap sensitivity of the new airfoils are only high for an angle of attack range around 15 degrees. In the design range of the new airfoils, the NACA 0018 has approximately 11% less flap authority and NACA 0030 has around 44% less flap authority. It is showed that the intention of creating airfoils with superior flap performance is reached. In Table 6.3 one can find the important aerodynamic properties of the airfoils. The  $C_{l\alpha}$  and maximum lift-to-drag ratio of the MGS airfoils are significantly larger than the NACA 0018 and 0030. The zero lift drag ( $C_{d0}$ ) of the MGS airfoils are in the same level as NACA 0018 and roughly 22% smaller than the value for NACA 0030.

**Table 6.3:** Aerodynamic properties of the airfoils.

Airfoil	$C_{l, stall}$ [-]	$\alpha_{stall}$ [-]	$C_{d0}$ [-]	$(\frac{L}{D})_{max}$ [-]	$C_{l, design}$ [-]	$C_{l\alpha}$ [ $\frac{1}{rad.}$ ]
MGS-270	1.632	14.5	0.00522	154.18	1.07	7.468
MGS-279	1.488	12	0.00573	180.52	1.25	7.447
MGS-292	1.332	12	0.0055	171.30	1.15	7.482
MGS-300	1.574	20	0.00688	131.78	0.90	7.389
MGS-313	1.486	14	0.00577	136.98	1.05	7.730
NACA 0018	1.820	20	0.00566	126.90	1.22	6.566
NACA 0030	1.557	20	0.00711	89.86	0.97	5.655

The transition locations at the suction and pressure sides of the airfoils are given in Figure 6.19.

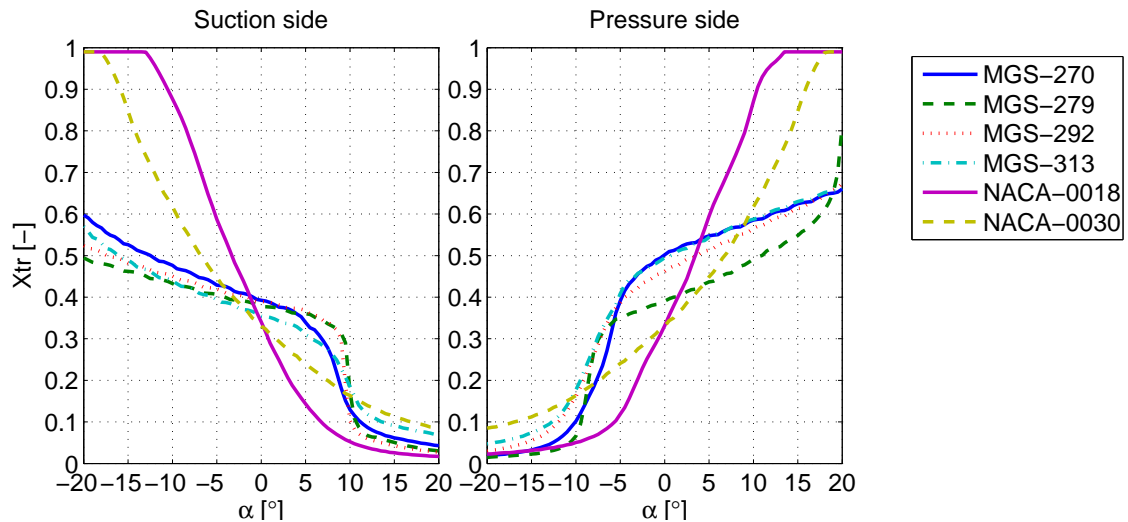


**Figure 6.19:** Boundary layer transition location of the airfoils in the clean conditions.

Even at the most negative angle of attack the suction sides of the MGS airfoils have transition around 0.55% of the chord. A similar relation can be observed for the pressure surfaces. During the optimization, the polar with positive flap deflection was used to for

the roughness insensitivity condition. Here we see that the condition worked well since the airfoils are having transition positions very close to 0.1% of the chord near their stall angles. For all the MGS airfoils the transition movement close to the stall region is very fast. This behavior is one of the major contributors to the optimized MGS airfoil shape.

The comparison of the VAWT performance with the undeflected airfoils at the clean and dirty conditions are shown in Figure 6.20. In the clean conditions, even without the flap operation, all of the MGS airfoils obtain higher  $C_{P,max}$  than NACA 0018. Overall performances along the  $\lambda$  range is also very promising. In the dirty conditions NACA 0018 outperforms all of the MGS airfoils. This is an inevitable property of the thick airfoils; still the dirty performances of MGS-270 and MGS-279 could be acceptable. The dirty airfoil performance mainly affects the  $C_{P,max}$  and the low  $\lambda$  performance. The root cause for these effects is the increased  $C_{d0}$  and narrowed drag bucket in the dirty conditions. NACA 0030 shows a very good dirty performance when compared with the MGS airfoils. On the other hand the clean performance of NACA 0030 is very poor with respect to the MGS airfoils.

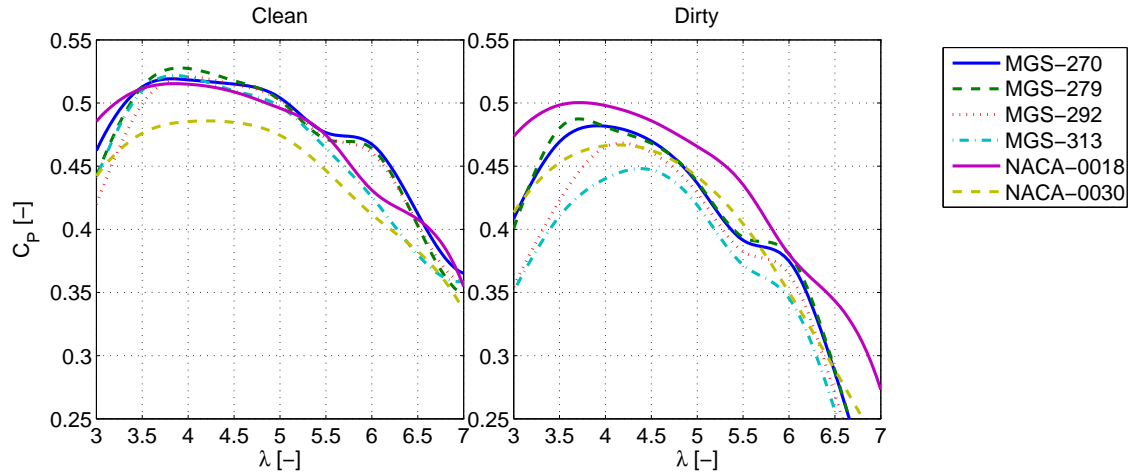


**Figure 6.20:** Comparison of the VAWT performances at clean and dirty conditions.

A demonstration of the active flap control is made on the MGS-279, MGS-292, NACA 0018 and NACA 0030 airfoils. As mentioned earlier, the Mod-Lin ACM code is used for the performance assessment. A 10% flap with maximum of  $\pm 20$  degree deflection is used both for the clean and the dirty airfoil polars. Figure 6.21 shows the performance of the undeflected airfoils estimated by the Mod-Lin ACM. This plot is given for two reasons: 1) to compare the viscous case with the PM estimations in Figure 6.20 and 2) to serve as a *reference* result for the flap-controlled cases in Figure 6.22. Although the absolute values vary slightly between two models, the trends and relations between airfoils are the same. Both for the ACM and PM, the MGS airfoils have lower  $C_P$  than the NACA 0018 when  $\lambda = 3$ . Because MGS airfoils are not designed for the angle of attack range in that condition. For a larger  $\lambda$  the MGS airfoils perform better than NACA 0018 in the clean case. The MGS-279 has the highest peak performance when the airfoil surface is clean. In the dirty conditions MGS airfoil performs in a level between the NACA 0018 and NACA 0030 performance. This is both valid for the ACM and PM estimations.

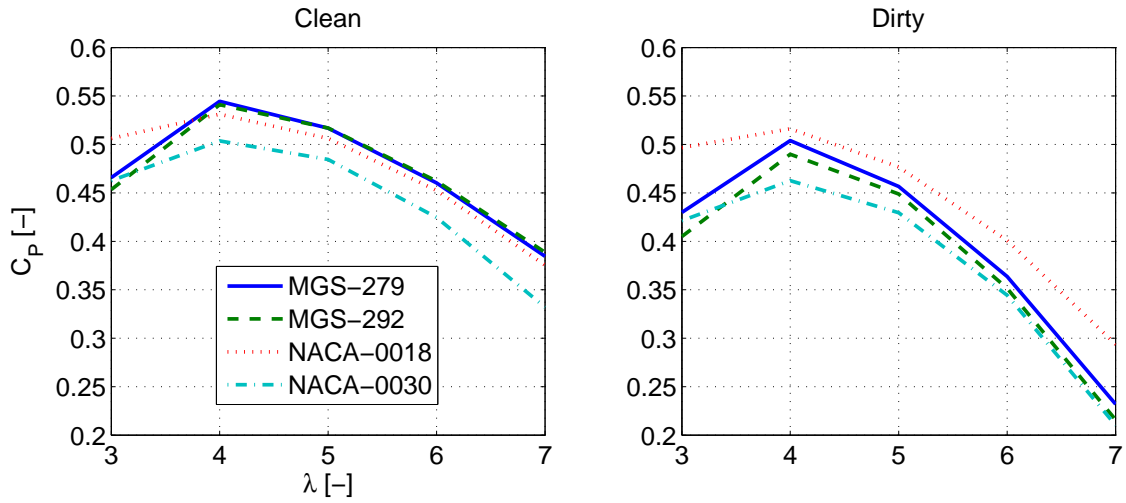


**Figure 6.21:** Performance of the undeflected airfoils in the ACM both for the clean and dirty airfoils - The reference case.

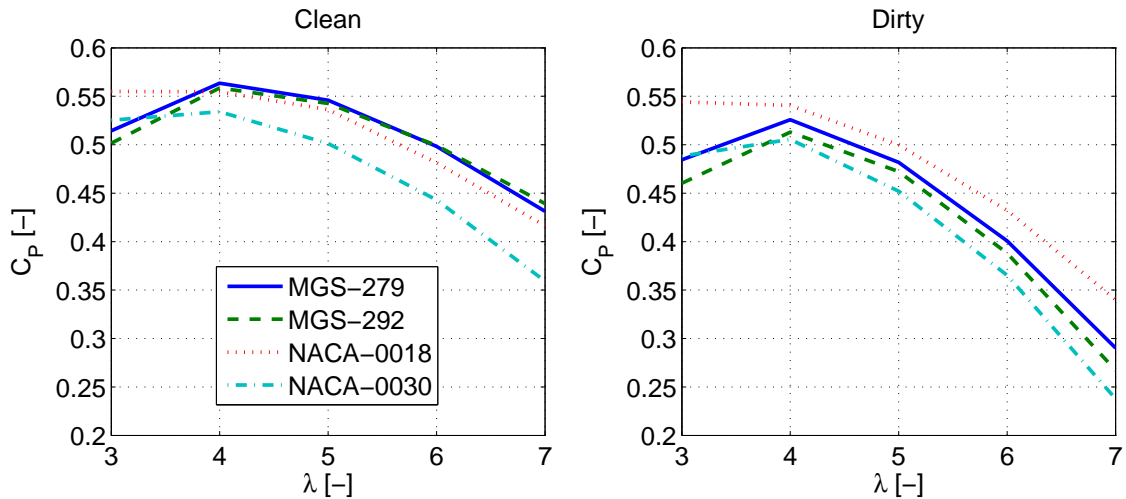


**Figure 6.22:** Performance of the clean and dirty airfoils in the presence of active flap control (10% flap with  $\pm 20^\circ$  deflection).

The  $C_P$  values of the flap-controlled airfoils have significant improvements. The relative gains for the clean and dirty airfoils are presented in Table 6.4. All of the airfoils exhibit the lowest gains either at  $\lambda$  of 4 or 5. This is due to the limited load-design space by the high reference  $C_P$  values. This relation was mentioned in the chapter 4. Similarly, the  $C_P$  gains increase as the reference values get lower which also explains why the dirty airfoils experience larger gains than the clean airfoils. Therefore it is partly shown that the flap control is more effective for the VAWTs with poor power efficiencies. We see that even if the reference  $C_P$  values are higher than the NACA airfoils, the MGS airfoils acquire similar or larger gains with respect to the NACA airfoils. This relation is based on the larger flap effectivity of the MGS airfoils.

**Table 6.4:** Improvements in the  $C_P$  in the clean and dirty conditions of airfoils with 10% flap.

Clean					
$\lambda$	3	4	5	6	7
MGS-279	10.41	3.52	5.62	8.28	12.15
MGS-292	10.59	3.26	4.97	8.02	12.97
NACA-0018	9.65	4.40	5.95	6.38	10.87
NACA-0030	13.55	6.04	3.48	4.34	8.19
Dirty					
$\lambda$	3	4	5	6	7
MGS-279	12.73	4.32	5.52	10.18	25.07
MGS-292	13.67	4.71	5.22	10.41	23.84
NACA-0018	9.57	4.73	4.85	7.83	15.80
NACA-0030	15.91	9.27	5.24	6.04	13.13

Figure 6.23 compares the normalized aerodynamic and structural scores of twelve MGS airfoils and two NACA airfoils. The normalization is done by the maximum scores inside the given group of airfoils. Note that the optimization penalties are also included in the score calculations. Eight of the MGS airfoils have not been mentioned in text before but one can find their detailed information in the Appendix A. The MGS airfoils are ordered with an increasing thickness in the figure. Among the airfoils that are presented in this chapter the MGS-279 has a better aerodynamic score than others while MGS-313 has the best structural score.

An overall look to the trend of the bar plots shows that the aerodynamically optimum airfoil is in the 27% - 28% thickness range while the structurally optimum airfoil should be as thick as possible. Thinner airfoils than 26.9% does not exist in the pareto front because the  $C_{l\alpha}$  values are lower for the thin airfoils. Thus, the thin airfoils have low aerodynamic and structural score. The thick airfoils suffer from the surface roughness effects in the means of aerodynamic goodness. The aerodynamic score of airfoils thicker than 31 - 32% decrease dramatically. The airfoils with the most balanced scoring are in the range of 30% - 32% thickness. As mentioned earlier, the MGS airfoils thinner than 29% have a positive camber smaller than 1% of the chord, while the thick airfoils exhibit negative camber values. The thickest airfoil MGS-349 has -2.7% maximum camber. As a final conclusion, it is observed that the flap-wise bending stiffness is not proportional to the maximum thickness. An airfoil like MGS-269 could have higher flapwise stiffness than a thicker airfoil such as MGS-279.

Finally, the CST variables of the suction and the pressure surfaces of the MGS airfoils are given in Table 6.5. These coefficients represent an 8<sup>th</sup> order surface. The chord-wise positions for the CST coefficients are:  $\frac{x}{c} = [0.0, 0.1429, 0.2857, 0.4286, 0.5714, 0.7143, 0.8571, 1.0]$ . The same chord-wise points are also valid for the CST variables given in the Appendix A.

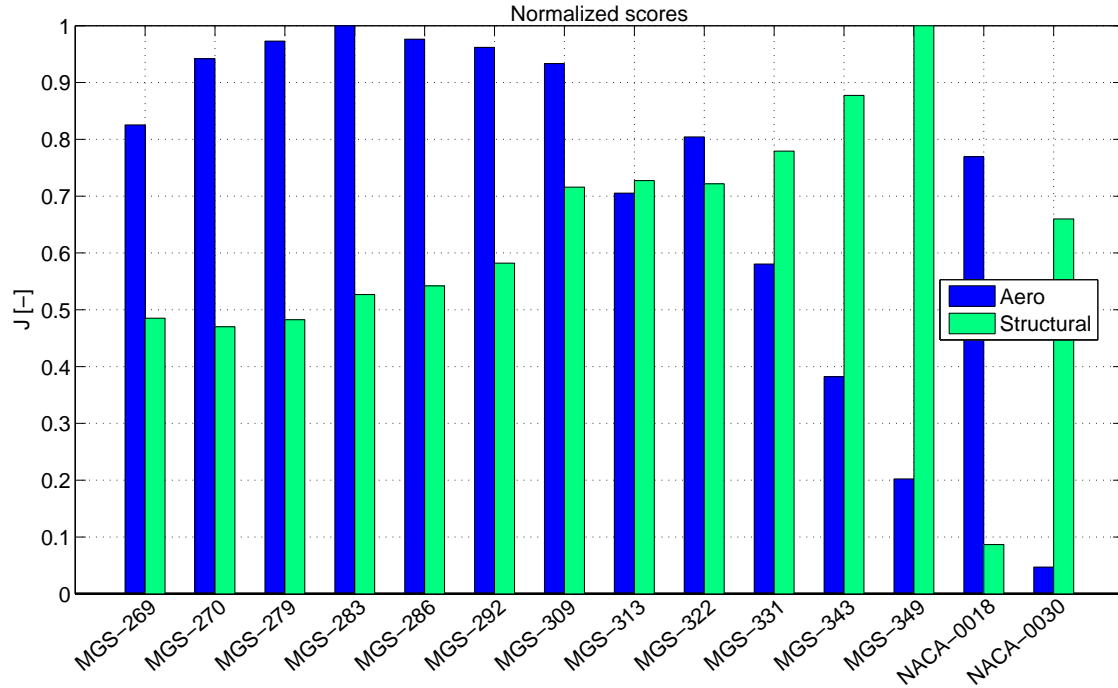


Figure 6.23: Normalized optimization scores of all the airfoils.

Table 6.5: CST variables for the MGS airfoils (270, 279, 292, 313).

Airfoil	MGS-270		MGS-279		MGS-292		MGS-313	
Side	SUC	PRES	SUC	PRES	SUC	PRES	SUC	PRES
$B_1$	0.33361	-0.25601	0.29960	-0.24347	0.29048	-0.29182	0.44380	-0.34429
$B_2$	0.33687	-0.34175	0.34156	-0.33672	0.32802	-0.35883	0.32967	-0.34852
$B_3$	0.39102	-0.31260	0.43336	-0.37814	0.46577	-0.36305	0.53334	-0.46049
$B_4$	0.44237	-0.33081	0.52199	-0.36940	0.47157	-0.38593	0.35606	-0.36969
$B_5$	0.23119	-0.48363	0.16278	-0.27789	0.24350	-0.44060	0.28880	-0.51191
$B_6$	0.21522	-0.15132	0.12460	-0.12637	0.18087	-0.18479	0.22026	-0.36749
$B_7$	0.22716	-0.23601	0.29484	-0.39531	0.25655	-0.34636	0.29023	-0.23671
$B_8$	0.16868	0.00522	0.12387	0.04734	0.19304	-0.00634	0.03948	-0.05400
$\zeta TE$	0.00428	0.00428	0.00347	0.00347	0.00358	0.00358	0.00472	0.00472

### 6.3 Conclusions of the chapter

- The new design methodology is proved that it can generate thick VAWT airfoils with a superior flapped and non-flapped aerodynamic performance. It is implicitly responsible of the weighting between the lift-curve slope and the flap sensitivity. Moreover, the airfoils with noticeable insensitivity to roughness are created.
- The importance of a wide drag bucket to the design is two-fold for the flapped airfoil. If the drag bucket is very narrow then the power loss due to flap deflection

will be pronounced. This behavior can play an important role in the feasibility of the trailing edge flaps on VAWT blades.

- The new airfoils spans between 27% to 35% thickness-to-chord ratios. The airfoils thinner than 29% have a positive maximum camber and the thicker airfoils have a negative camber. Instead of the popular aft-camber concept, the MGS airfoils have a fairly symmetrical geometry in the aft region. This is to provide high flap effectivity both in the positive and negative angle of attacks.
- The MGS airfoils around 28% thickness offer the best aerodynamic performance while the airfoils around 31% thickness have the best balance between the aerodynamic and structural goodness.
- The roughness insensitivity is hard to maintain for the airfoils thicker than 30%, therefore these airfoils come with an aerodynamic drawback. But, these airfoils possess high flapwise bending stiffness which increase their score as a VAWT airfoil. In an overall score analysis, it is seen that the airfoils around 30% thickness could be attractive candidates for the VAWT airfoils.
- The very large scale VAWT blades (10-20 MW) have an aerodynamic advantage due to high operating Reynolds numbers. Thanks to that, the roughness effects are alleviated up to a degree for the thick airfoils. Therefore, high Reynolds number regime supports the use of thick airfoils for the VAWT.
- In the presence of the active flap control dirty airfoil performance is increased more than the clean airfoil performance. This is a very promising result and a relief for the dirty operation. It also supports the idea that the flaps could be more effective for the VAWTs with poor power efficiencies.



## Final Remarks

### 7.1 Conclusion

This work documented a new research on the Vertical Axis Wind Turbines that are equipped with active trailing edge flaps and new airfoils. It has been shown that a flap can enhance multiple features of VAWTs by power maximization, power control and load control. Novel airfoil design is a key to increase the aerodynamic and structural performance of VAWT blades. Many supportive work to the main research aim has also been carried out during the project time span. These works include the exploration of the performance of an actuator cylinder, introduction of new methods for the search of the optimum flap sequences, comparisons of the actuator cylinder flow model (ACM) and 2D inviscid-unsteady panel model (PM). For the flap studies, the ACM is used as the primary tool where the PM is used as the verification tool. During the airfoil design the genetic algorithm and RFOIL are used as the numerical basis for the work. Detailed conclusions for the work has already been given at the end of each corresponding chapter. Here, the critical results will summarized briefly. These critical results can be listed as:

- The studies of a VAWT with infinite number of blades (actuator cylinder) showed that the optimum rotor loading is not a single ideal but can be obtained by various types of loadings (loadforms). This statement is supported by two different loadform studies, the analytical loadforms and the Bezier loadforms. Similarly, it has been shown that one can obtain different  $C_P$  while keeping the  $C_T$  constant and vice versa. These findings present important fundamental relations for the future VAWT blade designer.
- The optimum flap sequences are searched by two different methods: the inverse and direct method. The inverse method showed that it is quite fast and guarantees a superior performance. But it is hard to generalize the inverse method for every rotor, flow case, airfoil and flap type. One can easily get unrealistic flap demands from the inverse method. Because of these preliminary thoughts the inverse method

has not been used widely in this thesis. But it has a room for improvement. On the other hand, the direct method offers reliability with a drawback such as longer computation time. The inverse method needs few seconds while the direct method requires few minutes to find an optimum flap sequence for a specific case. Nevertheless, the direct method is chosen to explore the capabilities of the VAWT blade with an active flap.

- The optimum flap sequences regarding to three different aerodynamic objectives are found. These flap sequences showed that the VAWT performance can be dramatically changed with the existence of a trailing edge flap. The improvement levels depend on rotor solidity, tip speed ratio, airfoil and flap sizing. For  $\sigma = 0.1$  at  $\lambda = 4$ , a 10% flap with  $\pm 20$  degree actuation range can increase the  $C_P$  by 7%, alleviate the  $C_P$  by 10% and decrease the  $C_T$  around 12% while sustaining a favorable  $C_P$ . Higher flap authority (flap sensitivity, actuation range, etc.) is able to make a bigger effect on the performance. It is partly shown that a flap can be used as an air brake as well.
- The ACM is found as a robust tool to assess the VAWT performance. The modified-linear (Mod-Lin) version is used in this work. It has been experienced that this version gives reliable results except at the highly loaded rotor cases ( $C_T \sim 1$ ). The user should be aware of these cases. For the major part of the optimization cases, the ACM estimations are in line with the estimations by the PM.
- A new airfoil design methodology is formed to obtain VAWT airfoils with remarkable aerodynamic and structural performance. Few of the optimum airfoils are shown in the report. These airfoils have thicknesses between 27% and 31% of the chord and have a slight positive camber. They have favorable VAWT performance even without the flap actuation. They acquire very high flap sensitivities so that the flap system have higher authority on the rotor with a lower cost. The sensitivity of the new airfoils to the surface roughness is low within their thickness class.

As mentioned, these points can be shown as the main outcomes of this research. The 2-D lift-driven Vertical Axis Wind Turbine has shown that its performance can be increased dramatically by the introduction of the new concepts and methodologies. Although many results are shown as the "optimum", there is still a very large room for improvement. This report can be treated as the igniter to the more sophisticated future research on the flap and airfoil design for lift-driven VAWTs.

## 7.2 Future work

Throughout this project many sub-fields of research has been explored. These fields were required to present more reliable and refined results. Unfortunately most of these works remained untouched. Therefore they have been listed below to show possible directions to the future research.

- The Mod-Lin ACM needs a correction for the highly loaded cases. Its uncertainty is very high in such cases. The upwind estimation has a lower level of uncertainty

than the leeward, windward and downwind regions. Therefore the new correction could act as a local performance modifier. Local  $C_P$  and  $C_T$  could be used as the measures to assess the need for the high-loading correction. If the recent Mod-Lin ACM version is used in the further work, one has to limit the maximum  $C_T$  with a bound lower than 1, this value can be taken as 0.89.

- Additional aerodynamic models to mimic the dynamic stall, flow curvature and blade vortex interaction could be embedded into the ACM work-flow to have more reliable results, especially for the low tip speed ratio estimations and the rotors with high  $\frac{c}{R}$ .
- The  $C_P$  values obtained by the ACM in the viscous cases were very promising. A big reason for the high values was the neglected aerodynamic losses due to the structural components such as struts and tower. Therefore, these losses should also be included in the model in order to estimate the performance in a higher accuracy. If a 3D rotor is considered then one could also include the losses due to the trailing vorticity.
- The direct method to find the flap sequences uses the Bezier curves to define the azimuthal control demands. This was done since there was no concrete idea on how the optimum actuation demand would look like. Now it is known that most of the optimized sequences are close to the sinusoidal shapes. Therefore as a simplified and a faster approach one can optimize the flap sequences for the sinusoidal signals. The variables for such signals can be the signal magnitude, the shift on the magnitude and and the phase angle of the signal.
- The performance improvements shown by the flaps were preliminary. As a next step, one can find conduct a flap sizing study by considering the aerodynamic objectives, cost of the system and actuation power within the limits defined by recent trailing edge flap technology. Therefore more reliable "optimums" could be presented than the "optimums" shown in this work.
- The self-starting and braking capabilities of the VAWT should also be improved. These topics are not visited in this work and their feasibility study has to be done with the flaps. Note that to assess the self-starting capabilities one would need reliable estimations of the airfoil and rotor performance at high angle of attacks. Alternatively, slats could be a better choice than the flaps for the start-up considerations.
- The performance of the flap sequences has to be verified with higher order numerical models and experimental work.
- The aerodynamic objective function for the airfoil design is used as a representative of the exact analytic derivation. In the future research, a new aerodynamic function could be derived that is closer to the scope of the analytic expression. For the structural objective it is important to be aware of the constraints that are valid for the VAWT blade.



---

## References

- [1] Bak, C., Gaudern, N., Zahle, F., and Vronsky, T. (2014). Airfoil design: Finding the balance between design lift and structural stiffness. *Journal of Physics: Conference Series 524 012017*.
- [2] Barlas, T. K. and van Kuik, G. A. M. (2010). Review of state of the art in smart rotor control research for wind turbines. *Progress in Aerospace Sciences*, 46:1–27.
- [3] Bergami, L. (2013). *Adaptive Trailing Edge Flaps for Active Load Alleviation in a Smart Rotor Configuration*. PhD thesis, Technical University of Denmark.
- [4] Bizzarrini, N., Grasso, F., and Coiro, D. P. (2011). Genetic algorithms in wind turbine airfoil design. Technical report, ECN. ECN-M-11-035.
- [5] Björck, A. (1990). Coordinates and calculations for the ffa-w1-xxx, ffa-w2-xxx and ffa-w3-xxx series of airfoils for horizontal axis wind turbines. Technical report, The Aeronautical Research Institute of Sweden. FFA TN 1990-15.
- [6] Chougule, P. and Nielsen, S. (2014). Overview and design of self acting pitch control mechanism for vertical axis wind turbine using multi body simulation approach. In *Proceedings of Torque 2014 : The science of making torque from wind*.
- [7] Claessens, M. C. (2009). The design and testing of airfoils for application in small vertical axis turbines. Master’s thesis, Delft University of Technology.
- [8] Dahl, K. S. and Fuglsang, P. (1998). Design of the wind turbine airfoil family risø-a-xx. Technical report, Risø National Laboratory. Risø-R-1024(EN).
- [9] Drela, M. (1989). Xfoil: an analysis and design system for low reynolds number airfoils. In *Low Reynolds number aerodynamics*, volume 54, pages 1–12. Springer-Verlag.
- [10] EPO (1995). European patent specification no. 0 506 749 b1. Inventor: Brown K.C.
- [11] Eppler, R. and Somers, D. M. (1980). A computer program for the design and analysis of low-speed airfoils. Technical report, NASA. NASA TM-80210.

- [12] Erickson, D. W., Wallace, J. J., and Peraire, J. (2011). Performance characterization of cyclic blade pitch variation on a vertical axis wind turbine. In *49th AIAA Aerospace Sciences meetin including the New Horizons Forum and Aerospace Exposition*. AIAA 2011-638.
- [13] EWEA (2013). The european wind initiative - wind power research and developement to 2020. Technical report, European Wind Energy Association.
- [14] EWETP (2014). Strategic research agenda - market deployment strategy. Technical report, European Wind Energy Technology Platform.
- [15] Ferreira, C. S. J. (2009). *The Near Wake of the VAWT: 2D and 3D Views of the VAWT Aerodynamics*. PhD thesis, Delft University of Technology.
- [16] Ferreira, C. S. J., Barone, M., Zanon, A., Kemp, R., and Giannattasio, P. (2015). Airfoil optimization for stall regulated vertical axis wind turbines. In *AIAA SciTech 33rd Wind Energy Symposium*. AIAA 2015-0722.
- [17] Ferreira, C. S. J. and Geurts, B. (2014). Aerofoil optimization for vertical axis wind turbines. *Wind Energy*. doi:10.1002/we.1762.
- [18] Ferreira, C. S. J., Hofemann, C., Dixon, K., van Kuik, G., and van Bussel, G. (2010). 3d wake dynamics of the vawt: Experimental and numerical investigation. *48th AIAA Aerospace Sciences Meeting Including the New Horizons Forum and Aerospace Exposition*. AIAA 2010-643.
- [19] Ferreira, C. S. J., Madsen, H. A., Barone, M., Roscher, B., Deglaire, P., and Arduin, I. (2014). Comparison of aerodynamic models for vertical axis wind turbines. In *Proceedings of Torque 2014 : The science of making torque from wind*.
- [20] Ferreira, C. S. J. and Scheurich, F. (2014). Demonstrating that power and instantaneous loads are decoupled in a vertical-axis wind turbine. *Wind Energy*, 17(3):385–396.
- [21] Fuglsang, P. and Bak, C. (2004). Developement of the risøwind turbine airfoils. *Wind Energy*, 7:145–162.
- [22] Fujisawa, N. and Shibuya, S. (2001). 2001. *Journal of Wind Engineering and Industrial Aerodynamics*, 89:201–215.
- [23] Galbraith, R. A. M., Coton, F. N., and Dachun, J. (1992). Aerodynamic design of vertical axis wind turbines. Technical report, Glasgow University. GU aero report no. 9246.
- [24] Garcia, N. R. (2011). *Unsteady Viscous-Inviscid Interaction Technique for Wind Turbine Airfoils*. PhD thesis, Technical University of Denmark.
- [25] Gardner, B. A. and Selig, M. S. (2003). Airfoil design using a genetic algorithm and an inverse method. In *41st Aerospace Sciences Meeting and Exhibit*.
- [26] Grasso, F. (2011). Usage of numerical optimization in wind turbine airfoil design. *Journal of Aircraft*, 48:248–255.

- [27] Healy, J. V. (1978a). The influence of blade camber on the output of vertical axis wind turbines. *Wind Engineering*, 2:146–155.
- [28] Healy, J. V. (1978b). The influence of blade thickness on the output of vertical axis wind turbines. *Wind Engineering*, 2:1–9.
- [29] Islam, M., Ting, D. S. K., and Fartaj, A. (2007). Desirable airfoil features for smaller capacity straight bladed vawt. *Wind Engineering*, 31:165–196.
- [30] Johnson, S. J., van Dam, C. P., and Berg, D. E. (2008). Active load control techniques for wind turbines. Technical report, Sandia National Laboratories. SAND 2008-4809.
- [31] Kato, Y., Seki, K., and Shimizu, Y. (1980). Vertical axis wind turbine designed aerodynamically at tokai university. Technical report, Tokai University.
- [32] Katz, J. and Plotkin, A. (2010). *Low-Speed Aerodynamics*. Cambridge University Press.
- [33] Kemp, R. (2015). Airfoil optimization for vertical axis wind turbines. Master’s thesis, Delft University of Technology.
- [34] Kirke, B. K. (1998). *Evaluation of self-starting vertical axis wind turbines for stand-alone applications*. PhD thesis, Griffith University.
- [35] Kirke, B. K. and Lazauskas, L. (2011). Limitations of fixed pitch darrieus hydrokinetic turbines and the challenge of variable pitch. *Renewable Energy*, 36:893–897.
- [36] Klimas, P. C. (1982). Darrieus rotor aerodynamics. *Journal of Solar Engineering*, 104:102–105.
- [37] Klimas, P. C. (1992). Tailored airfoils for vertical axis wind turbines. Technical report, Sandia National Laboratories. SAND84-1062.
- [38] Klimas, P. C. and Sheldahl, R. E. (1978). Four aerodynamic prediction schemes for vertical axis wind turbines. Technical report, Sandia National Laboratories. SAND78-0014.
- [39] Kulfan, B. M. (2008). Universal parametric geometry representation method. *Journal of Aircraft*, 45:142–158.
- [40] Larsen, T. J. and Hansen, A. M. (December 2007). *How 2 HAWC2, the user’s manual*. Technical University of Denmark, risø-r-1597 edition.
- [41] Larsen, T. J. and Madsen, H. A. (2013). On the way to reliable aeroelastic load simulation on vawt’s. In *Proceedings of EWEA 2013*. European Wind Energy Association.
- [42] Lazauskas, L. (1992). Three pitch control systems for vertical axis wind turbines compared. *Wind Engineering*, 16(5):269–282.
- [43] Lazauskas, L. and Kirke, B. K. (1992). Performance optimisation of a self-acting variable pitch vertical axis wind turbine. *Wind Engineering*, 16(1):10–26.

- [44] Madsen, H. A. (1982). *The Actuator Cylinder - A flow model for vertical axis wind turbines*. PhD thesis, Aalborg University Centre.
- [45] Madsen, H. A., Larsen, T. J., Paulsen, U. W., and Vita, L. (2013). Implementation of the actuator cylinder flow model in the hawc2 code for aeroelastic simulations on vertical axis wind turbines. In *Proceedings of 51st AIAA Aerospace Sciences Meeting including the New Horizons Forum and Aerospace Exposition*. AIAA. 2014. AIAA 2013-0913.
- [46] Madsen, H. A., Paulsen, S. U., and Vita, L. (2012). Analysis of vawt aerodynamics and design using the actuator cylinder flow model. In *Proceedings of Torque 2012 : The science of making torque from wind*.
- [47] MathWorks (2012). *Matlab Primer for R2012b*. MathWorks Inc.
- [48] Migliore, P. G. and Fritschen, J. R. (1982). Darrieus wind turbine airfoil configurations. Technical report, Solar Energy Research Institute. SERI/TR-11045-1.
- [49] Migliore, P. G., Wolfe, W. P., and Fanucci, J. B. (1980). Flow curvature effects on darrieus turbine blade aerodynamics. *Journal of Energy*, 4. Article no. 79-0112R.
- [50] Oliveira, G. (2011). A novel approach to wind turbine airfoil design with boundary layer suction. Master's thesis, Delft University of Technology.
- [51] Paraschivoiu, I. (2002). *Wind Turbine Design: with Emphasis on Darrieus Concept*. Polytechnic International Press.
- [52] Paraschivoiu, I., Trifu, O., and Saeed, F. (2009). H-darrieus wind turbine with blade pitch control. *International Journal of Rotating Machinery*, 2009. Article ID 505343.
- [53] Pawsey, N. C. K. (2002). *Development and evaluation of passive variable-pitch vertical axis wind turbines*. PhD thesis, The University of New South Wales.
- [54] Ragni, D., Ferreira, C. S. J., and Barone, M. (2014). Experimental and numerical investigation of an optimized airfoil for vertical axis wind turbines. In *AIAA SciTech 32nd ASME Wind Energy Symposium*. AIAA 2014-0171.
- [55] Scheurich, F., Fletcher, T. M., and Brown, R. E. (2010). Simulating the aerodynamic performance and wake dynamics of a vertical axis wind turbine. *Wind Energy*, 14:159–177.
- [56] Shen, J., Yang, M., and Chopra, I. (2003). A parametric design study for a swash-plateless helicopter rotor with trailing edge flaps. *Journal of Aircraft*, 43:346–352.
- [57] Snyder, M. H. and Furukawa, N. (1979). Comparison of performance of darrieus wind turbines having 12% and 21% thick sections. Technical report, Wichita State University. Wind Energy Report no. 6.
- [58] Strickland, J. (1976). A performance prediction model for the darrieus turbine. In *Wind Energy Systems Symposium*.

- [59] Strickland, J. B., Webster, B. T., and Nguyen, T. (1981). Vortex model of the darrieus turbine: An analytical and experimental study. Technical report, Sandia National Laboratory. SAND 81-7017.
- [60] Sutherland, H. J., Berg, D. E., and Ashwill, T. D. (2012). A retrospective of vawt technology. Technical report, Sandia National Laboratories. SAND2012-0304.
- [61] Tangler, J. L. and Somers, D. M. (1995). Nrel airfoil families for hawts. Technical report, NREL. NREL/TP-442-7109.
- [62] Templin, R. J. (1974). Aerodynamic performance theory for the nrc vertical axis wind turbine. Technical report, NASA/STI Recon. LTR-LA-190.
- [63] Timmer, W. A. and Schaffarczyk, A. P. (2004). The effect of roughness at high reynolds numbers on the performance of aerofoil du 97-w-300mod. *Wind Energy*, 7:295–307.
- [64] Timmer, W. A. and van Rooij, R. P. J. O. M. (2003a). Roughness sensitivity considerations for thick rotor blade airfoils. *Journal of Solar Energy*, 125:468–478.
- [65] Timmer, W. A. and van Rooij, R. P. J. O. M. (2003b). Summary of the delft university wind turbine dedicated airfoils. *AIAA*.
- [66] Troldborg, N. (2005). Computational study of the risø-b1-18 airfoil with a hinged flap providing variable trailing edge geometry. *Wind Engineering*, 29:89–113.
- [67] Vandenberghe, D. and Dick, E. (1986). Theoretical and experimental investigation into the straight bladed vertical axis wind turbine with second order harmonic pitch control. *Wind Engineering*, 10(3):122–138.
- [68] Vandenberghe, D. and Dick, E. (1987). Optimum pitch control for vertical axis wind turbines. *Wind Engineering*, 11(5):237–247.
- [69] Vita, L. (2011). *Offshore floating vertical axis wind turbines with rotating platform*. PhD thesis, Technical University of Denmark.
- [70] Walters, R. E. and Migliore, P. G. (1977). The circulation controlled vertical axis wind turbine. *Third biennial conference and workshop on wind energy conversion systems, Massachusetts, U.S.A.*, 2:Washington D.C., U.S.A. Sep.19–21,1977.
- [71] Wolff, T., Ernst, B., and Seume, J. R. (2014). Aerodynamic behavior of an airfoil with morphing trailing edge for wind turbine applications. In *Journal of Physics; Conference Series: 524(2014)012018*.
- [72] Xiao, Q., Liu, W., and Incecik, A. (2013). Flow control for vawt by fixed and oscillating flap. *Renewable Energy*, 51:141–152.
- [73] Zanon, A., Giannattasio, P., and Ferreira, C. S. J. (2012). A vortex panel method for the simulation of the wake flow past a vertical axis wind turbine in dynamic stall. *Wind Energy*.
- [74] Zervos, A. (1989). Aerodynamic evaluation of blade profiles for vertical axis wind turbines. In *European Community Wind Energy Conference*.

- [75] Zervos, A., Dessipris, S., and Athanassiadis, N. (1985). Optimization of the performance of the variable pitch vertical axis wind turbine. pages 411–416.
- [76] Zhu, W. J., Shen, W. Z., and Sorensen, J. N. (2014). Integrated airfoil and blade design method for large wind turbines. *Renewable Energy*, 70:172–183.

---

# Appendix A

---

## MGS airfoils

*Table A.1: CST variables for the MGS airfoils (269, 283, 286, 309).*

Airfoil	MGS-269		MGS-283		MGS-286		MGS-309	
Side	SUC	PRES	SUC	PRES	SUC	PRES	SUC	PRES
$B_1$	0.34144	-0.26309	0.28631	-0.27684	0.30178	-0.29143	0.39364	-0.33693
$B_2$	0.32674	-0.34310	0.35409	-0.35431	0.33568	-0.35955	0.31967	-0.36178
$B_3$	0.38509	-0.31101	0.40943	-0.33378	0.43992	-0.36442	0.54841	-0.43761
$B_4$	0.37200	-0.33279	0.48145	-0.37889	0.47510	-0.34742	0.28532	-0.40350
$B_5$	0.27670	-0.53520	0.21228	-0.45867	0.23043	-0.44061	0.33670	-0.50389
$B_6$	0.25474	-0.18513	0.22653	-0.15736	0.18658	-0.18338	0.18709	-0.40583
$B_7$	0.41094	-0.34329	0.13299	-0.21632	0.23647	-0.18423	0.34062	-0.29277
$B_8$	0.16025	-0.02061	0.18977	0.03406	0.20094	0.01100	-0.01507	-0.09154
$\zeta TE$	0.00429	0.00429	0.00383	0.00383	0.00385	0.00385	0.00524	0.00524

*Table A.2: CST variables for the MGS airfoils (322, 331, 343, 348).*

Airfoil	MGS-322		MGS-331		MGS-343		MGS-348	
Side	SUC	PRES	SUC	PRES	SUC	PRES	SUC	PRES
$B_1$	0.36159	-0.61392	0.35643	-0.63002	0.35315	-0.62176	0.31027	-1.28086
$B_2$	0.32156	-0.35458	0.32098	-0.40996	0.31761	-0.45457	0.32531	-0.32617
$B_3$	0.52280	-0.49111	0.51463	-0.52572	0.57395	-0.56625	0.47619	-0.51383
$B_4$	0.42158	-0.46297	0.40638	-0.45449	0.33741	-0.40439	0.50061	-0.38666
$B_5$	0.14082	-0.43576	0.15444	-0.48400	0.23349	-0.55855	0.25568	-0.43408
$B_6$	0.02590	-0.22787	0.00498	-0.22684	0.08698	-0.18757	0.14551	-0.11397
$B_7$	0.41859	-0.20859	0.41887	-0.21038	0.41292	-0.29086	0.33096	-0.23815
$B_8$	0.07087	0.00927	0.03426	-0.00845	0.02502	0.06911	0.31328	-0.12680
$\zeta TE$	0.00339	0.00339	0.00342	0.00342	0.00379	0.00379	0.00403	0.00403

## MGS-269

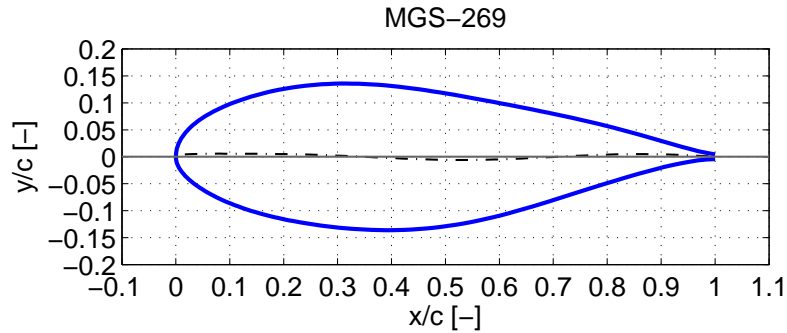


Figure A.1: Geometry of the MGS-269.

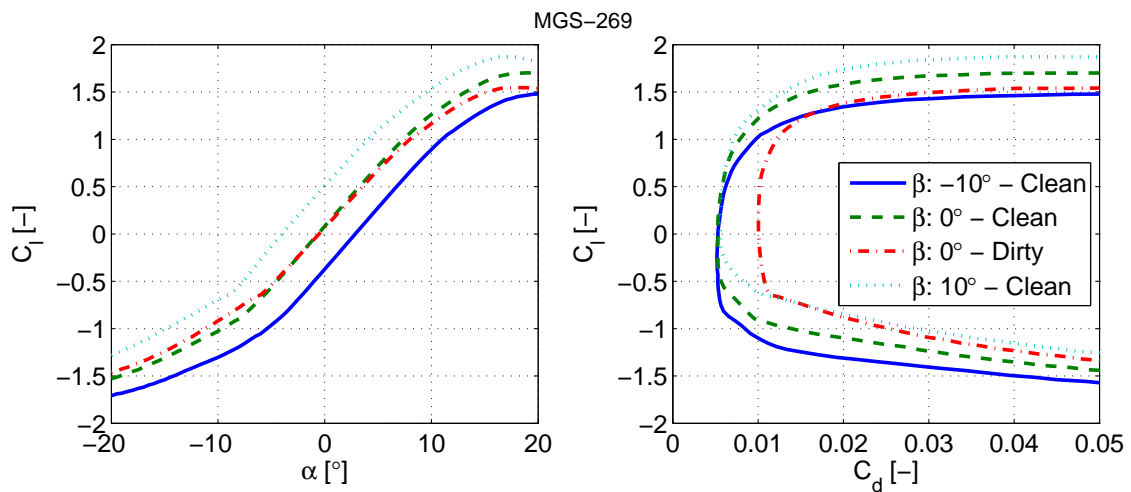


Figure A.2: Aerodynamic polars of the MGS-269.

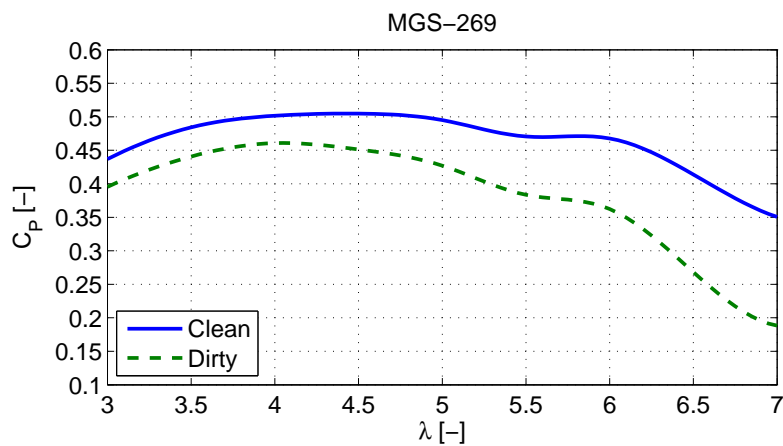


Figure A.3: VAWT performance of the undeflected MGS-269 for the clean and dirty conditions.

## MGS-283

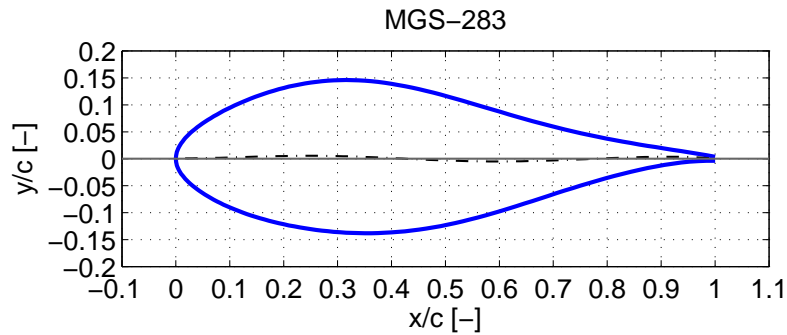


Figure A.4: Geometry of the MGS-283.

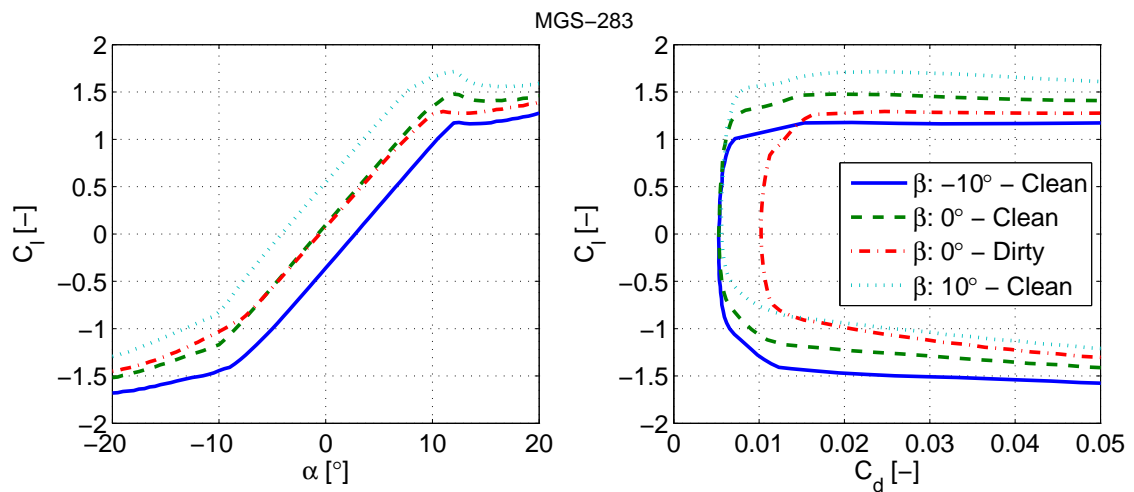


Figure A.5: Aerodynamic polars of the MGS-283.

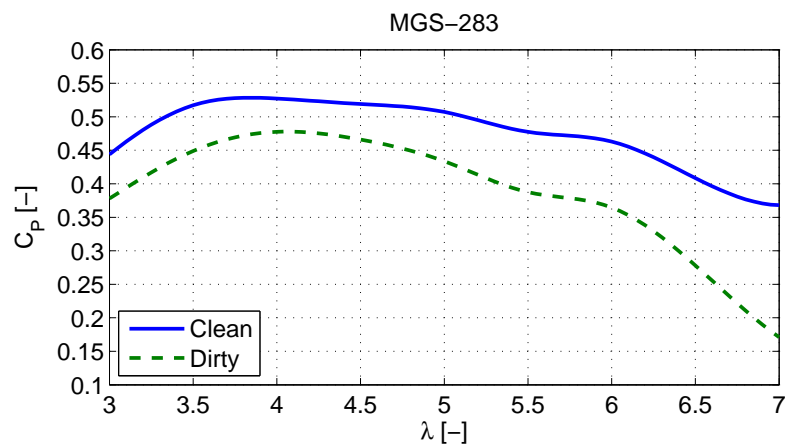
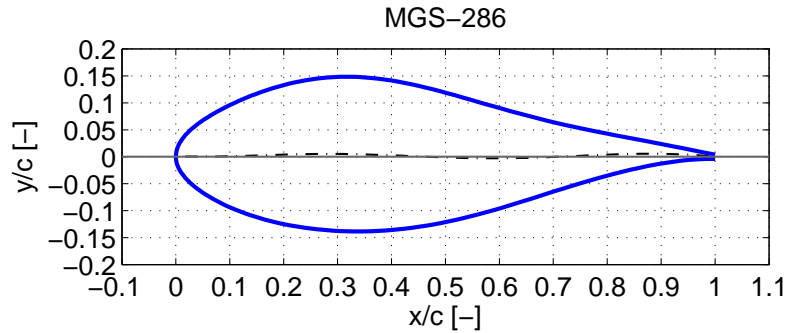
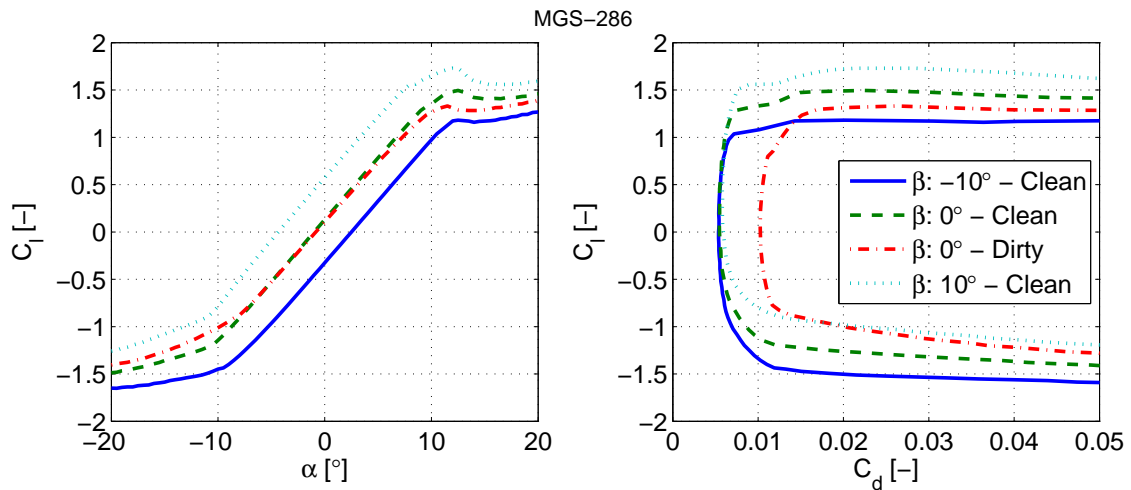


Figure A.6: VAWT performance of the undeflected MGS-283 for the clean and dirty conditions.

## MGS-286



*Figure A.7: Geometry of the MGS-286.*



*Figure A.8: Aerodynamic polars of the MGS-286.*

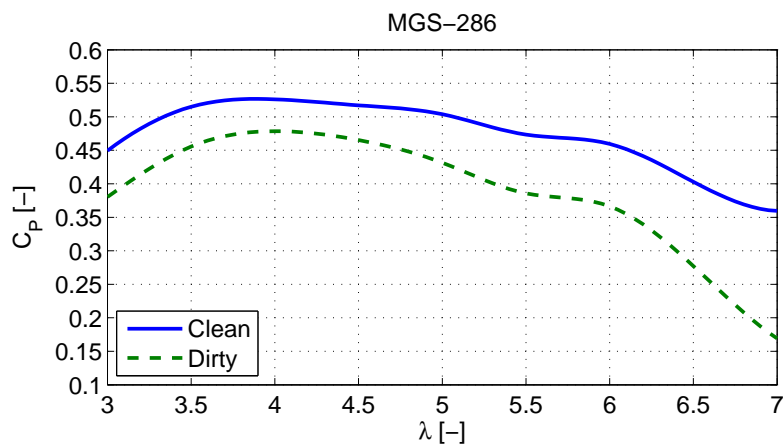


*Figure A.9: VAWT performance of the undeflected MGS-286 for the clean and dirty conditions.*

## MGS-309

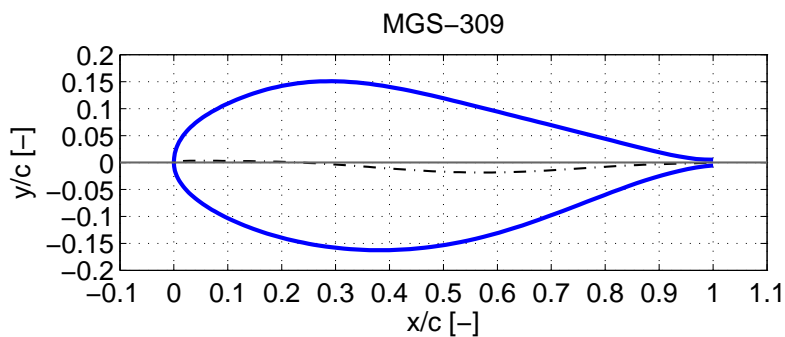


Figure A.10: Geometry of the MGS-309.

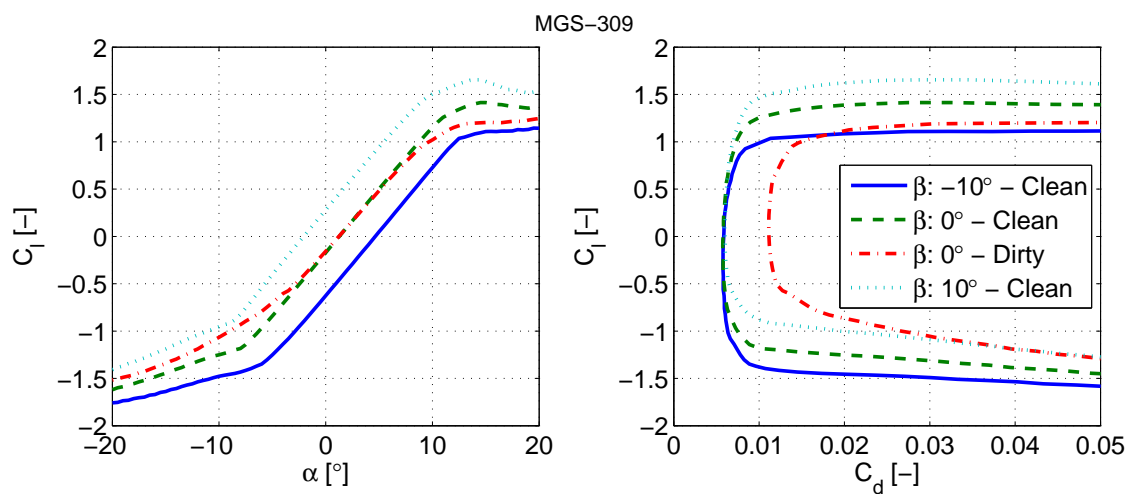


Figure A.11: Aerodynamic polars of the MGS-309.

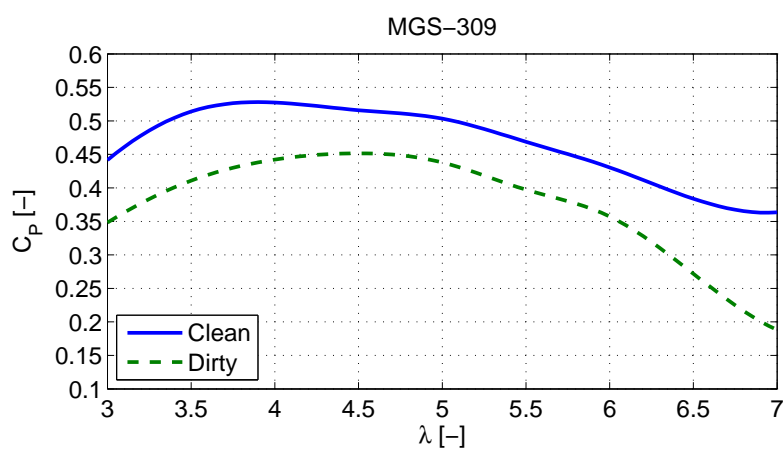


Figure A.12: VAWT performance of the undeflected MGS-309 for the clean and dirty conditions.

## MGS-322

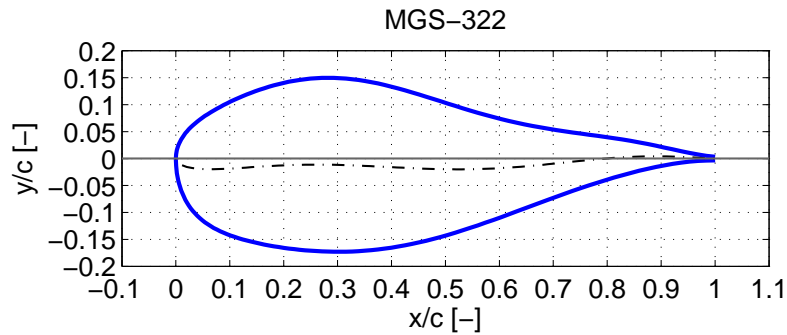


Figure A.13: Geometry of the MGS-322.

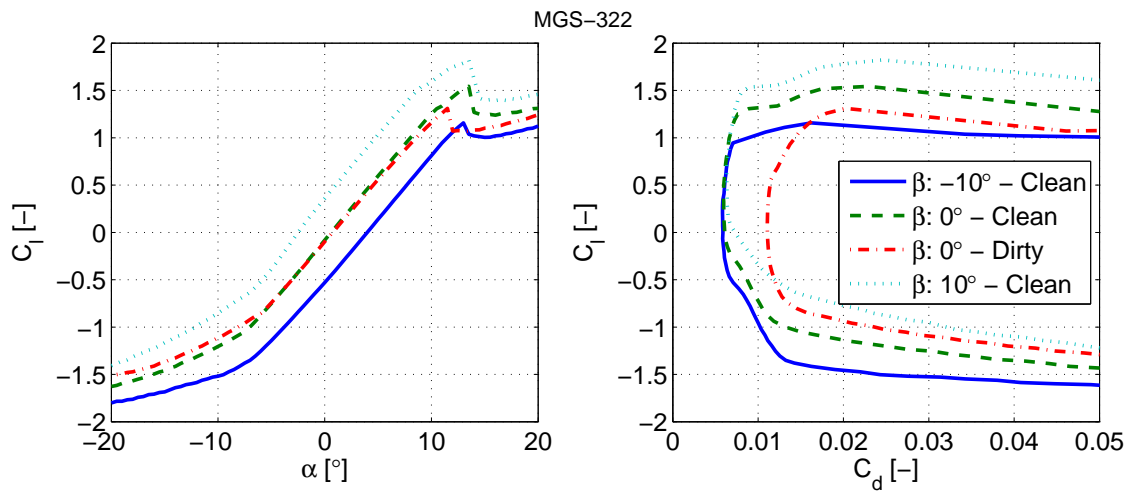


Figure A.14: Aerodynamic polars of the MGS-322.

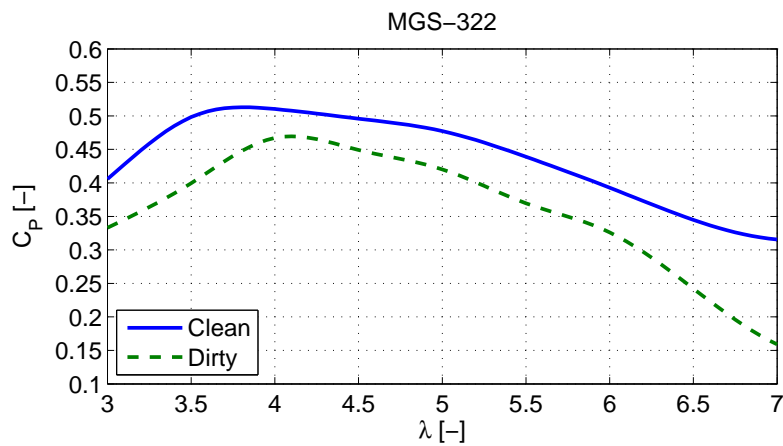


Figure A.15: VAWT performance of the undeflected MGS-322 for the clean and dirty conditions.

## MGS-331

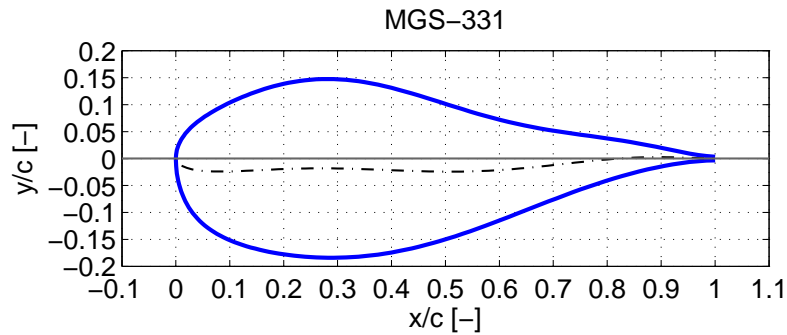


Figure A.16: Geometry of the MGS-331.

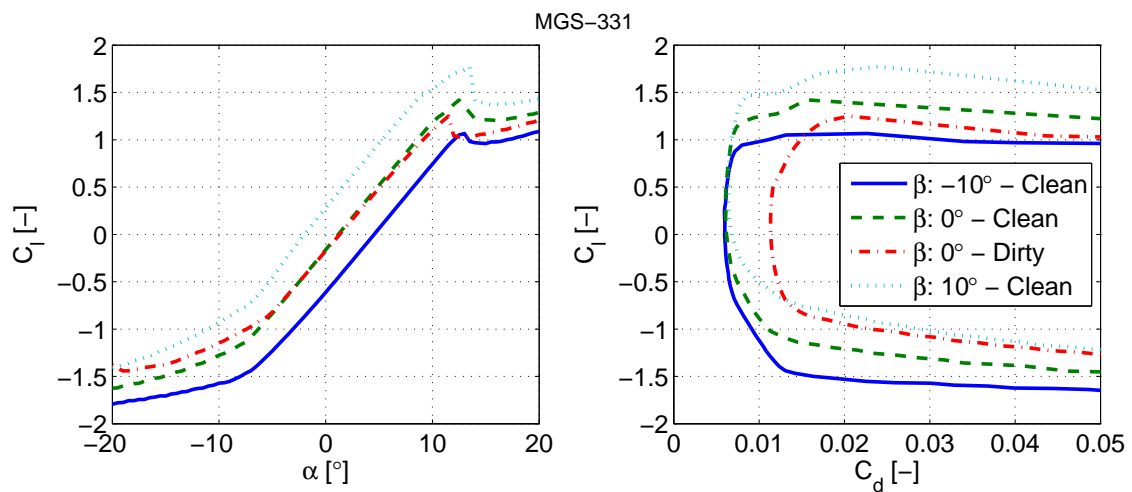


Figure A.17: Aerodynamic polars of the MGS-331.

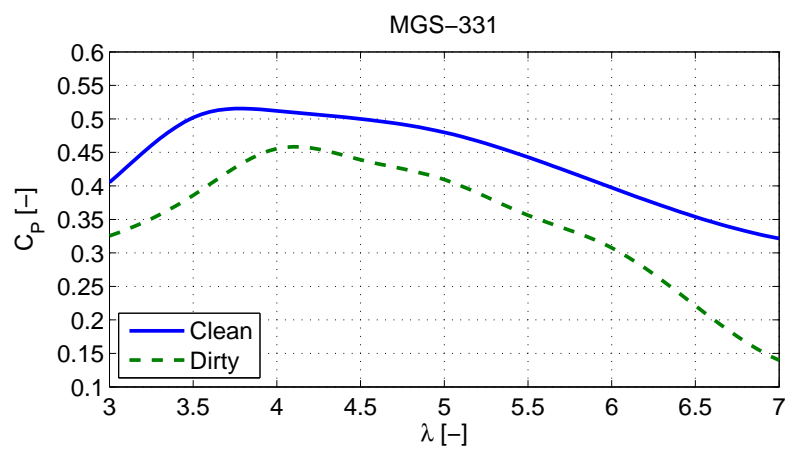


Figure A.18: VAWT performance of the undeflected MGS-331 for the clean and dirty conditions.

## MGS-343

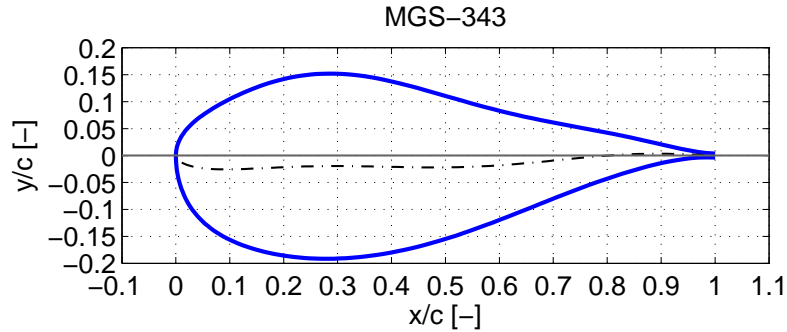


Figure A.19: Geometry of the MGS-343.

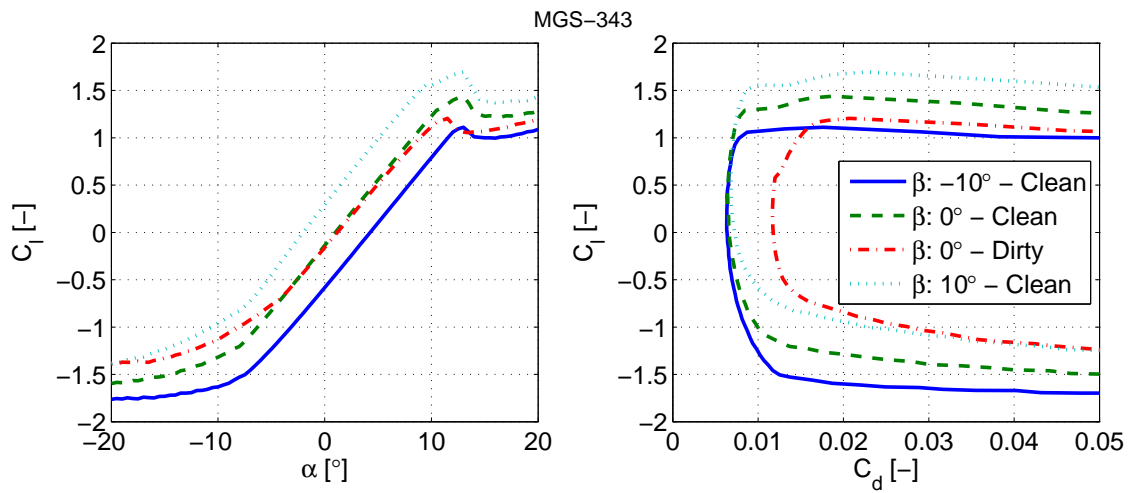


Figure A.20: Aerodynamic polars of the MGS-343.

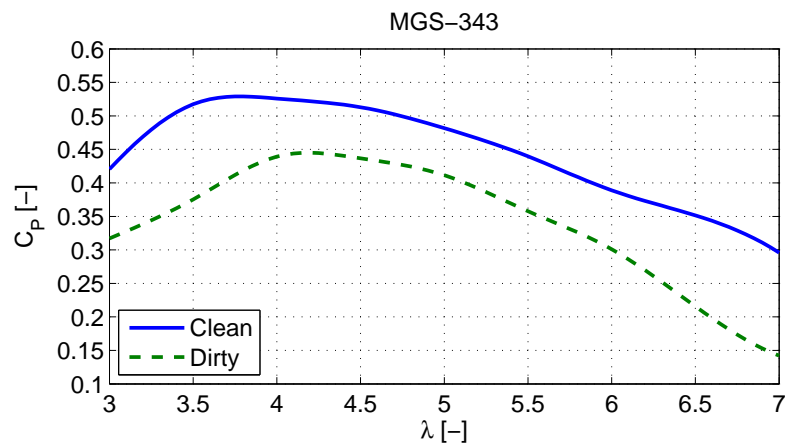


Figure A.21: VAWT performance of the undeflected MGS-343 for the clean and dirty conditions.

## MGS-349

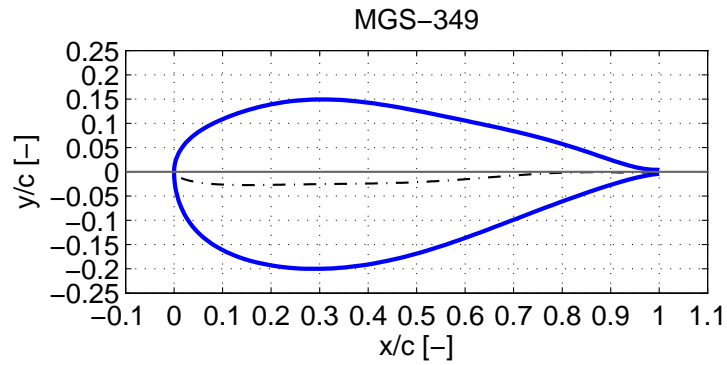


Figure A.22: Geometry of the MGS-349.

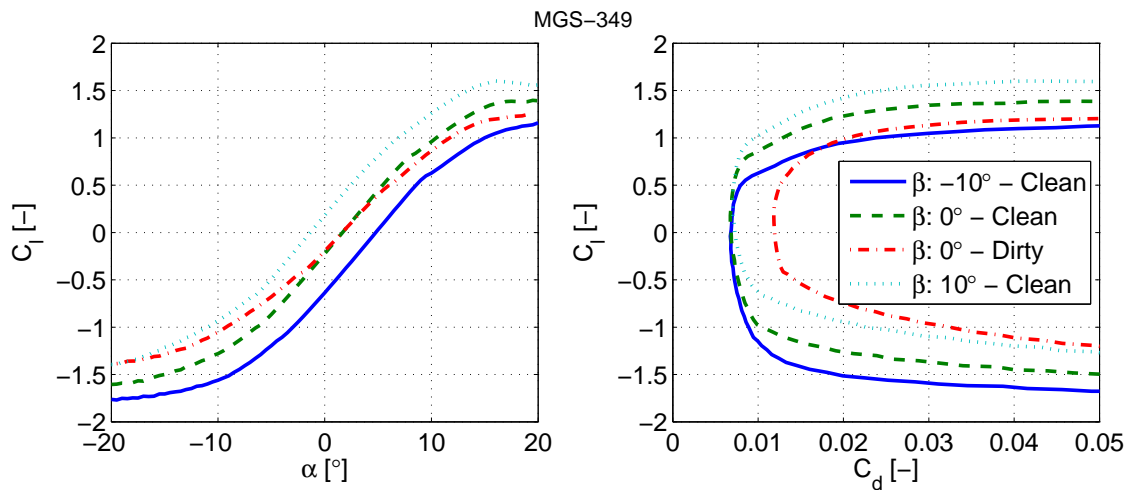


Figure A.23: Aerodynamic polars of the MGS-349.

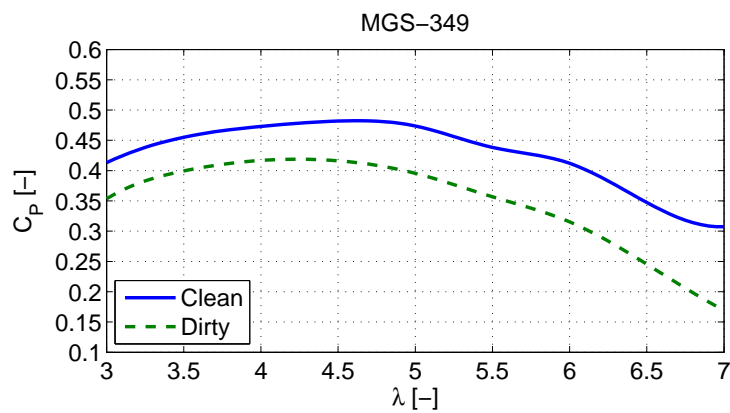


Figure A.24: VAWT performance of the undeflected MGS-349 for the clean and dirty conditions.

